OPTICAL DIAGNOSTICS OF METALS IN HIGH TEMPERATURE ENVIRONMENTS

LI-JEN HSU

2012

OPTICAL DIAGNOSTICS OF METALS IN HIGH TEMPERATURE ENVIRONMENTS

Li – Jen Hsu

Ph.D. thesis

May 2012

Centre for Energy Technology, The Environment Institute
School of Chemical Engineering
Faculty of Engineering, Computer & Mathematical Sciences
University of Adelaide, Australia.

Preface

The documentation is the demonstration of many years of study and submitted for the award of the Doctoral of Philosophy. The topic of research is “Optical Diagnostics of Metals in High Temperature Environments”. Alkali metals released from combustion of solid-fuel particles (Loy Yang Brown coal and pine wood) in premixed methane flat flame and iron in the plasma cloud generated by gas tungsten arc welding were investigated using optical diagnostic techniques. The consumption of renewable energy resources increasingly grows owing to the issues of global climate change and rapidly diminishing reserves of energy resources. Understanding of alkali metals released during combustion is important for the industrial interests to maintain and to improve the equipment for power generation. To apply the comprehensive laser diagnostic techniques extensively in extreme environments, the studying of iron in the welding plasma could favour the understanding of dynamic chemistry and the dispersion of chemical species in the plasma fumes.

The intention of this work is to assess techniques enabling the quantitative measure of sodium (Na) and potassium (K) released during the different stages of solid-fuel combustion so that industrial concerns can be satisfied. An understanding of the behaviour of iron (Fe) in atmospheric plasma would help reduce the hazard that it poses to operators.

Li-Jen Hsu

Declaration

This thesis contains no material which has been accepted for the award of any other degree or diploma in any university or other tertiary institution and, to the best of my knowledge and belief, contains no material previously published or written by another person, except where due reference has been referred in the text.

I give consent to this copy of my thesis when deposited in the University Library, being made available for loan and photocopying, subject to the provisions of the Copyright Act 1968.

The author acknowledges that the copyright of published works arising from this thesis (as listed in Appendix J-3) resides with the copyright holder(s) of those works.

I also give permission for the digital version of my thesis to be made available on the web, via the University's digital research repository, the Library catalogue, the Australasian Digital Theses Program (ADTP) and also through web search engines, unless permission has been granted by the University to restrict access for a period of time.

Li – Jen Hsu

Acknowledgements

I am grateful to appreciate the invaluable contributions from countless people who helped accomplish this thesis. First of all, it will be my honour to acknowledge my supervisors, Dr. **Zeyad T. Alwahabi**, Prof. **Graham (Gus) Nathan**, Prof. **Keith D. King** and A/Prof. **Peter J. Ashman** providing outstanding assistance not only for the thesis but also in the development of knowledge.

I also acknowledge Dr Zhongshan Li and Prof Marcus Aldén provided the opportunity for me to conduct part of my experiment in the Division of Combustion Physics, Lund University, Sweden. Other colleagues also helped me out in experiments and living in the Lund city.

It is also necessary to thank other colleagues, Dr. Philip van Eyk who shared his valuable experience and brilliant opinions on this thesis, Kenneth Ho who assisted with my experiments and Jian Wang helped with the data processing. I would like to thank Mary Barrow and Elaine Minerds, the Chemical Engineering School Officers, Sahn Tran from the IT support group, and Jason Peak and Jeffrey Hiorns from the workshops for their constant support throughout the course of this work. I apologize in advance for whom I have not personally thanked.

It is impossible for me to accomplish the thesis without my family's support, especially my parents, my wife and my children. My wife's support is always the strongest power for me to persist in my research while I feel depressed. Truly, I appreciate my dear families.

Abstract

The thesis presents results for the detection of metal species in high temperature environments using optical techniques. Three optical techniques, namely laser Polarisation Spectroscopy (PS), Atomic Emission Spectroscopy (AES) and Laser-Induced Breakdown Spectroscopy (LIBS) have been employed. Each technique possesses some unique characteristics to achieve the aims of this work.

The PS technique has been employed to detect atomic sodium (Na) in the seeded flames and plume of burning solid-fuel particles and to investigate atomic iron (Fe) in the welding fume plume. A mathematical equation has been developed to describe the lineshape of the target metal using PS technique in the high temperature environments, as follows:

$$I_{PS\_FIT}(\omega) = I_{baseline} + I_{PS} \times \left\{ \frac{1}{1+\left[\frac{2\times(\Delta\omega-\Delta\omega_{shift})}{\Delta\omega_{PS}}\right]^2} \right\}^n \times exp\left[\frac{-\alpha_0 \cdot L_{abs}}{1+\left(\frac{2\times\Delta\omega}{\Delta\omega_{abs}}\right)^2} \right]$$

Eq. 3-5

The capability of PS technique employed for the quantitative measurement has been assessed. Due to the nonlinear measurement, the quantitative measurement using PS is not applicable in this work. In particular, the atomic Na released from burning solid-fuel particles. However, the qualitative analysis of atomic Na and Fe has been demonstrated. The time-resolved records of atomic Na released from the burning solid-fuel particles and the Stark shift of atomic Fe in the welding fume have been observed.

The AES technique has been used to record the temporal atomic Na and K released from burning solid-fuel particles. The qualitative analysis of the simultaneous release of atomic Na

and K using AES has been demonstrated. However, the quantitative analysis is not applicable in the present experimental arrangement. The temporal records of atomic Na and K were associated with the instantaneous shrinkage of burning solid-fuel particles. This implies that the release of atomic Na and K is related to the burning particle size. It was observed that the peak release of atomic Na and K released from the burning solid-fuel particles occurred at the end of char phase simultaneously.

The quantitative measurement of atomic Na and K released from burning solid-fuel particles using LIBS has been achieved. The time-resolved histories of atomic Na and K released from burning solid-fuel particles are consistent with those measured using PS and AES. Unlike conventional quantitative measurement using LIBS, a particular absorption, termed as signal trapping to the calibration process, caused by the atomic Na or K in the outer seeded flames has been indentified.

The overall comparison among three optical techniques summarizes the advantages and disadvantages of the metal detection in high temperature environments. The PS technique is capable of being applied to detect metal species in strong background environments. The AES possesses the capability of multi-element detection in flames with the characteristics of low cost, good sensitivity and simple experimental arrangement. However, the quantitative analysis of target metal species is not eligible for both techniques. The LIBS technique demonstrates the quantitative analysis with an appropriate calibration curve.

Nomenclature

A	Pre-factor (experimentally determined), 1/concentration
	Empirical Pre-factor Coefficient, dimensionless
AFR_{exp}	Experimental AFR, dimensionless
AFR_{stoi}	Stoichiometric AFR, dimensionless
A_{21}	Spontaneous Emission, s^{-1}
A_r	Surface Area of a Sphere, m^2
a_1	Pre-factor, 1/concentration
a_2	Pre-factor Constant, dimensionless
a_m	Molar Ratio, dimensionless
B_{12}/B_{21}	Einstein Coefficient of Absorption / Stimulated Emission, $m^3 \cdot J^{-1} \cdot s^{-2}$
b	Absorption Coefficient, dimensionless
c	Specific Heat, $J \cdot kg^{-1} \cdot K^{-1}$
	Light Speed, $m \cdot s^{-1}$
C_s	Concentration of Alkali Salt, $g \cdot L^{-1}$
$C_{species}$	Concentration of Atomic Na or K in the flame, ppm
C_{Na}	Concentration of Na, ppm
C_K	Concentration of K, ppm
D_0	Diameter of Pump Beam, m
D_P	Diameter of Focused Pump Beam, m
D_{SD}	Diameter of Nebulised Salt Droplet, μm
ΔE	Energy Difference between Two Allowable Transition States, J
E_{BS}	Systematic Error Caused by Beam Steering, dimensionless
$F_{pump\text{-}probe\_geometry}(\gamma,\chi)$	Dependence of the I_{PS} on the Geometrical Polarisation Status of the

	Probe and Probe Beams
f_B	Boltzmann Fraction of Target Species, dimensionless
f_i	Boltzmann Distribution at the Energy State *i*, dimensionless
f_L	Focal Length of a Lens, mm
$G(\omega)$	Normalized Lineshape of the Target Species Absorption Function, dimensionless
g_i	Degeneracy of Energy State *i*, dimensionless
h	Planck's Constant (= 6.626×10^{-34}), J·s
	Surface Convection Coefficient, $W\cdot K^{-1}\cdot m^{-2}$
$\hbar$	Planck's Constant Divided by 2π, J·s
I_{abs}	Intensity of Absorption in PS Measurement, arbitrary unit
$I_{baseline}$	Intensity of Background in PS Measurement, arbitrary unit
I_{exp}	Experimental Radiation Intensity of Atomic Na or K, arbitrary unit
I_{act}	Actual Radiation Intensity of Atomic Na or K, arbitrary unit
I_{PS}	Intensity of PS Signal, arbitrary unit
I_{LIBS}	Intensity of Radiation using LIBS, dimensionless
$I_{PS\_FIT}(\omega)$	Simulation of PS Lineshape
I_{probe}	Intensity of Probe Beam in PS, arbitrary unit
I_{pump}	Intensity of Pump Beam in PS, arbitrary unit
k / k_p	Thermal Conductivity Coefficient, $W\cdot K^{-1}\cdot m^{-1}$
k	Boltzmann Constant, $J\cdot K^{-1}$
$[K]_{total}$	Total Concentration of K, ppm
$[K]_{total}^{max}$	Maximum Concentration of total K, ppm
L_{PS}	Probe Beam Path, m
M	Molar Mass, $g\cdot mol^{-1}$
ml_n	Normal Litre per Minute, L/min

$Mole_{oxy}$	Molar Ratio of Fed Oxidizer, mol
$Mole_{fuel}$	Molar Ratio of Fed Fuel, mol
$Mass_{oxy}$	Mass of Fed Oxidizer, g
$Mass_{fuel}$	Mass of Fed Fuel, g
$Mole_{stoi\text{-}oxy}$	Stoichiometric Molar Ratio of Oxidizer, dimensionless
$Mole_{stoi\text{-}fuel}$	Stoichiometric Molar Ratio of Fuel, dimensionless
$Mole_{exp\text{-}oxy}$	Experimental Molar Ratio of Oxidizer, dimensionless
$Mole_{exp\text{-}fuel}$	Experimental Molar Ratio of Fuel, dimensionless
$N_{species}$	Population of Target Species, atom·m^{-3}
n	Refractive Index, dimensionless
	Power of a Lorentzian function, dimensionless (3: Lorentzian-cubed; 1: Lorentzian)
n_s	Number Density of Target Species, atoms·m^{-3}
$[\mathrm{Na}]_{total}$	Total Concentration of Na, ppm
$[\mathrm{Na}]_{total}^{max}$	Maximum Concentration of total Na, ppm
P	Atmospheric Pressure, atm
Q	Hear Transfer, J
q	Partition Function, dimensionless
r	Radial Distance, m
r_c	Radii of Unconsumed Core, m
R	Radius of a Virgin Particle, m
	Gas Constant, J·g^{-1}·mol^{-1}·K^{-1}
$R_{K/Na}$	Release Ratio of K-to-Na, dimensionless
R_{coal}	First Order Reaction Rate of coal, s^{-1}
$R_{K\_char/de}$	Ratio of Peak Intensities of Atomic K at the Char and Devolatilisation Phases using AES, dimensionless
$R_{K\_total\_char/de}$	Ratio of Peak Intensities of Atomic K at the Char and

	Devolatilisation Phases using Quantitative LIBS, dimensionless
$R_{Na\_char/de}$	Ratio of Peak Intensities of Atomic Na at the Char and Devolatilisation Phases using AES, dimensionless
$R_{Na\_total\_char/de}$	Ratio of Peak Intensities of Atomic Na at the Char and Devolatilisation Phases using quantitative LIBS, dimensionless
S	Slope of Calibration Curve of LIBS Measurement, dimensionless
T	Local Particle Temperature, K
ΔT	Temperature Variation between Two Locations, K
T_0	Initial Particle Temperature, K
T_c	Temperature at Core Surface, K
T_f	Flame Temperature, K
T_g	Gas Temperature, K
T_P	Temperature of Coal Particle, K
T_s	Temperature at Particle Surface, K
T_r	Room Temperature, K (298 K)
υ_a	Air Flowrate, $L \cdot s^{-1}$
υ_f	Total Gas Flowrate, $L \cdot s^{-1}$
υ_g	Methane Flowrate, $L \cdot s^{-1}$
υ_m	Mass flowrate of seeding salt solution, $g \cdot s^{-1}$
υ_{mf}	Molar Flowrate of Total Gas, $mol \cdot s^{-1}$
υ_{ms}	Molar flowrate of seeded salt in the flame, $mol \cdot s^{-1}$
υ_s	Consumption Rate of Salt Solution, $L \cdot s^{-1}$
Δx	Shrinking Layer, m
x	Absorption Length, m
$[X]_{species}$	Concentration of target species, $atom \cdot m^{-3}$ or ppm

Greek Letters

Φ	Equivalence Ratio, dimensionless
$\alpha(\omega)$	Absorption Coefficient at Angular Frequency, m^{-1}
$\Delta\alpha_0(\omega)$	Induced Dichroism
$\sigma_a(\omega)$	Absorption Cross-Section at angular frequency, m^2
$\sigma_{J_f \leftarrow J_i}$	Absorption Cross-Section from the Initial to Final Rotational State, J
σ	Stefan-Boltzmann Constant, $W \cdot K^{-2} \cdot m^{-2}$
	Mean Relative Standard Deviation, dimensionless
θ	Angular Offset of the Two Polarisers, radians
λ	Wavelength, nm
ϕ	Phase of the Wave ($= k \cdot L_{PS}$)
δ	FWHM of the Lineshape of Wavelength Scan Measurement, cm^{-1}
ξ	Fractional Light Leakage, dimensionless
ρ	Particle Solid Density, $kg \cdot m^{-3}$
γ	Angle between the Polarisation Axis of the Probe Beam and the Vertical Axis, radians
κ	An Integral Constant, dimensionless
χ	Angle between the Pump and Probe Beam in the Horizontal Plane, Radians
$\zeta_{J_f \leftarrow J_i}$	Polarisation Dependent Numerical Factor, dimensionless
τ_{pump}	Laser Pulse Duration, ns
τ_d	Duration of the Devolatilisation Phase, *sec*
τ_c	Duration of the Char Phase, *sec*
τ_a	Duration of the Ash Cooking Phase, *sec*
ω_{12}/ω_{21}	Angular Frequency of the Transition, s^{-1}
ω	Chosen Angular Frequency, cm^{-1}
ω_0	Transition of Target Species, cm^{-1}

$\Delta\omega_{abs}$	FWHM of Absorption, cm^{-1}
$\Delta\omega_{collision}$	Collisional Broadening, cm^{-1}
$\Delta\omega^{H}$	Homogenous Line Broadening, cm^{-1}
$\Delta\omega_{n}$	Natural Linewidth, cm^{-1}
$\Delta\omega_{PS}$	FWHM of PS Signal, cm^{-1}
$\Delta\omega_{self}$	Self-broadening, cm^{-1}
ν	Frequency of Radiation, Hz
ε	Emissivity, dimensionless
	Ratio between Atomic Species and Total Amount of the Species, dimensionless
ψ	Surface Tension of Liquid, Water in This Work, $mN \cdot m^{-1}$
Λ	Total Electronic Orbital Angular Momentum Quantum Number
Σ, Π, Δ, Φ	Electronic Energy State corresponding to Λ = 0, 1, 2, 3, dimensionless

Subscripts

0	initial
a	air, area
abs	absorption
act	actual
c	core
cone	effective volume of the cone shape
exp	experimental
f	flame
g	gas
m	molar

max	maximum
probe	probe beam
PS	Polarisation Spectroscopy
pump	pump beam
r	room
s	salt
species	target species, such Na, K or Fe
total	total

Acronym

AES	Atomic Emission Spectroscopy
AFR	Air-Fuel Ratio
CNT	Carbon Nanotube
EDX or EDS	Energy-Dispersive X-Ray Spectroscopy
FTIR	Fourier Transform Infrared spectrometry
FWHM	Full Width at Half Maximum
GTAW	Gas Tungsten Arc Welding
HDP	High Density Plasma
HV	Heating Value
ICCD	Intensified Charge-Coupled Device
ICP-AES	Inductively Coupled Plasma Atomic Emission Spectroscopy
LIBS	Laser-Induced Breakdown Spectroscopy
LIPS	Laser-Induced Plasma Spectroscopy
LOD	Limit of Detection
IRPS	Infrared PS
IRLIF	Infrared LIF
LTE	Local Thermodynamic Equilibrium
MFC	Mass Flow Controller
MS	Mass Spectroscopy
ND filter	Neutral Density filter
NMR	Nuclear Magnetic Resonance
PLIF	Planar Laser-Induced Fluorescence
PS	Polarisation Spectroscopy

ppm	Part per Million
ppb	Part per Billion
SAES	Simultaneous Atomic Emission Spectroscopy
SEM	Scanning Electron Microscopy
SNR	Signal-to-Noise Ratio
TGA	Thermogravimetric Analysis
XRF	X-Ray Fluorescence
XRD	X-Ray Diffraction

Chemical Expression

Element

Aluminium	Al
Barium	Ba
Beryllium	Be
Carbon	C
Calcium	Ca
Chlorine	Cl
Chromium	Cr
Copper	Cu
Fluorine	F
Hydrogen	H
Iron	Fe
Lead	Pb
Manganese	Mn
Nickel	Ni
Nitrogen	N
Oxygen	O
Potassium	K

Silicon	Si
Sodium	Na
Strontium	Sr
Sulfur	S

Compounds

Acetylene	C_2H_2
Ammonia	NH_3
Carbon Radical	C_2
Carbon Monoxide	CO
Carbon Dioxide	CO_2
Cyanide	CN
Methylidyne	CH
Ethane	C_2H_6
Formaldehyde	H_2CO
Hydrogen Cyanide	HCN
Hydroxyl Radical	OH
Methane	CH_4
Methyl	CH_3
Nitrogen Monohydride	NH
Nitric Acid	HNO_3
Nitric Oxide	NO
Nitrogen Oxides	NO_x
Potassium Chloride	KCl
Potassium Sulphate	K_2SO_4
Sodium Chloride	NaCl
Sodium sulphite	Na_2SO_3

Content

List of Figures

List of Tables

CHAPTER 1

INTRODUCTION

In this chapter, a brief outline of the research field is conducted, motivating the work. The specific aims of this work are addressed followed by the dissertation layout. The literature overview demonstrates the metal detection and analysis in high temperature environments regarding the specific issues in this work. The metal detection and analysis can be achieved using *in situ* and indirect techniques. In this work, the findings of sodium (Na), potassium (K) and iron (Fe) detection in high temperature environments viz. flames and plasma using optical techniques were assessed. The optical techniques employed in this work include Atomic Emission Spectroscopy (AES) and two laser diagnostic techniques, namely Laser-Induced Breakdown Spectroscopy (LIBS) and laser Polarisation Spectroscopy (PS). The utilisation of each technique is determined by the purpose of the individual experiment.

1.1 Motivation

To assess metal detection in high temperature environments using optical techniques, three metals have been selected owing to the industrial interests of burning solid-fuel particles and welding hazards for human beings. The release of alkali metal compounds is potentially an issue causing corrosion in furnaces, in particular, sodium (Na) and potassium (K). The detection of iron (Fe) in the welding fume presents the welding performance.

Fossil fuels have been the major energy source for past decades. The alkali species released from coal combustion for power generation cause fouling and corrosion on heat transfer surfaces within the industrial coal-fired boilers [1]. These issues lead to unscheduled

shutdown for power plants. Hence, the understanding of emission of alkali species during coal combustion is useful for power generation industry. As a result of environmental issues and the shortage of fossil fuel, biomass has been considered to be an alternative energy source. However, due to the lower heat value (HV) of biomass compared to that of coal, the power generated using biomass currently is not enough for consumption demand and may not be cost effective. Although biomass employed for power generation reduces the emission of carbon dioxide (CO_2), similar issues to coal combustion, namely corrosion and fouling caused by the release of alkali metal species, also occur in biomass combustion [2-7]. Moreover, the atomic Na and K were found to be the precursor to cause corrosion while reacting with chlorine (Cl) [8] or sulfer (S) [9] on heat transfer surface.

Given significant issues caused by emission of alkali species, several techniques are available for analysis of alkali species released during solid-fuel combustion, such as ash analysis [10]. However, these techniques are indirect measurements of target species, which means the intermediate alkali species, such as atomic Na and K, are not applicable to be instantaneously detected. Hence, the laser diagnostic techniques become appropriate candidates to detect target species during solid-fuel combustion.

van Eyk et al. [11, 12] reported the quantitative measurement of atomic Na released from burning coal particles quantitatively and Saw et al. [13-15] reported the atomic Na released from burning black liquor droplets using quantitative planar laser-induced fluorescence (PLIF). Due to the significant scattering from soot, however, the quantitative PLIF measurement of atomic Na was not achieved during the devolatilisation phase of burning coal particles. Moreover, the total population of Na species in the flames during combustion comprises various compounds in addition to atomic Na. Hence, it is unrealistic to identify each alkali species simultaneously using LIF.

A particular laser diagnostic technique, namely polarisation spectroscopy (PS), possesses the excellent ability to suppress background noise [16] and is suitable to be employed in the

devolatilisation of burning solid-fuel particles for the detection of alkali species. Hence, the PS technique may be appropriate for the detection of atomic Na during the devolatilisation of burning solid-fuel particles.

The advantage of the PS technique over other laser diagnostic techniques is its unique ability to suppress background interference. The PS technique has been employed to detect atomic Na in atmospheric pressure plasma [17]. This work [17] is preliminary to verify the PS measurement is eligible to be used in welding plasma. To further consider the hazard from welding plasma, the Fe in the welding fume could cause the potential hazard to human bodies [17]. Hence, greater understanding of the behaviour of Fe atoms in the fume may potentially reduce the hazard.

Due to the intrinsic nonlinearity of the PS measurement, the feasibility of the PS technique to achieve quantitative measurement is always a complicated question. That is, the relationship between the arbitrary intensity and the corresponding reference concentration at a single transition is not linear using PS. Although theoretically quantitative PS is achievable by measuring the dichroism of the laser beam under the saturated regime, this is difficult to achieve in practice.

A particular property of PS measurement is that significant absorption occurs when it is employed in highly populated media. It can be observed in several previous wavelengthscan results [17, 18]. The absorption occurred in the central transition. Hence, a specific wavelength away from the central transition of target species then may be determined for the detection of atomic Na in the plume of burning solid-fuel particles.

In addition to Na species released in the plume of burning solid-fuel particles, the K species is also significant, especially for biomass fuels. Considering the wavelength difference between atomic Na and K in D_1 or D_2 lines, it is almost impossible to detect the both simultaneously using laser diagnostic techniques. The AES technique has been widely used to detect multiple

elements in flame samples [19] because it possesses good sensitivity and rapid response to some metal species, especially for alkali and alkaline elements. Moreover, the experimental apparatus is simple and cost-effective compared to those of laser diagnostic techniques. However, due to the difficulty of establishing calibration curves, quantitative AES may not be achievable.

The LIBS technique, a plasma-based spectroscopic measurement, is applicable for metal detection in a designated location of the sample medium. By spectral analysis it is feasible to determine the total population of the Na and K, which may exist in various chemical forms within the plume of burning solid-fuel particles. Unlike the PLIF technique, the spectral signals can be distinguished from the scattering with optimum experimental conditions. However, as it is a plasma-based technique, some intrinsic limits of the LIBS measurement need to be addressed to achieve the quantitative measurement.

The physical concepts of each technique selected to detect metals in this work is considered. Applying various techniques for metal detection can demonstrate the comprehensive investigation of technique applications and the relevant comparison among techniques to show the advantages and disadvantages in metal detection.

Due to the significant difference between each measurement, the experimental details of laser system, burners and other apparatus are described together with the results in each chapter. The details of the chosen transitions of atomic Na (the D_1 line: 589.592 nm) [20, 21], K (the D_1 line: 769.896 nm) [20, 22] and Fe (385.991 nm) [20, 23] used in the spectroscopic measurement are listed in **Table 1-1**.

1.2 Aims

To address the aforementioned issues, the aim of this work is to assess the potential at existing optical techniques to permit instantaneous detection of target metals in a high

temperature environment. Five specific aims of this work are listed below:

- To demonstrate the feasibility of polarisation spectroscopy for metal detection, in particular of atomic Na or Fe, in strongly radiating background environments.
- To assess the feasibility of polarisation spectroscopy to be used for the quantitative measurement of atomic Na in practical burning solid-fuel particles.
- To assess the capability of an existing AES technique in the detection of atomic Na and K released from the burning solid-fuel particles.
- To develop the quantitative LIBS technique to be employed to detect the time-resolved [Na] and [K] released from the burning solid-fuel particles.
- To compare the advantages and disadvantages among the three techniques used for metal detection in high temperature environments.

1.3 Dissertation Layout

This dissertation consists of seven chapters. The first chapter states the motivation, aims and literature overview. The literature overview confirms the need of developing optical techniques for metal detection in high temperature environments.

Chapter 2 describes the fundamental background theories of relevance to the chosen laser diagnostic techniques of atomic spectroscopy, and outlines the processes of combustion and

Table 1-1 The chosen transitions of atomic Na, K and Fe are employed in this thesis. The spectroscopic measurements include AES, LIBS and PS. Atomic Na and Fe were measured using PS in flames and welding fume, respectively. Atomic Na and K released from burring solid-fuels were measured using AES and LIBS.

Elements of interest	Chosen Transition	$E_i(cm^{-1})$	$E_j(cm^{-1})$	$A_{ij}(10^8\ s^{-1})$
Na	Na(I) 589.592nm	0.000	16956.172	0.614
K	K(I) 769.896nm	0.000	12985.170	0.374
Fe	Fe(I) 385.991nm	0.000	25899.987	0.0969

plasma. In addition, the details of systematic errors are addressed.

The first and second aims of the work are addressed in **Chapter 3** and in **Chapter 4** respectively. Due to the nonlinearity of PS measurements, a single wavelength is not always applicable to highly populated species. Unlike particular transitions chosen for the designated laser diagnostic techniques, the PS technique requires a wavelengthscan across the transition of the target species. This can reveal the behaviour of target species in the sample media. The capability of the PS technique, in the strong background noise (low signal-to-noise ratio, SNR), to provide the comprehensive application is accessed. A mathematical simulation has been developed to describe the lineshape of target species, which is atomic Na in the flames or atomic Fe in atmospheric plasma. This provides the insight for the future development of PS technique.

Chapter 5 presents the AES technique employed to achieve the third aim. The AES technique is capable of detecting atomic Na and K simultaneously released from the plume of burning Loy Yang brown coal and pine wood particles in rich premixed laminar methane flames. The time-resolved spectra of the release records of atomic Na and K are indirectly related to the combustion behaviour of burning solid-fuel particles.

Chapter 6 addresses the fourth aim using LIBS to measure total Na or K quantitatively at a designated location within the plume of burning coal and wood particles. As the LIBS measurement is a spectroscopic technique, the time-resolved records of total Na or K released from the burning solid-fuel particles were obtained. A novel calibration method adopted in the present experimental arrangement was developed for the quantitative LIBS used in flame samples.

Chapter 7 includes two parts, namely conclusions and recommendations for future work. The last aim is assessed in the conclusion by the assessment of three optical techniques employed to detect metal species in high temperature environments. The recommendations suggest the

further work which can be done to more completely address the unanswered questions of this thesis.

A significant portion of this work will be submitted to archival scientific journals. Currently, one paper has been accepted for publication and four papers are going to be submitted, as shown in **Appendix J-3**.

1.4 Importance of Optical Diagnostics

1.4.1 Overview of Laser Diagnostics

The concept of laser (Light Amplification by Stimulated Emission of Radiation) was firstly proposed in 1905 by Albert Einstein, who further developed the theoretical foundations into the Photoelectric Effect in 1917. This effect is the optical amplification based on the stimulated emission of photons in which electrons may be excited from the ground state to higher energy levels. Meanwhile, the excited electrons are not stable and tend to return the lower states leading to energy release in the forms of radiation. Owing to the law of energy conservation, the emitted radiation may excite particles to generate more photons. This process is termed resonance. Due to the repeating process, once, sufficient photons occur and then a laser beam can be generated. More and more laser applications have been developed since 1958, when laser devices became commercially available.

1.4.2 Significance of Laser Diagnostic Measurement

A laser beam exhibits particular properties of radiation, namely narrow wavelength width, intense energy, and temporal and spatial coherence [16]. These properties allow laser diagnostic measurements being characterised by non-intrusive, spatially resolved, remote, time-resolved and species selective [24]. Laser diagnostics have provided a wealth of

information for development of models that describe combustion processes, or for detections of target species in extreme environments. To understand the behaviour of alkali metals released from burning solid-fuel particles or iron in welding plasma, optical techniques are suitable for the measurements required in this work. However, each technique has certain limitation. Therefore, each measurement typically requires different diagnostic techniques, as discussed in the following sections. A review article has detailed various measurements of on-line diagnostic techniques [25].

1.4.3 Atomic Emission Spectroscopy

The atomic emission spectroscopy (AES) technique is to detect the transition (wavelength) of which target species characterise. This technique is widely employed in certain media, such as flames and plasma environments. The AES technique was first reported by Anders Jonas Ångström, a physicist in Sweden, in 1853. Ångström pointed out that an electric spark yields two superposed spectra and postulated that the luminous rays emitted from an incandescent gas can be absorbed, elucidating a fundamental principle of spectral analysis. Since then, spectroscopic analysis has become more and more important for metal analyte [19, 26, 27]. The intensity measured at a specific wavelength is proportional to the number density of the target element at that transition in the sample. The sensitivity of spectral lines of the target species using AES is determined by the characteristics of the spectrometer, the media and the other emission sources. The flame emission spectroscopy, for example, for certain alkali and alkaline earth elements [19, 26, 27], is appropriate for detecting the spectral lines of those elements with relatively strong intensities. For example, the AES technique is eligible for the detection of atomic Na and K in a flame environment.

The AES technique has also been further modified for plasma media. A widely applied technique, namely Inductively Coupled Plasma Atomic Emission Spectroscopy (ICP-AES) [28, 29], has been employed to measure the concentrations of samples given a proper

calibration curve. However, ICP-AES is typically not capable of quantitative measurement with high concentrations due to the significant and unavoidable self-absorption. This self-absorption occurs in any plasma application, leading to significant uncertainty in the measurement.

By choosing a proper emission media and optimizing detection conditions, some short lifetime species, such as radicals of C_2 [30-33], CN [30, 31, 34], C_2H_2 [35], NCH [34, 35], CH [33] and H [33, 35], have been detected in the synthesis of carbon nanotubes of which the growth mechanisms are determined. Hence, the AES technique can provide instantaneous measurement of multiple target species.

The AES technique possesses a rapid response, good sensitivity, wide detection range and the potential for multiple species investigation, such as for measurement of Na and K released in flame media simultaneously. In addition, time-resolved measurement is also possible, which is useful to investigate the historical release of atomic Na and K during combustion of solid-fuel particles. These advantages are significant, compared with other laser diagnostic techniques. However, there are certain difficulties of the AES technique when employed in a flame medium. Because species emit and absorb at the sample wavelength, it is difficult to separate the two processes when the species are spatially distributed within the entire flame media. This issue causes difficulty in quantitative measurements, which seek to determine the number density of target species. The distribution of atomic Na [11, 13] or K in flame media changes along the flame axis because the chemical reactions in the flame media dominate atomic Na or K and alkali compounds. Hence significant development required before quantitative AES is applicable.

1.5 Laser Diagnostic Techniques

Laser diagnostic techniques are capable of the instantaneous measurement of many scalar

physical properties, such as temperature and the identification of species that may be either stable substance or intermediates, either qualitatively or quantitatively. In this section, two laser diagnostic techniques employed in this work to identify the target species will be reviewed. The fundamentals of each technique are introduced in **Chapter 2**.

1.5.1 Laser-Induced Fluorescence

Due to the significant similarities between PS, AES, LIBS and LIF, it is useful to briefly introduce the LIF technique although it is not being used in this work.

Species generated during combustion include precursors, intermediates and soot (fine particles). Ash is also generated by the combustion of solid-fuel particles. The precursors and intermediates which exist temporally may not be identified at the end of process because most of the species (intermediates) of interest are produced and consumed during the process itself. This implies that those species need to be identified *in-situ*. The particular intermediates, hydroxyl radical (OH) [36-38] and formaldehyde (H_2CO) [36, 39], generated by combustion have been measured using LIF. The detail principles and experimental arrangement has been academically described [16, 24, 40]. The species of OH and H_2CO are usually employed to identify the flame structure. The species of OH has also been used to determine the flame temperature based on matching the measured spectrum to a numerical model [41]. The precursors, such as C_2 generally found in the synthesis process of carbon nanotubes (CNTs) [30-33], tend to react with other species to form final products. This requires an instantaneous measurement to investigate the formation of carbon clusters because C_2 is a precursor that exists briefly.

The LIF technique has also been employed to detect various radical species in combustion processes. Nitrogen oxides (NO_x) are important radical of interest to the environment concern. One of combustion products, nitric oxide (NO) [36] has been investigated [42]. In terms of

environmental effects, NO is implicated in acid rain and both NO and nitrogen oxide (NO_2) participate in ozone (O_3) layer depletion. Much effort to apply LIF for NO has been invested [43, 44]. The isotope of nitric monoxide, $^{14}N^{18}O$ [45], was measured using LIF to investigate the breath mode in order to understand the formation of NO.

It is possible for LIF to be applied in a two-dimensional measurement. Planar LIF (PLIF) has been performed to investigate the two-dimensional distribution of carbon monoxide (CO) and carbon dioxide (CO_2) [46]. The PLIF technique provides planar distribution of target species within flames, which is crucial for development and validation of combustion models. PLIF has been employed to measure atomic Na quantitatively in the plume of burning Loy Yang coal particles [11, 12] and black liquor droplets [13-15]. The distribution of atomic Na revealed that the concentration of atomic Na decreases along the central axis of the plume. However, significant scattering noise occurs in certain measurement environments leading to the low signal-to-noise ratio (SNR). The noise, for instant, caused by soot induces the intensity of the target species during the devolatilisation of burning coal particles using PLIF induces the sufficient uncertainty due to the same detection wavelength from the soot scattering [11]. Potentially three-dimensional LIF may be achieved by using multiple PLIF images revealing the structures of flames.

Various forms of any species occur during the combustion of solid-fuel particles. Regarding the interests of Na released from burning solid-fuel particles, it is difficult to determine the total amount of Na release using the LIF measurement because of the wavelength selective as described. Although the total amount of Na may be estimated from the flux related to the combustion conditions [11], it may be obtained by using other laser diagnostic techniques.

1.5.2 Laser-Induced Breakdown Spectroscopy

The LIBS technique was first developed by Brech in 1962 [47]. The LIBS measurement is an alternative and complementary technique to LIF that offers the possibility to measure the total

amounts of multiple species at a single location. It has now been applied to solid, liquid and gaseous samples [48]. The accuracy of LIBS is dominated by three effects, namely matrix effect [49-51], spectral interference [51] and self-absorption [24, 51, 52]. In addition to interferences, the physical state and size of the samples should be taken into account [53, 54].

Yamamoto and co-workers [55] reported that the Limit of Detection (LOD) of barium (Ba), beryllium (Be), lead (Pb) and strontium (Sr) in contaminated soil samples were 265, 93, 298 and 42 ppm, respectively. The LOD of solid samples are significantly high due to the matrix effect [51], in particular for solid samples [51] and the energy transfer is used to ablate samples leading to the lower plasma temperatures. Generally, the matrix effect resulting from components other than analyte in the samples can be eliminated by appropriate calibration [56]. Yamanoto et al. [57] also reported that the LOD for chromium (Cr), copper (Cu), manganese (Mn), nickel (Ni), and silicon (Si) in steel ranged from 0.11 to 0.24% using a long-pulse (150 ns) Q-switched Nd:YAG Laser. The quantitative LIBS measurement requires a reference to establish a calibration curve of the target species.

Arca et al. [58] also quantified Na, K, calcium (Ca), Cr and chlorine (Cl) in drinking water. The LOD of LIBS applied inside the liquid was relatively high due to the relatively low temperature of the plasma resulting from the high heat loss. That is, LOD is highly dependent on the plasma temperature. Dudragne [59] reported that LIBS was quantitatively applied to measure sulfur (S), fluorine (F), Cl and carbon (C) in the atmosphere. Other studies [60-63] evaluated C, oxygen (O), hydrogen (H) and nitrogen (N) for various equivalence ratios of laminar premixed methane flames using LIBS.

As LIBS attracts more and more attention, it has been employed to detect pollutants released from solid-fuel combustion. For the interest of alkali species released from burning solid-fuel particles, Na and K cause the major issues in power plants due to fouling, slagging and corrosion [1, 9, 64]. The LIBS technique has also been employed to determine the compositions of fly ash [65] and other ash samples [66] from a coal fired power plant. Blevins

et al. also investigated multiple-elements released at high temperatures in industrial boilers and furnaces [67]. Molina et al. also reported the measurement of Na and K in the high-temperature exhaust from a laboratory glass furnace [68]. The investigation of multi-elements has been conducted in aerosols, gases and in the mixtures of both phases using LIBS, providing new understanding of target elements. Chlorine has been determined to form potassium chloride (KCl) and sodium chloride (NaCl) facilitating corrosion by this method [8, 69]. The compositions of coal and wood particles have been investigated quantitatively by applying LIBS [70, 71]. However, this can be achieved by applying ICP-AES with better accuracy due to the self-absorption free in IPC-AES measurement [29].

To quantify the emission of Na and K during combustion by LIBS requires an appropriate calibration process based on comparison of the intensities of the chosen spectral lines between the target species and standard samples [51, 59, 72-78] although some researchers have reported a calibration-free LIBS measurement [79, 80]. The conventional calibration process is based on the intensity ratios and the concentration ratios between the testing and standard samples. LIBS has been employed with various types of solid samples, steel [49, 81], slag [82], aluminium (Al) [83] and wood preservatives [84]. The significant matrix effect leading to the poor coefficient of determination (R^2) before correction has been observed in solid samples. In addition to the matrix effect, which is negligible in the flames of burning solid-fuel particles (gaseous samples), it is necessary to account for the interferences of self-absorption and spectral overlapping, which limit the accuracy of quantitative LIBS [51]. The influence of spectral overlap can be reduced by optimizing the gate delay and gate width for a specific wavelength, based on the lifetimes of the intermediates. Self-absorption cannot be avoided and becomes significant under high population levels of target species. Nevertheless, it can be reduced by selecting other alternative persistent spectral lines for calibration other than the major resonant ones [51]. For example, the chosen line of Na(I) is 589.592 nm (D_1) instead of 588.995 nm (D_2) due to the strong absorption; the selected lines of

K(I) may be 404.414 and 404.721 nm instead of 769.896 (D_1) and 766.490 nm (D_2). Likewise, the chosen spectral line for calibration of Fe(I) is 404.582 nm instead of 248.328 nm to avoid self-absorption in highly populated level of Fe [51].

The LOD for quantitative LIBS can also be improved by choosing appropriate reference wavelengths because LOD is related to the relative standard deviation (R.S.D.) and the slope of the calibration curve [51, 77, 85-87]. Due to the matrix effect and the heat loss of solid and liquid samples, the better LOD may be obtained in gaseous samples rather than in solid samples.

1.5.3 Laser Polarisation Spectroscopy

Laser polarisation spectroscopy (PS) is a technique developed by Wieman and Hansch in 1976 [88] as a Doppler free method related to saturation spectroscopy but providing a considerably higher SNR. The PS technique generates a laser-like signal beam and permits remote detection so that the signal collection can be far away from the samples to avoid the background interference, for instance, from luminous environments with the presence of fine particles. In the case of sooty flames, the scattering affects LIF measurement when the elastic laser scattering possesses the same laser frequency with the fluorescence of the target species. Hence, it is necessary to detect LIF signals at a different wavelength from the laser frequency in such environments, which is not always possible. It has been observed that strong scattering is present at the investigation of atomic Na during the devolatilisation of the burning coal particles in lean laminar premixed flames [11]. In contrast, one-colour PS is conducted at the same laser wavelength so that it is not necessary for the target species involved to possess two different optical transitions. PS has been employed in gas tungsten arc welding (GTAW) to detect Na seeded into welding arc demonstrating the eligibility of PS employed in the environment with strong background noise [17].

Teets et al. [89] proposed a model used to describe the case of a pulsed unsaturated laser pumping with the laser pulse length shorter than the ground-state relaxation time, to describe the optical anisotropy using a direct approach related to rate equations. The PS technique was first applied in a flame by Tong and Yeung to measure seeded Na and Ba and achieve a LOD of 0.03 and 37 $ng \cdot mL^{-1}$, respectively [90]. Later, Zizak et al. [91] also applied PS of atomic Na in a seeded flame. It is proposed that the poor sensitivity of atomic Na using PS may be improved using better polarisers (with a better extinction ratio). An investigation of the PS signal strength related to the included angle (up to 7°) between the pump and the probe beams was performed by Zizak et al. [91] in the Na seeded flame.

The PS technique applied in the infrared (IRPS) provides additional possibilities since most molecules possess infrared-active vibrational transitions, such as for hot water lines (H_2O), carbon monoxide (CO), carbon dioxide (CO_2) and nitrous oxide (N_2O) which do not possess accessible visible or UV transitions. The CO_2 molecule was investigated using IRPS at the wavelength of 2 μm [18, 92, 93]. Alwahabi et al. [92] reported a linear dependence of the IRPS signal on the CO_2 mole fraction indicating that the IRPS signal is nearly independent of the molecular collisions and that the molecular alignment at the time scale of the measurements does not strongly respond to the energy transfer processes between inter- and intra- molecules. This indicates that IRPS has the potential for quantitative measurement of gas concentrations instantaneously. Li et al. [93] also employed IRPS to detect nascent CO_2 and H_2O in atmospheric pressure flames. This demonstrated the species-selective application of IRPS. Alwahabi et al. [18] also employed IRPS and infrared LIF (IRLIF) in CO_2/N_2 binary mixtures to determine the full width half maxima (FWHM) pressure broadening coefficients of CO_2, which measured with IRPS, are 8% greater than those acquired using IRLIF.

Motivated by the importance of OH radicals in combustion processes, the PS technique has been comprehensively used to detect OH radicals with single-photon [38, 94-98], two-photons [99] and two-dimensional measurements [100, 101]. The two-dimensional OH

using PS provides superior resolution to that achieved by using PLIF due to the better SNR. Other combustion products and intermediates have also been investigated using single-photo excitation of C_2 [102], NH [96, 103], NO [104], methane (CH_4) and C_2H_6 [105], C_2H_2 [106], CH [107], CH_3 [108] and two-photon excitation of NH_3 and CO [109] and N_2 [110, 111]. Kulatilaka et al. [112] applied PS measurement in atmospheric pressure hydrogen/air flames with equivalence ratios ranging from 1.1 to 2.1 to detect atomic H. The PS signal of atomic H was found to be approximately proportional to the square of the pump beam power. These results show that PS can overcome some of the inadequacies of other laser diagnostic techniques for combustion processes.

To enable quantitative detection with PS techniques, comprehensive calculations of lineshapes and saturation effects have been performed using direct numerical integration [113]. The experimental investigation of lineshapes of saturated PS signals [114] have been provided to verify theoretical calculations. These theoretical calculations predict that the signal intensity for the low power of the pump beam at the transition is proportional to k^{-6} (k is the collisional rate), which complicates the concentration measurement of target species. For the case of high pump beam energy (which is generally employed in the saturation regime), the PS signal possesses a weak dependence on the collision rates. This is crucial for quantitative measurements because the collision leads to quenching during measurements. Furthermore, in the unsaturated regime, the intensity of the PS signal (I_{PS}) is expected to be described by a cubic dependence on laser power ($I_{LPS} \propto I_{pump}^2 \cdot I_{probe}$, where I_{pump} and I_{probe} are the intensities of the pump and probe beams, respectively). In the saturated regime, the PS signal is expected to be independent of the intensity of the pump beam so that it scales linearly with the intensity of the probe beam ($I_{PS} \propto I_{probe}$). The results of quantitative OH measurement performed [114] in an H_2/air flame indicate that an energy of the pump beam (~ 100 GW/m^2) is enough to access the saturation regime.

The PS signal is strongly dependent on the included angle between the pump and probe

beams. This dependence varies with the polarisation status and polarisation direction of the pump and probe beams. Reppel and Alwahabi [101] proposed a uniaxial gas model to describe the geometrical dependence of the PS signals. They presented a theoretical description of the dependence on the included angle to account for beam steering effects. The beam steering effect is a result of the variations in the refractive index of the media, typically caused by temperature gradients, which are present in flames and plasmas.

Being a coherent technique with a laser-like signal, PS measurement presents the superior characteristics of an efficient signal collection and excellent discrimination against background noise from scattering and flame emission (spectral overlap). Hence, PS measurement is potentially suitable for detecting species in plasma environments [17, 115]. Indeed, the PS technique has already been employed to measure the local temperature of atoms in a discharge plasma [116].

To understand the GTAW process for the reduction of hazard during welding, it is crucial to study iron (Fe) in the welding plasma [117]. Due to the characteristics of the PS technique, it is suitable for the detection of Fe in plasma environments.

1.6 Indirect Analysis of Solid-fuel Particles

The indirect analysis takes place later when the reaction is finished. Off-line analysis of the ingredients of fuels and ash has been used to identify the pollutant emission during combustion. Generally these analysis techniques are indirect measurement although the continuous monitor analysis has been commenced in the flue gas of combustion [118]. This continuous monitor, however, cannot detect the instantaneous species generated in the reaction. Indirect measurement methods Include X-ray Fluorescence (XRF), Energy-Dispersive X-ray spectroscopy (EDX or EDS), scanning electron microscopy (SEM), Nuclear magnetic resonance (NMR), X-ray Diffraction (XRD) and Mass Spectroscopy (MS)

[119]. Another technique, Fourier Transform Infrared Spectrometry (FT-IR), has been widely used to determine the unexpected molecules [120, 121] in ash samples.

An ultimate analysis of fuels is used to determine elemental compositions of carbon (C), hydrogen (H), nitrogen (N), sulfur (S), chlorine (Cl) and oxygen (O) (by difference) in the gaseous products and organic substance, including calcium (Ca), iron (Fe), magnesium (Mg), titanium (Ti), sodium (Na), potassium (K), silicon (Si), aluminum (Al) and even mercury (Hg). The ultimate analysis of coal and wood samples employed in this thesis is shown in **Appendix B**. It should be noted that the term “combustion” indicates the thermal pyrolysis under air or oxygen. During this process, since coal and biomass contain inorganic compositions, some metals will be released in the flame plumes, including Na and K. The SEM/EDX measurement has been used to analyse the compositions of coal [10, 120, 122-124], biomass [5, 124-127] and coal/biomass blends [128]. The SEM measurement provides the morphology of ash and the EDX measurement can be used to determine the relative concentration between all ingredients (semi-quantitative analysis) and the quantitative analysis may be achieved if a proper calibration is applied. Other indirect analysis methods, ICP-based techniques, for instance, ICP-AES [10] have been used to determine the concentrations of target species in the coal ash, and provide results that are consistent with concentrations obtained using EDX [10]. Moreover, the XRD measurement [10, 121, 123, 124, 129] has also been applied to identify the mineralogical and physical properties of the ash compounds. Apart from those methods introduced above, MS, an early developed technique, has also been employed [130]. Generally, the MS samples extracted from flue gases are used to identify the species in the fly ash providing data for combustion modelling. However, the MS technique cannot be used to identify combustion intermediates or precursors due to the quenching effects.

1.7 Combustion Models

Given that alkali species are released into the plume of burning solid-fuel particles, the combustion behaviour of these burning particles may be related to the release mechanism. Unlike the indirect measurement and analysis of solid-fuel particles combustion, the TGA (thermogravimetric analysis) technique provides a direct measure of mass loss of solid-fuel particles during combustion. The kinetic properties of coal and wood then can be obtained from TGA results. Various models of coal combustion have been proposed to describe single coal particle combustion [131-142] and reviewed widely in the past several decades [143-146]. A critical parameter in coal particle combustion is its porous structure [147-150]. Regarding the pore structure, the combustion mechanism has been described as the shrinking core [151]. The mechanism of coal combustion based on the pore structure has been extensively applied to describe the burning coal particles [152]. Hence, the combustion time related to the particle size can be determined [152].

A global model of wood particle combustion has been proposed by Branca and Di Blasi [153] and Branca et al. [154]. The devolatilisation stage is associated with hemicellulose, cellulose and lignin degradation [153]. Kinetic models ranging from one-step global to multi-step mechanisms have been proposed to describe wood char pyrolysis [153, 155]. These mechanisms based on TGA measurements describe the intrinsic properties of wood char pyrolysis. The multi-step mechanisms may be parallel- or series- have been reported [155, 156].

Similar to the coal char combustion, the combustion of wood char is often modelled by the shrinking core model which is based on the formation of pore structure [157-159]. To consider the shrinking core model [160-165], the particle size [166] and shape [167] of wood particles are also crucial. Moreover, the combustion time of wood particles is also dependent on the particle size and shape [168].

1.8 Issues of Burning Coal and Wood

1.8.1 Alkali Species

Burning solid-fuels generates various gaseous products and particulate matter [169]. For the interest of this thesis, alkali metals, namely Na and K, can cause slagging, fouling and corrosion on the heat transfer surfaces of combustors or boilers [1, 170]. Due to the chemical and physical complexity of burning solid-fuels, the combustion conditions, varied from lean to rich conditions, dominate the forms of alkali species released, such as the concentration variation of atomic Na released from a burning black liquor droplet [13, 14]. It is useful to understand the background regime of alkali species released during combustion. Alkali species have been demonstrated to form the initial deposit, which facilitates subsequent agglomeration of other ash substances. Alkali species also form complex sulphates, leading to corrosion of combustor heat transfer surfaces [9, 171]. Fuels with high chlorine content facilitate the formation of alkali chlorides, which also cause corrosion in furnaces [8, 172]. Chlorine has been shown to be a major factor in deposit formation [172, 173]. In particular, potassium chloride is among the most stable high-temperature, gas-phase compounds and leads to severe problems in boilers.

Elemental alkalis in low rank Australian brown coal from Victoria and pine wood pellets are present in several forms [174, 175]. The forms of sodium and minor potassium compounds in low rank coal are typically water-bound, organically bound or clay bound. In pine wood pellets, alkali species are biologically bound represented in hemicellulose, cellulose and lignin [172]. Alkali species in volatile substances were shown to condense in cooler zones of boilers, and to form sticky deposits on the surfaces [9, 172]. Clay-bound alkali species in coal [176] and in wood [172] form silica melts that are important in initiating slagging.

In the past decades, due to the concern about the increasing global warming, biomass, renewable energy sources indeed, has been considered as one of the feasible energy sources for its renewability and zero net carbon dioxide emission. The CO_2 released from burning biomass is equivalent to the amount of that consumed during photosynthesis. In addition, there are some problems with the utilisation of biomass, such as low heating value, high chlorine and ash content. The heating value (HV) of biomass is much lower than that of fossil fuels leading to the higher cost of power supply owing to the less efficient electricity generation. A higher ash content of biomass fuel facilitates slagging faster than that caused by burning coal. Apart from two issues of burning biomass, high chlorine content can favour corrosion and fouling on the heat transfer surface due to the occurrence of higher concentration of alkali chloride, in particular potassium chloride (KCl) released from some biomass fuels, straw, for instance [5, 177-179]. Although alkali metals and chlorine can be leached out prior to the biomass combustion [180] to reduce the emission of alkali chlorides, the leaching process increases the cost and complexity of energy generation. Sulfur has been found to favour the formation of alkali sulfates so that the emission of alkali chlorides during co-firing of coal and biomass combustion has been reduced [8]. The co-firing of coal and biomass may benefit from higher HV and the reduction of CO_2, compared with coal combustion. Moreover, the emission of alkali chlorides can be reduced by adding sulphur because alkali sulfate can be collected in the slag [181].

1.8.2 Other Pollutant Emission

The pollutants released during the burning of solid and liquid fuels are classified as fine particles, which includes soot and ash powder, and flue gases, including CO_2, N_2O, NO_x (NO and NO_2) and SO_x etc [169]. The earth absorbs part of the sun's radiation (shorter wavelengths) and emits in the forms of longer wavelengths, partially IR radiation, which is re-absorbed by the greenhouse gases, namely CO_2, NO_x, CH_4, O_3 and chlorofluorocarbon

(CFCs), and re-emitted, in the form of IR, back to the environment leading to the raising atmospheric temperature.

The CO_2 molecule, most significant greenhouse gas released from burning fossil fuels every year, has attracted much attention in the past few decades due to the burning fossil fuels contribution to the increase global warming [182]. NO_x absorbs ultraviolet light in the atmosphere facilitating O_3 formation [183].

1.9 Particular Measurement in Welding Plasma

Plasma generates a broad range of spectra from various species. Given that the spectra from one species may overlap with that from other species, the spectral interference needs to be accounted for. However, this is not always possible. For LIF applied in a plasma plume, a correction ought to be performed to suppress the spectral interference that possesses the same transition with that of target species. As introduced in **Section 1.5.3**, the PS technique is suitable to be employed in plasma environments [16, 17, 24].

1.9.1 Low Signal-to-Noise Ratio Environment

For LIF measurement with the possible interference of scattering emitting the radiation at the same wavelength causing the low signal-to-noise (SNR) signals, the level of noise signal is such significant [16, 24]. To avoid the interference, the chosen wavelength of target species needs to be different from that of scattering signals. Unlike LIF signals measured directly from samples, the polarisation change of the laser beam at the chosen transition is detected. This allows PS to avoid the scattering interference indicating the PS technique is eligible to be employed to measure target species in the strong background environments [17, 115-117]. The detailed explaination of PS technique will be introduced in **Chapter 2**.

CHAPTER 2

THEORIES AND EXPERIMENTAL BACKGROUND

This chapter contains the fundamental theories of optical diagnostic techniques followed by the last section which evaluates the systematic errors of the present experimental arrangement.

2.1 Laser Diagnostic Techniques

Laser diagnostic techniques are well-known as a convenient manner providing the measurement non-intrusively, spatially, temporally, and spectrally selective excitation. Laser diagnostic techniques are capable of measuring a pool of radical species, such as OH, CH, NH, cyanide (CN), HCN and elements in flames. There are three techniques widely applied to detect target species in flames [16].

2.1.1 Laser-Induced Fluorescence

Laser-induced fluorescence (LIF) is capable of detecting species in flames qualitatively and quantitatively (with an appropriate calibration curve). Fluorescence, the spontaneous emission of radiation from an excited energy state, is characterised as a specific wavelength. For example, the D_1 and D_2 lines of atomic Na are respectively 588.995 and 589.592 nm and those of atomic K are 766.490 and 769.896 nm, respectively [20]. For iron (Fe), various transitions are well-known, such as 248.327, 248.814, 385, 991 nm et al [20].

LIF is a widespread technique detecting species in flames. There are several fundamental criteria which must be satisfied to achieve LIF measurement [16, 40]:

- The known transition is essential for the target species.
- The absorption transition of the target species is accessible by the laser source.
- An appropriate calibration curve is necessary for the quantitative measurement.
- Relaxation effects must be considered.

The LIF technique has limitations, which are the single wavelength (wavelength dependence to the target species) and low signal-to-noise ratio during the devolatilisation phase of burning solid-fuel particles [11, 12], so that LIF is not eligible for investigating species released from the devolatilisation of burning solid-fuel particles due to the significant scattering and for detecting multiple species in flames simultaneously.

2.1.2 Laser-Induced Breakdown Spectroscopy

Laser-induced breakdown spectroscopy (LIBS) is also nominated as laser-induced plasma spectroscopy (LIPS) due to the characteristics of the technique. The LIBS technique is a type of atomic emission spectroscopy as a pulsed laser is focused to form plasma, by which samples are atomized and excited. As the characteristics of LIBS, similar to the inductively coupled plasma atomic emission spectroscopy (ICP-AES) and arc/spark emission spectroscopy, the measurement takes place in a single point of measurement volume and hence it seems difficult to achieve planar LIBS measurement.

LIBS is eligible to be utilized to analyse any matter in physical forms of solid, liquid or gas [52]. Due to the spectroscopic characteristics of the LIBS measurement, some interference ought to be taken into consideration, namely matrix effect, spectral interference and self-absorption [52]. The matrix effect, which generally occurs in solid samples, is negligible

to the gaseous environment. Flame samples can be considered as gaseous media. The occurrence of spectral interference depends on the background noises (emission radiation) and the overlapped spectral lines (other species). This can be eliminated by optimizing the gate delay and gate width specifically for the target species. As to the self-absorption, it is the intrinsic property that is unavoidable in plasma-base measurement techniques. As a result of the focused laser beam, the temperature of the early LIBS plasma plume can exceed 100,000 K and decreases ranging from 5,000 to 20,000 K while it expands to reach the local thermodynamic equilibrium (LTE) in about 1 μs. During the early plasma that characterises a continuum of radiation, the target species dissociates into excited and atomic states. The target species in the LTE plasma where the measurement takes place possess the major resonant lines (the main persistent lines) leading to the absorption of the radiation in the following plasma generation. Certain radiation of the target species emitted in the following plasma will be absorbed by the target species in the previous plasma at the LTE stage. The absorption is nominated as “self-absorption” due to the characteristics of absorption mechanism. The characteristic radiation of target species is re-absorbed by which is in the outer plasma (LTE plasma), as indicated in **Figure 2-1**. Therefore, the self-absorption is not negligible as the significant amount of target species is present. However, the self-absorption can be reduced by choosing other weak persistent transitions.

Generally speaking LIBS is capable of detecting all elements simultaneously depending on the chosen grating (normally ranging from 200 to 800 nm). The wavelength range also relates to the resolution of LIBS measurement. The limit of detection (LOD) is varied by:

- The sensitivity of the detector
- The optical window for radiation collection
- The strength of the selected transition

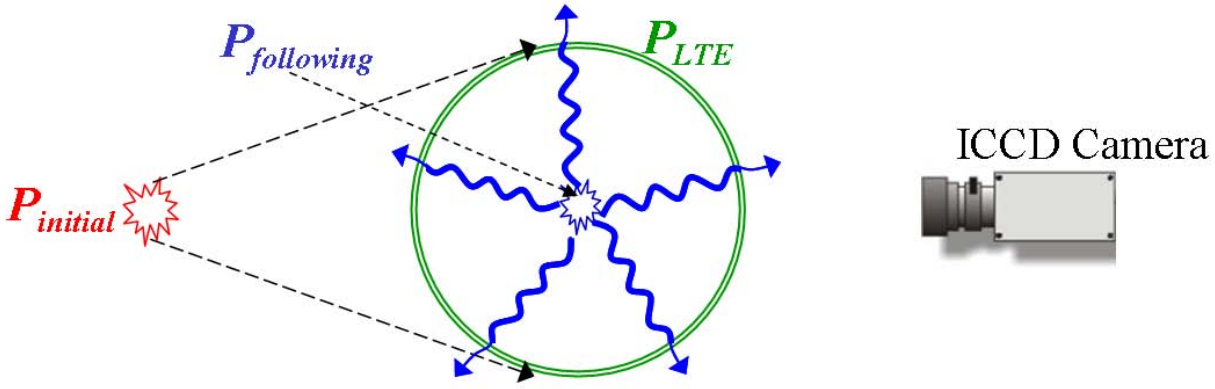

Figure 2-1 Illustration of self-absorption occurring when the initial plasma ($P_{initial}$) reaches LTE status (P_{LTE}); the following plasma ($P_{following}$) generated in the centre of plasma is re-absorbed in the edge of P_{LTE}. Hence, the intensity of radiation measured by an ICCD camera is weaker (represented in thinner blue arrow).

The temperature of LIBS plasma is determined by the applied laser energy and types of samples. As a result of the types of samples, the certain amount of laser energy is consumed to ablate and to dissociate the target species leading to the lower plasma temperature. Moreover, the heat loss, due to LIBS plasma applied inside the liquid samples, significantly reduces the temperature of LIBS plasma. For the gaseous samples, such as the flame environment which is the case of this thesis, small amount of energy is utilized to dissociate the target species and hence the LIBS plasma relatively obtains the highest temperature leading to the better LOD. The absorption of radiation caused by the material of optical window can slightly reduce the LOD. This can be improved by selecting the low absorption index of optical lens to the viewed transition. Although the chosen strong transition improves the LOD, it also enhances the self-absorption, especially under high concentrations of target species. Therefore, it is necessary to optimize measurement conditions by adjusting the gate width and gate delay of the ICCD camera.

As the practical purpose of quantitative measurement with LIBS, it is essential to conduct a calibration process which generally demonstrates the direct relationship (linear) between the intensity of LIBS radiation and the concentration of the target species. An empirical equation based on Lomakin-Scheibe formula [184, 185] with the consideration of negligible

self-absorption (ideally without self-absorption) is presented below:

$$I_{LIBS} = A \cdot [\mathrm{X}]_{species}$$

Eq. 2-1

where, I_{LIBS} is intensity of radiation using LIBS; A is an empirical pre-factor coefficient and $[\mathrm{X}]_{species}$ is the concentration of target species. It has been commonly employed in inductively coupled plasma atomic emission spectroscopy (ICP-AES) technique and can be utilized in LIBS owing to the plasma characteristics of LIBS measurement. However, this empirical equation is practically applicable while the tested $[\mathrm{X}]_{species}$ is low so that the self-absorption is not significant in the experimental I_{LIBS}. The case of saturated regime, which is caused by the gradually significant self-absorption with the increasing population level of target species, requires certain experimental consideration. For example, samples for ICP-AES measurement are dissolved in acidic solution, which may be nitric acid (HNO_3), and seeded into ICP-AES system. The concentration of target element can be obtained using a calibration curve based on **Eq. 2-1**. In order to reduce self-absorption and to improve the accuracy of measurement, the diluted sample solution is seeded into ICP-AES system. Hence, the diluted concentration is obtained so that the actual concentration can be derived. This method is specifically used in the analysis of ash composition. However, it is not applicable to analyse the instantaneous elements released burning solid-fuel particles. Hence, self-absorption to the quantitative LIBS is not avoidable.

2.1.3 Laser Polarisation Spectroscopy

2.1.3.1 Introduction

Given the difficulty to measure atomic Na species release during the devolatilisation of burning solid-fuel particles using LIF [11, 12], laser polarisation spectroscopy (PS) is

potentially appropriate due to the characteristics of laser-like signals and the advantage of signal-to-noise ratio (SNR). Unlike saturation absorption spectroscopy, it measures a small change in absorption against a strong background leading to the limiting sensitivity of the probe beam. The PS signal results from a polarisation variation of the probe beam (the induced dichroism) against a small background and is detected as a modulation of the probe beam while it passes through the crossed polarisers. The PS signals are measured by an ICCD camera or a photo-diode and hence characterise a laser-like behaviour which differs from the fluorescence measurement using LIF. The intensity of LIF signal is varied with the measurement conditions, which are delay time and gate width of an ICCD camera. Unlike LIF signals, the PS signal is a form of absorption spectroscopy so that quenching does not significantly affect the PS signal.

The schematic description, as indicated in **Figure 2-2** [16], PS measurement requires two beams arbitrarily crossed owing to no phase matching required. However, the included angle between the probe and pump beams has been investigated to be less than 30˚ [91]. For PS measurement, a single laser beam is split into a low (~ 5 % of that in the original laser beam) and a strong (~ 95 %) energy beams, which are crossed in the measurement location, for the

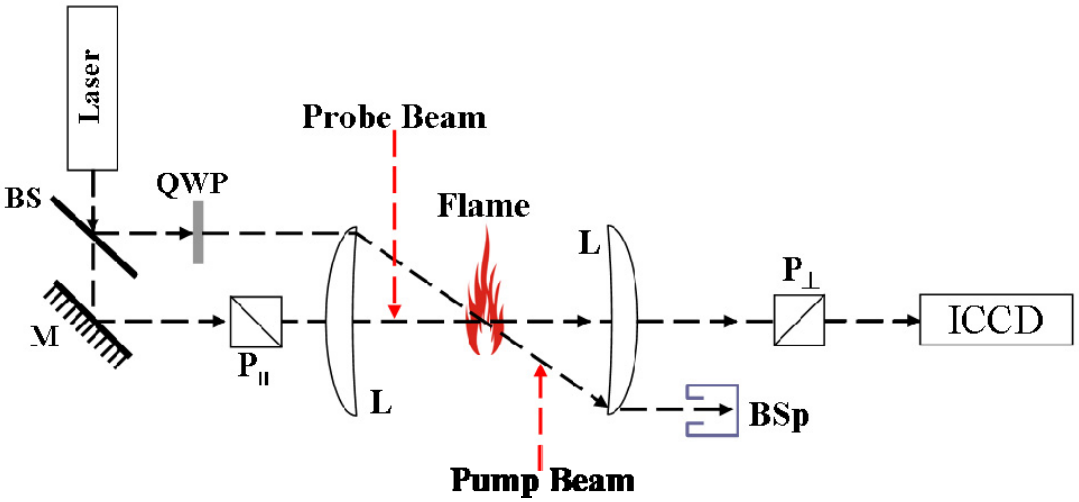

Figure 2-2 Schematic arrangement of PS measurement [16]; BS: Beam Splitter, M: Mirror, L: Lens, QWP: Quarter-Wave Plate, $P_{\perp}$ and $P_{\parallel}$: vertical and horizontal polarisers, respectively; BSp: Beam Stopper

case of this thesis, inside the laminar premixed methane flames. Due to the transition nature of the target species (branches of P, Q and R), the pump beam is either circularly polarised by applying a quarter-wave plate ($\lambda/4$) or linearly polarised 45° to the polarisation of the probe beam. The probe beam through the first polariser (P_{II}, can be $P_{\perp}$), as shown in **Figure 2-2**, is polarised and passes through the flame samples in which the probe and pump beams are crossed. Furthermore, the probe beam passes through the second polariser ($P_{\perp}$) and, therefore, the polarisation variation (the induced dichroism) can be detected by an ICCD camera.

2.1.3.2 Theory

The probe beam in the interaction zone perceives dichroism, which is induced by beam absorption and birefringence, due to the presence of electronic resonance. Refraction index is elliptically polarised, which is induced by dichroism, and hence it is eligible for the probe beam to pass through the blocking polariser. The PS technique is a form of saturation spectroscopy [16] with the change in the real and imaginary parts of the refractive index which are proportional to the fluence of the pump beam. It indicates that $|E^2|$ needs to be taken into account. To discuss $|E^2|$ as the signal equation for PS summarized by Zizak [91], it is necessary to consider the orientation of pump beam circular polarisation weather it is right or left handed. For linearly polarised probe beam, it could be considered to be right (termed +) and left (termed −) circularly polarised beams with equal intensity. These probe beam components responds differently to the pump beam and experience different absorption coefficients, α^{+} and α^{-}, and different refractive indices, n^{+} and n^{-}. Given the length of the interaction volume measured along the probe beam path, L_{PS}, with the pump beam, the probe beam components are introduced, as presented below [40]:

$$E^{+} = E_0^{+} \cdot \exp[i \cdot (\omega \cdot t - k^{+} \cdot L_{PS} + i \cdot \frac{\alpha^{+}}{3} \cdot L_{PS})]$$

$$E^{-} = E_0^{-} \cdot \exp[i \cdot (\omega \cdot t - k^{-} \cdot L_{PS} + i \cdot \frac{\alpha^{-}}{3} \cdot L_{PS})]$$

Eq. 2-2

The transmitted component of light emerging from the second polariser can be expressed in the following equation:

$$E_t = E_{0P} \cdot \sin[\frac{1}{2}(k^{+} - k^{-} - \frac{\alpha^{+} - \alpha^{-}}{2} \cdot i) \cdot L_{PS}] \cdot \exp[(\omega \cdot t + \phi) \cdot i]$$

Eq. 2-3

where, E_{0P} is the amplitude of probe wave and ϕ (= $k \cdot L_{PS}$) is the phase of the wave. As $\Delta k \equiv k^{+} - k^{-}$ and $\Delta\alpha(\omega) = \alpha^{+} - \alpha^{-}$ (the induced dichroism at the probe beam angular frequency) are assumed to be very small (<< 1), the **Eq. 2-3** can be modified and presented in the following equation:

$$E_t = E_{0P} \cdot [\theta + \frac{1}{2}(\Delta k - \frac{\Delta\alpha(\omega)}{2} \cdot i) \cdot L_{PS}] \cdot \exp[(\omega \cdot t + \phi) \cdot i]$$

Eq. 2-4

where, θ is the angular offset of the two polarisers which are nominally crossed. Moreover, by applying the Kramers-Kronig relation (as shown in **Appendix E**) between absorption and dispersion, it describes the difference of refractive index, as presented below:

$$\Delta n = \frac{\lambda_0}{2\pi} \cdot (\frac{\omega_0 - \omega}{2\delta}) \cdot \Delta\alpha(\omega)$$

Eq. 2-5

where, δ is the FWHM of the lineshape and the subscript 0 refers to the centre of the scan lineshape. The transmitted irradiance, $I_{PS}(\omega)$, derived from $E_t^{*} \cdot E_t$ is presented in the following equation:

$$I_{PS}(\omega) = I_{probe}(\omega) \cdot \{\xi + \theta^2 + \frac{L_{PS}}{2} \cdot \theta \cdot \Delta\alpha(\omega) \cdot (\frac{\omega_0 - \omega}{\delta}) + [\frac{\Delta\alpha(\omega) \cdot L_{PS}}{4}]^2 \cdot [1 + (\frac{\omega_0 - \omega}{\delta})]^2\}$$

Eq. 2-6

where, I_{probe} is the input probe beam intensity; ξ is the fractional light leakage owing to birefringence in the polarisers and optics. As the result of a Lorentzian shaped absorption profile (Doppler-free or pressure broadened), $\Delta\alpha(\omega)$ may be expressed:

$$\Delta\alpha(\omega) = \Delta\alpha_0(\omega)\cdot(\frac{1}{1+x^2})$$

Eq. 2-7

where, x is the relative detuning of the probe beam from line centre for the transition (J,M) to (J",M"), defined as $(\omega_0-\omega)/\delta$ and $\Delta\alpha_0(\omega)$ is the line centre induced dichroism for the probe beam. By substitute **Eq. 2-7** into **Eq. 2-6**, the transmitted irradiance, I_{PS}, is modified and presented as following:

$$I_{PS}(\omega) = I_{probe}(\omega)\cdot[\xi+\theta^2-\frac{L_{PS}}{2}\cdot\theta\cdot\Delta\alpha_0(\omega)\cdot(\frac{x}{1+x^2})+(\frac{\Delta\alpha_0(\omega)\cdot L_{PS}}{4})^2\cdot(\frac{1}{1+x^2})]$$

Eq. 2-8

The first two terms, ξ and θ^2, represent the unintentional and intentional light leakage. The ξ (the unintentional leakage) is caused by the imperfect extinction of the crossed polarisers and birefringence induced by optics. The last two terms are recognized as the signal terms. The first signal term represents a dispersive modulation of an intentional background at which a non-zero θ is recognized. As to the second signal term, it represents the absorption-like line profile. To compare **Eq. 2-8** to **Eq. 2-7** (the Lorentzian profile), from the diagnostic point of view, it is assumed that the PS measurement takes place with absence of the intentional light leakage (θ = 0). This indicates the maximum detection of limit results from minimizing the value of ξ since the signal-to-noise ratio (SNR) is generally the ratio of the fourth and first terms in **Eq. 2-8**. It is the order of 10^{-5} to 10^{-6} that the finest polarisers generally have indicating ξ will be equal to or larger than that depending on the quality of the intervening optics.

For the purpose of quantitative measurement, $\Delta\alpha_0(\omega)$ has been summarized [16, 40] and is related to the number density of the target species:

$$\Delta\alpha_0(\omega) = N_{species} \cdot f_B \cdot \frac{I_{pump} \cdot \tau_{pump}}{\hbar\omega} \cdot \sigma^2_{J_f \leftarrow J_i} \cdot \zeta_{J_f \leftarrow J_i}$$

Eq. 2-9

where, $N_{species}$ is the population of the species in ground state; f_B is the Boltzmann fraction of the target species; I_{pump} is the irradiance of pump beam; τ_{pump} is the pulse duration; $\sigma_{J_f \leftarrow J_i}$ is the absorption cross section from the initial rotational state, *J*, to the final rotational state and then $\zeta_{J_f \leftarrow J_i}$ is a polarisation dependent numerical factor, as indicated in **Appendix F**, which has been proposed by Teets et al. [89]. It is noted that $\sigma_{J_f \leftarrow J_i}$ is not polarisation dependent since it is the summation of all the magnetic sublevels. Moreover, $\Delta\alpha_0(\omega)$ (in **Eq. 2-9**) is substituted into **Eq. 2-8** so that I_{PS} is further expressed:

$$I_{PS}(\omega) = I_{probe}(\omega) \cdot [\xi + \theta^2 - \frac{L_{PS}}{2} \cdot \theta \cdot \Delta\alpha_0(\omega) \cdot (\frac{x}{1+x^2}) + \frac{N^2_{species} \cdot f_B^2 \cdot I^2_{pump} \cdot \tau^2_{pump}}{16 \cdot \hbar^2\omega^2} \cdot \sigma^4_{J_f \leftarrow J_i} \cdot \zeta^2_{J_f \leftarrow J_i} \cdot L^2_{PS} \cdot (\frac{1}{1+x^2})]$$

Eq. 2-10

It clearly indicates that PS signal scales as the third power of the intensity of the pump beam ($I_{PS} \propto I_{probe} \cdot I^2_{pump}$). Hence, PS signal possesses a third-order nonlinear regime. The PS signal also experiences the square power of number density of the target species and the interaction length.

Given that polarisers are perfectly crossed and without birefringent interference from optics in the pathway of the probe beam in the unconfined combustion, the transmitted PS signal, $I_{PS}(\omega)$, can be modified below:

$$I_{PS}(\omega) = I_{probe}(\omega) \cdot [\xi + (\frac{\Delta\alpha_0(\omega) \cdot L_{PS}}{4})^2 \cdot (\frac{1}{1+x^2})]$$

Eq. 2-11

To further consider the dependence of the $I_{PS}(\omega)$ on the geometrical polarisation status of the probe and pump beams, **Eq. 2-11** is specifically developed, as shown below [101]:

$$I_{PS}(\omega) = I_{probe}(\omega) \cdot [\xi + (\frac{\Delta\alpha_0(\omega) \cdot L_{PS}}{4})^2 \cdot \mathrm{G}(\omega)] \cdot F_{pump-probe\_geometry}(\gamma, \chi)$$

Eq. 2-12

where, ξ is the extinction ratio of the polarisers (mentioned above), $\Delta\alpha_0(\omega)$ is the induced dichroism (mentioned above), and $\mathrm{G}(\omega)$ represents the normalized lineshape of the target species absorption function. The function, $F_{pump-probe\_geometry}(\gamma, \chi)$, represents the dependence of the I_{PS} on the geometrical polarisation status of the probe and pump beams, where γ is the angle between the polarisation axis of the probe beam and the vertical axis, and χ is the angle between the pump and probe beams in the horizontal plane.

The PS lineshapes were firstly reported in 1976 by Wieman and Hänsch [88] to be Lorentzian if the Doppler width was greater than the collision width. However, Teets et al. [89] and Demtröder [24] proposed that the PS lineshapes are generally Lorentzian and outlined it based on the Lorentzian profiles [24, 89]. In addition, Reichardt and Lucht [113] further extended Wieman's and Hänsch's work in the theoretical calculation of PS lineshapes in 1988. The direct numerical integration of the time-dependent density matrix equation has been conducted to predict that PS lineshapes approach the Lorentzian limit with larger values of Doppler width and non-saturated pump beam energy. Moreover, the PS lineshapes characterise the Lorentzian-cubed with small values of the Doppler width and non-saturated pump beam energy.

The PS line profiles distinguish significantly from LIF line profiles [18]. Regarding the low pump beam fluence (unsaturated regime), the PS line profiles are Lorentzian cubed [92, 106]. As to high pump beam fluence applied (saturated regime), the PS line profiles are described as a Lorentzian function, even whilst the Doppler broadening is larger than the collisional broadening [92]. To describe the PS lineshapes to account for the parameters of the PS measurement, a general Lorentzian function form of power *n* is introduced, as outlined below:[17]:

$$I_{PS\_FIT}(\omega) = I_{PS} \cdot \left\{ \frac{1}{1+\left[\frac{2\cdot(\omega-\omega_0)}{\Delta\omega^H}\right]^2} \right\}^n$$

Eq. 2-13

where, $I_{PS\_FIT}(\omega)$ is the simulation of PS lineshape, I_{PS} is the intensity of pure PS signal, ω is the chosen frequency, ω_0 is the transition frequency (centre wavelength), $\Delta\omega^H$ is the homogenous line broadening, and the values of n as 1 and 3 indicate the saturation and non-saturation pump beam conditions, respectively.

Compared the particular characteristic of PS technique to that of LIF technique indicated in **Figure 2-3**, the mechanisms of target species, such as Fe and Na, detected by using PS and LIF are illustrated. In the case of atomic Fe (**Figure 2-3** a-1), it is excited to the excited state (the red dash line) and emits radiation with different transitions. By selecting the transition different from that used to excite Fe atoms, the detection of atomic Fe in the environment with strong background noise may be achievable using LIF. For the detection of atomic Fe in welding arc, it requires a filter to eliminate the radiation emitted from plasma.

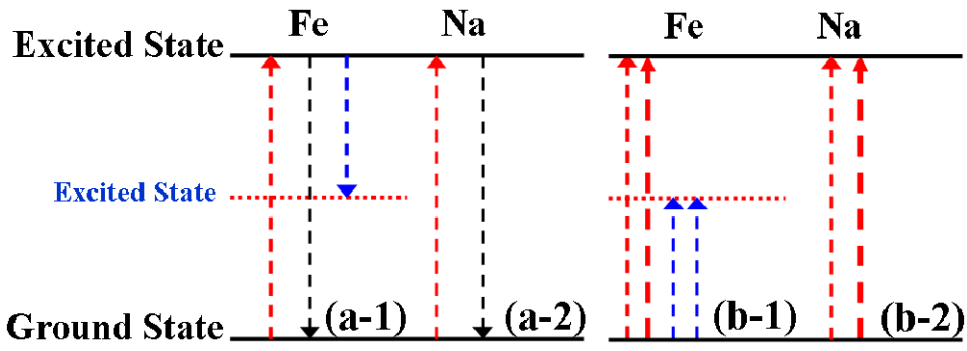

Figure 2-3 Difference between techniques of (a) LIF and (b) PS demonstrate the capability of suppressing strong background noise using PS. (a-1) Atomic Fe can be detected in other transition different from that used to excite Fe atoms using LIF. (a-2) The transition used to excite and detect atomic Na is identical. For PS measurement, two laser beams (two long red or short blue dash lines in b-1) are used to excite Fe or (two long red dash lines in b-2) to excite Na atoms and the polarisation variation is detected instead of the detection of fluorescence. Thus, the PS technique is capable of suppressing background noise.

For the case of atomic Na, the detection mechanism of LIF is simple, as shown in **Figure 2-3** a-2. The fluorescence of atomic Na possesses the same transition which is used to excite Na atoms. Hence, the detection of atomic Na in the volatile flames of burning solid-fuel particles becomes difficult to distinguish the scattering nosie from the fluorescence signals as the noise characterises at the same transition of atomic Na.

For PS technique, two laser beams, namely probe and pump beams, are used to excite the Fe or Na atoms. The pump beam excites the Na atoms and the polarisation variation occurs while the polarised probe beam, which has the same wavelength, passes through the excited Fe or Na atoms. By detecting the polarisation variation of the probe beam, the intensity of PS signal can be detected. The two long red or short blue dash lines, as shown in **Figure 2-3** (b-1), represent two persistent transitions of atomic Fe and two long red dash lines, as shown in **Figure 2-3** (b-2), indicates the D_1 line of atomic Na.

2.2 Atomic Spectroscopy Overview

2.2.1 Introduction

Energy was considered as a continuum in classical physics. However, it is not always the case for certain experiments, such as the model of atom, determination of light speed, atomic spectroscopy and black body radiation etc. In 1900 Max Planck reported the revolutionary concept that energy can be described as discrete levels which only occur by means of allowable transitions between two distinct energy levels, as given by:

$$v = \Delta E / h \qquad \text{Eq. 2-14}$$

where, ν is the frequency of radiation (Hz); ΔE is the energy for the allowable transition between two states (J) and h is the Planck's constant, which is a universal constant ($=6.63\times10_{-34}\,\mathrm{J\cdot s}$). As shown in **Figure 2-4**, energy is absorbed or released while the allowable transition takes place. A beam with a single frequency is absorbed leading to excitation from E_i (initial energy state) to E_j (higher energy state). The excited state intends to stay in the initial state so that the absorbed energy is released. By collecting radiation of a beam with a broad range of frequencies, a term of white light, interacting with the target species, the absorbed energy shown in left side of **Figure 2-4**, demonstrates a dark area producing an absorption spectrum. On the other hand, if the energy is released as indicated in right side of **Figure 2-4** reveal an emission spectrum. In atomic spectrum, the absorption spectrum is naturally complementary to the emission spectroscopy.

The energy change being restricted to a finite value related to a frequency of radiation possesses characteristics of a specific atom or molecule which gives rise to applications of spectroscopy. By examining the wavelengths of radiation related to the energy change, therefore, it is feasible to determine the Na, K or Fe, in the case of this thesis, in the sample.

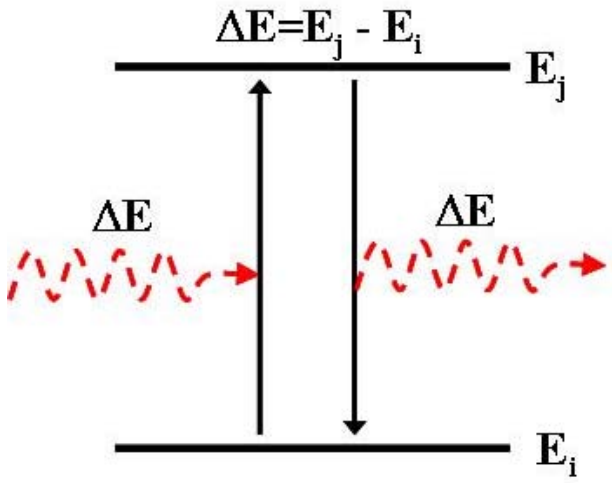

Figure 2-4 Energy (ΔE) is used to excite the target species from the initial energy state (E_i) to a higher energy state (E_j). In other words, the energy, ΔE, is absorbed by the target species and excited to a higher energy state. The same amount energy, ΔE, released when the target species returns to the initial energy state can be detected.

The theory applied by Bohr to describe energy change in an atom from one state to another is feasible to be extended to describe the energy excitation or relaxation between states. Due to the fact of quantized energy levels, each state has a corresponding quantum number. However, the energy states of molecules or radicals need to be considered thoroughly.

2.2.1.1 Electronic Energy

Each atom characterises with a set of orbiting electrons. When an atom is excited owing to absorbing energy, electrons are excited to the higher energy states. This can be characterised by the principal quantum number, *n*, which can be considered to be the radius of the orbit where electrons suppose to be. It should be noticed that the distinct orbits can not be observed, which is described by the Heisenberg Uncertainty Principle, because the orbit is a descriptive concept. However, the energy levels characterised by quantum number are discrete with the values of n = 0, 1, 2, 3, 4..., which are represented X, A, B, C…, respectively.

Since electrons of a molecule orbit the nucleus, it is necessary to consider the orbital angular momentum, ℓ, which is characterised with $\ell = 0, 1, 2, 3, 4...n-1$. Not only is the consideration of electrons orbiting the nucleus, electron spin should be also taken into consideration with a corresponding spin quantum number, *s*. Regarding of the charge of the electrons for the orbital angular momentum in the confined states, the spin intends to characterise the preferred orientations which are described by the designated quantum numbers, m_ℓ and m_s. Due to the insufficiency to describe each orientation only applying n and ℓ, another symbol, λ, where $\lambda \equiv m_\ell$, is conducted. However, it should be noticed that λ does not account for the positive or negative values of m_ℓ so that λ states ought to be doubly degenerate.

For the most of major situations involving more than one electron, a stated description of energy state can be represented by the total electronic orbital angular momentum quantum

number, Λ, as defined by:

$$\Lambda = \sum_i \lambda_i - \sum_i m_{\ell_i}$$

Eq. 2-15

where, *i* indicates each constituent electron.

The described state, Λ, are $\Lambda = 0, 1, 2, 3....$ associated with symbols corresponding to $\Sigma, \Pi, \Delta, \Phi....$, respectively. Then, the spin is further taken into consideration of the electronic designation, as described: $n^{2S+1}\Lambda$. An popular radical in combustion, as an example, OH whose electronic ground state is described as $X^2\Pi$, where X represents the electronic ground state; the 2 superscript indicates the multiplicity (as $|S| = 1/2$) and Π is the total electronic orbital angular momentum quantum number as $\Lambda = 1$.

2.2.2 Boltzmann Populations

The effective energy level of a molecule has been defined in the preceding section, each energy level correspond with a specific quantum number which is only appropriate to describe a single molecule. Within a gas, however, there are a lot of molecules which may not possess the same energy levels. It is possible to determine the fraction of the population exhibiting in the state (*i*), as denoted f_i by the Boltzmann distribution, as presented by:

$$f_i = \frac{g_i \cdot \exp(-E_i/k \cdot T)}{q}$$

Eq. 2-16

where, g_i is the degeneracy of state *i*; E_i is the energy of state *i*; *k* is Boltzmann's constant; T is the absolute temperature in Kelvin (K) and q is the partition function. The *q* can be obtained by finding the total sum of all the population fractions, given by:

$$q = \sum_i g_i \cdot \exp(-E_i/k \cdot T)$$

Eq. 2-17

2.2.3 Collision Processes

Collisions with other molecules can lead to variation in the energy level of the target species and hence the absorption and emission wavelengths will be altered. The energy transfer caused by collisions may be classified based on its effect. As to the electronic energy transfer, it changes the electronic states of the species. Quenching is a specific form of electronic transfer, where the species is returned to its electronic ground state without light emission. Due to the energy conversation, energy is transferred (lost from the excited species). Hence, quenching is generally considered to result from collision processes. However, it is still controversial. Moreover, the complexity introduced by collision processes, which causes the difficulty of the quantitative LIF, is a temperature dependent process.

2.3 Combustion Process

2.3.1 Premixed Methane Flame

Combustion is a sequential process of exothermic chemical reactions of a fuel and an oxidant going with heat generation representing in the form of either glowing or a flame. In a complete combustion reaction, the compounds of a fuel react with an oxidizing element and thus the products are the gross compounds of the fuel and oxidizing element.

In the fundamental combustion of premixed flames, two scenarios need to be considered when air or pure oxygen is used as an oxidant. Stoichiometric combustion with pure oxygen and hydrocarbon is represented in a general form, as presented below:

$$C_xH_y + (x + \frac{y}{4}) \cdot O_2 \rightarrow x \cdot CO_2 + (\frac{y}{2}) \cdot H_2O + \Delta H$$

Eq. 2-18

For example, methane (CH_4) is used, which is shown in the following equation:

$$CH_4 + 2 \cdot O_2 \rightarrow CO_2 + 2 \cdot H_2O + \Delta H$$

Eq. 2-19

where, ΔH is the released energy. Carbon dioxide (CO_2) is the only pollutant emission. In some circumstance combustion takes place with insufficient oxygen leading to emission of toxic gas, carbon monoxide (CO), as described in a general expression:

$$2 \cdot z \cdot C_x H_y + 2 \cdot z \cdot (x + \frac{y}{2}) \cdot O_2 \rightarrow \frac{2 \cdot z \cdot x}{3} \cdot (CO + CO_2 + C) + (z \cdot y) \cdot H_2O + \Delta H$$

Eq. 2-20

and the case of methane is shown as bellow:

$$6 \cdot CH_4 + 9 \cdot O_2 \rightarrow 2 \cdot CO + 2 \cdot CO_2 + 2 \cdot C + 12 \cdot H_2O + \Delta H$$

Eq. 2-21

In most industrial applications air is the major oxygen source and so stoichiometric chemical reaction is slightly modified, as shown in a general form:

$$C_x H_y + (x + \frac{y}{4}) \cdot (O_2 + 3.76 \cdot N_2) \rightarrow x \cdot CO_2 + (\frac{y}{2}) \cdot H_2O + 3.76 \cdot (x + \frac{y}{4}) \cdot N_2 + \Delta H$$

Eq. 2-22

and a practical example of methane is obtained, as presented:

$$CH_4 + 2 \cdot (O_2 + 3.76 \cdot N_2) \rightarrow CO_2 + 2 \cdot H_2O + 7.52 \cdot N_2 + \Delta H$$

Eq. 2-23

The air-fuel ratio (AFR) for two cases of using oxygen and air as an oxidant are different and so the equivalence ratios (Φ). In the following section the detailed discussion of air-fuel ratio and equivalence ratio will be expounded. Moreover, as shown in equations introduced above, nitrogen is not involved in reaction. High temperature, however, could facilitate the formation of nitride (NO_x) which includes nitrogen monoxide (NO) and nitrogen oxide (NO_2), as presented in the following equation:

$$CH_4 + 2 \cdot O_2 + N_2 \rightarrow CO_2 + 2 \cdot H_2O + N_2 + CO + NO_x + \Delta H$$

Eq. 2-24

In industrial power plants, therefore, NO_x could be a potential issue to environment.

2.3.2 Equivalence Ratio

In the preceding section the global chemical reactions of premixed methane flame using air and pure oxygen have been introduced although the sequential reactions of premixed methane flame were not discussed. These reaction equations only pointed out the stoichiometric condition which the oxidant and fuel fully reacted. In order to define combustion conditions, the Air-Fuel Ratio (AFR) is introduced bellow:

$$\mathrm{AFR} = \frac{Mole_{oxy}}{Mole_{fuel}} = \frac{Mass_{oxy}}{Mass_{fuel}}$$

Eq. 2-25

where, $Mole_{oxy}$, $Mole_{fuel}$, $Mass_{oxy}$ and $Mass_{fuel}$ consecutively describe the molar and mass ratios of fed oxidizer and fuel. The value of AFR could be expressed differently by two definitions (as shown in **Eq. 2-25**) leading to difficulties in comparison of different conditions. This issue will be discussed later.

AFR is a ratio of oxidizer-to-fuel in the combustion reaction. Combustion conditions can be defined by equivalence ratio (Φ) which is mathematically described as a ratio of actual and stoichiometric AFR (termed as AFR_{act} and AFR_{stoi}, respectively), as described below:

$$\Phi = \frac{\mathrm{AFR}_{\mathrm{stoi}}}{\mathrm{AFR}_{\mathrm{act}}} = \frac{\dfrac{Mole_{stoi-oxy}}{Mole_{stoi-fuel}}}{\dfrac{Mole_{act-oxy}}{Mole_{act-fuel}}}$$

Eq. 2-26

where $Mole_{stio-oxy}$ and $Mole_{stoi-oxy}$ are the molar ratios in chemical reactions, respectively, and $Mole_{act-oxy}$ and $Mole_{act-fuel}$ are respectively the molar ratios of fed gas reactants. Equivalence

ratio of 1.0 is at stoichiometry and thus rich and lean conditions are greater and less than 1.0, respectively.

It is the advantage that equivalence ratio can avoid the issue mentioned in **Eq. 2-25**. By applying **Eq. 2-25** in **Eq. 2-19** to calculate AFR_{act} with one mole of each reactant, for example, it shows two different values, as given below:

$$AFR_{act} = \frac{Mole_{act\text{-}oxy}}{Mole_{act\text{-}fuel}} = \frac{1}{1} = 1$$
$$= \frac{Mass_{act\text{-}oxy}}{Mass_{act\text{-}fuel}} = \frac{1\text{x}2\text{x}16}{1\text{x}(12+1\text{x}4)} = 2$$

Eq. 2-27

It demonstrates the difference between two definitions of AFR_{act}, as shown in **Eq. 2-27**, leading to different equivalence ratios. The AFR_{stoi} is described below:

$$AFR_{stoi} = \frac{Mole_{stoi\text{-}oxy}}{Mole_{stoi\text{-}fuel}} = \frac{2}{1} = 2$$
$$= \frac{Mass_{stoi\text{-}oxy}}{Mass_{stoi\text{-}fuel}} = \frac{2\text{x}2\text{x}16}{1\text{x}(12+1\text{x}4)} = 4$$

Eq. 2-28

Therefore, the same equivalence ratio (defined by **Eq. 2-26**) can be obtained combining **Eq. 2-27** and **Eq. 2-28**, as shown below:

$$\Phi = \frac{AFR_{stoi}}{AFR_{act}} = \frac{\dfrac{Mole_{stoi\text{-}oxy}}{Mole_{stoi\text{-}fuel}}}{\dfrac{Mole_{act\text{-}oxy}}{Mole_{act-fuel}}} = \frac{2}{1} = 2$$
$$= \frac{\dfrac{Mass_{stoi\text{-}oxy}}{Mass_{stoi\text{-}fuel}}}{\dfrac{Mass_{act\text{-}oxy}}{Mass_{act-fuel}}} = \frac{4}{2} = 2$$

Eq. 2-29

Hence, it is necessary that the calculation of Φ is performed under the unique definitions of

air and fuel.

For the AFR_{act} measurement in this thesis, the flowrates of air and fuel controlled by two mass flow controllers (MFC) were performed instead of mass or molar ratio. The AFR_{act} of air and methane mixture in the following experiments was calculated using flowrates (L/min,). According to ideal gas law, the flowrate could be corrected, as detailed below:

$$\Phi = \frac{AFR_{stoi}}{AFR_{act}} = \frac{\frac{Mole_{stoi\text{-}oxy}}{Mole_{stoi\text{-}fuel}}}{\frac{Flowrate_{act\text{-}oxy} \text{x} 22.4}{Flowrate_{act-fuel} \text{x} 22.4}}$$

Eq. 2-30

where, $Flowrate_{act\text{-}oxy}$ and $Flowrate_{act\text{-}fuel}$ respectively represent the actual flowrates of oxygen and fuel. In fact, the correction is not necessary while the mixture is considered as an ideal gas. Based on the **Eq. 2-23** and **Eq. 2-26**, equivalence ratios employed in the following experiments were obtained.

2.4 Calculation of Seeded Species in the Flames

Conventionally the absolute concentration of a target species is achieved using absorption measurement. In flame media, the target species may exist in various forms. For example, sodium in the flames may be in the forms of atomic Na, Na_2O or NaOH. Therefore, it is almost impossible to identify the absolute concentration of each form of target species without conducting the absorption measurement. For the convenience to establish calibration curves for the quantitative LIBS measurement, it is reasonable to determine the concentration of seeded target species by using the Ideal Gas Law in flame media.

Assume that the rate of seeded salt (υ_m, g/s) is known, the molar flowrate of the target species (υ_{ms}, mol/s) in the flame can be governed by:

$$\upsilon_{ms} = a_m \cdot \upsilon_m / M$$

Eq. 2-31

where, a_m and M are molar ratio and atomic mass of the target species, respectively. The υ_m can be easily and simply determined by conducting a long term seeding experiement. The total gas flowrate (υ_f, L/s) at the flame temperature (T_f, K) can be obtained:

$$\upsilon_f = (\upsilon_g + \upsilon_a) \times T_f / T_r$$

Eq. 2-32

where, υ_g and υ_a are the flowrates of fuel and air (L/s), respectively; T_r is the room temperature (K). Hence, the number density of the target species (mol/L or atoms/m^3) can be obtained by dividing **Eq. 2-31** with **Eq. 2-32**. To represent the concentration of target species in the dimensionless unit, part per million (ppm), the molar flowrate of total gas (υ_{mf}, mol/s) in the flame is given by applying the Ideal Gas Law:

$$\upsilon_{mf} = \mathrm{P} \cdot \upsilon_f / \mathrm{R} \cdot T_f$$

Eq. 2-33

Hence, the concentration of target species ($C_{seeding}$, ppm) is presented by:

$$C_{seeding} = \upsilon_{ms} / \upsilon_{mf}$$

Eq. 2-34

2.5 Plasma Overview

2.5.1 Introduction

Plasma, a gas-like substance, contains various types of particles which are free electrons, cations and neutral substance. Since an electron is accelerated by electrical field to increase kinetic energy of the electron which collides with neutral particles, it may ionize the particle

to generate another electron. New electrons, based on the same scenario, will collide with more neutral particles leading to sequential generation of electrons. Plasma occurs while the electron density reaches the critical level. During the elastic and non-elastic collision occurring between electrons and neutral particles leading to energy transfer, while non-elastic collision takes place, most of electron energy is transferred to particles leading to excitation, ionization, relaxation and recombination.

Due to the properties of the plasma, it was catalogued as the fourth phase of material compared to solid, liquid and gas phases. Ionization ratio which depends on the electron energy of the plasma is less than 0.001 per cent in the most of plasma applications and 1 per cent for high density plasma (HDP). In addition, the ionization ratio in the Sun is 100 per cent. Plasma possesses electrical conductivity and responds strongly under electromagnetic fields.

Two type of ionized gas, owing to temperature levels, are marked as high and low temperature plasmas. Generally the temperature range of particles in high temperature plasma could reach 10 million and up to 100 million Kelvin. High temperature plasma can be used to investigate nuclear fusion for energy purpose. As to low temperature plasma whose temperature is from thousands to dozens thousands Kelvin, it has been widely employed in various fields to improve technologies.

2.5.2 Plasma Generation

2.5.2.1 Methodology of Plasma Generation

There are many techniques widely used to generate plasma for specific purposes, such as thermo-induced plasma, low pressure arc discharge, radio frequency discharge, laser ablation and welding arc et al [186], cataloged as low temperature plasma. Thermo-induced plasma generally indicates flames eligible to excite atoms or molecules. The excited species release

energy when jumping to lower energy state and thus spectra are observed. The low pressure arc discharge is operated under low pressure of chosen shielding gases, such as helium and argon, around 100 torr, to vaporize the anode substance and deposit forms in the cathode. The arc is induced by the electric field varied by the applied currents. This process is typically operated under the fixed voltage as the anode substance is consuming. By continuous feeding anode material [187], the arc plasma stably vaporizes target species depositing on the cathode. This method have been applied to produce fullerene (C_{60}) [188] and carbon nanotube (CNT) [187, 189]. Radio frequency discharge operated under low pressure plasma which is generated by AC power has been widely applied to produce thin films on subtracts [190]. Laser beam focused on the target bulk is used to ablate target species forming thin films on the substrates. The focused laser beam leading to high energy density generates a plasma plume containing the vaporized target species (molecular forms) [191]. As to welding arc, it will be introduced in the following section.

2.5.2.2 Gas Tungsten Arc Welding

One of the common welding arc application, gas tungsten arc welding (GTAW), is similar with the low pressure arc discharge but is operated under atmospheric pressure. A welding arc is induced by the applied voltage, which is varied by the applied currents, while the constant voltage is performed in low pressure arc discharge. The GTAW process is most commonly utilized to weld thin sections of stainless steel and other metals, which are aluminum, copper and magnesium alloys. The buffer gas, such as helium (He), argon (Ar), nitrogen (N_2), neon (Ne) or gas mixtures, dominates the resistances between the anode and cathode leading to the various current densities. Regarding the complexity of multi-parameters, it is difficult and complicated to control GTAW precisely [192]. For the purpose of application, the welding current is maintained constantly indicating the constant number density of iron can be achieved.

2.6 Thermogravimetric Analysis

2.6.1 Introduction

Thermogravimetric analysis or thermal gravimetric analysis (TGA) is commonly employed in research and testing to determine characteristics of materials such as polymers, to determine degradation temperatures, absorbed moisture content of materials, the level of inorganic and organic components in materials, decomposition points of explosives, and solvent residues. It is also often used to estimate the corrosion kinetics in high temperature oxidation measuring mass variation

Thermogravimetric analysis (TGA) has been widely employed to predict and to model coal pyrolysis [136] and combustion [131, 193] and biomass pyrolysis [194, 195] and combustion [155, 196, 197] mechanisms. The pyrolysis and combustion mentioned here are meant to be the thermal degradation carried out under presence and absence of oxygen.

TGA is also used to analyse kinetic properties of materials related to mass change in relation to temperature. Due to similarity of mass loss profiles, transformation with different purposes may require to interpret mass loss curves. Derivatives of mass loss profiles can be applied to reveal the critical temperature at which mass loss becomes dramatic. In this thesis, two solid-fuel particles, Australian Loy Yang Brown coal and pine wood pellets, have been employed for ultimate and proximate analysis, as shown in **Table 2-1**, analysed by HRL technology Ltd. The original test report and analysis standard are indicated in **Appendix B**.

2.7 Error Analysis

The potential sources of error typically common to all measurements in the experiments have been recognized in the following sections.

Table 2-1 Ultimate and proximate analysis of (a) Loy Yang coal and (b) pine wood particles analyzed by HRL Technology Pty Ltd (in Australia).

% (Dry ash free basis)		Loy Yang coal	(a)
C	67.8	Moisture(%)	8.9
H	5.20	Ash Yield(815 ℃)	0.8
N	0.57	Volatile Matter (%)	52.6
S	0.24	Fixed Carbon (%)	46.6
Cl	0.06	Hg (mg/kg)	0.16
O(By difference)	26.13		
% (Ash basis)			
SiO_2	12.9	MgO	12.2
Al_2O_3	31.4	Na_2O	11.3
Fe_2O_3	6.7	CaO	5.5
TiO_2	0.7	SO_3	16.9
K_2O	0.77		

% (Dry ash free basis)		Pine wood	(b)
C	51.3	Moisture(%)	7.1
H	6.00	Ash Yield(815 ℃)	0.8
N	< 0.01	Volatile Matter (%)	76.1
S	0.02	Fixed Carbon (%)	23.0
Cl	0.09	Hg (mg/kg)	N/A
O(By difference)	42.59		
% (Ash basis)			
SiO_2	43.3	MgO	8.3
Al_2O_3	0.97	Na_2O	4.9
Fe_2O_3	0.82	CaO	24.8
TiO_2	0.15	SO_3	3.9
K_2O	5.7		

2.7.1 Laser Energy

Daily adjustment of the laser energy has been conducted before experiments to reduce fluctuation of laser energy. For PS measurement, the energies of the Nd:YAG and dye lasers were maintained around 3.2 and 0.42 W, respectively. The variation of laser energy was experimentally determined to be 8%. As to variation of laser energy for LIBS measurement, the energy of fundamental wavelength, 1064 nm, was controlled by an attenuator. Hence, the variation for LIBS measurement was typically less than 5%.

2.7.2 Flowmeters

The flowmeters were used in **Chapter 3** and **Chapter 4**. The flowmeter specifications list an accuracy of 2% with repeatability of 0.5% which was determined at full-scale reading. However, it is not always possible for all measurements so that the errors might be a little higher. Three types of rotameters (ABB Inc.), namely Flowrator Tube FP ¼'-25-G-5/81, Precision Tube ¾'-21-G-10/83 and Precision Tube ½'-21-G-10/83, have been utilised in **Chapter 6**. To determine the actual operation errors of flowmeters applied to control air and fuel flowrates, the errors were experimentally determined to be 8% for main air stream

(Precision Tube ½'-21-G-10/83), 7% for seeding air flow (Precision Tube ¾'-21-G-10/83) and 4% (Flowrator Tube FP ¼'-25-G-5/81) for fuel flow. The major source of error is caused by the net force between the dragging force of floats and gas flow force. Therefore, the net force significantly varies with non-full-scale pressure leading to higher errors. Although it is possible that errors come from fluctuation of air and natural supply systems, the air and fuel were switched on 15 minutes before the experiments to stabilize the gas system.

2.7.3 Mass Flow Controller (MFC)

The mass flow controllers (MFCs) were used in **Chapter 5** and **Chapter 6** to control the flowrates of main stream air, seeding air and methane. The specifications specify accuracies of three MFCs for the adjustment of main stream air, seeding air and methane to be 0.47, 2.86 and 0.69%.

2.7.4 Variation of Solid-Fuel Particles

Loy Yang Brown coal (23±3 mg, approximately spherical 3 mm diameter) from Vitoria Australia and pine wood particles (63±3 mg, approximately spherical 4 mm diameter), were used in the experiments of the thesis. Due to the variability of each solid-fuel particle, the variation between coal and wood particles can be considered in two aspects, the weight and volume. The volume variation was identified to be 8.4 and 3.5 % for coal and wood, respectively, using the approximate sphere calculation. The weight variation for coal and wood particles was obtained to be 13 and 4.8 %, respectively. This will cause the variation in the release of alkali species and the combustion timeframe. Due to the difficulty to determine the uncertainty of alkali metals released from burning solid-fuel particles using optical measurement techniques, it is reasonable to consider the variation as the uncertainty. However, to select weight variation is better than that of volume because the it is an approximation

determined using ICCD images.

2.7.5 Nebulising System

A nebulising system, as presented in **Figure 2-5**, was used to generate salt solution droplets, which were entrained into flames. The stability of nebulising system is performed by the seeding air flowrate using the flowmeter (Precision Tube ¾'-21-G-10/83) with the error 7% or by the MFC with the error 2.86%. The error of the seeding solution flow using the flowmeter and the MFC were experimentally determined to be 8.14 % and 4.17%, respectively, by conducting the long term seeding process. By measuring the difference of the consumed salt solution before and after four hours, the average consumption of seeding salt solution was experimentally obtained. Moreover, this seeding process was repeated three times to evaluate the variation of the nebulising system.

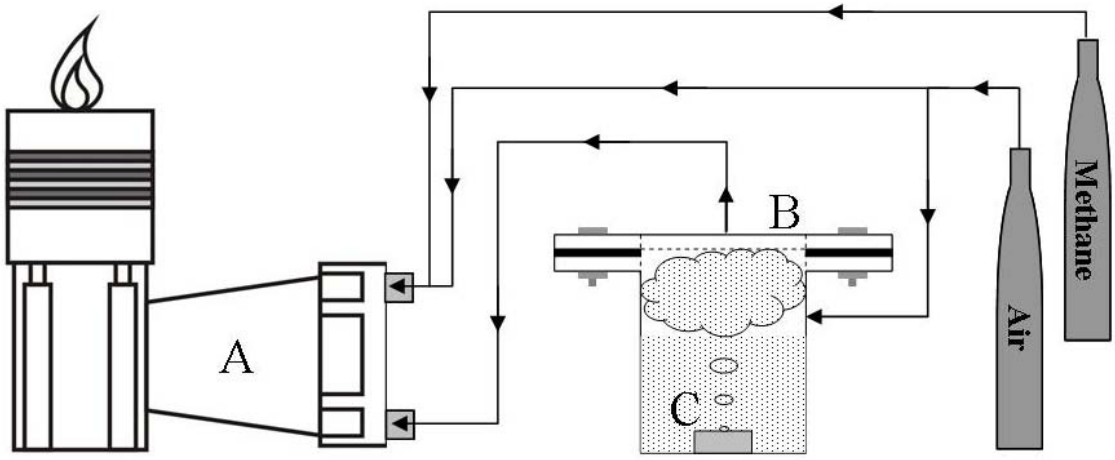

Figure 2-5 A seeded flame system comprises (A) a burner, (B) a nebulising system and a gas and fuel supply system. A nebuliser (C) is used to generate salt solution droplets, which are entrained into a flame.

CHAPTER 3.

Assessment of Polarisation Spectroscopy in Atomic Sodium Detection

3.1 Introduction

This chapter describes how the ability of laser Polarisation Spectroscopy technique (PS) to detect atomic Na in two types of environments was assessed. In the first experiment, a well-defined sodium concentration seeded into the premixed laminar methane flames was studied. In the second experiment, the PS technique was applied to detect atomic Na released in a plume produced by the burning of solid-fuel particles.

The first experiment was designed to decouple the dependencies associated with the PS detection process. The PS signal level is influenced by several physical and chemical factors: pump beam fluences, wavelength dependence, seeded population of Na atoms and flame conditions. In the second experiment, the PS technique was applied to detect the time-resolved records of atomic Na released from burning solid-fuel particles at a single wavelength.

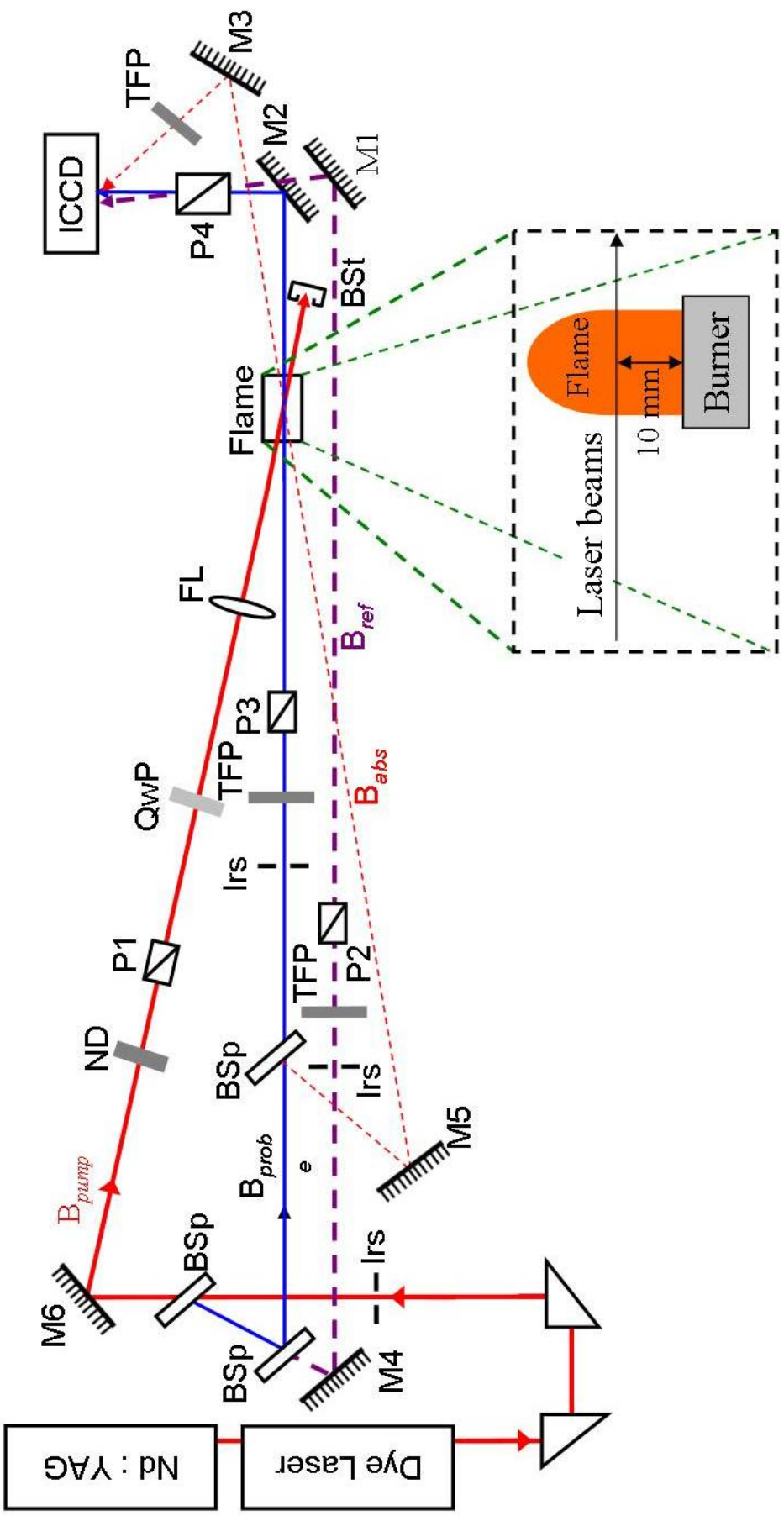

Figure 3-1 Schematic diagram of PS optical arrangement, Mirrors: M1, M2, M3, M4, M5; Focal Lens: FL; Beam Splitter: BSp; Beam Stop: Bst; Iris Diaphragm: Irs; Polariser: P1, P2, P3, P4; Thin Film Polariser: TFP; Neutral Density files: ND; Pump Beam: B_{pump}; Probe Beam: B_{probe}; Reference Beam: B_{ref}; Absorption Beam: B_{abs}, Quarter-wave Plate ($\lambda/4$): QwP. The probe and pump beams were located 10 mm above the burner.

3.2 Experimental Arrangement

3.2.1 Laser Diagnostic System

The experimental arrangement (Figure 3-1), consisted of a laser system (Nd:YAG pumping a dye laser) synchronized with an intensified CCD camera (ICCD camera, Princeton Instruments, ICCD-576-G/RB-E) operated at 20 nano-seconds (ns) gate width and 35 ns gate delay, a premix laminar burner and a nebuliser seeding system. The probe and pump beams were located 10 mm above the burner in the case of seeded flames, as shown in **Figure 3-1**. For the case of burning solid-fuel particles, the laser beams were located 10 mm above the particles. To unify the metal detection in the flame media, the 10 mm height was employed throughout the experimental process. The laser system consisted of a tuneable dye laser (Lambda Physik Scanmate) pumped by a Nd:YAG laser (Coherent Brilliant B) synchronized with the ICCD system, as presented in **Figure 3-2**. The powers of radiation output for the Nd:YAG and the dye lasers were maintained at 3.2 ± 0.5 and 0.42 ± 0.02 W with 10 Hz repetition (320 mJ/pulse and 42 mJ/pulse), respectively. The line width and the duration of the

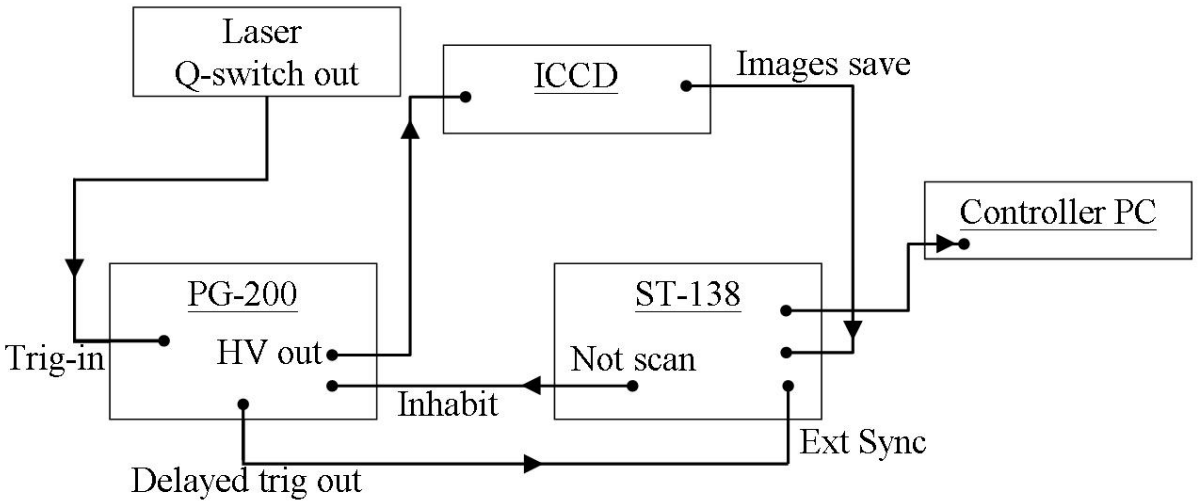

Figure 3-2 Schematic diagram for the synchronization of the laser and an ICCD systems

tuneable output were specified to be 0.08 cm^{-1} and 7 ns, respectively. The pulse-to-pulse energy jittering of the output radiation was measured to be 14% with 100 shots at the wavelength of 589.592 nm (D_1 line). Three beam splitters (BSp) were used to generate four beams, as shown in Figure 3-1, which are the pump beam (B_{pump}), probe beam (B_{probe}), reference beam (B_{ref}) and absorption beam (B_{abs}). The B_{ref} provided the instantaneous correction for the jitter in laser power. The B_{abs} was used to perform a simultaneous absorption measurement, a quantitative measurement of atomic Na.

Both the B_{pump} and B_{probe} were tuned to the same optical transition of the target species (one-colour PS). A small change in the polarisation of the B_{probe} can be detected by applying two Glan Taylor polarisers (extinction ratio ~ 5×10^{-6}) in the probe beam path, enclosing the region of optical pumping. To unify the properties of the B_{probe} and B_{ref}, two crossed Glan Taylor polarisers were also applied in the reference beam path, as presented in **Figure 3-1**. The intersection angle between B_{pump} and B_{probe} in the experimental arrangement was calculated to be 5.6˚.

The B_{probe} was linearly polarised and the B_{pump} could be either linearly or circularly polarised. For the linearly polarised B_{pump}, the two components were set to be equally parallel and perpendicular to the polarisation direction of the B_{pump}. For the circularly polarised B_{pump} used here, the linearly polarised B_{probe} was equally decomposed into right and left circularly polarised components. A detailed arrangement of the quarter-wave plate (QwP), which was applied to achieve appropriate circular polarisation of the B_{pump}, was described in Figure C-1 (in **Appendix C**).

3.2.2 Power Dependence

The power of the B_{pump} was measured before the flames to identify the energy loss caused by the optics absorption and by the energy diverged to form the B_{probe}, which was experimentally determined to be 66 ± 0.5 % of the initial laser power (42 mJ per pulse). The B_{pump} was

Table 3-1 Pump beam fluences (GW/cm^2) applied in the detection of atomic Na using PS were listed. The theoretical values of the laser powers were obtained by using the laser energy multiplied by the transmittances of the ND filters. The measured values of the laser powers were obtained directly after the ND filters.

Trasmittance (%)	Power (mJ) Before Flame		Error (%)	Fluence (GW/cm^2)
	Theoretical	Measured		
100	14.0	14.0	0.00	6.36
50.1	7.00	7.01	0.20	3.18
31.6	4.50	4.42	-1.69	2.01
15.8	2.20	2.21	0.45	1.00

focused by a spherical lens (500 mm focal length). The area of the focused laser beam resulted from the diameter of the focused pump beam based on the diffraction limit, governed by:

$$D_P = 1.27 \cdot f_L \cdot \lambda / D_0$$

Eq. 3-1

where, D_P is the diameter of the focused pump beam dot, f_L is the focal length, λ is the wavelength of the laser (589.592 nm for atomic Na in the D_1 line) and D_0 is the diameter of the input laser beam (0.2 cm in this work). Hence, D_P was calculated to be 18.72×10^{-3} cm, i.e. the area was 2.75×10^{-4} cm^2. Hence, the fluences of the B_{pump} were obtained by using laser beam power divided by the dot area. The fluence of the B_{pump} was later varied by four ND filters to provide fluences ranging from 6.36 to 1.00 GW/cm^2, as shown in **Table 3-1**.

The energy of the B_{probe} was generally very weak, less than 5% of the B_{pump} energy in the experimental arrangement. Because the ICCD camera detects the B_{probe} and B_{ref} directly, the powers of two beams were too strong that could damage the ICCD camera. Two thin film polarisers (TFP) were used to reduce the intensities of the B_{probe} and B_{ref} to protect the ICCD camera and also to adjust the powers of the B_{probe} and B_{ref}. Although the B_{abs} was also directly

introduced into the ICCD camera, the power of the B_{abs} has been adjusted to protect the camera. Due to the sensitivity of the power meter, it is too low to measure the power of the B_{probe}. Hence, the intensity of the B_{probe} was represented using the value of the ICCD count (the maximum was about 70 ± 10 counts) to maintain the consistent experimental conditions.

3.2.3 Premixed Laminar Burner

Two types of the laminar burners were used for the current study. Rich flames were generated using the premix laminar burner, while lean flames were produced using van Eyk's Diffusion Burner [11].

3.2.3.1 Rich Flame in the Premix Laminar Burner

The rich flames were generated using the premix laminar burner illustrated in **Figure 3-3**, to provide a stable and geometrically symmetrical environment. It should be noted that the term, 'stable flame', represents the un-lifted flames. Detailed drawings of the burner are provided in **Figure A-1**. A stable flame environment is crucial for conducting quantitative measurement. The honeycomb of the burner is made of Aluminium Oxide (Al_2O_3) making it difficult to remove residues from the surface of the burner due to the porous surface of Al_2O_3. The residues are thermally released into the premixed laminar flames, leading to contamination when the premixed flames directly attach to the top of the burner. To maintain the flame stability of premixed laminar flames and avoid contamination, the flames were operated right above the top of the burner. Allowing for the burning velocity of Australian natural gas, the designated flames could only be operated between the equivalence ratios of 1.3 and 1.4.

To perform the equivalence ratio of 1.3, the flowrates of the air and methane were controlled by two flowmeters set at 36.5 ± 2.92 (ABB Precision Tube ½'-21-G-10/83) and 5 ± 0.2 L/min (ABB Flowrator Tube FP ¼'-25-G-5/81). For the equivalence of 1.4, the flowrates of

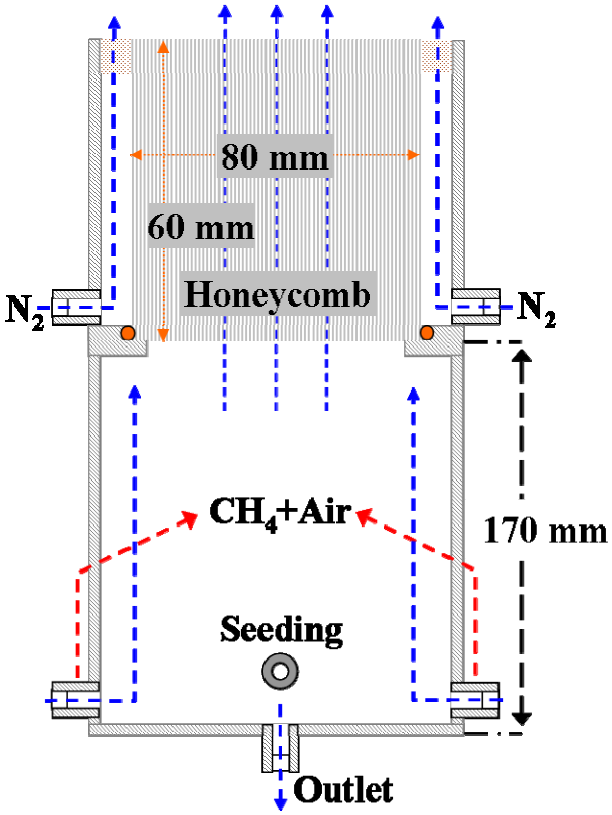

Figure 3-3 Schematic structure of the premix laminar burner; the two-layer structure consists of the honeycomb and the co-flow (top layer) and a premixed chamber (bottom layer). The seeded droplets were entrained from the bosses near the bottom and the outlet is utilized to drain out the excess condensed salt solution.

the air and methane were set to be 33.3 ± 2.67 and 5 ± 0.2 L/min.

As shown in **Figure 3-3**, air, fuel and seeded fine droplets of salt solution were premixed in the mixing chamber to reduce the fluctuation of the flowrate of the gaseous mixture created by the condensed seeding droplets. The salt solution was nebulised using an ultrasonic nebuliser to generate nominally 1 μm diameter salt droplets, which is governed by [198]:

$$D_{SD} = 0.34 \cdot \left(\frac{8\pi \cdot \psi}{\rho \cdot f_N} \right)^{1/3}$$

Eq. 3-2

where, D_{SD} is the median diameter of the salt droplets (μm), f_N is the exciting frequency of the ultrasonic nebuliser (MHz), ψ is the surface tension of water (mN·m^{-1}) and ρ is the density of water (kg·m^{-3}).

Table 3-2 Total seeded [Na] with the constant seeding air flowrate of 5 L/min was calculated using **Eq. 2-31** ~ **Eq. 2-34**. The seeding air flowrate was included in the total air flowrates.

Φ	CH_4 (L/min)	Air(L/min)	C(ppm)
1.3	5±0.2	36.5±2.92	1.503
			2.254
			3.757
1.4	5±0.2	33.3±2.67	1.628
			2.443
			4.071

The flowrate of the seeding air is 5 ± 0.35 $L \cdot min^{-1}$ determined by a flowmeter (ABB Precision Tube ¾'-21-G-10/83). Therefore, the consumption rate of the salt solution was experimentally determined to be 40 ± 0.3 $ml \cdot hr^{-1}$. The consumption rate then was used to estimate the total number density of Na atoms seeded into the flames using **Eq. 2-31** divided by **Eq. 2-32**. The result of the calculation is used to provide a reference concentration to verify the number density of atomic Na obtained using absorption spectroscopy. The three concentrations of sodium carbonate (Na_2CO_3) in wt%, namely 0.5, 1 and 5 g/L, seeded into the flames, were mathematically and physically converted into a concentration (part per million, ppm), as presented in **Table 3-2**, based on the constant salt consumption rate using **Eq. 2-31** ~ **Eq. 2-34**.

3.2.3.2 Lean Flame in the van Eyk's Diffusion Burner

To perform the lean laminar methane flames, a van Eyk's diffusion burner was used (**Figure 3-4**) [11-15]. The detail of the burner has been described in Ref. [11]. The particular design used in this study is presented in **Figure 3-5**. Each fuel port is hexagonally surrounded by six air ports. Hence, the fuel and air were not premixed before combustion. A separate air shroud surrounds the central burner and is used to stabilize the flame and to prevent puffing. Although diffusion flame allows much wider range of stoichiometries to be generated, it

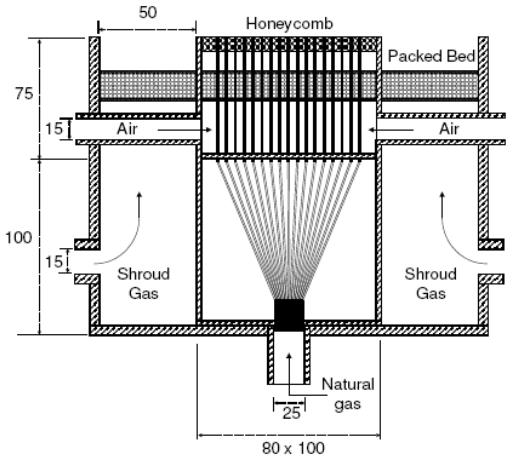

Figure 3-4 Schematic structure of the van Eyk's diffusion laminar burner, which is used to provide well-defined laminar flame environments with lean conditions (all lengths in mm) [11]. The measurement was carried out 10 mm above the burner, which is considered to be the zone of the premixed flame.

should be mentioned that the mixture fraction is not completely developed. Nevertheless, the mixture fraction becomes reasonably developed at a short distance (here 10 mm) above the burner matrix.

3.2.4 Data Acquisition and Processing

The optical layout was configured to allow the ICCD camera to record three laser beams simultaneously, namely B_{probe}, B_{abs} and B_{ref} (as introduced in **Figure 3-1**), as presented in **Figure 3-6**, providing comprehensive information of atomic Na in the flame. The beams were located in three areas, termed as the zones of PS, Absorption and Reference, as indicated in

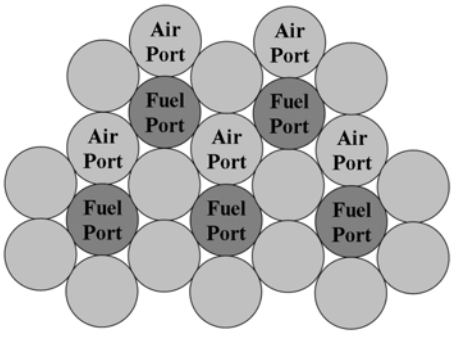

Figure 3-5 Hexagonal structure of fuel and air ports; each fuel port surrounded by six air ports generates premixed laminar methane for lean conditions.

Figure 3-6.

The image size varies from shot to shot indicating that the PS intensity of the atomic Na extrapolated from each image is different. The variation resulting from the size of the chosen pixel array is therefore expected. To reduce the fluctuation caused by energy jitter in the beams and by variable beam steering effect, it is necessary to determine the experimental intensity of PS signals of atomic Na (I_{PS}) in a chosen pixel array ($n\times n$ matrix) instead of averaging the intensity within the whole beam area (approximately 150×150 pixels). The imaging process in the chosen $n\times n$ matrix (n^2 pixels) was performed using Matlab 7.0 to demonstrate the variation in the experimental intensity of atomic Na. To optimize the dimensions of the chosen pixel array ($n\times n$ matrix), the errors among $n\times n$ matrices were investigated, as shown in **Figure 3-7**. The error becomes significant when n is larger than 11. Hence, the 9×9 matrix was chosen to determine the I_{PS} of atomic Na. The same image processing using Matlab 7.0 was conducted to achieve the average intensities of B_{abs} and B_{ref}.

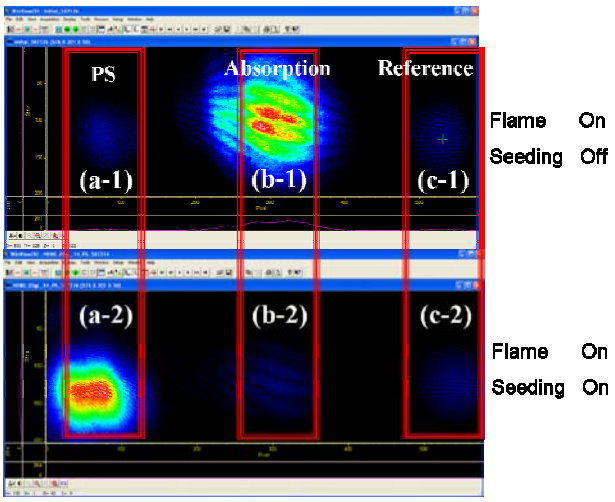

Figure 3-6 The three types of signal recorded in three locations of a single ICCD detector: (a) PS signal detects the concentration of atomic Na. (b) The absorption measurement is used for the quantitative measurement of atomic Na in the seeded flame. (c) The B_{ref} provides the instantaneous correction for the laser power. (a-1) and (b-1) show the intensities of B_{probe} and B_{abs}, respectively, operated in the unseeded methane flames. (a-2) and (b-2) demonstrate the intensities of B_{probe} and B_{abs}, respectively, performed in the Na seeded methane flames. The B_{ref} in (c-1) and (c-2) bypasses the methane flames and remains constant.

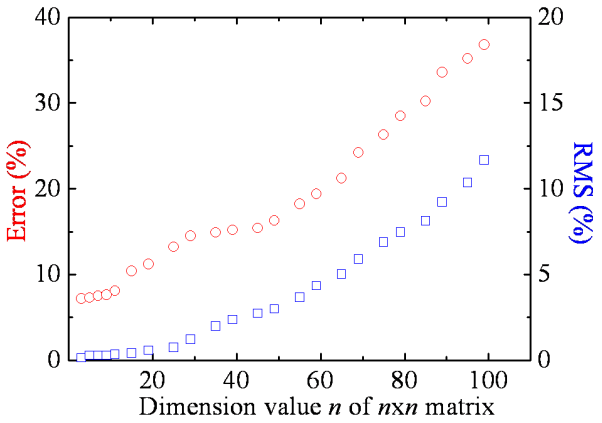

Figure 3-7 Errors and Root-Mean Square (RMS) of $n \times n$ pixel arrays show the variation of I_{PS} among n^2 pixels. The values of n were examined from 3 to 99. The error significantly increases when n = 11.

The $n \times n$ matrix is centred on the pixel array with maximum intensity. The I_{PS} in the chosen pixel array is obtained by averaging the intensities in each pixel. Details of the Matlab codes used to process the images of B_{probe}, B_{abs} and B_{ref} are provided in **Appendix I-1**. The I_{PS} of the chosen 9×9 pixel array is indicated in **Figure 3-8**. The red dot represents the pixel with the maximum intensity. The red dot among the pixels in each ICCD image was determined by sorting the pixel array in two dimensions.

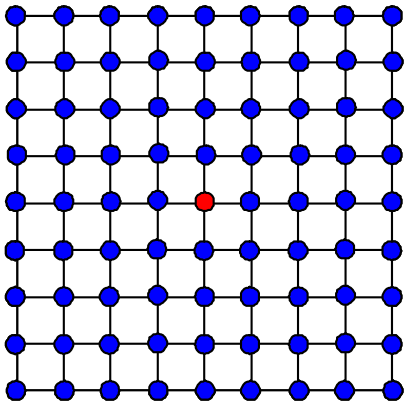

Figure 3-8 Illustration of image processing: 9×9 pixel array is centred on the instantaneous pixel (the red dot ●), in which is the strongest intensity of the chosen matrix. This varies from shot to shot.

3.3 Results and Discussion

3.3.1 Fitting of PS Lineshape

The lineshapes of atomic Na with various experimental conditions using PS have been obtained from the wavelengthscan. While **Eq. 2-13** provides a valid description of PS lineshapes for minor species, it is necessary to account for the nonlinear PS and linear absorption signals when PS measurement is used to detect a highly populated species, as indicated in **Figure 3-9**. The generation of PS signals occurs in the interaction zone shown as a shaded grey region, labelled '*a*', where the probe and pump beams cross (the blue dash in **Figure 3-9**). The probe beam, carrying the PS signal (the variation of polarisation) continues through the flame line along the path, labelled '*b*' where is it subjected to absorption (the red dash in **Figure 3-9**). The significant absorption increases with the population of the target species. This indicates that a highly populated sample results in significant absorption for a PS measurement, a fact which needs to be taken into account in the PS lineshape.

General absorption, [G(ω) mentioned in **Eq. 2-12**] occurs in the intersection area, *a*, in **Figure 3-9** when the PS signal is generated. The particular absorption in the current study, however, was caused by the flame and G(ω) was negligible. The absorption occurring in $I_{PS}(\omega)$ was

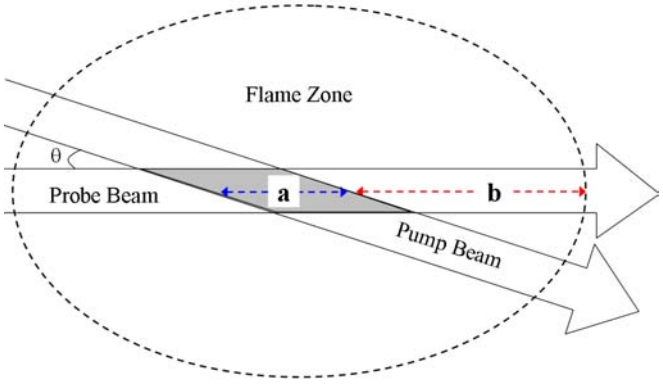

Figure 3-9 The PS signal consists of pure PS and absorption signals in highly populated media: *a*: Probe/Pump beams interaction length (L_{PS}), *b*: Probe beam absorption length (L_{abs})

analysed using the Beer-Lambert law and the experimental PS lineshape could be determined by extending Eq. 2-13 to account for the absorption [114] which is described by a Lorentzian function, governed by:

$$I_{PS}^{exp}(\omega) = I_{probe}(\omega)\cdot\left\{\xi + \left(\frac{[\mathrm{Na}]^2\cdot f_B^2\cdot I_{pump}^2\cdot\tau_{pump}^2}{16\cdot\hbar^2\omega^2}\cdot\sigma_{J_f\leftarrow J_i}^4\cdot\zeta_{J_f\leftarrow J_i}^2\cdot L_{PS}^2\right)\cdot\left(\frac{1}{1+[2\cdot(\omega-\omega_0)/(\Delta\omega_{PS})]^2}\right)^n\right\} - I_{abs}(\omega)$$

Eq. 3-3

where, $I_{PS}^{exp}(\omega)$ is the experimental PS signal; L_{abs} is the absorption path length of the B_{probe} (m); [Na] is the number density of atomic Na in the seeded flame and $\Delta\omega_{PS}$ is the combination of three broadening widths, which are natural linewidth ($\Delta\omega_n$, cm^{-1}), the self-broadening ($\Delta\omega_{self}$, cm^{-1}) caused by the target species itself and collisional broadening ($\Delta\omega_{collision}$, cm^{-1}) caused by other species in the sample media, as described in the Ref. [18]. The $I_{abs}(\omega)$ is an absorption function with respect to the transition (ω) of whichever lineshape is governed by the Lorentzian function. In the current study, the individual broadening width was not evaluated directly but the combination of broadening widths could be obtained from the PS lineshape.

Looking again at **Eq. 3-3**, the $I_{abs}(\omega)$ should be addressed by considering the $I_{PS}(\omega)$ in the absorption regime. The lineshape of $I_{PS}(\omega)$ in the absorption regime is different from that in the PS regime. This indicates that the lineshape of $I_{PS}(\omega)$ in the absorption regime is dominated by the absorption Lorentzian function. The absorption of $I_{PS}(\omega)$ inside the seeded flame is governed by the Beer Lambert Law. To mathematically and physically describe the absorption profiles, The **Eq. 3-3** is insufficient for the Beer Lambert Law. Therefore, **Eq. 3-3** can be expressed as follows:

$$I_{PS}^{exp}(\omega) = I_{probe}(\omega)\cdot\xi + I_{PS}\cdot\left(\frac{1}{1+[2\cdot(\omega-\omega_0)/(\Delta\omega_{PS})]^2}\right)^n \times exp\left(-\alpha(\omega)\cdot L_{abs}\cdot\right)$$

Eq. 3-4

where, $\Delta\omega_{abs}$ is the FWHM of atomic Na in the absorption regime. It should be noted that the absorption that occurred after the probe beam, $I_{probe}(\omega)$ passed through the seeded flame, as illustrated in **Figure 3-9**, was not considered in **Eq. 3-4** due to the physical complexity.

A red dashed line is used to approximately describe the experimental PS linshape in **Figure 3-10**. Using the Marquardt's algorithm [199], a modified equation based on **Eq. 3-4** that incorporates the absorption of the probe beam can be employed to calculate the six parameters introduced in **Figure 3-10**. See the following equation:

$$I_{PS\_FIT}(\omega) = I_{baseline} + I_{PS} \times \left\{ \frac{1}{1+\left[\frac{2\times(\Delta\omega-\Delta\omega_{shift})}{\Delta\omega_{PS}}\right]^2} \right\}^n \times exp\left[\frac{-\alpha_0 \cdot L_{abs}}{1+\left(\frac{2\times\Delta\omega}{\Delta\omega_{abs}}\right)^2} \right]$$

Eq. 3-5

where, the first term of $I_{baseline}$ is the background (baseline); $\Delta\omega$ is the wavelength different between the selected transition and the central transition; $I_{PS}(\omega)$, $\Delta\omega_{PS}$ and $\Delta\omega_{shift}$ are related to the PS signals; $I_{abs}(\omega)$ is the absorption function of the PS signal occurring in the flame represented in the third term of **Eq. 3-5**. The $\Delta\omega_{abs}$ is used to describe the absorption line width. The second and the last parts of **Eq. 3-5** are the intensities of PS and absorption signals, respectively; the $\Delta\omega_{PS}$ and $\Delta\omega_{abs}$ are FWHM of nonlinear PS and linear absorption signals, which account for the collisional width; the $\Delta\omega_{shift}$ is the wavelength offset (detuning) between the central transition and PS wavelengthscan results. Due to the shift caused by collision (Na atoms collide with any gaseous species in the flame), the $\Delta\omega_{shift}$ is used to account for the collisional shift present in some lineshapes of atomic Na.

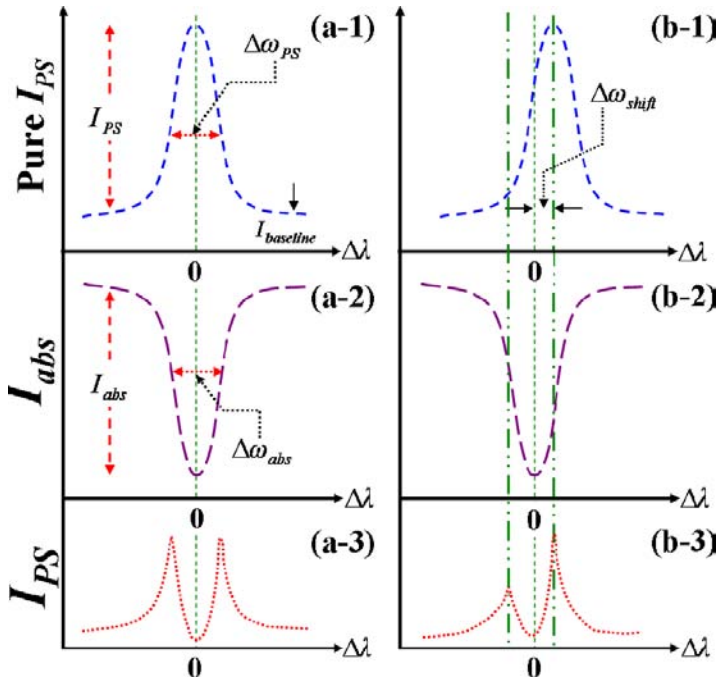

Figure 3-10 Schematic description of PS lineshape (a-3 and b-3), comprising pure PS (a-1 and b-1) and absorption (a-2 and b-2) signals; $I_{baseline}$ is the baseline of pure PS lineshape; I_{PS} and I_{abs} are the maximum intensities of pure PS and absorption signals, respectively; $\Delta\omega_{PS}$ and $\Delta\omega_{abs}$ are FWHM of pure PS and absorption signals. (b-1) $\Delta\omega_{shift}$ is the detuning width occurring in the PS lineshape.

By applying **Eq. 3-3** and **Eq. 3-5**, the number density of atomic Na may be extracted from $I_{PS}(\omega)$ or $I_{abs}(\omega)$ during the fitting of the wavelengthscan results because $I_{PS}(\omega)$ and $I_{abs}(\omega)$ are the consequences of the number density of the target species, atomic Na in this case. A comparison of **Eq. 3-3** and **Eq. 3-5** shows that $I_{PS}(\omega)$ and $I_{abs}(\omega)$ are proportional to $[\mathrm{Na}]^2$ and $e^{-\sigma(\omega)\cdot[\mathrm{Na}]\cdot L_{abs}}$, respectively. The PS technique is therefore nonlinear because the PS intensity is proportional to $[\mathrm{Na}]^2$.

The wavelengthscan of atomic Na using PS allows the direct measurement of the concentration of the target species in the seeded flames. However, this requires the constant concentration of the target species in the flame media throughout the scan. This method is, therefore, only suitable for steady flames, or for those for which the time-scale of variation is small compared with temporal variations in a flame. For solid-fuel particles of ~ 4 mm diameter, the scan-time is much longer than the burn-time, which lasts up to several minutes.

A fast-wavelengthscan laser system, therefore, is able to achieve the lineshape scan within a certain range of wavelengths in microseconds [200-203]. The wavelengthscan of atomic Na in the seeded flames using PS is reliable because the atomic [Na] in the media is relatively constant with the scan-time. Under the conditions, it is possible to obtain reliable results for the concentration of atomic Na from the wavelengthscan data.

A calibration process for the PS of atomic Na was performed by applying the simultaneous absorption measurement to a chosen wavelength, as presented in **Figure 3-1**. It should be noted that the intensities of the chosen atomic or molecular transitions were not proportional to the population densities of the target species due to the significant absorption present, as described in **Figure 3-10**. This indicates that the chosen wavelength (transition) is not always appropriate for the detection of the target species when attempting to use a single wavelength for the PS measurement. The chosen wavelength is only valid within a certain range of population levels of the target species.

3.3.2 Saturation Curves

To obtain quantitative PS measurements, it was necessary to perform PS within the saturation regime [16, 204], as presented in the following equation:

$$I_{PS} = \eta \cdot \left[\frac{I_{pump}}{I_{pump} + I_{Sat}^{PS}} \right]^2$$

Eq. 3-6

where, I_{PS} is the intensity of the measured PS signal, I_{pump} is the pulse fluence of the pump beam, I_{Sat}^{PS} is the saturation pulse fluence of pump beam and η is a scaling factor. As described in **Section 3.3.1**, the D_1 line of high population atomic Na suffered from severe absorption in the central transition. To detect minor species in the flame media, the chosen wavelength might be the transition due to the negligible absorption in I_{PS}. It is therefore

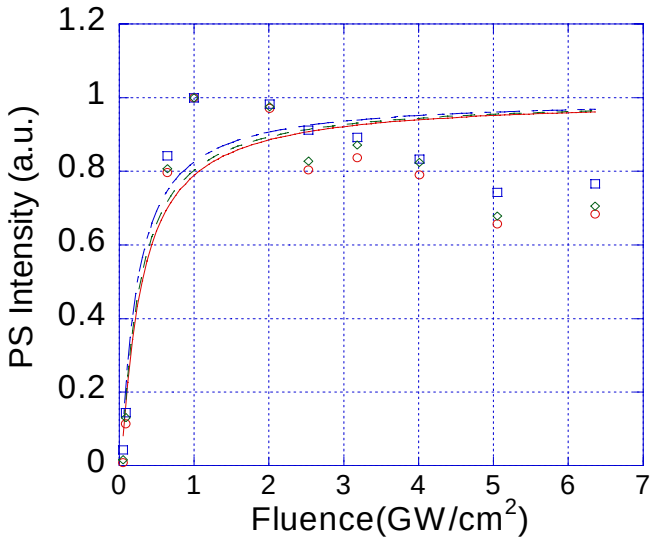

Figure 3-11 Saturation curves of PS measurement in the flames seeded with salt droplets of (a) 0.5 g/L (red dots and line) (b) 1 g/L (green dots and line) (c) 5 g/L (blue dots and line) with various fluences of the pump beam; each datum point is the average of 50 single-shot results. The solid lines are the best-fit (based on **Eq. 3-6**) for determining the saturation fluences. The best-fit is based on the first five data points. The variation between the best-fit and PS intensities at high fluences (the rest of the dot symbols) are estimated to be 20 %.

difficult to carry out quantitative detection of highly populated species using a single wavelength. However, it is reasonable to select a particular wavelength for the detection within a certain range of concentration of atomic Na in the saturation regime.

Figure 3-11 shows the saturation curves for the chosen wavelength, 589.590 nm, under various concentrations of seeded [Na], namely 1.503, 2.254 and 3.757 ppm (or 0.5, 1 and 5 g/L). The concentration of seeded [Na] was calculated using **Eq. 2-31** ~ **Eq. 2-34**. Under the constant seeding rate of salt droplets, the concentration of salt droplets can be represented as the uniform concentration of seeded [Na] distributed within the flames. The saturation fluences of pump beams (I_{Sat}^{PS}) extracted from those saturation curves are described using **Eq. 3-6** as the base and Marquardt's algorithm [199] (**Table 3-3**). The coincidence result of the first two population levels is about 1.5 ± 0.5 GW/cm^2 and with the last is about 1.38 ± 0.37 GW/cm^2, consistent with the seeded [Na]. This indicates the feasibility of the quantitative PS measurement employed on the target species at one specific wavelength. Due to the

Table 3-3 The saturation fluences for the pump beam were obtained from the PS measurement under three concentrations of total seeded Na at the equivalence ratio of 1.3 using **Eq. 3-6**. The total seeded [Na] was determined by using the method introduced in **Section 2.4**.

Concentration (ppm)	1.503	2.254	3.757
Fluence (GW/cm^2)	0.16±0.05	0.15±0.05	0.14±0.04

significant variation in the higher fluences, the best-fit of saturation curves were obtained using the first five points. The variation between the best-fit and PS intensities in higher fluences (the rest of the points in **Figure 3-11**) was estimated to be around 20 %. This demonstrates that excess fluence can lead to a lower PS intensity, especially for a low number density target species.

3.3.3 Lineshapes of Atomic Na in Polarisation Spectroscopy

The population densities of seeded Na directly affect the intensities of PS and absorption at the scanning wavelength, as described in **Eq. 3-5**. The absorption becomes stronger at the higher concentrations of seeded salt droplets leading to the significant absorption at the central wavelength (transition). The experimental PS lineshapes result from the superposition of nonlinear pure PS and linear absorption signals. Hence, two peaks can be observed in the experimental PS profiles [**Figure 3-12** (b), (c), (e) and (f)] when the effects of absorption are as significant as the single peaked lineshape, as occurs in **Figure 3-12** (a) and (d), indicating that the influence of linear absorption on the PS signal is weak. It is clear that the absorption becomes significant in the highly populated media.

In order to simulate the wavelengthscan results using **Eq. 3-5**, the raw PS intensities in **Figure 3-13** ~ **Figure 3-19** were normalised by the maximum intensity in the individual wavelengthscan result and multiplied by a factor of 150 (can be a radom number). **Figure**

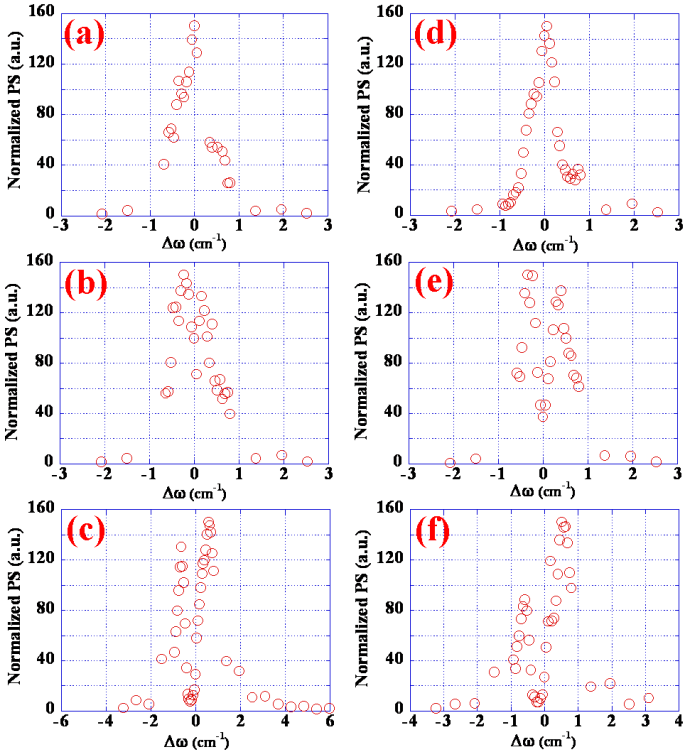

Figure 3-12 PS lineshapes with the pump fluence 6.36 GW/cm^2 while Φ = 1.3 with [Na] = (a) 1.503 (b) 2.254 (c) 3.757 ppm; Φ = 1.4 with [Na] = (d) 1.628 (e) 2.443 (f) 4.071 ppm. The concentrations of seeded [Na] were calculated using **Eq. 2-31** ~ **Eq. 2-34**.

3-13 presents the calculation results of **Figure 3-12** based on **Eq. 3-5** showing the good agreement with the lineshapes of atomic Na. A particular phenomenon was observed during this process: the right-shift [**Figure 3-12** (b) and (e)] and left-shift [**Figure 3-12** (c) and (f)] of the central absorptions occurred in a certain range of concentrations. The shift was obtained from the calculation of lineshape results by extracting the $\Delta\omega_{shift}$ from **Eq. 3-5**. The right-shift occurred in concentrations of about 2 ppm and the left-shift was observed in concentrations of about 4 ppm (the concentrations in detail are listed in **Table 3-1** and **Figure 3-12**).

The explanation for the right- and left-shift is not yet clear. It might be caused by the collision altering the PS signals. However, the shift caused by major perturbers in D_1 and D_2 lines of atomic Na in the flame media, namely Ar, H_2, H_2O, N_2 and CO/CO_2 has been determined as negative (right-shift) [205]. Hence, this requires further investigation both theoretically and experimentally to verify the shift results of atomic Na in the D_1 line.

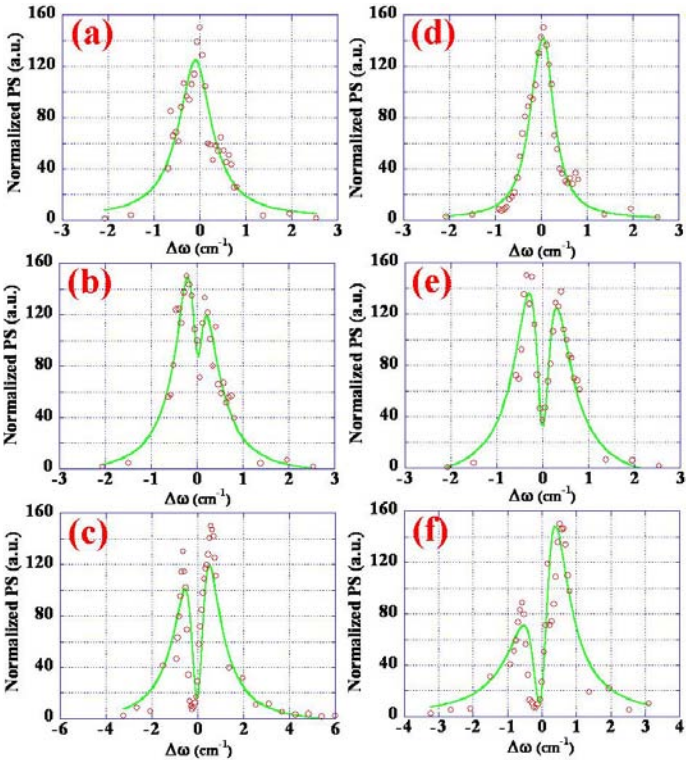

Figure 3-13 Best-fit of PS lineshapes based on **Eq. 3-5** indicate the absorption overpowers the PS signals resulting in two-peak shapes. Φ = 1.3 with [Na] = (a) 1.503 (b) 2.254 (c) 3.757 ppm; Φ = 1.4 with [Na] = (d) 1.628 (e) 2.443 (f) 4.071 ppm with the pump fluence 6.36 GW/cm^2.

The absorption see ms more significant with the higher concentrations of seeded Na indicating that with the FWHM of absorption, $\Delta\omega_{abs}$ in **Eq. 3-5**, becomes wider. This will be a problem when $\Delta\omega_{abs}$ dominates $\Delta\omega_{PS}$ leading to a wider range of wavelengths for the vanishing I_{PS}. Hence, the chosen transition may not be always applicable for the detection of [Na] in the PS measurement.

To measure concentrations of the target species using PS requires careful planning of the experimental arrangement. Generally, there are two scenarios able to achieve quantitative measurement using PS. These are the development of conventional calibration curves and extraction from the simulation of wavelengthscan results using **Eq. 3-5**.

A conventional calibration curve requires a particular wavelength at which the intensities are measured, corresponding to the concentrations in the sample media. However, the chosen wavelength is not always applicable for highly populated sample media. The wavelength may

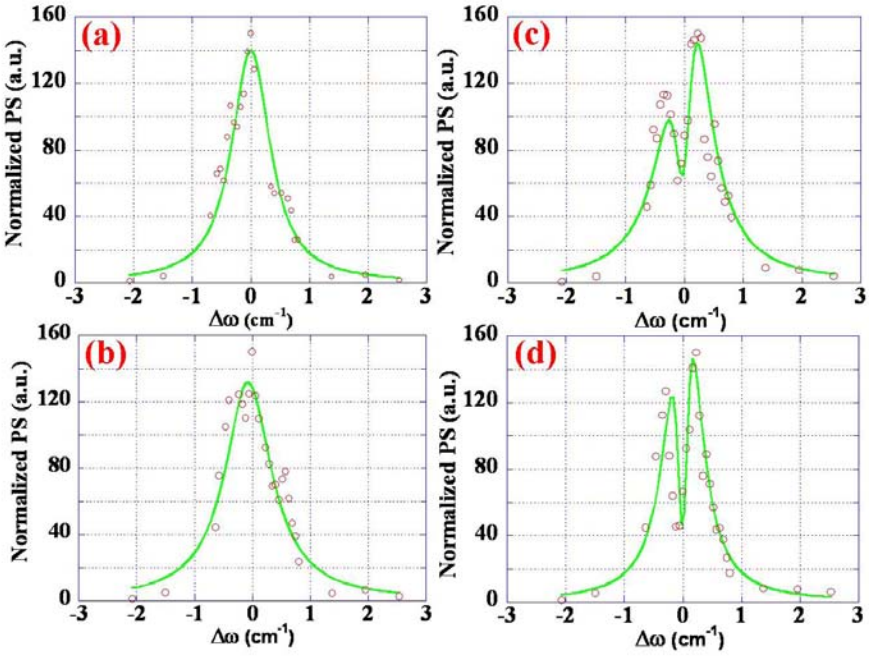

Figure 3-14 Lineshapes of I_{PS} wavelengthscan into the seeded flame for concentration of Na of 1.503 ppm and Φ = 1.3 were performed with fluences of (a) 6.36, (b) 3.18, (c) 2.01, (d) 1.00 GW/cm^2.

be achievable if a database containing the PS intensities at a certain range of wavelengthscans corresponds to the concentrations of target species under various fluences of pump beam. Such a database requires much more work in the future. To avoid the difficulty of calibration curves, the concentration of target species in the sample media might be able to be extracted from the wavelengthscan results simulated by **Eq. 3-5**. Some groups have used a diode-laser-based device to achieve a fast wavelengthscan in the detection of OH radicals [201, 203].

As measured in **Figure 3-13**, both quantitative measurements of atomic Na may not be applicable. Although it is possible to extract concentrations from the wavelengthscan data using **Eq. 3-5** without conducting a calibration process, the I_{PS} is not proportional to the number density of atomic Na. More effort to achieve quantitative measurements using PS in seeded flames is required in the future.

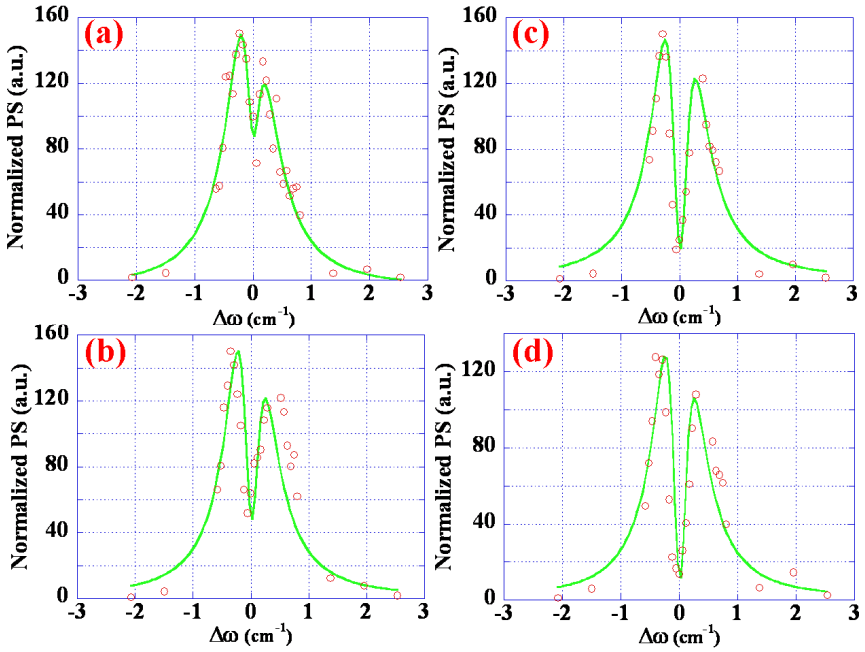

Figure 3-15 Lineshapes of I_{PS} wavelengthscan into the seeded flame for concentration of Na of 2.254 ppm and Φ = 1.3 were performed with the fluences of (a) 6.36, (b) 3.18, (c) 2.01, (d) 1.00 GW/cm^2.

3.3.4 Fluence Dependence of the Pump Beam

The energy of the pump beam was controlled by various neutral density filters (ND filters) to provide various fluences at a point with an 18.72×10^{-3} cm diameter (the area is 2.75×10^{-4} cm^2). Due to the nonlinear PS measurement [16, 24], the saturated PS signal was critical for the quantitative analysis. The saturated PS signal indicated that the intensity of PS did not vary with the pump beam fluences under the saturated regime. Moreover, the critical fluence varied with the number density of the target species, as shown in **Table 3-3**. Therefore, the results of fluence dependence under various populated levels of atomic Na could be investigated.

The wavelengthscan lineshapes of PS intensities for various concentrations of seeded Na droplets were investigated for Φ = 1.3 as presented in **Figure 3-14** to **Figure 3-16** and for Φ = 1.4 in **Figure 3-17** to **Figure 3-19**. The equivalence ratio is dominated by the flowrates of air and methane. Based on the same flowrate of methane, a richer condition was achieved by reducing the flowrate of air. The higher concentration of seeded Na, therefore, occurred in the

richer condition. Although a higher concentration of seeded Na was achieved, it was not the only factor that induced the stronger intensity of atomic Na. The intensity of atomic Na was expected to be stronger in the flame media with richer conditions under the same seeded concentration of Na. Therefore, the I_{PS} of atomic Na with a higher number density of H atoms was induced by hydrogen reduction [15, 38]. The H atoms in this study were supplied by the decomposition of $CH_{4(g)}$ instead of from $H_{2(g)}$. However, H atoms play the same role in hydrogen reduction, as illustrated below:

$$NaOH_{(g)} + H_{(g)} \leftrightarrow Na_{(g)} + H_2O_{(g)}$$
$$Na_2O_{(g)} + 2H_{(g)} \leftrightarrow 2Na_{(g)} + H_2O_{(g)}$$

Eq. 3-7

The tests recorded in **Figure 3-14** to **Figure 3-16** were conducted at the equivalence ratio of 1.3, leading to concentrations of 1.503, 2.254 and 3.757 ppm, and the fluences of 6.36, 3.18, 2.01 and 1.00 GW/cm^2 were performed. **Eq. 3-5** was used to model the $I_{PS}(\omega)$ of atomic Na in the seeded flames. **Figure 3-14** (a) is modelled with the saturated PS (n = 1, in **Eq. 3-5**). With

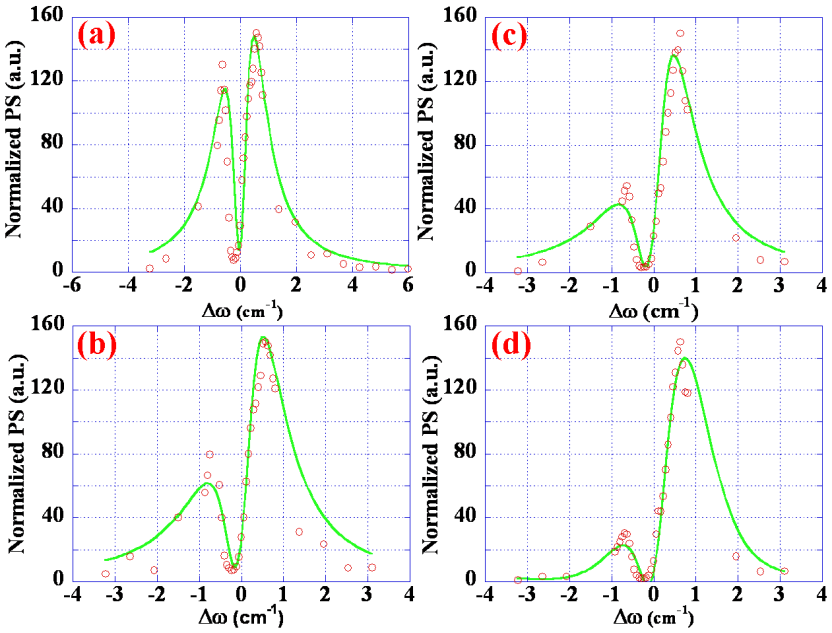

Figure 3-16 Lineshapes of I_{PS} wavelengthscan into the seeded flame for concentration of Na of 3.757 ppm and Φ = 1.3 were performed with the fluences of (a) 6.36, (b) 3.18, (c) 2.01, (d) 1.00 GW/cm^2.

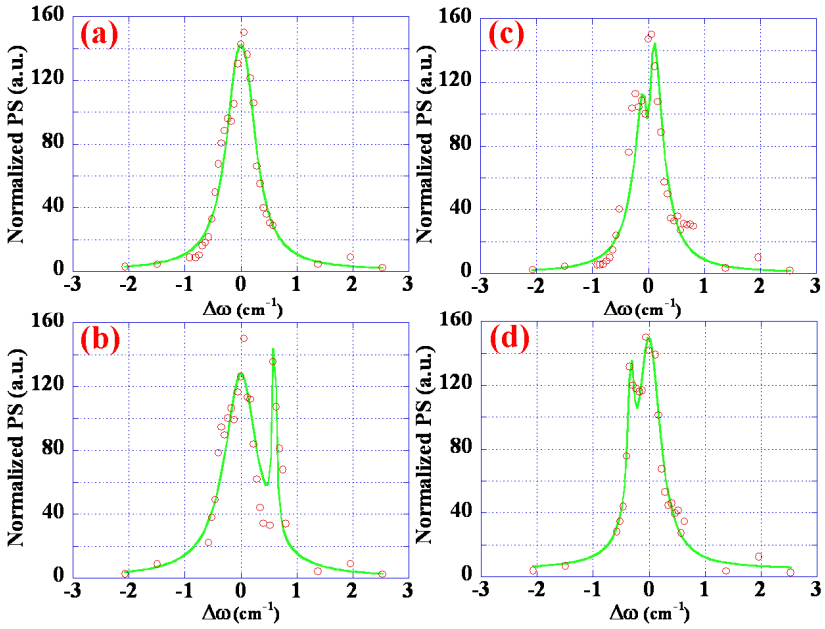

Figure 3-17 Lineshapes of I_{PS} wavelengthscan into the seeded flame for concentration of Na of 1.628 ppm and Φ = 1.4 were performed with the fluences of (a) 6.36, (b) 3.18, (c) 2.01, (d) 1.00 GW/cm^2.

the decreasing pump beam fluences, the absorption (in the third part of **Eq. 3-5**) dominated the pure PS signal (the second part of **Eq. 3-5**) revealing a lineshape similar to that represented in **Figure 3-13**. It was notable that the left-shift occurred in the PS wavelengthscan data as the pump beam fluences decreased, indicating the non-zero $\Delta\omega_{shift}$ in **Eq. 3-5** had been reached.

Figure 3-15 demonstrates the PS lineshapes with scanning wavelength and various pump beam fluences at the entrained Na concentration of 2.254 ppm. Unlike the profiles shown in **Figure 3-14**, the absorption was significant, as illustrated in **Figure 3-15**(a). The absorption became increasingly significant as the pump beam fluences decreased, as indicated in **Figure 3-15** (b) ~ (d). The solid green line represents the modelling result using **Eq. 3-5**, showing the good agreement with the experimental results. In addition, the peculiar phenomenon of the right-shift occurred. The similar tendency was also recorded in **Figure 3-14** with the left-shift.

The PS profiles under the seeded [Na] of 3.757 ppm with various fluences were conducted, as shown in **Figure 3-16**. The absorption possesses excessively strong, leading to the 'deep-canyon' lineshape in the central wavelength. Two particular phenomena were observed

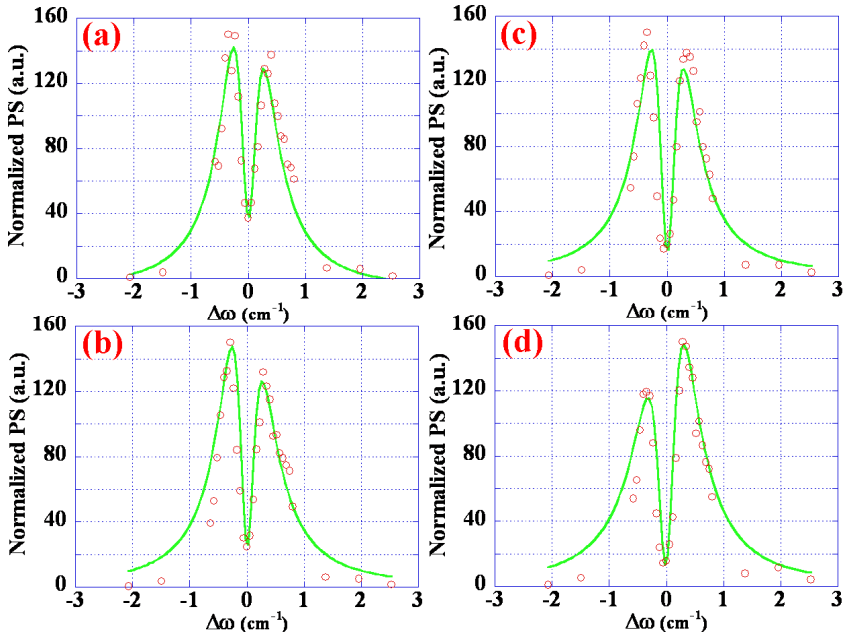

Figure 3-18 Lineshapes of I_{PS} wavelengthscan into the seeded flame for concentration of Na of 2.443 ppm and Φ = 1.4 were performed with the fluences of (a) 6.36, (b) 3.18, (c) 2.01, (d) 1.00 GW/cm^2.

in the profiles, as presented in **Figure 3-16**. One is the similar trend observed in **Figure 3-14** and **Figure 3-15**, which is the occurrence of the left-shift. The other is the broadened FWHM of pure PS signal results from the self-collisional broadening [24], compared to the results obtained under lower concentrations of seeded Na.

In the case of Φ = 1.4, due to the stability of the flame, an anomaly occurred in some results for the PS lineshapes. However, the major tendency was consistent with that in the case of Φ = 1.3. The lineshapes, as shown in **Figure 3-17** and **Figure 3-19**, except for the anomaly in **Figure 3-17** (b), demonstrate the consistent behaviours, which are the left-shift and absorption effect, observed in **Figure 3-14** and **Figure 3-16**. The right-shift that occurred in **Figure 3-18** was consistently observed in **Figure 3-15**, except for the anomaly in **Figure 3-18** (d). Moreover, the broadening profiles were also observed in **Figure 3-19**, as highlighted in **Figure 3-16**. As the lineshapes of atomic Na using PS demonstrate, the profiles are highly dependent on the pump beam fluences, as reported by [17, 113].

The mechanism of right- or left-shift is not yet clear. However, the shift behaviour was consistently observed at both equivalence ratios, 1.3 and 1.4. However, it seems that the shift

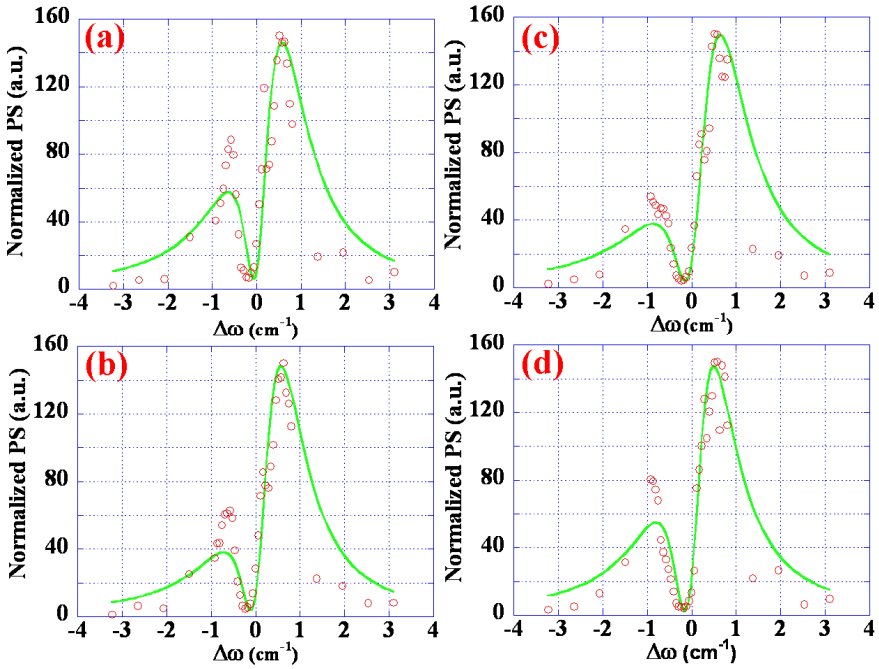

Figure 3-19 Lineshapes of I_{PS} wavelengthscan into the seeded flame for concentration of Na of 4.071 ppm and Φ = 1.4 were performed with the fluences of (a) 6.36, (b) 3.18, (c) 2.01, (d) 1.00 GW/cm^2.

is dominated by the seeded population of atomic Na as the left-shift occurs at population levels of approximately 1.5 and 4 ppm. The right-shift occurs at population levels of approximately 2 ppm. The phenomenon requires further investigation. There is the implication that the collision among atomic Na and gaseous molecules is responsible for the shift.

3.3.5 Repeatability of the Lineshape Fitting

The lineshapes were determined by optimizing six terms introduced in **Eq. 3-5** namely $I_{baseline}$, $I_{PS}(\omega)$, $\Delta\omega_{shift}$, $\Delta\omega_{PS}$, $I_{abs}(\omega)$ and $\Delta\omega_{abs}$. The fitting process initiated with the six values given by KaleidaGraph 4.1, which provided primary guessing. The $I_{baseline}$ was modified based on the data points if the value of was not appropriate. For example, the initial value of $I_{baseline}$ given by KaleidaGraph 4.1 is 1, which may be 0.01 (estimated from the smallest value of data points). The fitting value of $I_{baseline}$ is changed to obtain new values of other parameters. Generally, the values of the five parameters (except for $I_{baseline}$) are determined. In some cases,

the values of the five parameters required minor modification, which is less than 5% of the fitting values. However, some fitting lineshapes (shown in **Figure 3-16** and **Figure 3-19**) reveal significant error between the experimental data and the fitting lineshapes. This might be due to pump beam scattering or fluctuation caused by the higher number density of atomic Na in the measurement. Moreover, a particular anomaly observed in Figure 3-17 may be caused by unexpected disturbance during the experiment because other lineshapes are consistent with the concentration variation.

The same procedure was performed in all data sets to verify the repeatability of the lineshape fitting using **Eq. 3-5** although the six values (as introduced in **Eq. 3-5**) can be determined individually. However, parameters are related to each other. This indicates that each parameter has a particular value, which fits the experimental data. Although the value of each parameter is allowed being justified approximately 5%, the modification is quite sensitive, even 1% variation in one parameter. This indicates that small variation to one parameter causes significant difference in the lineshape fitting. It is worth nothing that to achieve very good line shape fitting, a large data set is required.

3.3.6 Beam Steering Effect

Figure 3-20 presents a two-dimensional representation of the position of the B_{probe} on the ICCD camera to illustrate the amount of deflection that the probe beam experienced when travelling through the laminar premixed flames with seeded Na. The temperature gradient within the flame produces a refractive index gradient. As a result, both probe and pump beams experience the beam steering effect because the PS signal is generated in the interaction volume of the B_{pump} and the B_{probe}. The beam steering effect may cause significant uncertainty in current PS measurements when the effect is larger than the interaction volume. It must, therefore, be taken into account when analysing the experimental results.

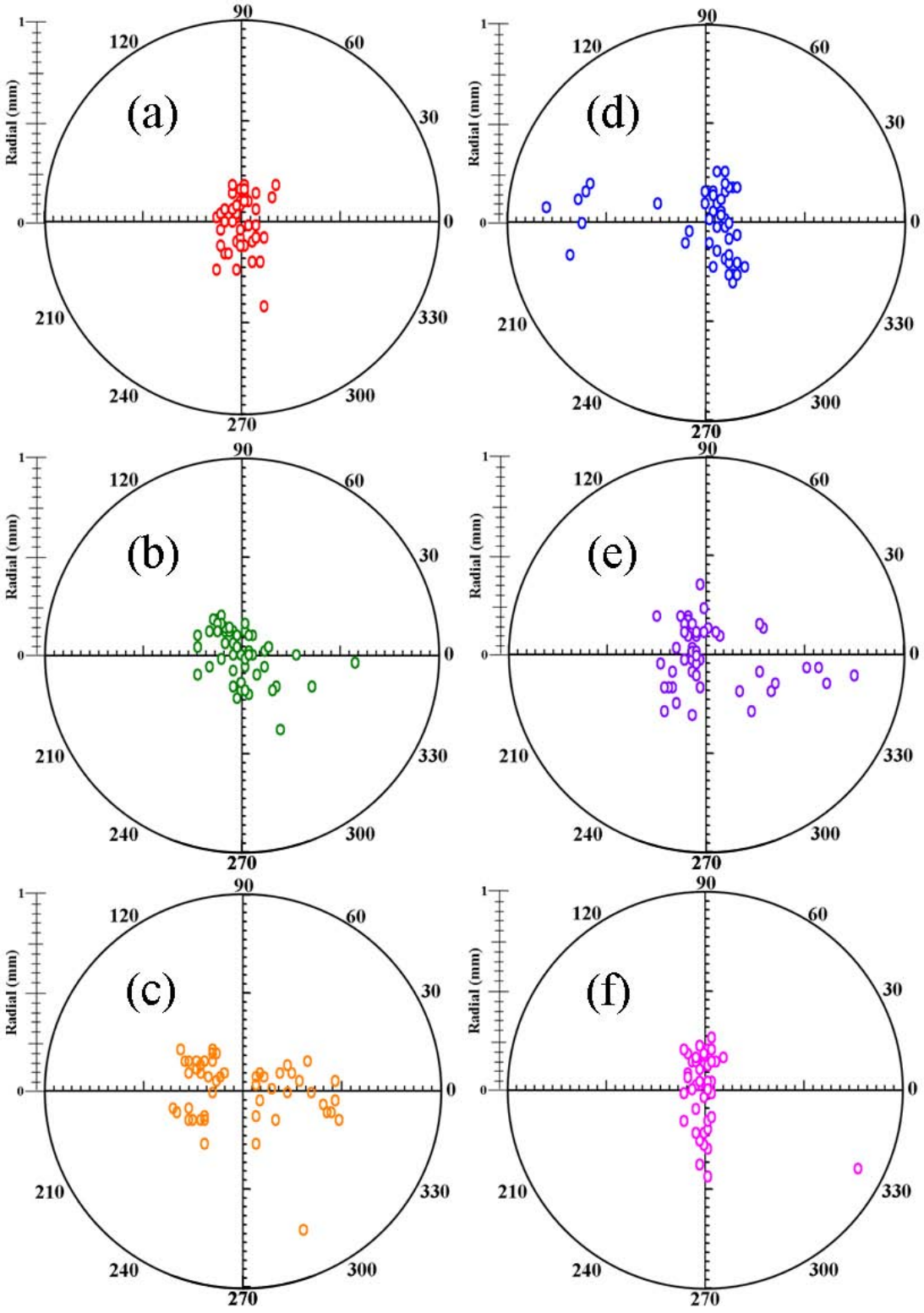

Figure 3-20 Beam steering effects are investigated under Φ = 1.3 with (a) 0.5 g/L, (b) 1 g/L, (c) 5 g/L and under Φ = 1.4 with (d) 0.5 g/L, (e) 1 g/L, (f) 5 g/L. The scale of radius is 1 mm.

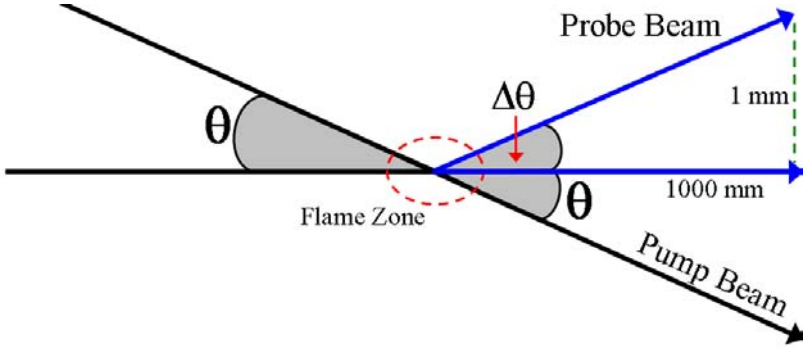

Figure 3-21 Illustration of the systematic error caused by the beam steering effect; the displacement of images caused by beam steering has been identified to be around 1 mm from **Figure 3-20**. The distance between the intersection location and the ICCD camera is about 1000 mm. Hence, the $\Delta\theta$ can be calculated.

Given that I_{PS} is proportional to $\cot^2(\theta)$ [91, 100], the random error caused by the beam steering effect in the present experimental arrangement can be estimated. As shown in the illustration of beam steering effect (**Figure 3-21**), the $\Delta\theta$ (the angle variation caused by the beam steering effect) is obtained by:

$$\Delta\theta = \tan^{-1}\left(\frac{x_{steering}}{D_{PS}}\right)$$

Eq. 3-8

where, $x_{steering}$ and D_{PS} are the beam steering measured in the ICCD camera and the distance between the sample position and the ICCD camera, respectively. The beam steering effect was found to be approximately 1 mm ($x_{steering}$) at 1000 mm distance (D_{PS}) from the intersection location to the ICCD camera. Hence, the variation of I_{PS} caused by the beam steering effect is proportional to:

$$I_{PS} \propto \cot^2(\theta + \Delta\theta)$$

Eq. 3-9

Given that the intersection angle (θ) is 5.6°, the systematic error (E_{BS}) caused by the beam steering can be obtained:

$$E_{BS} = \frac{\cot^2(\theta) - \cot^2(\theta + \Delta\theta)}{\cot^2(\theta)} \times 100\%$$

Eq. 3-10

Here, the E_{BS} was calculated to be 2.03 % in the present PS optical arrangement. It presents the negligible random error in the PS measurement, compared to the other systematic errors.

3.3.7 Atomic Na Detection in Lean Combustion Conditions

As mentioned when discussing the limitations of the premix laminar burner, the diffusion flame burner, as shown earlier in **Figure 3-4**, was employed to achieve the stoichiometric on lean conditions of laminar methane flames [11-15]. A lean equivalence ratio of 0.61 was achieved by the air and fuel flowrates which were respectively 23.5 and 1.51 L/min. The air flowrate included the seeding air flowrate of 5 L/min. Given that the concentration of atomic Na in the lean flame is much lower than that in the rich flame [38], the saturation energy, which was expected to be lower than that presented in **Figure 3-11**, was 0.014 ± 0.006 GW/cm^2, as shown in **Figure 3-22**, although the concentration of seeded Na in the 0.61 stoichiometric flame was 3.740 ppm similar to that in the 1.3 stoichiometry flame.

Since Na compounds form in the lean flames [38], the absorption effect described in **Eq. 3-5** is considered to be weaker, compared to that in **Figure 3-16**. The wavelengthscan data, as presented in **Figure 3-23**, therefore, offer the evidence by which to verify the model, which is

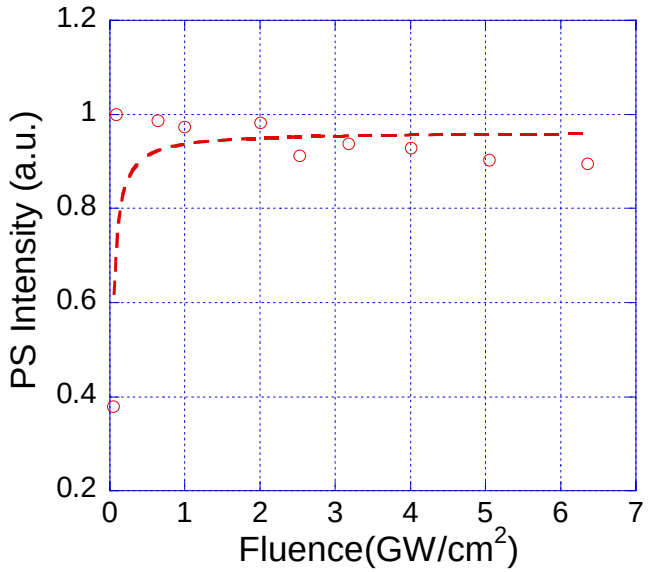

Figure 3-22 Saturation curves of PS signals at the Φ = 0.61; the saturation fluence was found to be 0.0134 ± 0.006 GW/cm^2 extracted from Eq. 3-6.

described using **Eq. 3-5**, of atomic Na behaviour in the PS measurement.

Unlike the strong absorption observed in **Figure 3-16**, significant absorption can be observed while the weaker I_{PS} is present at the lower fluence of the B_{pump}, as shown in **Figure 3-23** (g) ~ (j). The weaker absorption indicates less atomic Na is present because atomic Na forms other Na compounds in the lean flames, such as Na_2O and NaOH [38]. The lineshapes of atomic Na obtained in the wavelengthscan data, as shown in **Figure 3-23**, are modelled using **Eq. 3-5**, with a Lorentzian (saturation regime), except for the **Figure 3-23** (j). Although **Figure 3-23** (j-2) shows a good agreement with the model, **Figure 3-23** (j-1) demonstrates an excellent match indicating an unsaturated PS profile was obtained with the fluence.

3.3.8 Simultaneous Absorption Measurement

In the conventional measurement to determine the absolute concentrations of the target species in the flame media, in the case of quantitative atomic Na [11, 13], laser absorption technique has been widely employed [206, 207]. To provide a reference concentration for quantitative PS, the absorption measurement has been conducted simultaneously in seeded flames for the measurement of atomic Na using PS. A PS signal is sensitive to pump beam fluence, the concentration of target species and the chosen transition owing to the nonlinear PS technique. The calibration curve is not always applicable at single wavelength for all ranges of concentrations and conditions of experiments. Hence, the simultaneous absorption measurement can provide the instantaneous concentrations of target species during the PS measurement. The simultaneous absorption was performed in rich premixed laminar flames using the burner (as shown in **Figure 3-3** previously).

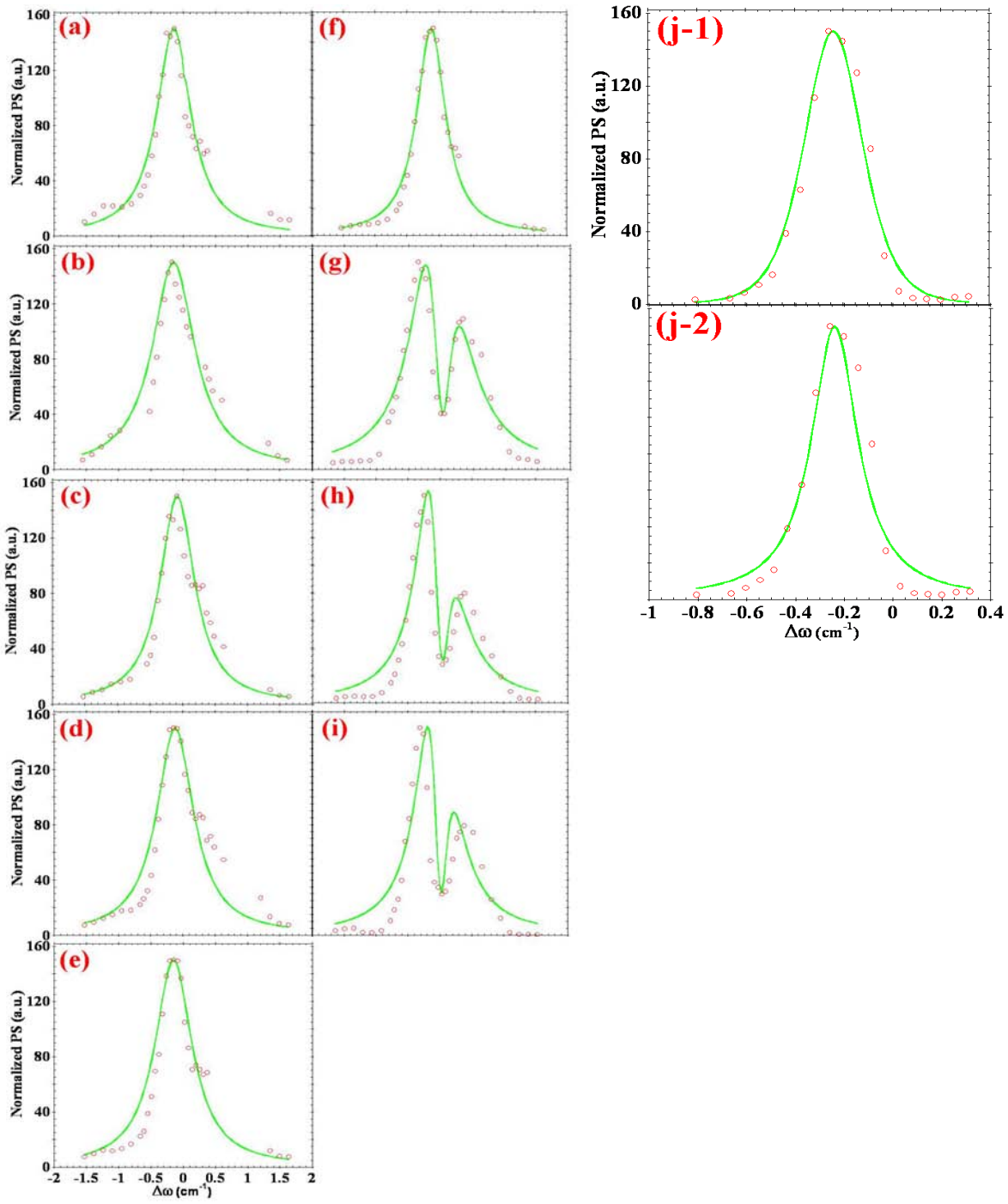

Figure 3-23 Wavelength scanning profiles of atomic Na in the flame with Φ = 0.61; the fluences for (a) ~ (j) are 6.36, 5.05, 4.01, 3.18, 2.53, 2.01, 1.00, 0.64, 0.09 and 0.05 GW/cm^2, respectively. (a) ~ (i) demonstrate the PS in saturation regime and (j) reveals (j-1) the unsaturation and (j-2) the saturation regime, respectively. (j-1) represents the excellent agreement with data points indicating the profile obeys the Lorentzian cubic (n = 3).

3.3.9 Quantitative Measurement

3.3.9.1 Laser Absorption Measurement

To apply laser absorption measurements to the laminar flames with seeded Na, the Beer-Lambert law was employed, as described below:

$$\ln(\frac{I_{in}}{I_{out}}) = \alpha \cdot x$$

Eq. 3-11

where, the I_{in} and the I_{out} are the input and output laser beam intensities measured in the ICCD camera at the chosen wavelength; x is the absorption length in the flame (m); α is the absorption coefficient of atomic Na. Unlike conventional laser absorption measurement, the input laser beam (I_{in}) is acquired by averaging the intensities of 500 pulses of the B_{abs}, immediately before the absorption measurement commences. The output intensity (I_{out}) is obtained by averaging the intensities of 50 shots of the B_{abs} through the flame media. In order to eliminate the fluctuation of laser beam energy, both the I_{in} and the I_{out} are normalized by the instantaneous B_{ref} which is directly introduced into the ICCD camera. The absorption path length, x, was measured to be 0.065 m in the flame media so that the absorption coefficient α was obtained.

The absorption coefficient is a function of the number density (n_s) of atomic Na (in this study) and absorption cross-section (σ_a) of atomic Na, given by:

$$\alpha = n_s \cdot \sigma_a$$

Eq. 3-12

The n_s of atomic Na can be obtained when the absorption cross-section is determined. The method has been introduced in detail [207]. To determine σ_a, the Einstein coefficients for spontaneous emission, A_{21}, stimulated emission, B_{21}, and absorption, B_{12}, at a specific

transition, which is 589.592 nm for the D_1 line of atomic Na, can be given by [207]:

$$B_{21} = (\frac{\pi^2 \cdot c^3}{\hbar \cdot \omega^3}) \cdot A_{21}$$

$$B_{21} = \frac{g_1}{g_2} \cdot B_{12}$$

Eq. 3-13

where, c is the light speed ($m \cdot s^{-1}$), ω is the transition of atomic Na (s^{-1}) and $\hbar$ is the Planck's constant divided by 2π ($J \cdot s$). For the D_1 line of atomic Na, the A_{21} is 6.14×10^7 [20]. In addition, the degeneracy state (g_i) of atomic Na in the D_1 line is $g_1 = g_2 = 2$ [20]. Thus, B_{12} of atomic Na was determined to be 4.75×10^{21} $m^3 \cdot J^{-1} \cdot s^{-2}$. Moreover, the relationship between B_{12} and σ_a is governed by:

$$\sigma_a = \frac{\hbar \cdot \omega \cdot B_{12} \cdot I(\omega)}{c}$$

Eq. 3-14

where, $I(\omega)$ is a normalised function that is used to describe the variation of the system and is governed by:

$$\int_{-\infty}^{+\infty} I(\omega) \cdot d\omega = 1$$

Eq. 3-15

$I(\omega)$ was determined by measuring the variation of the system with ω for a narrow band around the D_1 line of atomic Na (589.592 nm) to obtain a function of the angular frequency, $f(\omega)$. This function was numerically integrated to obtain the constant, κ, which is given by:

$$\int_{-\infty}^{+\infty} f(\omega) \cdot d\omega = \kappa$$

Eq. 3-16

By dividing $f(\omega)$ by the constant, κ in **Eq. 3-16**, which compared to **Eq. 3-15**, $I(\omega)$ is determined. Therefore, the absorption cross-section of the atomic Na in the seeded flames was experimentally determined to be 1.716×10^{-16} m^2. The number densities of atomic Na were

Table 3-4 Number densities of atomic Na were obtained using laser absorption measurement, representing the concentrations of seeded Na of 0.5, 1 and 5 g/L

Φ	[Na] in solution (g/L)	Seeded [Na] into flame by Calculation		[Na] Experimental Measurement		Reliability
		Total [Na] seeded (atoms/m^3, x10^{18})	Atomic [Na]($[Na]_{cal}^{atomic}$) Total [Na] x 0.02 (ε) (atoms/m^3, x10^{18})	Atomic [Na]($[Na]_{exp}^{atomic}$) (atoms/m^3, x10^{18})	Standard Deviation(%)	$\frac{([Na]_{exp}^{atomic})-([Na]_{cal}^{atomic})}{[Na]_{cal}^{atomic}}$ (%)
1.3	0.5	7.35	0.147	0.127	22.1	-13.6
	1	11.0	0.220	0.258	20.3	17.3
	5	18.4	0.368	0.428	19.1	16.3
1.4	0.5	7.96	0.159	0.161	20.1	1.3
	1	12.0	0.240	0.241	23.2	0.4
	5	19.9	0.398	0.466	20.5	17.1

experimentally obtained and are described in **Table 3-4** (the experimental measurement column).

The standard deviation across 50 shots was approximately 20%. This may be caused by the error accumulation owing to the systematic error of the flowmeters or the instability of the air and methane supply system. More critically, condensation of the seeded salt droplets occurs constantly during the seeding, disturbing the premixing process. Instability of seeded flames is the major issue of using the designated burner (**Figure 3-4**).

To verify the concentrations of atomic [Na], the experimental results were compared with the calculated concentrations derived from the **Eq. 2-31** divided by **Eq. 2-32**. The calculated number density is the total amount of seeded [Na]. Due to the 1500 K flame temperature, it is assumed that 2% of total seeded Na atoms are presented in the atomic form. The deviation of number density of atomic Na between the experimental and predicted results was investigated, as shown in **Table 3-4**. The calculated total seeded Na, which was based on the present seeding flowrate, was multiplied by the factor (ε = 0.02) as the predicted value of atomic Na. Although the derived results are not perfectly aligned with the experimental outcome (up to 17% variation between the experimental and predicted values), it is still sufficient to verify the number density of atomic Na obtained from absorption spectroscopy measurement.

3.3.10 Wavelengthscan in the D_2 Line of Atomic Sodium

There was concern that the strong absorption in the D_2 band of atomic Na (588.995 nm) [11] would make PS measurement difficult. As shown in **Figure 3-24**, the wavelengthscan of PS signals performed under conditions of the 6.36 GW/cm^2 pump beam fluence, 0.5 g/L salt solution level and Φ = 1.3 was modelled by applying **Eq. 3-5** with n = 3. Their performance indicated that the PS signals were in the unsaturated regime. It should be noted that the seeded population level of atomic Na was low and the high fluence of pump beam was employed. However, the measurement could not be performed under the saturation regime established for the current study. For quantitative measurement using PS, therefore, the D_2 line of atomic Na is not appropriate. Significant absorption occurs in the D_2 line of atomic Na so the D_1 line was chosen to detect atomic Na released from burning coal particles using quantitative PLIF [11].

Further investigation using PS in the D_2 line involved the use of a higher concentration of seeded salt solution (1 g/L). **Figure 3-25** shows that the wavelengthscan results reveal significant absorption. The consistency of the profiles is noticeable and implies that the absorption might dominate the PS measurement in the D_2 lines.

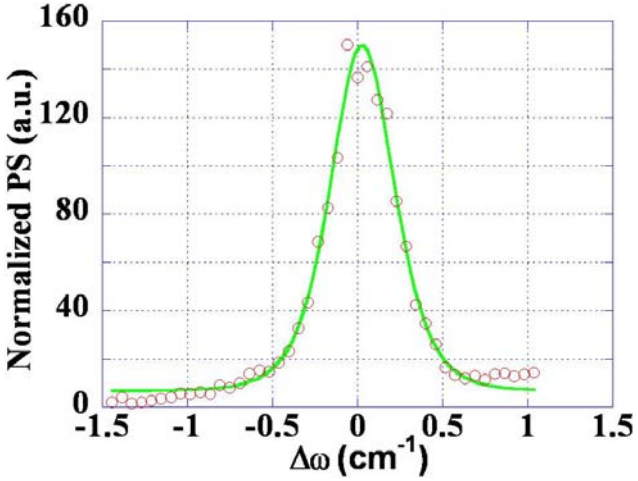

Figure 3-24 Wavelengthscan of I_{PS} with a pump beam fluence of 6.36 GW/cm^2 and with a concentration of salt droplets of 0.5 g/L at Φ = 1.3 is modelled by **Eq. 3-5** with n = 3 presenting the unsaturated I_{PS}.

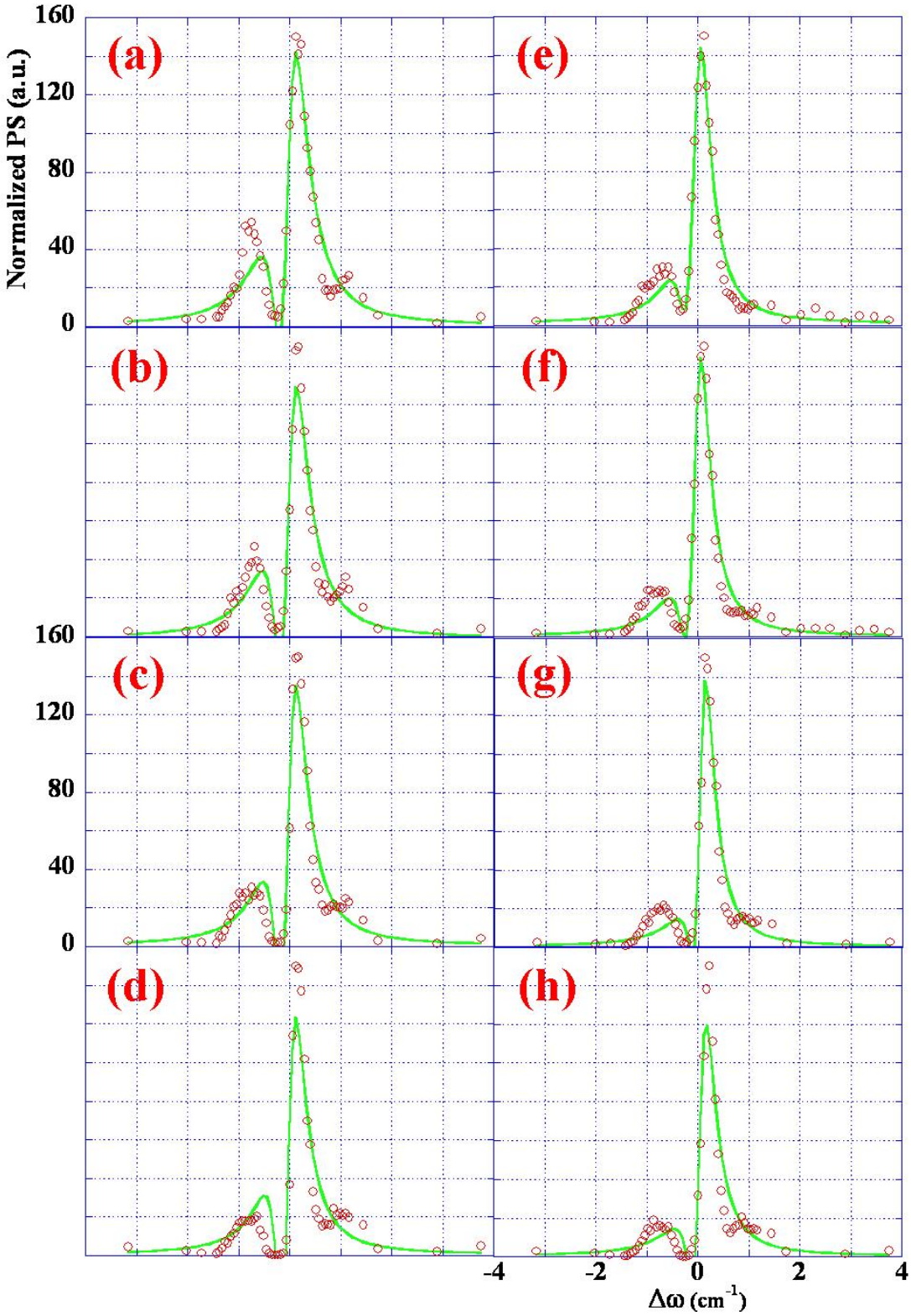

Figure 3-25 Lineshapes of I_{PS} with four fluences of 6.36, 3.18, 2.01 and 1.00 GW/cm^2 and with a concentration of salt droplets of 1 g/L at Φ = 1.3 (a ~ d) and at Φ = 1.4 (e ~ h) are modelled by **Eq. 3-5** with n = 3 presenting the unsaturated I_{PS}.

3.3.11 Pure Signal of Polarisation Spectroscopy

Each wavelengthscan result of the PS signals of atomic Na in the seeded flames was normalized to the individual maximum intensity for the lineshape modelling using **Eq. 3-5**. The result was not sufficient to describe the relationship between I_{PS} and the experimental parameters, however. The pure PS intensity (I_{PS_pure}) was therefore extracted from the mathematical simulation results to demonstrate the behaviour of atomic Na measured using PS.

3.3.11.1 Fluence Dependence

As shown in **Section 3.3.3**, it is clear that the absorption becomes more significant when the pump beam fluence is weaker. This indicates that the I_{PS} increases with the fluence of the B_{pump} since the absorption is constant in the medium with the same populated species. The behaviour of I_{PS_pure} lineshape was extracted from the results that had been calculated using **Eq. 3-5**. The I_{PS_pure} lineshapes extracted from three concentrations of atomic Na, namely 0.127,0.258 and 0.241 x10^{18} atoms/m^3 (listed in **Table 3-4** previously) compared to the corresponding I_{PS} lineshapes have been presented in **Figure 3-26** ~ **Figure 3-28**. **Figure 3-26** demonstrates the PS lineshape under the 0.127×10^{18} atoms/m^3 concentration of atomic Na varying with four pump beam fluences of 6.36, 3.18, 2.01 and 1.00 GW/cm^2. **Figure 3-27** and **Figure 3-28** reveal the PS lineshape variation for the concentrations of atomic Na, 0.258 and 0.241 ×10^{18} atoms/m^3, respectively, with four fluences of the pump beam. Consistently the I_{PS_pure} increases are associated with increasing pump beam fluences.

It should be noted that the lineshapes of I_{PS_pure} presented in **Figure 3-27** are not as intense as those shown in **Figure 3-26** and **Figure 3-28**. The reason for this is not yet clear. However, similar behaviour, the intensity fluctuation, has been observed in saturation curves (**Figure**

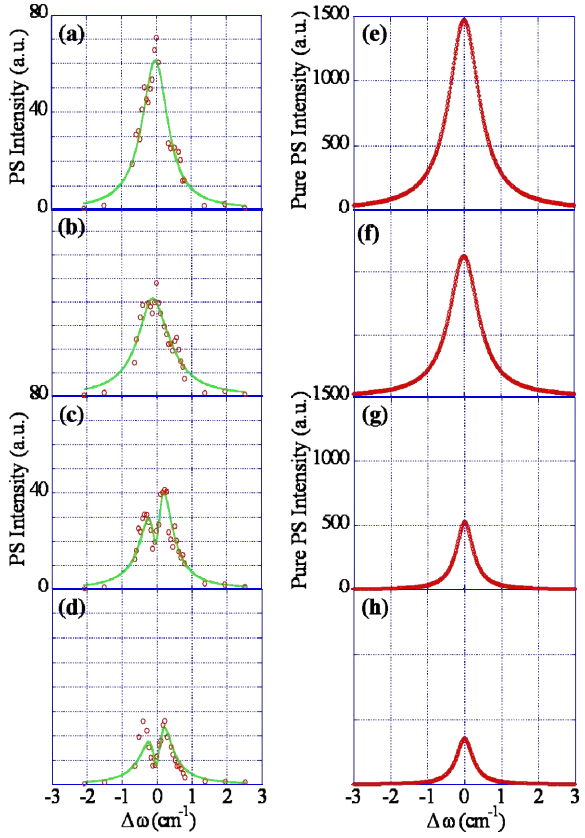

Figure 3-26 (a ~ d) Wavelengthscan is conducted to investigate the lineshape of I_{PS} under the atomic [Na] of 0.127×10^{18} atoms/m^3. The maximum I_{PS} in the lineshape decreases with the descending pump beam fluences of 6.36, 3.18, 2.01 and 1.00 GW/cm^2. (e ~h) The pure I_{PS} decreases with the descending pump beam fluences.

3-11), and in the higher atomic [Na], 0.428 and 0.466 $\times10^{18}$ atoms/m^3, as indicated in **Figure 3-29**.

A possible mechanism leading to the intensity fluctuation may be the diffusion effect under the saturation regime. The diffusion effect is caused by the pump beam heating Na atoms which are mobile enough to drift out of the interaction volume. Moreover, the flame is a peculiar medium possessing both complicated chemical and physical properties. In particular, H atoms in the rich flames favour the formation of atomic Na [38]. Hence, the I_{PS_pure} lineshape of atomic Na is unlikely to be identical whenever the PS measurement is conducted in the rich flame media. The complicated outcome reveals the value of **Eq. 3-5** in providing the possibility of a qualitative analysis of PS measurement performed in highly populated media.

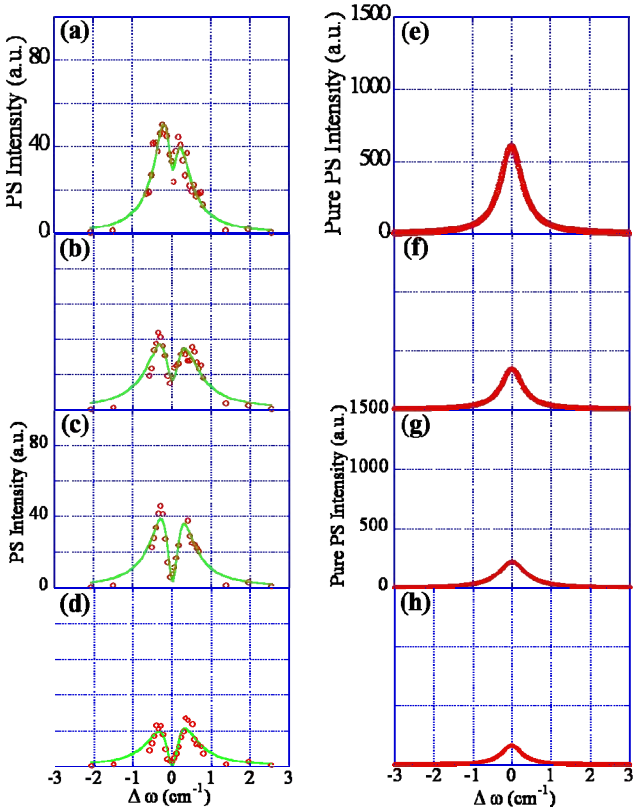

Figure 3-27 (a ~ d) Wavelengthscan is conducted to investigate the lineshape of I_{PS} under the atomic [Na] of 0.258×10^{18} atoms/m^3. The maximum I_{PS} in the lineshape decreases with the descending pump beam fluences of 6.36, 3.18, 2.01 and 1.00 GW/cm^2. (e ~h) The pure I_{PS} decreases with the descending pump beam fluences.

Although the fluctuation of pure I_{PS} is difficult to describe due to the complicated experimental environments, the tendency of the maximum pure I_{PS} ($I_{PS\_pure}^{max}$) of atomic Na associated with the dependence on pump beam fluence and atomic [Na] was observed, as indicated in **Figure 3-30** and **Figure 3-31**, respectively. The best-fit for the fluence dependence is modelled as linear and polynomial regimes. The linear best-fit, as shown in **Figure 3-30**(a), does not match the characteristics of PS measurement, which is a nonlinear technique although the R^2 of best-fits are above 0.95. For the polynomial best-fits, as shown in **Figure 3-30**(b), there is the better agreement and behaviour similar to a saturated regime.

Figure 3-31 represents the variation of the maximum I_{PS} among the pump beam fluences in the premixed laminar flames with the same population level of atomic Na. The $I_{PS\_pure}^{max}$ demonstrates the most significant fluctuation while the strongest pump beam fluence, 6.36

GW/cm^2, followed by the fluence, 3.18 GW/cm^2. In particular, the $I_{PS\_pure}^{max}$ fluctuates intensively when the strong pump beam fluence is applied in the high concentration media. The variation fluctuation was observed to be slightly influenced by the fluences. These results might indirectly support the assumption of a diffusion effect.

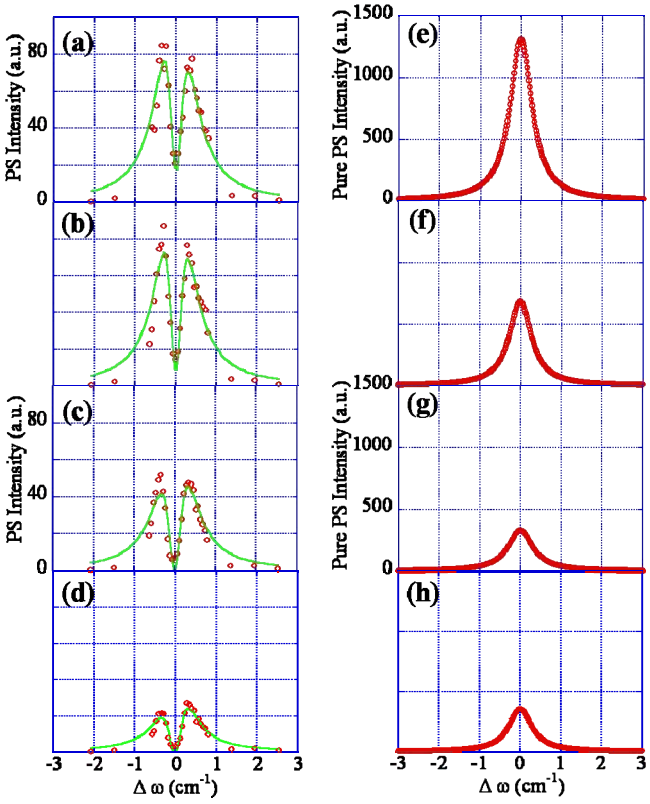

Figure 3-28 (a ~ d) Wavelengthscan is conducted to investigate the lineshape of I_{PS} under the atomic [Na] of 0.241×10^{18} atoms/m^3. The maximum I_{PS} in the lineshape decreases with the descending pump beam fluences of 6.36, 3.18, 2.01 and 1.00 GW/cm^2. (e ~h) The pure I_{PS} decreases with the descending pump beam fluences.

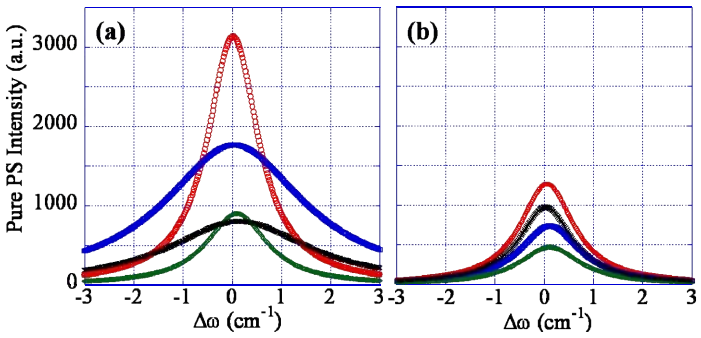

Figure 3-29 Lineshapes of pure I_{PS} are extracted from the wavelengthscan data with atomic [Na] (a) 0.428×10^{18} atoms/m^3 (b) 0.466×10^{18} atoms/m^3. These dot lines represent the pump beam fluences of 6.36 (red), 3.18 (blue), 2.01 (green) and 1.00 (black) GW/cm^2 were employed in the measurements.

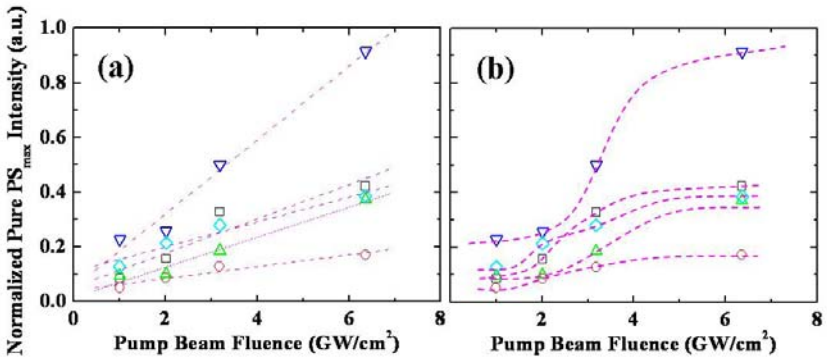

Figure 3-30 Fluence dependence of the pure PS intensities under the atomic [Na] (□) : 0.127; (○): 0.258; (△): 0.241; (▽): 0.428; (◊) : 0.456 $\times10^{18}$ atoms/m^3 ; (a) Linear best-fit with R^2 > 0.95 (b) Polynomial best-fit with R^2 =1.

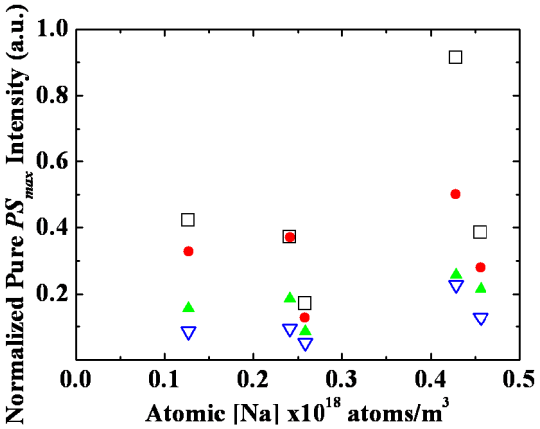

Figure 3-31 Atomic [Na] dependence of the pure PS signals under the pump beam fluences (□): 6.36; (●): 3.18; (▲): 2.01; (▽): 1.00 GW/cm^2

3.3.12 Line Broadening

Three types of line broadening were investigated during the study: Doppler, collisional and power in the PS optical arrangement. Before the discussion about the collisional and power broadenings of atomic Na in the seeded flame, due to the non-Doppler-free measurement in the present experimental arrangement, the Doppler width ought to be assessed and is governed by [24]:

$$\delta_{\omega D} = \frac{2 \cdot \omega_0}{c} \cdot \sqrt{\frac{2 \cdot k_B \cdot \mathrm{T} \cdot \ln 2}{m}} = \frac{2 \cdot \omega_0}{c} \cdot \sqrt{\frac{2 \cdot \mathrm{R} \cdot \mathrm{T} \cdot \ln 2}{M}}$$

Eq. 3-17

or

$$\delta_{\nu D} = 7.16 \times 10^{-7} \cdot \nu_0 \cdot \sqrt{\mathrm{T}/M} \ \ (\mathrm{Hz})$$

Eq. 3-18

where, $\delta_{\omega D}$ is the Doppler width, $\delta_{\nu D}$ is the Doppler width in frequency units, ω_0 is the transition of an atom at angular frequency (s^{-1}), ν_0 is the frequency of an atom (s^{-1}), c is the light speed ($m \cdot s^{-1}$), k_B is the Boltzmann constant (= $1.3806503 \times 10^{-23}$ $m^2 \cdot kg \cdot s^{-2} \cdot K^{-1}$), T is the temperature in the sample medium, R is the gas constant, m is the mass of an atom and M is the atomic mass (g/mol). By using **Eq. 3-18** and M = 22.99 and ν_0 is 5.088×10^{14} for Na at the flame temperature of 1500 K, the Doppler width of atomic Na in the atmospheric seeded flame was calculated to be 2.943 GHz, which is equal to 0.098 cm^{-1} (1 GHz = $0.0\bar{3}$ cm^{-1}). Moreover, the natural width of atomic Na corresponding to the transition between the $3^2P_{3/2}$ and the $3^2S_{1/2}$ levels is 10 MHz, which is equal to 3×10^{-4} cm^{-1}. In the following section, the collisional broadening is negligible if it is smaller than the Doppler width. A particular collisional broadening of atomic Na is nominated as self-broadening under the influence of other Na perturbers. The self-broadening of atomic Na in the D_1 line is about 150 MHz/torr, which is equivalent to 3.80 cm^{-1} [24]. The properties of atomic Na at D_1 line ($3^2S_{1/2} - 3^2P_{1/2}$)

Table 3-5 Doppler width, natural width and self-broadening of atomic Na at the D_1 line ($3^2S_{1/2} - 3^2P_{1/2}$) under one atmospheric pressure (760 torr)

Broadening	FWHM(cm^{-1})	Ref.
Doppler Width	0.098	Eq.3-17
Natural Width	0.0003	Ref.[24]
Self-broadening	3.8	

with one atmospheric pressure (760 torr) described above have been listed in **Table 3-5**.

3.3.12.1 Collisional Broadening

The effects on the target atoms that have been perturbed by other atoms in the atmospheric flame media, conventionally nominated as collisional broadening requires assessment. In flames media, the collisional broadening is caused by not only noble-gas perturbers but also molecular perturbers, namely N_2, H_2O, CO_2 and H_2 [205]. Comprehensive studies of pressure broadening in the D_1 lines of atomic Na perturbed by various molecules have been reported in literature [24, 205, 208-218]. The summary of pressure broadening for atomic Na at the D_1 line under the temperature of 300 K reported in the literature has been listed in **Table 3-6**, providing the results that describe the potential pressure broadening in this work. One should

Table 3-6 Collisional broadenings of atomic Na at D_1 line ($3^2S_{1/2} - 3^2P_{1/2}$) under one atmospheric pressure (760 torr) and temperature of 300 K are caused by nitrogen and noble gases.

Na-D1 ($3^2S_{1/2}$-$3^2P_{1/2}$)(589.592nm)		FWHM (cm^{-1})	Shift (cm^{-1})	Ref.
Perturbed by	Helium	0.405	0.000	[24]
	Neon	0.329	-0.076	
	Argon	0.742	-0.196	[208]
		0.734	-0.215	[24]
	Krypton	0.709	-0.152	
	Xenon	0.760	-0.152	
	Nitrogen	0.526	-0.230	[208]
		0.456	-0.203	[24]

be aware that the values adopted in Ref. [24] were the average of all values in Ref. [216-218] due to the significant variation between experimental results.

Table 3-6 demonstrates the collisional broadening for atomic Na at T = 300 K, which at 0.5 cm^{-1}, is larger than the Doppler width of atomic Na (0.098 cm^{-1}) at T = 1500 K. This indicates that the collisional broadening of atomic Na in the flame media is not negligible. As to the shift shown in **Table 3-6**, it exhibits a different tendency with $\Delta\omega_{shift}$ in the simulation results obtained by using **Eq. 3-5**. Further work is, therefore, required to completely describe the lineshape of atomic Na.

Collisional broadening of atomic Na in the flame media appears to also be perturbed by N_2, H_2O, CO_2, H_2 and other hydrocarbon radicals. Jongerius et al. [205] and Allard et al. [210] have investigated the collisional broadening of atomic Na at the D_1 line in flames and brown dwarfs, respectively, using a temperature range of 500 to 2000 K, as shown in **Table 3-7**. The collisional broadening of atomic Na in the transition of $3^2S_{1/2} - 3^2P_{1/2}$ caused by the perturbers, namely H_2O, CO_2, N_2, H_2 and Ar in flames is found to be around 0.7 cm^{-1} at 500 K. The collisional broadening varies from around 0.9 cm^{-1} for Ar, N_2 and CO/CO_2 perturbers and to about 1.2 cm^{-1} for H_2O and H_2 at 2000 K. It is, therefore, reasonable to speculate that the collisional broadening caused by H_2O and H_2, which are major products in flames, at 1500 K

Table 3-7 Collision broadening of atomic Na at the D_1 line ($3^2S_{1/2} - 3^2P_{1/2}$) perturbed by N_2, H_2O, CO/CO_2, H_2 and Ar measured in flames [205] and perturbed by H_2 in brown dwarfs is computed [210].

Perturber	Temperature(K)	FWHM(cm^{-1})	Shift(cm^{-1})	Ref.
N_2	2000	0.856±0.041	-0.310±0.020	[205]
	500	0.664±0.025	-0.213±0.008	
H_2O	2000	1.343±0.076	-0.144±0.038	
CO/CO_2	2000	0.912±0.202	-0.096±0.089	
H_2	500	0.707±0.020	-0.149±0.008	
	1500	0.547		[210]
	2000	1.241±0.279	-0.198±0.137	[205]
Ar	500	0.671±0.025	-0.203±0.008	
	2000	0.930±0.038	-0.347±0.020	

is as significant as that at 2000 K. The collisional broadening caused by H_2 reported by Allard et al. [210] is significantly lower than that measured in flames [205]. This may be the result of the interaction (reduction reaction) between H and Na atoms in rich flames [38].

D.M. Bruce [219] and F. Biraben [220] reported the collisional broadening of atomic Na in the transition of $3^2S_{1/2} - 4^2D_{3/2,5/2}$ (578.7 nm) summarised in **Table 3-8**. The collisional broadening caused by N_2 is similar to that reported by Jongerius et al. [205], which was summarised in **Table 3-7**, although the collisional broadening caused by Ar is significantly larger. Moreover, the tendency of the shift results, which reveal the positive values for He and negative values for other perturbers, is consistent with those reported in the literature [208, 213, 214, 216-222].

Given that the major perturbers, N_2, H_2O, H_2 and CO_2, are not negligible (greater than the Doppler width of atomic Na), the collisional broadening of atomic Na at the D_1 line ($3^2S_{1/2} - 3^2P_{1/2}$) should be taken into account in the lineshapes of atomic Na using PS.

3.3.12.2 Collisional Broadening

As mentioned in the preceding section, the collisional broadening of atomic Na at the D_1 line ($3^2S_{1/2} - 3^2P_{1/2}$, 589.592 nm) caused by major perturbers, N_2, H_2O, H_2 and CO_2, is significant in atmospheric flame media. **Figure 3-32** illustrates the occurrence of collisional broadening

Table 3-8 Collisional broadening of Na at 578.7 nm ($3^2S_{1/2} - 4^2D_{3/2,5/2}$) were reported by D.M. Bruce [219] and F. Biraben [220] at 600 K.

Collisional Broadening at 578.7 nm of Na				
D.M. Bruce [219]			F. Biraben[220]	
GAS	FWHM(cm^{-1})	Shift(cm^{-1})	FWHM(cm^{-1})	Shift(cm^{-1})
He	0.567±0.112	0.101±0.020	0.983±0.112	0.395±0.061
Ar	1.115±0.203	-0.375±0.071	1.216±0.101	-0.436±0.041
N_2	0.699±0.132	-0.365±0.061		

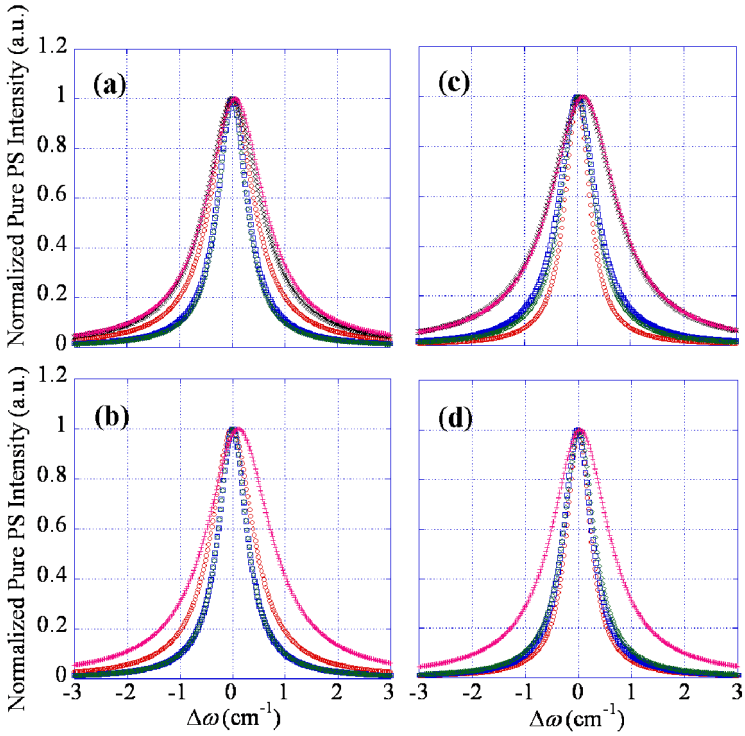

Figure 3-32 Normalized pure PS lineshapes experience collisional broadening under the pump beam fluences (a) 6.36 (b) 3.18 (c) 2.01 (d) 1.00 GW/cm^2 with atomic [Na] (○): 0.127; (□): 0.258; (◊): 0.241; (×): 0.428; (+): 0.456 ×10^{18} atoms/m^3. The result of (×): 0.428×10^{18} atomis/m^3 is absent in (b) due to the huge experimental variation.

under various concentrations (n_s) of atomic Na, namely 0.127, 0.258, 0.241, 0.428 and 0.456 ×10^{18} atoms/m^3, associated with the pump beam fluences of 6.36, 3.18, 2.01and 1.00 GW/cm^2. The FWHM of atomic Na shown in **Figure 3-32** was found to be associated with n_s under the same fluence of pump beam indicating the occurrence of collisional broadening. The FWHM of atomic Na with n_s = 0.456×10^{18} atoms/m^3 was found to be about 1.6 cm^{-1} under three fluences except for 1.4 cm^{-1} under 1.00 GW/cm^2. The FWHM of atomic Na with n_s = 0.428×10^{18} atoms/m^3 was found to be about 1.6 cm^{-1} under three fluences except for 0.8 cm^{-1} under 1.00 GW/cm^2. These results could indicate the contribution of power broadening. Moreover, the FWHM of atomic Na with lower concentrations (n_s = 0.258 and 0.241 ×10^{18} atoms/m^3) was found to be around 0.8 cm^{-1} consistently under four pump beam fluences. This might have resulted from the reduction of power broadening.

A particular anomaly evident in **Figure 3-32** (a) is the concentration of 0.127×10^{18} atoms/m^3,

which indicates a broader FWHM (~1.2 cm^{-1}) than cases of higher concentrations. The same result for the broader FWHM could be caused by the 3.18 GW/cm^2 pump beam fluence, as presented in **Figure 3-32** (b). With the reduction of the pump beam fluences, the FWHM of n_s = 0.127×10^{18} $atoms/m^3$ becomes smaller by about 0.8 cm^{-1}. This appears to provide evidence that power broadening is significant under low number densities of atomic Na. With higher concentrations, the power broadening may appears dominated by the collisional broadening: (**Figure 3-32**c and **Figure 3-32**d, respectively)

The particular FWHM of n_s = 0.428×10^{18} $atoms/m^3$ behaves differently from that of n_s = 0.456×10^{18} $atoms/m^3$ under the fluence of 1.00 GW/cm^2, which is likely the results of the reduction reaction caused by H atoms in the flames [38] because more H atoms are present in the flames based on the chosen equivalence ratio of 1.4. This H reduction reaction leads to significant collisional broadening [205]. It is reasonable, therefore, that the FWHM in the n_s = 0.456×10^{18} $atoms/m^3$ is consistently 1.6 cm^{-1}, except for 1.4 cm^{-1} under the fluence of 1.00 GW/cm^2. The results of collisional broadening were generally consistent with the theoretical prediction reported by Reichardt and Lucht [113], although the theoretical prediction was simulated using an unsaturated regime.

As the fluences were reduced, the FWHM of four concentrations of atomic Na shown in **Figure 3-32** appeared to be influenced not only by collisional broadening but by power broadening. This made it necessary to assess the possible power broadening in the present PS optical arrangement.

3.3.12.3 Power Broadening

In preceding section, **Figure 3-32** appeared to demonstrate a combination of collisional and power broadenings. Hence, the FWHM of atomic Na under the same n_s influenced by four fluences of the B_{pump} was investigated and the results presented in **Figure 3-33**. Power

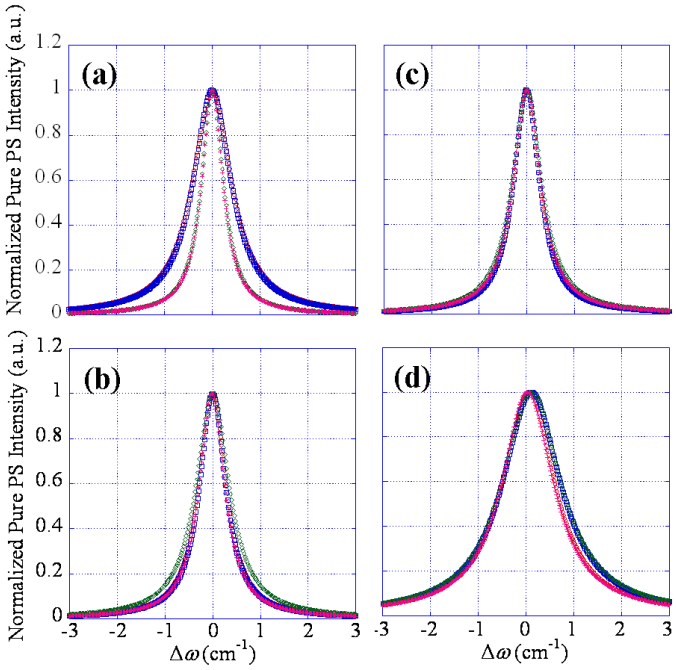

Figure 3-33 Normalized pure PS lineshapes experience the power broadening under atomic [Na] (a) 0.127 (b) 0.258 (c) 0.241 (d) 0.456 $\times 10^{18}$ atoms/m^3 with the pump beam fluences (○): 6.36; (□): 3.18; (◊): 2.01; (+): 1.00 GW/cm^2.

broadening, as theoretically predicted by Reichardt and Lucht [113], means that the higher pump beam fluence should facilitate a broader PS lineshape between unsaturated and strongly saturated regimes. The power broadening is significant in the atomic [Na], 0.127×10^{18} atoms/m^3, as shown in **Figure 3-33** (a), and it becomes approximately identical in higher population levels of atomic Na, as presented in **Figure 3-33** (b) ~ (d). This indicates that collisional broadening dominates the broadening effects in highly populated atomic Na. The power broadening was not as broad as predicted by Reichardt and Lucht [113] because the experiments in this study were performed using a saturated regime.

The summaries of collisional and power broadenings under the experimental parameters are presented in **Figure 3-34**. It can be observed that the power broadening is significant in low concentration media because the collisional broadening in high concentrations media dominates the line broadening in the present PS optical arrangement.

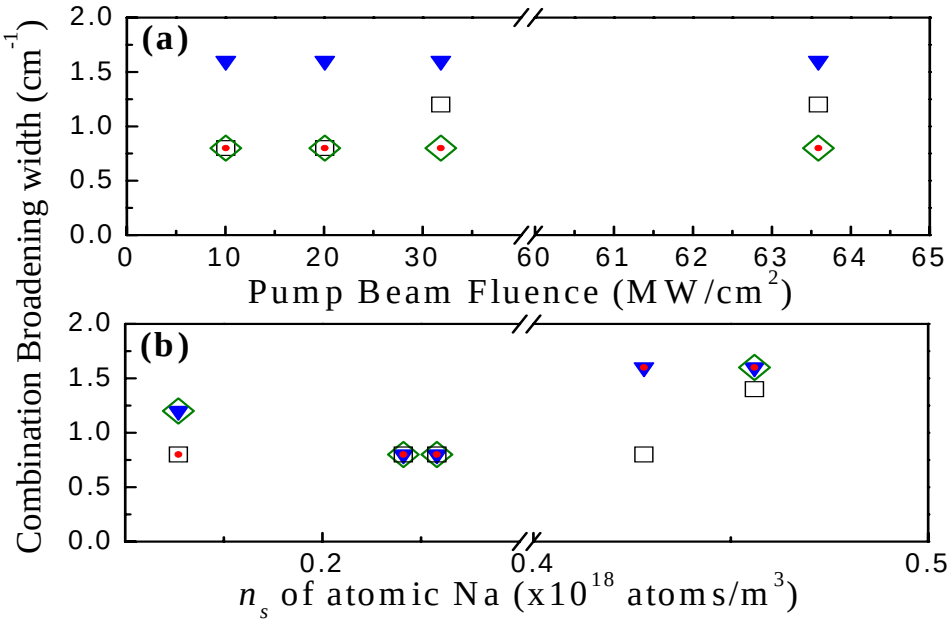

Figure 3-34 (a) Power broadening under n_s of atomic Na (□) 0.127 (●) 0.258 (◊) 0.241 (▼) 0.456 $\times 10^{18}$ atoms/m^3 (b) Collisional broadening under the fluence of (□) 1.00 (●) 2.01 (◊) 3.18 (▼) 6.36 GW/cm^2; the errors are respectively 20% and 1% for n_s of atomic Na and broadening width.

3.3.13 Atomic Na Released from Burning Solid-Fuel Particles

3.3.13.1 Qualitative Measurement

The wavelength that had been experimentally determined to investigate the saturation curve in **Section 3.3.2** was also employed to detect atomic Na released from burning solid-fuel particles. As mentioned in the preceding section, it was not necessary to establish a calibration curve using PS owing to the nonlinear PS measurement. However, the PS technique possesses the ability to suppress background noise, in particular during the devolatilisation phase of burning solid-fuel particles. **Figure 3-35** presents the atomic Na measured using PS during the devolatilisation phase of burning coal and wood particles in premixed laminar methane flames with Φ = 1.4. Compared with the results of atomic Na measured during the devolatilisation of coal particles using quantitative PLIF reported by van Eyk et al. [11], the

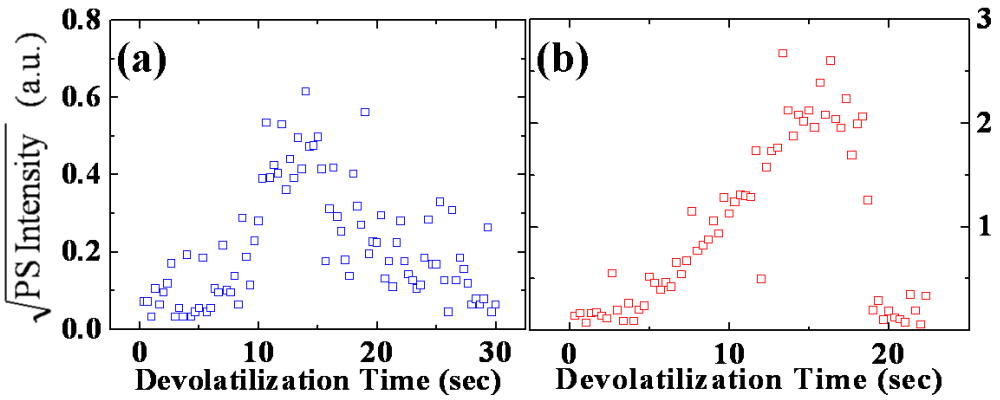

Figure 3-35 Atomic Na released during the devolatilisation phase of burning (a) Loy Yang Brown coal and (b) pine wood particles using PS in a premixed laminar methane flame with Φ = 1.4. The timeframe of devolatilisation phase of coal and wood are 9 and 13 seconds, respectively. The chosen wavelength for the present PS measurement was 589.590 nm and the employed pump beam fluence was 1.00 GW/cm^2.

result of atomic Na using PS reveals the better SNR. This outcome indicates the capacity of the PS technique applied in the environments with strong background noises. The atomic Na was released from the devolatilisation of burning coal and wood particles, which lasted for 9 and 13 seconds, respectively.

As noted in the preceding section, the PS signal is dependent on the applied fluence of the B_{pump}. **Figure 3-36** demonstrates the PS intensity of atomic Na measured using PS with a pump beam fluence of 0.893×10^4 J/m^2 during combustion of solid-fuel particles. It is clear that the atomic Na is not detectable if there is a strong fluence. This may be indirect evidence

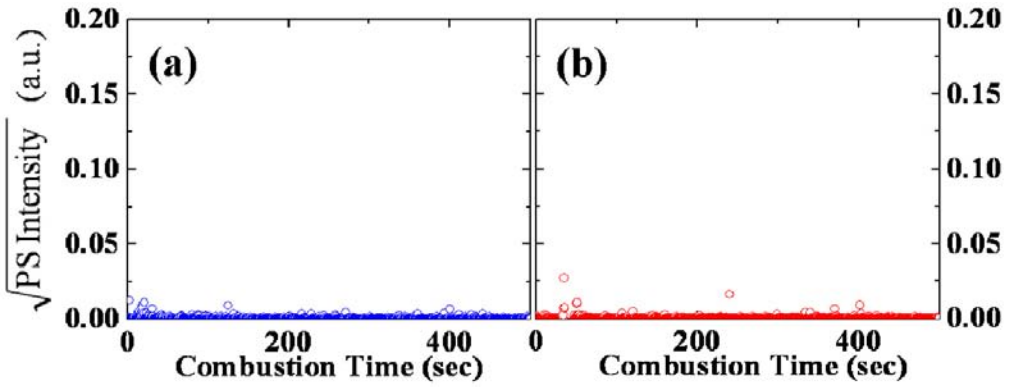

Figure 3-36 Atomic Na is not detectable using PS when there is a strong fluence of pump beam, 3.18 GW/cm^2 was employed in burning (a) coal and (b) wood particles.

that the thermal diffusion effect caused by the strong pump beam fluence results in atomic Na vanishing in the interaction volume. A similar tendency was observed in the investigation of saturation curves (**Figure 3-11**) where a lower PS intensity occurred when a higher pump beam fluence was employed. The difference between **Figure 3-11** and **Figure 3-36** is the number density of atomic Na. For the lower [Na] (**Figure 3-36**), the atomic Na diffuses out of the interaction volume due to the heat generated by the high pump beam fluence resulting in the extremely low PS signal. Moreover, the intensities of the PS signals in **Figure 3-11** exhibited a significant variation when the higher pump beam fluences were employed. The PS intensity was, however, still significant due to the high concentration of atomic Na in the interaction volume.

When an appropriate pump beam fluence is applied, the PS measurement is capable of being used to detect atomic Na during the char and ash phases of the burning of solid-fuel particles. **Figure 3-37** shows the historical release of atomic Na during the combustion of solid-fuel particles with Φ = 1.4. The historical results of atomic Na released from burning Loy Yang coal particles are consistent with those reported by van Eyk [11], which indicates that the qualitative analysis of atomic Na released from burning solid-fuel particles might be achievable but the quantitative measurement is not.

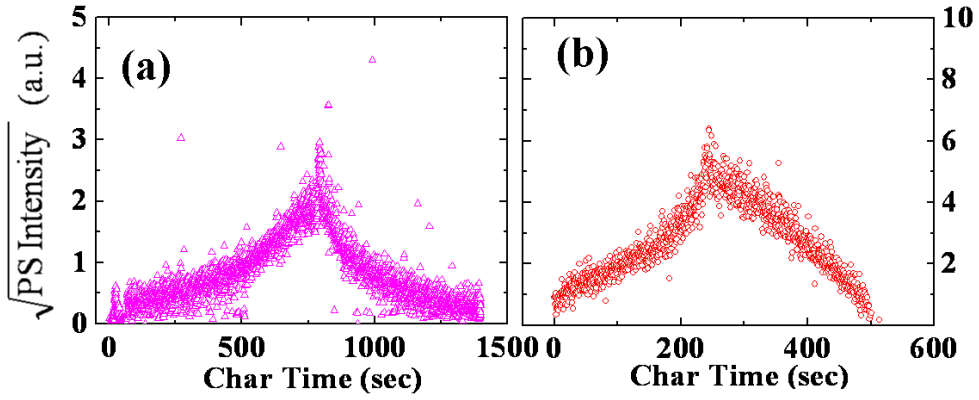

Figure 3-37 Historical release of atomic Na recorded using PS during the char and ash phases of burning (a) coal and (b) wood particles in the premixed laminar flame with Φ = 1.4.

3.3.13.2 Difficulty of Quantitative Measurement

To achieve quantitative measurement, a calibration curve is necessary, which is very difficult to achieve at high [Na]. However, the flame absorption coexisted with PS signals, which caused difficulties of building up a calibration curve in the current PS measurement. Wavelengthscan is performed to obtain the relationship between PS intensities and the concentration of the target species because the lineshape is a function of laser fluencies and Na concentrations. The I_{PS} is nonlinear to the n_s of the target species in a typical PS measurement. However, the flame absorption in the current PS measurement made the quantitative PS measurement almost impossible because the absorption varied the lineshapes, as presented in **Figure 3-13 ~ Figure 3-19**. This reveals that the magnitude of the I_{PS} at a single wavelength is not always proportional to the concentration of the target species. Therefore, a calibration process is not reliable in the current PS measurement at high [Na] with strong atomic transition. In addition, atomic Na released from burning solid-fuel particles must be recorded without wavelengthscan because the period of scanning (15 minutes) across the wavelength range (0.5 nm) is much longer than the lifetime of atomic Na in D_1 transition. Although a single wavelength can still be used to detect atomic Na released from burning solid-fuel particles, due to flame absorption, the intensity of atomic is not always proportional to [Na].

3.3.14 Potential Quantitative Measurement using PS

Although quantitative measurement using PS seems unachievable in this study, some experimental arrangements may be considered to overcome the issues in the future work:

1. To perform seeded flame in a slot burner
2. To potentially achieve quantitative PS measurement using **Eq. 3-5**

3. To utilise a fast-scan laser system

The flame absorption can be reduced using a slot burner because the absorption length can be minimised. However, it is unavoidable in the flame media because the thickness of the flame is still large to the detection volume using PS. The second and the third arrangements can potentially overcome the effect caused by the flame absorption to achieve quantitative PS measurement.

To achieve quantitative measurement using PS, a calibration curve is required. However, the quantitative measurement of atomic Na in the flames may be possibly obtained using **Eq. 3-5** as a calibration curve was not achievable in this study. By examining the $I_{PS}(\omega)$ in **Eq. 3-5**, which is a function of the number density of the target species (as introduced in **Eq. 2-9** and **Eq. 2-11**), the number density of the target species may be extracted from the fitting results (lineshapes). To achieve this, a fast-scan laser system is required to scan the wavelength range (about 2 nm) within few micro- or milli-seconds. Unlike the slow scan employed in this study (20 minutes for 1 nm scan range), the number density of the target species was not constant during the time leading to concentration uncertainty in wavelengthscan results. Moreover, the determination of concentration of the target species relies on the lineshape fitting. Significant concentration variation can be fatal to the application. Therefore, the lineshape obtained from the fast-scan process can represent the instantaneous concentration of the target species without a calibration curve. This is why the potential of quantitative PS was performed in this study rather than demonstrating the quantitative measurement.

3.4 Conclusions

The lineshape of atomic Na in the seeded flames using PS were modelled, governed by **Eq. 3-5**:

$$I_{PS\_FIT}(\omega) = I_{baseline} + I_{PS} \times \left\{ \frac{1}{1+\left[\frac{2\times(\Delta\omega - \Delta\omega_{shift})}{\Delta\omega_{PS}}\right]^2} \right\}^n \times exp\left[\frac{-\alpha_0 \cdot L_{abs}}{1+\left(\frac{2\times\Delta\omega}{\Delta\omega_{abs}}\right)^2} \right]$$

Eq. 3-5

The PS measurement employed in highly populated media consists of two effects: the PS signal, described by either Lorentzian (saturated PS signal, n = 1) or Lorentzian cubic (unsaturated PS signal, n = 3), and absorption effect. The model successfully describes the wavelengthscan of atomic Na using PS under various seeded population levels of atomic [Na], pump beam fluences and flame conditions. The regime of the right- or left-shift is not clear yet. It seems to be affected by the collision of atomic Na but this proved difficult to establish during the current study.

The quantitative measurement of atomic Na using PS was not achievable in current study due to the difficulty to establish a calibration curve. Moreover, the study showed the potential of quantitative PS measurement performed in a fast-scan laser system without a calibration curve because the instantaneous number density of the target species can possibly be obtained from the lineshape fitting in the future work.

The collisional and power broadenings have been identified from the pure PS lineshapes extracted from **Eq. 3-5**. The FWHM of atomic Na at the D_1 line ($3^2S_{1/2} - 3^2P_{1/2}$) was found to vary with the seeded [Na] under higher fluences of B_{pump}. The FWHM of atomic Na was found not to vary with seeded [Na] of 0.456×10^{18} atoms/m^3 indicating that collisional

broadening dominates power broadening. This has been verified by examining the broadening of FWHM under the same fluence of pump beam.

The saturation curves of atomic Na measurement using PS were found to be significantly different in lean and rich flames. They reflect the saturation fluence (about 0.13 ± 0.06 GW/cm^2) in the lean flame, which is much lower than that (about 1.5 ± 0.5 GW/cm^2) in the rich condition for the same population level of seeded [Na]. This is because the atomic [Na] in the lean flame is lower than that in the rich flame due to hydrogen reduction reaction [38].

Three effects have been identified. The beam steering effect was found to be approximately 1 mm at 2 m distance from the intersection location, occurring in PS measurement. It led to approximately 2.03% error in this measurement. The power broadening is significant in the low population level of atomic Na. The collision broadening was found to dominate the broadening effect in the present experiment.

The mathematical simulation successfully not only describes the wavelength scan results of atomic Na in the seeded flames but also indicates the disadvantage of PS measurement suffering from strong absorption in the highly populated media. However, the advantage of the PS technique is its ability to detect species in environments with strong background noise. The pure PS signals were extracted from the simulation results. The collision dominates the power broadening in the higher population of atomic Na and the intensity of pure PS is related to the fluence of the pump beam.

The chosen wavelength of 589.590 nm was used to detect the time-resolved history of atomic Na released from burning Loy Yang brown coal and pine wood particles. It demonstrates the capacity of the PS technique to suppress background noise during the devolatilisation phase. However, due to the nonlinearity of the PS measurement, it is unable to perform quantitative PS in the detection of atomic Na released from burning solid-fuel particles. The timeframe of atomic Na released from the devolatilisation of burning coal and wood particles was found to

be 9 and 13 seconds, respectively.

The PS signal of atomic Na may not be achievable given the excess pump beam fluence due to the thermal diffusion in the interaction volume leading to the vanishing atomic Na. These phenomena have been observed in **Figure 3-11** and **Figure 3-36** providing the experimental evidence for thermal diffusion in the PS measurement.

The simultaneous laser absorption measurement is associated with PS measurement to provide the instantaneous number density (n_s) of atomic Na. The measured n_s is compared to the product of the assumed ratio, ε, multiplied by the total amount of seeded Na calculated based on **Eq. 2-31** divided by **Eq. 2-32**. The measured n_s was found to be a good agreement with the predicted value, which indicated that the proportion of atomic Na in the flame assumed to be 0.02 was appropriate.

CHAPTER 4

The Application of Polarisation Spectroscopy in Atmospheric Plasma

4.1 Introduction

The chapter describes the use of polarisation spectroscopy (PS) to detect atomic species in atmospheric pressure welding plasma, in which very strong background emission occurs. To investigate iron (Fe) in the environment with such strong background emission, various experimental conditions were put in place. The wavelengthscan of atomic Fe determines the wavelength employed in the following parameters of applied current, mixture fraction of buffer gas and radial position within the plasma. Of the characteristics of PS measurement, the energies of the pump beam and wavelengthscan were studied.

4.2 Experimental Arrangement

4.2.1 Laser and Welding Systems

A schematic diagram of the experimental set-up is depicted in **Figure 4-1**. A tuneable dye laser with a frequency mixing unit (Quantel, TDL90) pumped by a frequency doubled Nd:YAG laser (Quantel, YG980) was used. The output radiation from the dye laser near 605.6 nm and a small part of the Nd:YAG fundamental frequency at 1064 nm, were directed to an Optical Compensator (OC) and a Mixing Crystal, as shown in **Figure 4-1**.

Both the OC and MC were placed on an actively controlled mount to ensure maximum laser power while scanning the dye laser. The output radiation from the mixing unit was then directed to a set of four Pellin Broca prisms to suppress the dye and the fundamental Nd:YAG laser frequencies and permit the tuneable UV radiation, near 385 nm, to exit. The laser

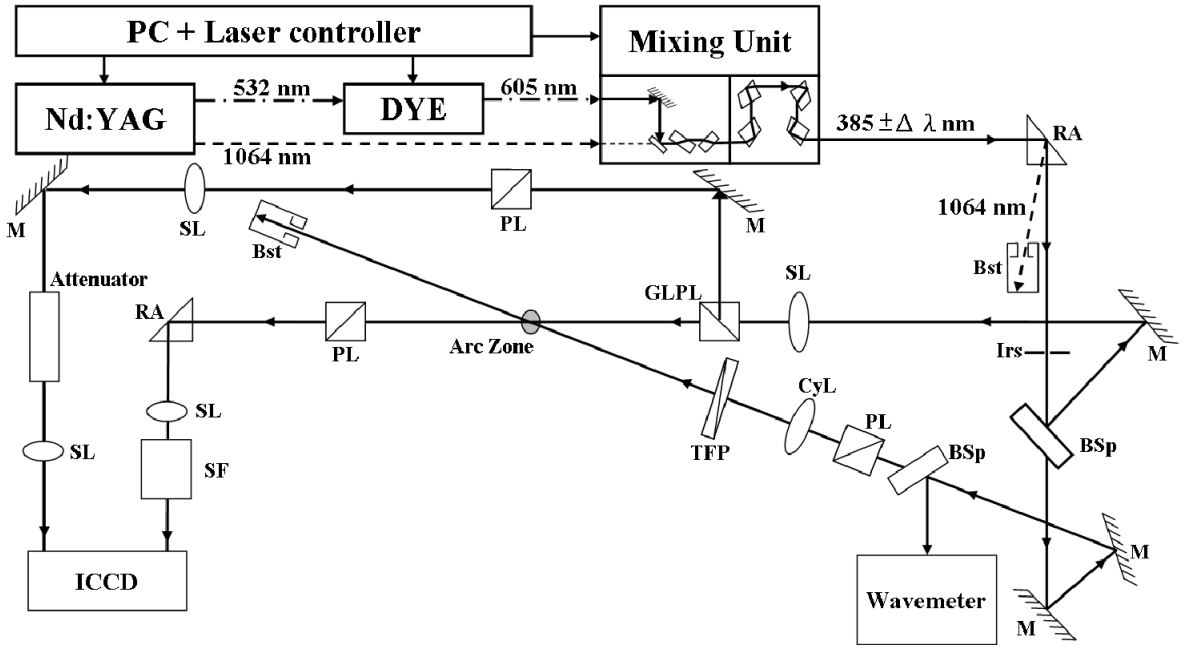

Figure 4-1 Schematic arrangement of PS: (M) Mirror, (CyL) Cylindrical Lens, (BSp) Beam Splitter, (Bst) Beam Stop, (SF) Spatial Filter, (SL) Spherical Lens, (RA) Right Angle Prism, (PL) Polariser, (GLPL) Glan Polariser, (Irs) Iris Diaphragm, and (TFP) Thin Film Polariser.

radiation near 385 nm was split into pump and probe beams by a quartz plate (beam splitter, BsP). The pump beam was expanded by a beam expander and then passed through a thin film rotatable polariser. The thin film polariser was used to control the pump beam energy without introducing any beam displacement. To form the laser sheet, the pump beam was directed to a cylindrical lens. The laser sheet was then directed to a polariser set vertically and then to a variable quarter wave-plate. The height of the pump beam sheet was ~ 7 mm while the probe beam was round with a diameter of ~ 1 mm. The angle between the probe and the pump beam was 8.8 degrees. A small part of the laser beam was sent to a pulsed wavemeter (Burleigh 5500) for absolute wavelength calibration. The probe was directed through two Glan Laser Polarisers (GLP) (extinction ratios ~ 5×10^{-6}), a spatial filter, and finally to an intensified CCD camera (Princeton Instruments, ICCD-576-G/RB-E) operated at 20 ns gate width. A very small portion, selected by the fourth polariser, of the laser output from the GLP was focused on the ICCD camera and acted as a reference energy beam.

The welding drum was made from mild steel with an outside diameter of 220 mm and a wall thickness of 7mm. Water was circulated through a closed loop system to reduce the drum temperature. In all of the experiments, a tungsten electrode tip of 2.5mm diameter with a point ground to 60˚ degree was used. The height of the tungsten electrode above the drum was 4 mm. Some gases, such as pure Ar, He and a mixture of Ar and He, were used as the shielding gases [223]. **Figure 4-2** illustrates the welding fume plumes with shielding gases of pure Ar, 50% He

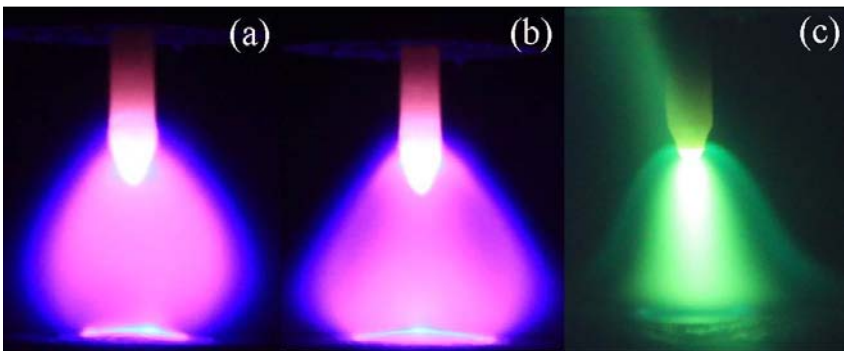

Figure 4-2 Welding fume is operated under (a) pure He (100%) with 35 A current (b) He + Ar (50 + 50 %) with 120 A current (c) pure Ar (100 %) with 120 A current.

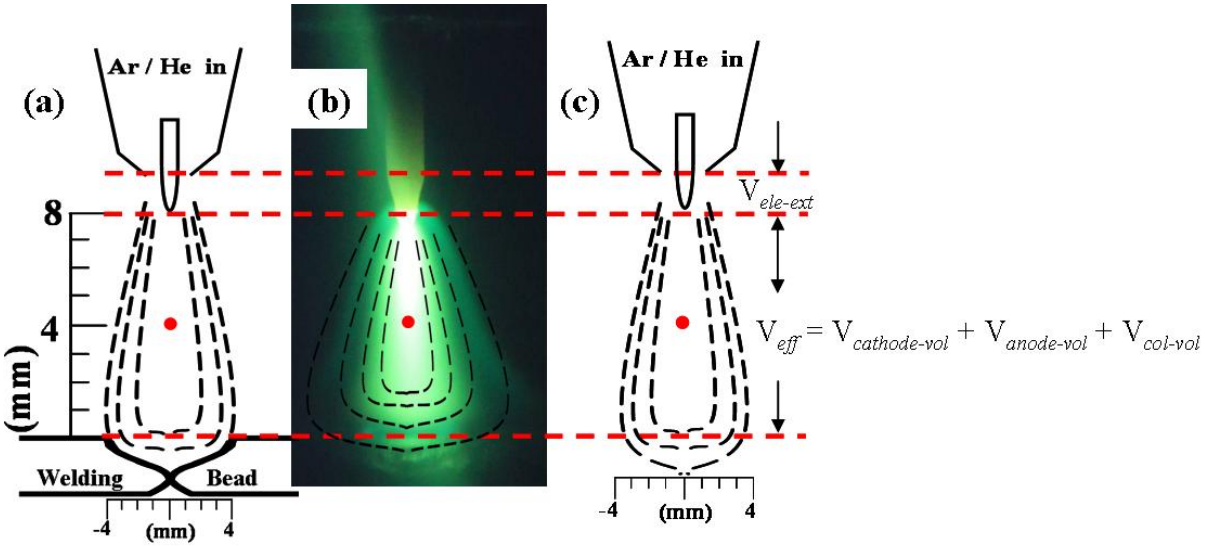

Figure 4-3 (a) Schematic diagram of PS measurement in a GTAW process; the location where the PS (red dot) is performed is 4 mm below the anode. The dashed lines represent temperature distribution within the welding fume. (b) Photograph shows the real-time welding fume using Ar as buffer gas and the location where the laser beam (red dot) is applied. (c) The total arc voltage is governed by $V_{ele\text{-}ext} + V_{eff}$ between anode and cathode.

+ 50% Ar and pure He. The details of the experimental arrangement with respect to the gas flow, welding torch, welding drum and are shown in **Figure 4-3**a. The ceramic shroud of the torch has an internal exit diameter of 11.5 mm and was positioned 8mm above the drum. **Figure 4-3**b shows the laser beam was placed in the middle of the fume plumes, 4 mm above the working piece.

4.2.2 Nascent Iron in Welding Fume

The induced voltage of the applied current between the cathode (working piece) and the anode (tungsten electrode), governed by the Ohm's Law, heats up the working piece which vaporises to provide nascent Fe atoms. The population of Fe atoms in the welding fume plume is determined by the strength of the induced current which determines the temperature of the plume. The total welding voltage including the electrode extension drop ($V_{ele\text{-}ext}$) and effective voltage (V_{eff}) which is equivalent to the cathode fall voltage ($V_{cathode\text{-}vol}$), arc column drop

($V_{col\text{-}vol}$), and anode fall voltage ($V_{anode\text{-}vol}$), as shown in **Figure 4-3**c, is governed by [223, 224]:

$$\begin{aligned} V_{total} &= V_{ele-ext} + V_{eff} \\ &= V_{ele-ext} + V_{cathode-vol} + V_{anode-vol} + V_{col-vol} \end{aligned}$$

Eq. 4-1

The $V_{cathode\text{-}vol}$ and $V_{anode\text{-}vol}$ are dominated by the properties of a given buffer gas as a function of the arc current, as well as the cathode and anode materials. As for the column drop ($V_{col\text{-}vol}$), it can be considered to be related to the thermal and electrical equilibrium of the welding fume. Moreover, the three voltages ($V_{cathode\text{-}vol}$, $V_{anode\text{-}vol}$ and $V_{col\text{-}vol}$), following Ohm's Law, provided a constant resistance for the experimental arrangement. The $V_{ele\text{-}ext}$ is physically identical in the entire experiment due to the same experimental apparatus. The $V_{ele\text{-}ext}$ is constant, subject to the experimental apparatus. It is reasonable to consider that the V_{total} is constant with the chosen shielding gas and the applied current. Therefore, the nascent number density of Fe in the welding fume plume is dominated by the applied current.

4.2.3 Data Acquisition and Processing

The intensities of the B_{probe} and B_{ref} in two locations of each measurement image were extracted using Matlab 7.0. Similar image processing described in **Chapter 3** was employed in this chapter. To reduce the variation resulting from the beam steering effect, the intensities of the PS signals were integrated by selecting an area of 121 pixels (11x11 matrix) surrounding the central pixel where the maximum intensity was located, similar to the setup shown earlier in **Figure 3-7**. This avoids the beam steering effect, which is smaller than the interaction volume. Due to the strong beam steering effect in plasma media compared to that in flame environment, the 11x11 matrix was used here to reduce the variation between each ICCD image.

4.3 Results and Discussion

The PS signals of Fe in the welding fume are dependent on the applied currents, chosen buffer

gases and fluences of the pump beam. The conditions of welding currents and the chosen shielding gases are directly related to the population of Fe atoms in the welding arc. The welding arc is generated by the electric field induced by the applied current, and the resistance is dominated by the combination of shielding gases and the gap between anode and cathode. The resistance is only related to the dissociation energy of the chosen buffer gas when the gap remains constant. Therefore, the ultimate voltage of Ar, as the shielding gas, is lower than that of He because the dissociation energy of He is 2372.3 kJ/mol [225] higher than the 1520.4 kJ/mol of Ar [225]. This has been observed by Murphy et al. [226]. The voltage of the welding arc used He as a buffer gas with a 150 A current, which is higher than that using Ar. The Fe population level, therefore, can be dominated by the operation conditions of the welding process, which behaves differently at various wavelengths using PS. Apart from that, the intensities of Fe at the scanning wavelength using PS are related to the optical conditions, such as the fluences of the B_{pump}. In the following sections, a detailed discussion is provided of the investigation into Fe detection in the welding fume using PS.

4.3.1 Wavelength Dependence

The PS signal strength as a function of laser frequency was investigated. The current was set at 32 A and pure He was used as a shielding gas. The laser was scanned form 605.668 to 605.753 nm with 0.001 nm steps, which generated the designated wavelength range (385.96 nm to 386 nm with 0.0004 nm step) using the mixing crystal. It was set to stay at 30 images per each wavelength position (10 Hz image acquisition, 3 sec per measurement). To compute the PS intensity (I_{PS}) at each wavelength position, the intensity of each pixel of each probe beam image was summed and averaged for 30 images. The values obtained were corrected for laser power variation using the reference beam intensity. The typical wavelengthscan using PS was introduced in **Chapter 3**. As Fe atoms possess strong UV transition at 385.99114 nm, corresponding to the transition $3d^64S^2$-$3d^6(^5D)4s4p(3P)$ [23], it was expected that only one

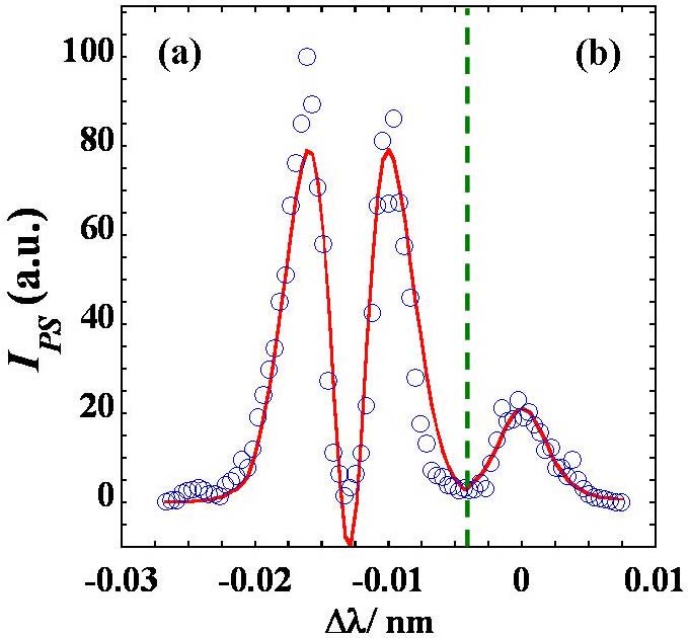

Figure 4-4 Wavelength scan across the Fe transition at 385.991 nm, using He as the buffer gas with a 32A current; (a) Stark-shift area (b) Original transition area; the red line represents the simulation of experimental results based on **Eq. 3-5**. The green dashed line separates two areas where the Stark-shift and original transition, respectively.

peak or strong absorption at 385.991 nm would be observed. However, the PS wavelength scan of Fe reveals more complicated feature, as shown in **Figure 4-4**.

Figure 4-4 shows a peak at 385.991 nm, which is almost identical in value to the strong Fe transition at 385.99114 nm. This peak was attributed to the strong population of Fe atoms in the plasma zone. Another strong spectral feature was observed at 385.977 nm where significant absorption occurred. This is consistent with the results noted in the preceding chapter about the detection of atomic Na in the flame using PS, and indicates that significant absorption occurred in the transition of 385.977 nm with a larger population of Fe atoms. This feature may appear to present two transitions. However, after close inspection and with lineshape taken into consideration, it was concluded that this feature could be attributed to one transition only.

The signal was generated by a non-linear optical process at intersection of the pump/probe beams, which is much smaller than the plasma zone. The B_{probe} experiences significant

absorption because of the highly populated Fe in the plasma media, an optical linear process, which results in the decrease of the intensity. The shift in the recorded wavelength, namely $\Delta\lambda$ = +0.013 nm, can be attributed to the Stark effect, which results in a wavelength shift to the red part of the spectra. In the case of Fe, it was reported by Panter and Foster [227] that the D orbital experience a stark shift to the blue part of the spectra, which was observed in this study. To avoid the Stark shift in the following experiments, the chosen wavelength was 385.99 nm.

The wavelength scan in the present experiment could only be achieved using He as a shielding gas due to the fact that the high current in the Ar environment led to enormous heat generation, causing the welding machine to shutdown. A completed wavelength scan not only takes 255 seconds (three seconds a step and 85 steps a complete scan), but also the wavelength adjustment takes another three seconds (30 blank images) between two wavelength positions. This means that the completed scan will take 510 seconds, which Ar as the buffer gas cannot tolerate. Using a different buffering gas, this experiment became the first time that a completed wavelengthscan of Fe across the transition, 386 nm, in welding plasma was achieved. Moreover, the result also implies that potentially the persistent transition, 385.99 nm, of Fe in the welding plasma can be selected as the detection wavelength for future experiments.

The wavelengthscan result, as shown in **Figure 4-4**, can be mathematically described using **Eq. 3-3** and modelled using **Eq. 3-5** by applying Marquardt's algorithm [199, 228], which were introduced in **Chapter 3**. Two equations are repeated for convenience, as follows:

$$I_{PS}^{exp}(\omega) = I_{probe}(\omega)\cdot\left\{\xi + \left(\frac{[Na]^2\cdot f_B^2\cdot I_{pump}^2\cdot\tau_{pump}^2}{16\cdot\hbar^2\omega^2}\cdot\sigma_{J_f\leftarrow J_i}^4\cdot\zeta_{J_f\leftarrow J_i}^2\cdot L_{PS}^2\right)\cdot\left(\frac{1}{1+[2\cdot(\omega-\omega_0)/(\Delta\omega_{PS})]^2}\right)^n\right\} - I_{abs}(\omega) \quad \text{Eq. 3-3}$$

and

$$I_{PS\_FIT}(\omega) = I_{baseline} + I_{PS} \times \left\{ \frac{1}{1+\left[\frac{2\times(\Delta\omega - \Delta\omega_{shift})}{\Delta\omega_{PS}}\right]^2} \right\}^n \times exp\left[\frac{-\alpha_0 \cdot L_{abs}}{1+\left(\frac{2\times\Delta\omega}{\Delta\omega_{abs}}\right)^2} \right] \quad \text{Eq. 3-5}$$

The wavelengthscan result has been separately described, namely the Stark shift and original transition areas in **Figure 4-4** (a) and (b), respectively. For the Stark shift area, the Lorentzian function (n = 1) was employed and the Lorentzian-cubed function was applied in the original transition area. Therefore, the simulation of the experimental results can be obtained by the superposition of two equations, indicated by the red line in **Figure 4-4**.

4.3.2 Mixture Fraction

To investigate the behaviour of Fe atoms in different shielding gases, a mixture fraction of He/(Ar + He) was performed from 0 to 1. The measurement was performed with the current at 80 A and the pulsed pump beam energy at 2 mJ. **Figure 4-5** illustrates the Fe intensities measured by applying PS. The Fe signals became stronger while the amount of He was increasingly entrained. This indicated that welding could be achieved in a low current environment, in which the stable welding process was performed using He as the shielding gas. Due to the effective collision caused by the Ar ions in the plasma media, a significant number of Fe atoms are excited to higher energy states leading to lower Fe signals using PS. This indicates that the greater efficiency of GTAW can be achieved when He is utilized as the shielding gas. Therefore, the intensity of the Fe atoms at 385.99 nm using PS grows stronger as the amount of He increases. The Fe signal reaches maximum intensity when the pure He was applied as a buffer gas. .

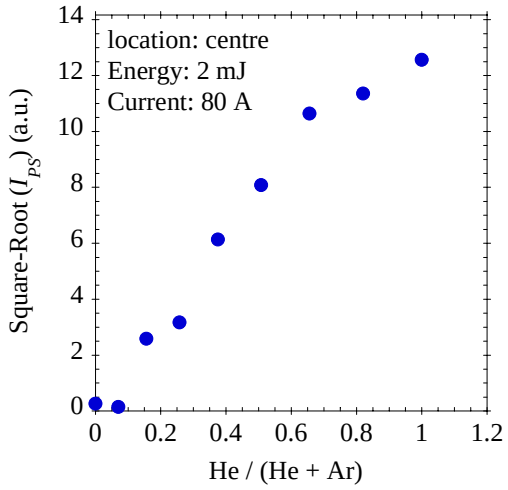

Figure 4-5 Intensities of neutral Fe detection using PS with mixture fractions of Ar and He under 80 A current and 2 mJ pulsed pump beam energy

4.3.3 Current Dependence

As discussed in the preceding section, a low current is required in the welding process to provide a significant population of Fe atoms with He as the buffer gas. **Figure 4-6** illustrates the strength of the Fe signal using Ar as a buffer gas with various currents, ranging from 90 to 130 A. It was observed that the Fe signal at λ = 385.99 nm increased significantly while the applied current exceeded 120 A. This is consistent with the observation results that the higher current is necessary in the welding process when Ar is the buffer gas [223].

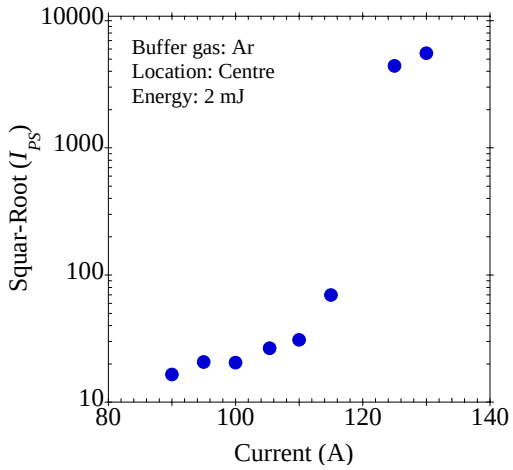

Figure 4-6 PS signals significantly increase while the applied currents are tuned from 90 to 130 A. Ar is applied as buffer gas and 2 mJ of the pulsed pump beam energy is used in the PS measurement.

4.3.4 Energy Dependence

The PS signal is dependent on the pump beam energy, as given by **Eq. 3-6** [16, 204]:

$$I_{PS} = \eta \cdot \left[\frac{I_{pump}}{I_{pump} + I_{Sat}^{PS}} \right]^2 \qquad \text{Eq. 3-6}$$

As noted in **Chapter 3**, the saturated energy of the B_{pump} can be extracted using **Eq. 3-6**. However, **Figure 4-7** shows that the square root of the intensity of PS signal () is linearly proportional to the energy of the B_{pump} with an applied current of 35 A and He as buffer gas. It is clear that the intensity of the PS signal is proportional to the energy of the B_{pump} within the unsaturated regime. This is consistent with the results demonstrating that the Fe signal is much stronger in pure He media than it is in a pure Ar environment. Moreover, the Fe signal using PS in the He media with a low welding current, 35 A, compared to 80A, (**Figure 4-5**), indicates that the same performance of the welding process can be achieved by using He as the shielding gas. In addition, due to the low current process, the potential hazard of GTAW fumes can be reduced. On drawback is that it is difficult to start a welding arc with pure He. In this experiment, therefore, the welding arc was generated using pure Ar and the buffer gas was gradually switched to pure He.

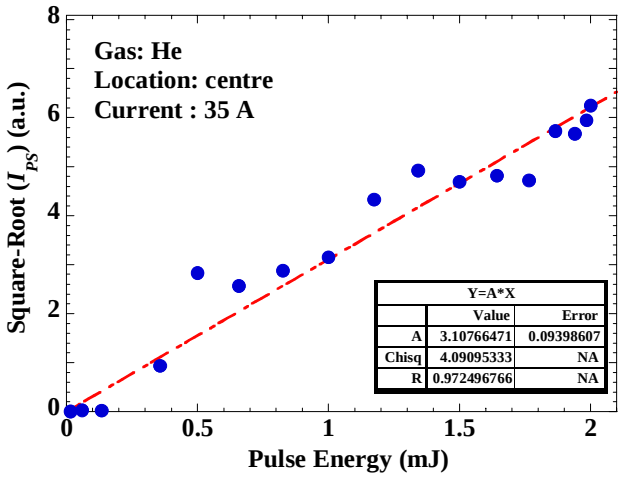

Figure 4-7 Fe intensity (●) using buffer gas of He and 35 A current is measured at the centre of plasma associated with the energies of the pulsed pump beam.

4.3.5 Iron in a Radial Position

Given that the intensity of atomic Fe is related to the applied currents (as presented in **Figure 4-6** and **Figure 4-7**), to verify the relation between the plume temperature and populated level of atomic Fe, it was also important to investigate Fe in the radial position along with the cathode. It was observed that the PS signals of atomic Fe consistently decreased from the centre to the edge of the welding arc [223], as presented in **Figure 4-8**. It is reasonable, therefore, to correlate the temperature distribution with the Fe intensity within the welding fume. This experimental Fe intensity demonstrates a good agreement with the temperature gradient.

4.3.6 Beam Steering Effect

The beam steering effect caused by the thermal gradient in the sample medium, which in this case was plasma, is important for PS measurement because it represents the reliability of the results. If the beam steering effect is greater than the interaction volume, it leads to

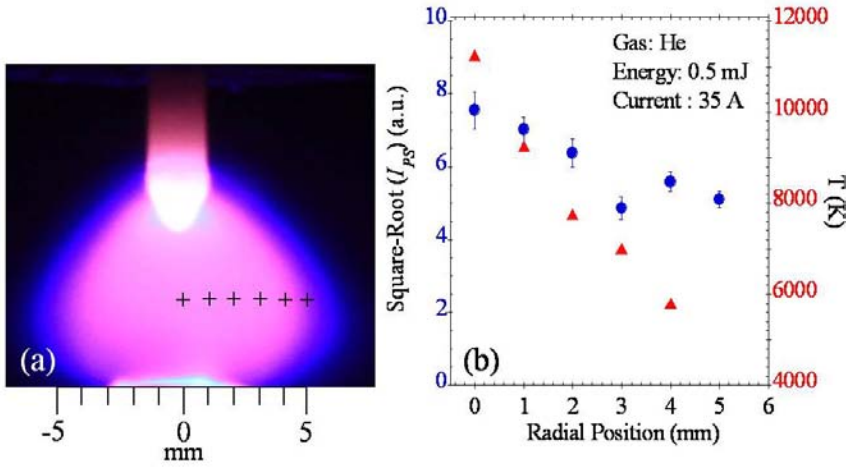

Figure 4-8 (a) The laser beam was employed in the centre of the welding fume, 4 mm above the cathode and radially switched to the edge of the welding fume. (b) Intensities of Fe (●) in the welding fume using PS were measured at the radial locations from the centre to the edge of welding fume. The measurement was performed using He as the buffer gas with a 35 A current and 0.5 mJ pump beam energy. The temperatures (▲) were adopted from Ref. [223] to estimate the plasma temperature.

uncertainty in the measurement. It is therefore necessary to identify the effect. **Figure 4-9** shows that the statistic of occurrence of the beam steering effect in three areas (*a*, *b* and *c*) was 17.71, 71.35 and 10.94 %. By applying the methodology in **Eq. 3-8**:

$$\Delta\theta = \tan^{-1}\left(\frac{x_{steering}}{D_{PS}}\right) \qquad \text{Eq. 3-8}$$

It becomes clear that the major and overall beam steering effect was 1 and 2 mm, respectively, and that the distance between the arc zone and the ICCD camera was 2.42 m, as in the following:

$$\Delta\theta_{major} = \tan^{-1}\left(\frac{1}{2420}\right)$$
$$\Delta\theta_{overall} = \tan^{-1}\left(\frac{2}{2420}\right)$$

Eq. 4-2

By applying **Eq. 3-9**, the PS intensity possesses beam steering identified as:

$$I_{PS} \propto \cot^2(\theta + \Delta\theta_{major})$$
$$I_{PS} \propto \cot^2(\theta + \Delta\theta_{overall})$$

Eq. 4-3

Hence, the E_{BS} caused by the major and overall beam steering in the present experiment using **Eq. 3-10** was obtained, as below:

$$E_{BS} = \frac{\cot^2(\theta) - \cot^2(\theta + \Delta\theta_{major})}{\cot^2(\theta)} \times 100\%$$
$$= \frac{\cot^2(\theta) - \cot^2(\theta + \Delta\theta_{overall})}{\cot^2(\theta)} \times 100\%$$

Eq. 4-4

The E_{BS} caused by major and overall beam steering was calculated to be 0.54 and 1.08%, respectively. It is clear that the E_{BS} caused the minor random error for the detection of atomic Fe in the present experimental arrangement.

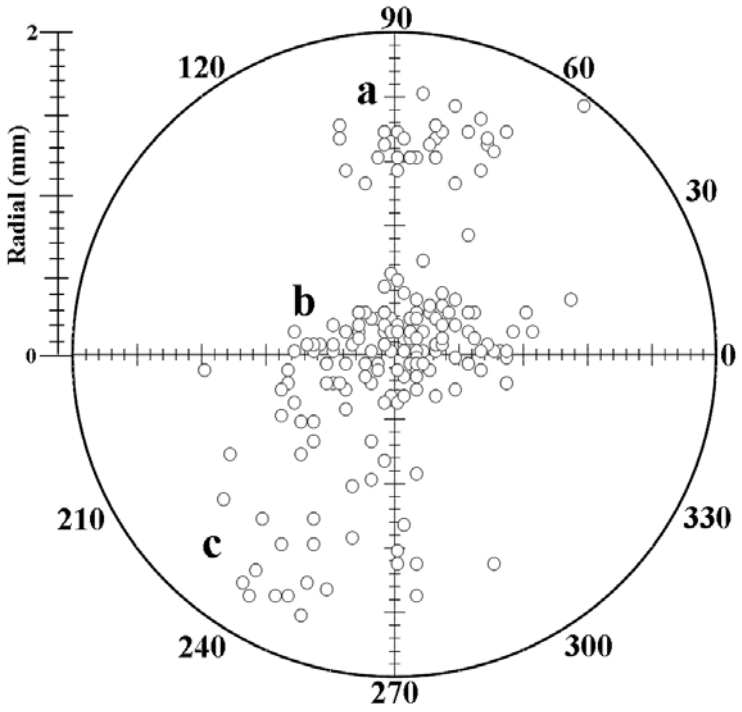

Figure 4-9 Beam steering effect of the detection of atomic Fe using PS in the GTAW process; the *a*, *b* and *c* represent the ratios of beam steering effect in three areas to be 17.71, 71.35 and 10.94 %. The major beam steering (the *b* area) was observed to be around 1 mm. The overall beam steering, including (*a*, *b* and *c* areas), was found to be around 2 mm.

4.4 Conclusion

This chapter explains the outcome of applying the polarisation spectroscopy (PS) technique gas tungsten arc welding (GTAW). The experimental work revealed a significant capacity for detecting metals, Fe of this case, in plasma using the PS technique because it possesses the ability to greatly suppress background noise [24].

The shielding gas, helium (He) plays an important role in the GTAW process when it comes to improving welding efficiency. The welding current was set to 35 A using pure He as the buffer gas leading to a significantly high concentration of Fe atoms. Moreover, the Fe concentration was significantly improved when as little as 10% He was added to pure Ar shielding gas. When using Ar as the shielding gas, the concentration of Fe increased with the increasing currents.

For the first time in the GTAW process, it was observed in the wavelengthscan that the Stark shift occurred (at +0.013 nm), leading to significant absorption at the transition of 385.977 nm. The wavelength scan result was described mathematically based on **Eq. 3-5**. This indicates that the PS signals of the original Fe transition at 385.99 nm and Fe with the Stark shift at 385.977 nm possess good agreement with the theoretical model.

The major and overall beam steering effect was identified to be 1 and 2 mm, respectively, which results in 0.54 and 1.08 % systematic error in the present PS measurement. It demonstrates that the beam steering is negligible in the present PS measurement.

CHAPTER 5

Atomic Sodium and Potassium Detection using Atomic Emission Spectroscopy

5.1 Introduction

This chapter describes the use of the optical technique, atomic emission spectroscopy (AES), was used to detect atomic Na and K simultaneously released from a plume of burning solid-fuel particles. The approximately spherical particles, compoased of Loy Yang Brown coal from Victoria, Australia, and pine wood particles, were burned in premixed laminar methane flames with rich conditions. The rich flames provided a stable combustion environment in which to observe the release of alkali metals.

The simultaneous shrinking and burning of the solid-fuel particles were recorded, along with the associated release of atomic Na and K in order to better understand their behaviour during combustion.

5.2 Experimental Arrangement

5.2.1 Laminar Premixed Flame

In order to study the fundamental behaviour of alkali species released from individual burning solid-fuel particles, a stable and simple combustion environment is necessary. Therefore, a

laminar premixed flame is more suitable than non-premixed or turbulent flames owing to the stable and uniform combustion environment in which solid-fuel particles are burned constantly.

The Perkin-Elmer seeding burner is a well-known laminar premixed burner (**Figure 5-1**) which contains a bottom chamber to premix air and fuel, connected to an upper honeycomb matrix with the circular shape of which the diameter is 23 mm. This central matrix was mounted within a concentric honeycomb with a diameter of 45 mm. The burner is specially designed to investigate the spectral lines of certain elements using flame atomic emission spectroscopy. It was designed so that the excess seeding solution can be removed from a drain in the bottom chamber.

The flowrates of air and methane were controlled by mass flow controllers (MFCs, Bronkhorst) and four equivalence ratios: 1.149, 1.252, 1.287 and 1.336 were undertaken, as listed in **Table 5-1**. The detailed calculation of the equivalence ratios is presented in **Section 2.3.2**. To verify that higher temperatures [229] occurred in leaner conditions with the same flowrate of air or fuel, the four equivalence ratios were specifically arranged using the same

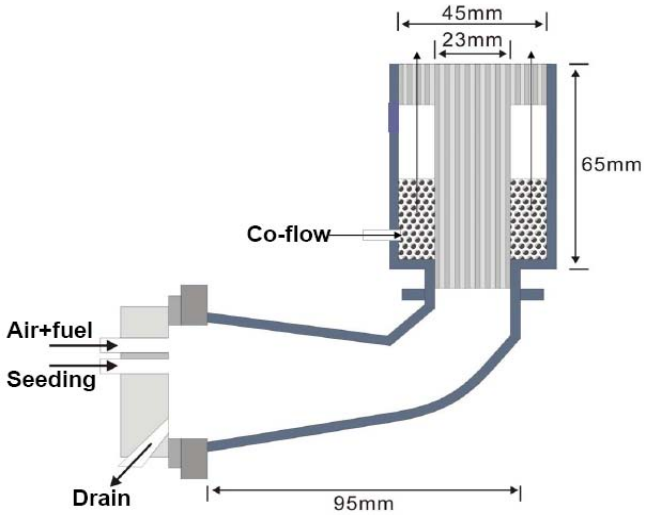

Figure 5-1 A Perkin Elmer burner is used to generate the premixed laminar flame. Salt droplets, methane and air were entrained and premixed in the bottom chamber. The drain is designated for removing the excess salt solution in order to maintain the volume of the mixing chamber.

Table 5-1 Flowrates of air and methane employed in four equivalence ratios (Φ) controlled by two MFCs; the calculation of Φ is based on **Eq. 2-30**.

Φ	1.149	1.252	1.287	1.336
Air (ml_n)	6.450	6.630	6.450	5.550
Methane (ml_n)	0.779	0.872	0.872	0.779

flowrate of methane or air. For example, 0.779 ± 0.006 and 0.872 ± 0.006 ml_n (normal litre per minute) of methane was used in Φ = 1.149, 1.336 and 1.252, 1.287, respectively, while the corresponding air flowrates were 6.450 ± 0.03, 5.550 ± 0.03 and 6.630 ± 0.03, 6.450 ± 0.03 ml_n, respectively.

As presented in **Figure 5-2**, the flowrates of air and methane were established at equivalence ratios that would result in stable laminar flames. The unstable flames shown in **Figure 5-3** were not employed since the uncontrolled oxygen content present in the flame front of the vortex inside the flame would lead to the unpredictable release of atomic Na and K from the burning solid-fuel particles. Given the dimensions of the burner and the burning velocity of methane, stable flames based on equivalence ratios between 1.149 and 1.336 were achievable.

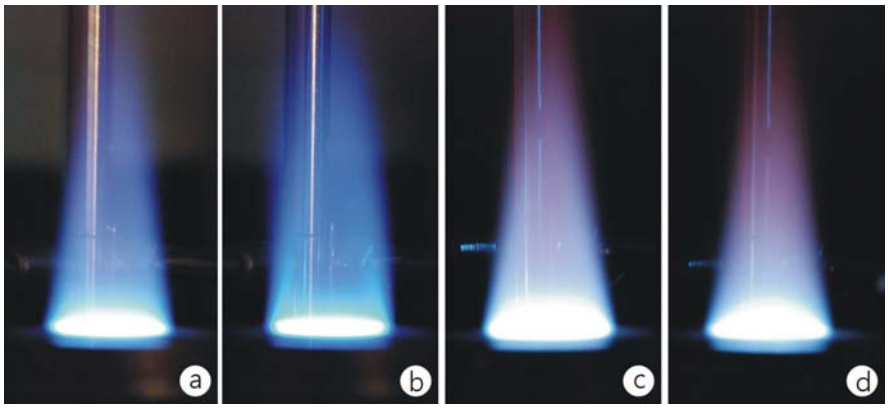

Figure 5-2 Laminar premixed flames with Φ = (a) 1.149 (b) 1.252 (c) 1.287 (d) 1.336. Equivalence ratios of 1.149 and 1.336 are the boundary conditions for stable laminar flames.

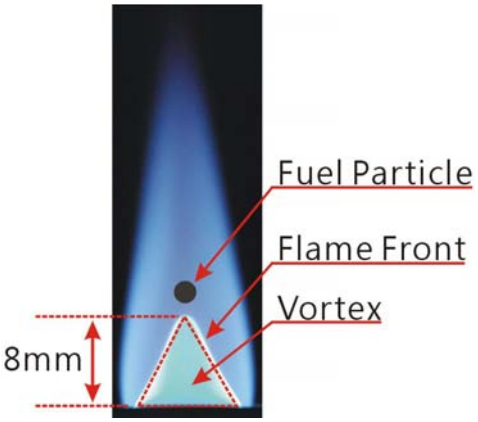

Figure 5-3 The flame was operated with the equivalence ratio, Φ = 1.560. The vortex was caused by excess CH_4 leading to an uncertain flame environment.

5.2.2 Experimental Signal Acquisition

The spectrometer, an Ocean Optics USB 2000, was used to measure natural emission spectra from 200 to 850 nm, indicating that atomic Na (589.592 nm) and K (769.896 nm) could be measured simultaneously. This technique is capable of time-resolved measurement of the fluorescence of atomic Na and K released from coal and wood combustion. Due to sensitivity of the spectrometer caused by the wide spectrum range (from 200 to 850 nm), the signals of the weak emission spectra results are not detectable for the low SNR. The weak signals can be enhanced by increasing the integration time of the spectrometer. The longer integration time allows the spectrometer collect more emission radiation. However, the enhanced signals, including the enhanced noise, are not reliable owing to the low SNR. The integration time and the signal acquisition interval were set to be 3 milliseconds (ms) and 1 second (s), respectively.

The solid-fuel particles were suspended by a platinum wire (Pt) 0.5 mm in diameter which was located 10 mm above the laminar premixed flame, as shown in **Figure 5-5** and **Figure 5-4**. The particles were placed so as to avoid, reducing heat loss and disturbance through the wire. This arrangement provided a comparatively uniform heating environment in which to

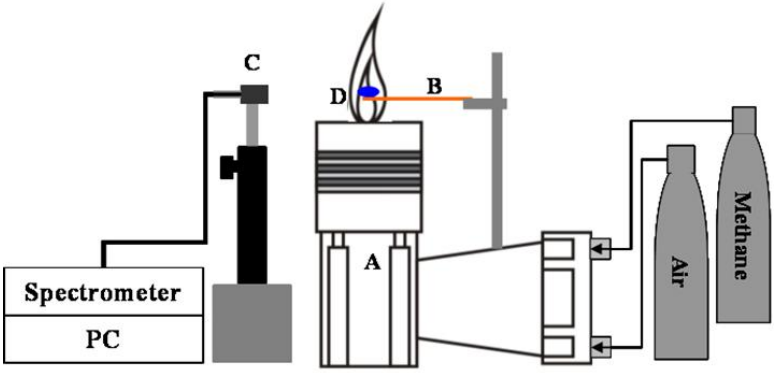

Figure 5-5 Arrangement of the spectrometer (Ocean Optics USB2000, marked as C) and the laminar burner (A) were employed for the measurement of atomic alkalis released from burning solid-fuel particles (D) suspended by a Pt wire (B).

study single particle combustion [11].

To stabilize signal acquisition, an optical fibre detector 0.1 mm in diameter was located 200 mm from the flame and aimed 5 mm above the coal or wood pellets, which reduced any influence of the puffing flames.

5.2.3 Data Acquisition and Processing

The spectrometer is quite sensitive to the background noises so that the intensities of atomic Na and K (at 589.592 nm and 769.896 nm, respectively) were corrected by subtracting an average of 100 seconds of background noise. The methane flame and environment both

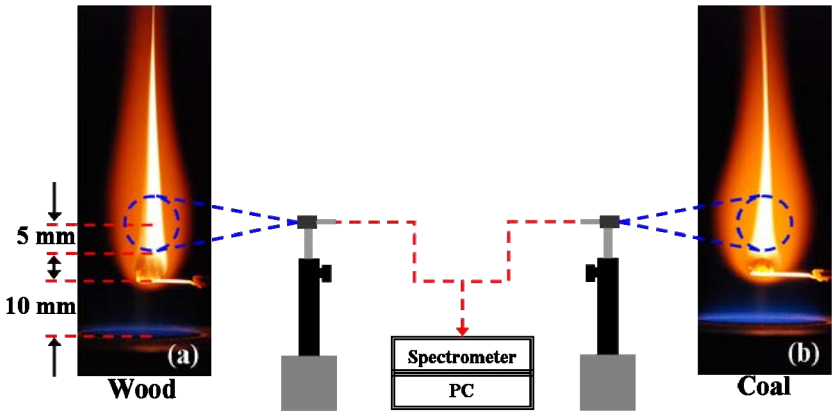

Figure 5-4 Measurement volumes of atomic sodium and potassium on plumes of burning wood and coal particles were represented in the areas of the blue circles aimed 5 mm above the particles. Then particles were suspended 10 mm above the burner.

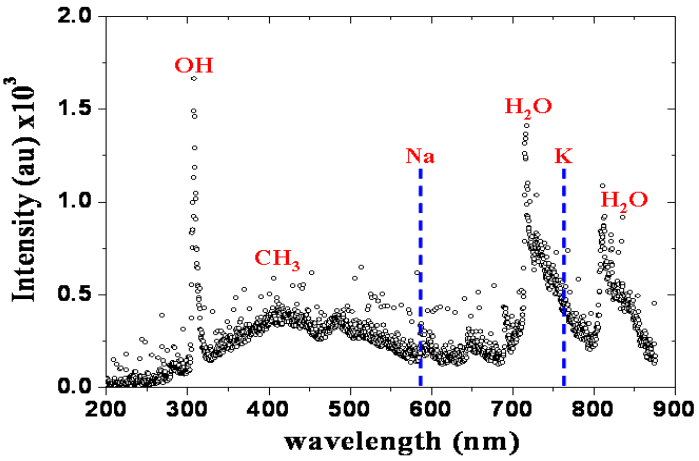

Figure 5-6 Lines of CH radicals (CH_3), hydroxyl (OH) and water (H_2O) from pre-mixed laminar methane flames were recorded with an integration time 300 ms. Dashed lines represent the transitions of atomic Na and K.

contributed the background noise, as shown in **Figure 5-6**. In order to recognize the strong lines of background noise, an integration time of 300 ms was carried out. The spectral lines were recognized as methyl (CH_3), hydroxyl (OH) and water (H_2O) [230]. The lines of CH_3 and OH radicals did not interfere with the lines of atomic Na and K.

Several water lines, however, widely overlapped the lines of atomic Na and K, from 700 to 800 nm, leading to a minor error. Due to the wide range of water line overlap of the D_1 line of atomic K, background noise had to be considered a problem. Water lines with an integration time of 300 ms indicated that spectrum interference might be a significant issue when using laser-induced breakdown spectroscopy owing to the anticipated strong water lines in the plasma.

The spectra during devolatilisation contained significant background emissions along the continuum, leading to uncertainty in the measurement shown in **Figure 5-7**, and hence a correction was required to reduce the effect. **Figure 5-8** revealed that the baseline value used for the correction could be determined by averaging two values (two red lines) across the entire peak of atomic Na and K. Therefore, the intensities of atomic Na and K during the devolatilisation phase were obtained by subtracting the baseline values (the green line shown in **Figure 5-8**).

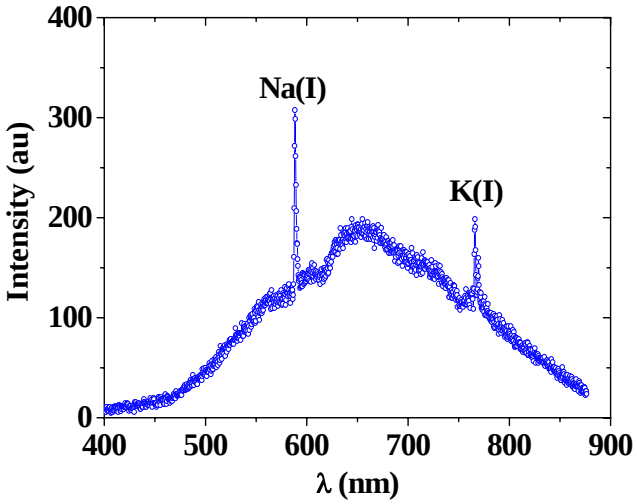

Figure 5-7 Typical emission spectrum of atomic Na (589.592 nm) and K (769.896 nm) during the devolatilisation phase with integration time (3ms); this contains significant background emissions from the continuum.

In order to reduce signal fluctuation and systematic error, the time-resolved intensities of atomic Na and K were obtained by integrating five data points, including the wavelengths at the transitions, instead of choosing only a single intensity at the transitions, as marked in **Figure 5-8**, from point 1 to point 5.

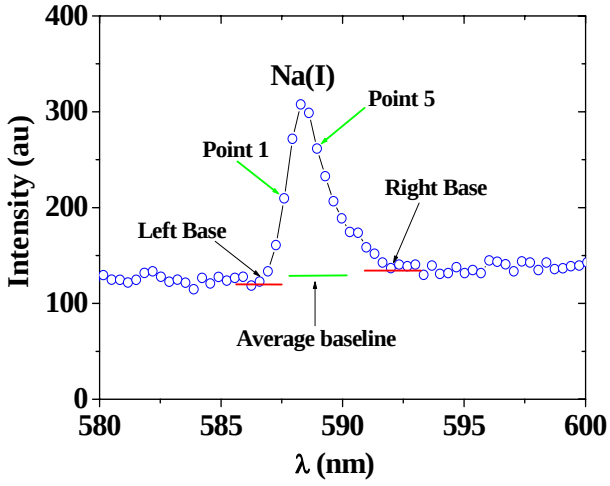

Figure 5-8 The baseline obtained by averaging the left base and right base was employed to correct intensities of atomic Na during the devolatilisation. The time-resolved intensities of atomic Na were integrated by five data points (point 1 to point 5). The same data process was also performed at the intensity of atomic K, as presented in **Figure 5-7**.

5.3 Results and Discussion

In this section, atomic Na and K released from burning particles of Loy Yang Brown coal and pine wood pellets are assessed under four rich equivalence ratios of 1.149, 1.252, 1.287 and 1.336. Four richer conditions, namely 1.149, 1.252, 1.287 and 1.336, have been chosen to provide slow but gradual release rates of alkali species owing to oxygen rich flames leading to faster combustion [11-15] rates and the occurrence of hydrogen reduction favouring the weaker intensities of atomic Na and K [38]. In addition, the emission of atomic Na and K were assessed with the shrinking of burning solid-fuel particles, which might provide insight into the mechanisms of atomic Na and K release.

5.3.1 Empirical Analysis using AES

The major persistent the D_1 lines of atomic Na (589.592 nm) and K (769.896 nm) have been selected for AES measurement. For the purpose of quantitative measurement using AES, the **Eq. 2-1** (mentioned previously in **Chapter 2**) is further considered based on Lomakin-Scheibe formula [184, 185], as shown below:

$$\ln(I_{exp}) = \ln(A) + b \cdot \ln(C_{species})$$

Eq. 5-1

where, I_{exp} is the experimental radiation intensity of atomic Na or K; b is the self-absorption coefficient where b = 1 indicates negligible self-absorption and $C_{species}$ is the concentration of atomic Na or K in the flame. To achieve quantitative AES, a calibration curve is required. However, two difficulties arise, the number density of the target species and the radiation volume that might occur during the calibration process.

Alkali species exist in various forms within the flame so that the determination of the absolute

concentration of Na or K in a specific form is not always possible. van Eyk et al. [11] discovered that atomic Na distribution within the plume of a burning coal particle descends along the flame axis using quantitative PLIF. Although the absolute concentration in a single location can be measured using laser absorption spectroscopy, the radiation volume for the AES measurement contains spatial distribution, which contributes the intensity of the natural emission of the target species. Therefore, the AES technique was only useful and appropriate for detecting atomic Na and K qualitatively in the present experimental arrangement.

5.3.2 Atomic Alkali Release

5.3.2.1 Loy Yang Brown Coal

Atomic Na and K released from burning Loy Yang Brown coal particles using AES were assessed under four rich equivalence ratios of 1.149, 1.252, 1.287 and 1.336 in premixed laminar methane flames, as represented in **Figure 5-9**. Three combustion stages, namely devolatilisation (τ_d), char (τ_c) and ash cooking (τ_a), consistent with atomic Na release reported by van Eyk [11] using quantitative PLIF, were observed. However, due to the significant scattering resulting from sooty substances while using PLIF (the scattering signal possesses the same wavelength, as introduced in **Figure 2-3**), the instantaneous release of atomic Na

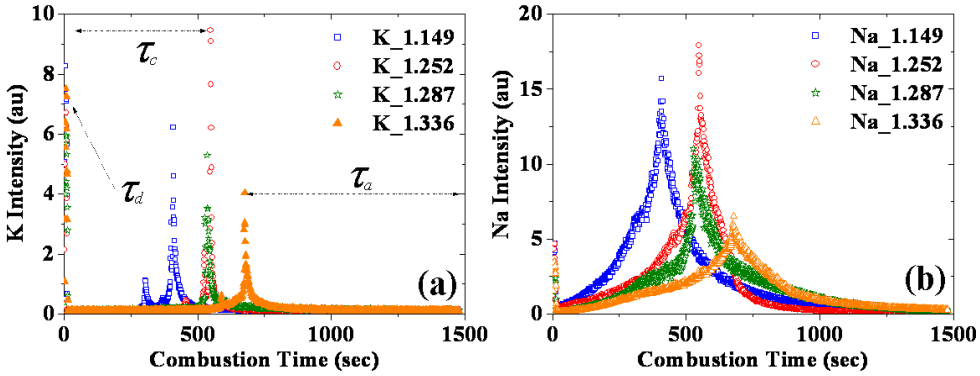

Figure 5-9 Atomic (a) K and (b) Na were released during three stages of the entire combustion process of burning Loy Yang Brown coal particles, namely devolatilisation (τ_d), char (τ_c) and ash cooking (τ_a),with four equivalence ratios of 1.149, 1.252, 1.287 and 1.336.

during the devolatilisation stage was not clear. Besides, unlike the AES technique, the LIF technique is not able to detect the release of atomic Na and K simultaneously.

Intensity (I_{exp}) of natural emission is related to the species concentration ($C_{species}$), as mentioned in the **Eq. 5-1** previously. It is possible to quantify the historical release of atomic Na or K with an appropriate calibration curve, which determines the empirical constant (A) under weak self-absorption, i.e. linear regime (b = 1). However, due to the difficulty of determining concentrations for trace species within the flame, the quantitative measurement using AES was not adequate in the experimental arrangement. The integral intensities of atomic Na and K, therefore, provide a relatively qualitative analysis during combustion. The quantitative measurement of historical $[Na]_{total}$ and $[K]_{total}$ released from burning solid-fuel particles would be investigated in the following chapter using quantitative LIBS.

The three stages and the intensities were found to be associated with the equivalence ratio. The richer equivalence ratios led to a longer combustion process and lower instantaneous intensities of atomic Na and K being released during the three stages. However, the anomaly occurred at the intensities where the equivalence ratio of 1.252 was employed. This might have been caused by the variation between coal particles, which was observed in the preceding chapter using SAES. It is possible that variation in the particles could cause fluctuation in the release rates of alkali species, as these are likely to be related to combustion conditions. The combustion conditions determine the pore structure formed from the inside to the surface of the coal char particles during the devolatilisation phase [146]. Therefore, the equivalence ratios might lead to the similar formation of the core structures during the devolatilisation phase of wood particles. Details of this occurrence will be provided in **Section 5.3.4** using the *Shrinking Core Model*. The anomaly is part of combustion behaviour and is reasonably negligible in the context of the overall scenario.

For all four equivalence ratios, the devolatilisation stage of the burning coal particles consistently last for 12 seconds, as presented in **Figure 5-10**. The flame conditions during the

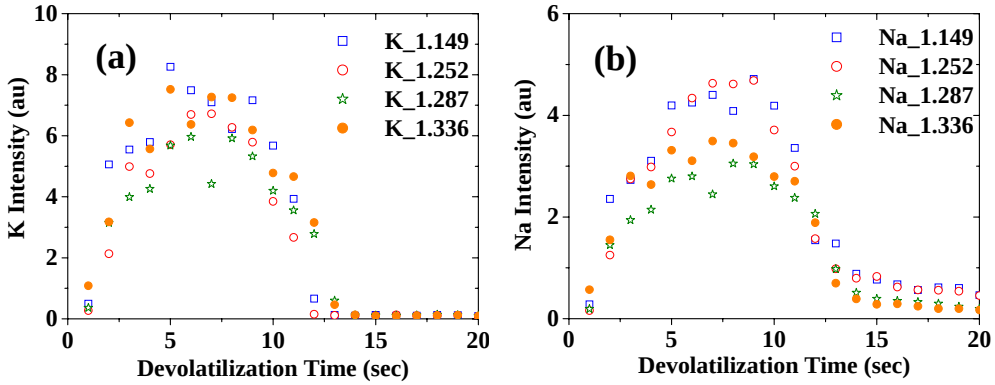

Figure 5-10 Atomic (a) K and (b) Na released from burning Loy Yang Brown coal particles under four equivalence ratios of 1.149, 1.252, 1.287 and 1.336 during the devolatilisation phase which was found to be slightly affected by the equivalence ratios.

devolatilisation stage are crucial for the formation of the pore structures [146, 152], since it relies on the development of channels from which volatile substances are released from the inside to the outside of the coal char particles. This stage of the devolatilisation can be physically considered to be a sintering process that encourages density variation within the entire coal char particle. Denser pore structures mean that lean flames lead to faster combustion rates [146] and hence higher intensities of atomic Na and K are released.

As shown in **Figure 5-10**, atomic Na and K exhibited intensities that were inconsistent with the changing equivalence ratios as described by the shrinkage core model [152]. This is because that the amount of volatile substance in each coal particle is highly variable. To identify the uncertainty of volatile content between coal particles, the total intensities of atomic Na and K were obtained in the devolatilisation phase of 10 experiments with the equivalence ratio of 1.149. Therefore, the variation was evaluated to be about 17%, which could cause significant uncertainty. It should be noted that the variation may be different in other batches of coal particles.

Given that the pore structure is determined during the devolatilisation phase associated with the equivalence ratios [146], it is the critical parameter of the combustion rate of the coal char particles. van Eyk et al. [11] have also demonstrated that the atomic Na that is released is associated with the shrinkage of burning coal char particles until the end of the char stage.

Compared with the experimental results in this study related to particle sizes and flame conditions, the combustion rate with a lean equivalence ratio of 0.8 represented in Ref [11] was faster, indicating that flame condition plays an important role. Moreover, the intensities of atomic Na and K in lean conditions will be weaker owing to the formation of alkali oxide during combustion [38].

The historical records of atomic Na and K released during the char phase under four equivalence ratios are marked in **Figure 5-11**. The intensities and the char stages were found to be associated with combustion conditions. Greater intensities of atomic Na and K were released at the end of the char stage under leaner equivalence ratios. With equivalence ratios between 1.149 and 1.336 intensities and combustion rates were consistent with the observed configuration of the pore structures of the char particles [146].

As well as the pore structures and flame conditions affecting the combustion rates associated with atomic Na and K released from burning coal particles, chlorine (Cl) also plays an important role [231, 232]. When released, atomic Na and K behaved diversely, as shown in **Figure 5-11**. Particle shrinkage accompanied atomic Na release, while atomic K did not release significantly until the end of char stage. Chlorine mobilized alkali species from the inside to the surface of char particles [233], in particular K. In the case of biomass with high

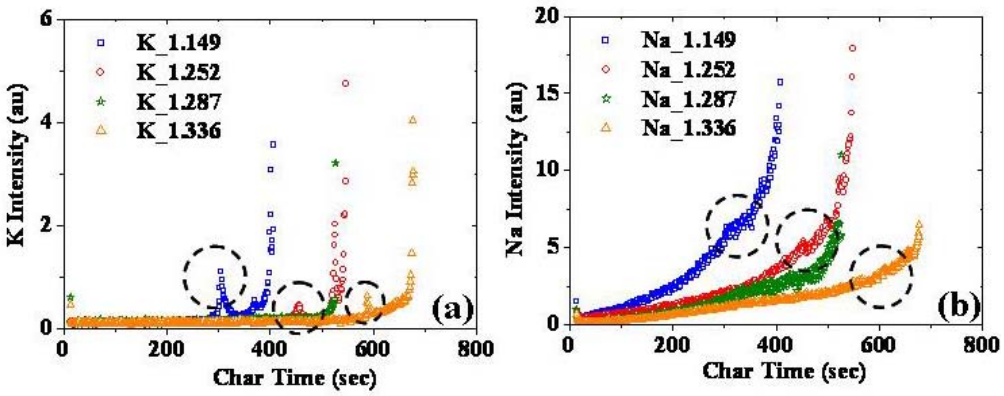

Figure 5-11 Atomic (a) K and (b) Na released during the char stage of coal were assessed under different equivalence ratios of 1.149, 1.252, 1.287 and 1.336. Due to the cracking of coal char particle during char stage, sudden peaks of atomic K occurred while the increased intensities of atomic Na were not intensive.

Cl content, such as straw [177, 178, 234], an enormous amount of alkali species are released and form alkali chlorides when it is burned. Loy Yang Brown coal, however, contains low Cl content and hence the violent release of atomic alkali was not observed in the experiments reported in this thesis. Moreover, the release of atomic K occurred at the end of the char phase while the atomic Na was released with shrinking coal char particles [12].

Given that coal is low in Cl content and that the behaviours of the atomic Na and K diverged from what had previously been observed during the char stage, it appears that Na release can be affected by pore structure favouring combustion rates that lead to more intense release during the char phase. Due to the lack of Cl mobilizing K to the surface, atomic K was not significantly released until end of the char stage.

Few peaks circled in **Figure 5-11** were caused by sudden cracking, indicating that the intensities of atomic K grew without significantly affecting the intensities of atomic Na. This indicates that atomic K was released from the fresh surface of the coal char particles. When the small cracking was burnt out, the intense release of atomic K dissipated. The intense release of atomic K implies that mobile K has been released during the devolatilisation phase and the rest of K needs to be mobilized from the inside to the surface of the char particles by Cl [233]. Therefore, a significant amount of KCl can be found if a Cl additive is entrained in the premixed laminar flame. This might alter the behaviour of the atomic K release during the coal combustion.

Figure 5-12 illustrates the profiles of atomic Na and K released during the ash phase of Loy Yang Brown coal under four equivalence ratios. The ash of coal contains significant silicate and alumina, as shown in **Table 2-1**, and thus the major alkali compounds are Sanidine ($K_2O \cdot Al_2O_3 \cdot 6SiO_2$), Albite ($Na_2O \cdot Al_2O_3 \cdot 6SiO_2$) and Kaolinite ($K_2O \cdot Al_2O_3$). Unlike the intensity of atomic sodium (**Figure 5-12**b), the intensity of atomic K (**Figure 5-12**a) decayed dramatically toward the end of char stage. Atomic K took around 50 seconds to dissipate whilst atomic Na still possessed significant intensity.

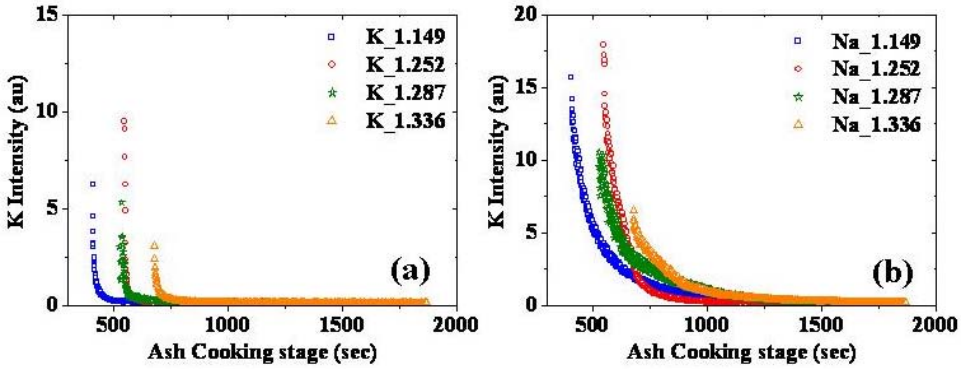

Figure 5-12 Atomic (a) K and (b) Na released during the ash phase of coal were assessed under four equivalence ratios of 1.149, 1.252, 1.287 and 1.336. Given higher temperature occurring in the leaner conditions facilitated faster release rates, the initial intensities atomic Na and K during the ash phase are descending with equivalence ratios.

Although K species content in Loy Yang Brown coal is much less than Na species, it should behave like Na release. Nevertheless, the release of alkali species is dominated by the thermal decomposition. Hence an alkali species was released from the alkali compound while it was experiencing low dissociation energy. This may have been alkali sulphate in the early ash phase when the greater intense intensities of atomic Na and K were observed. Later, atomic Na and K were released in substantial quantities from alkali alumina silicates due to thermal decomposition.

5.3.2.2 Pine Wood Pellet

Using the same experimental arrangement as was used to process the burning coal particles, the atomic Na and K released from burning pine wood particles were also processed and analysed (**Figure 5-13**). Three combustion stages were also observed consistent with results in preceding section. It was noticed that profiles of atomic Na and K released from burning wood particles affected by equivalence ratios, which has been observed in coal combustion (**Figure 5-9**). The longer char stage of the wood combustion occurred while richer conditions were in place. Ash content also increased under richer conditions. The profiles of atomic K released from burning wood particles were observed to be consistent with those of the brown

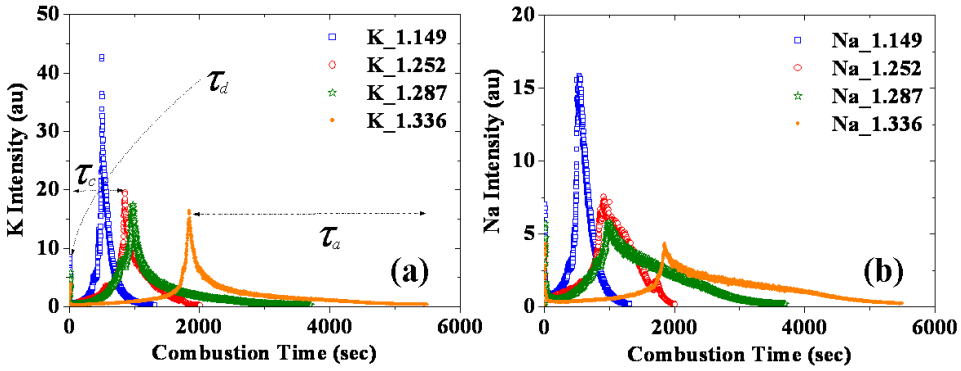

Figure 5-13 Atomic (a) K and (b) Na were released during three stages of the entire combustion process of burning pine wood pellets particles, namely devolatilisation (τ_d), char (τ_c) and ash cooking (τ_a), as presented in (b) with four equivalence ratios of 1.149, 1.252, 1.287 and 1.336.

coal. Atomic K was mainly released at the end of char stage and decayed dramatically at the beginning of the ash phase.

The devolatilisation of the wood combustion under four equivalence ratios is illustrated graphically in **Figure 5-14**. This stage generally lasted for 22 seconds except under equivalence ratio of 1.336 when it lasted for 25 seconds indicating that the volatile substance was released slowly because of the low density of the pore structures [146].

Due to the fact that temperature variation induced violent devolatilisation, the intensities of atomic Na and K during the devolatilisation phase were found to be equivalence ratio dependent. The pore structures were determined by equivalence ratios during the devolatilisation phase [146] which dominated the intense release of atomic Na and K. Other alkali species were released under leaner conditions during the devolatilisation phase, leading to a rapid combustion rate in the char phase. Pine wood ash therefore, contained fewer alkali species (shorter ash cooking stage). These experimental results indirectly prove that the pore structures are equivalence ratio dependent. If the pore structures had been independent of combustion conditions, the period of the devolatilisation would not have been consistent in the combustion conditions.

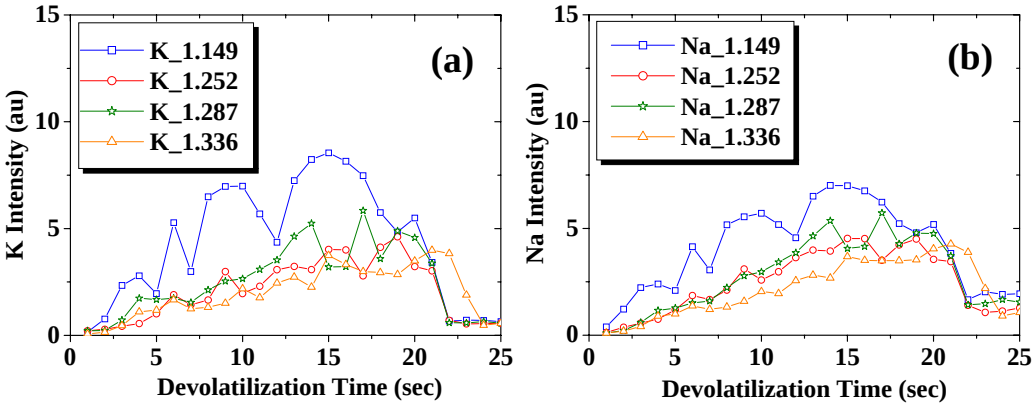

Figure 5-14 Atomic (a) K and (b) Na released from burning pine wood pellets particles under four equivalence ratios during devolatilisation which were found to be affected by equivalence ratios.

Atomic Na and K released from burning particles of pine wood were assessed under four equivalence ratios (**Figure 5-15**), were brown coal particles. The char stage of the pine wood increased with richer conditions indicating that combustion rate decay was associated with combustion conditions. Due to insufficient oxygen in the flame, higher temperature occurred in the leaner conditions [229].

The temperature variation between the equivalence ratios of 1.149 and 1.336 measured by a R-type thermocouple calibrated by radiation law, was approximately 50K. The temperature variation could be relevant to combustion rate. It is insufficient, however, for characterising the char phase of pine wood. The pore structures of the char particles as determined by the

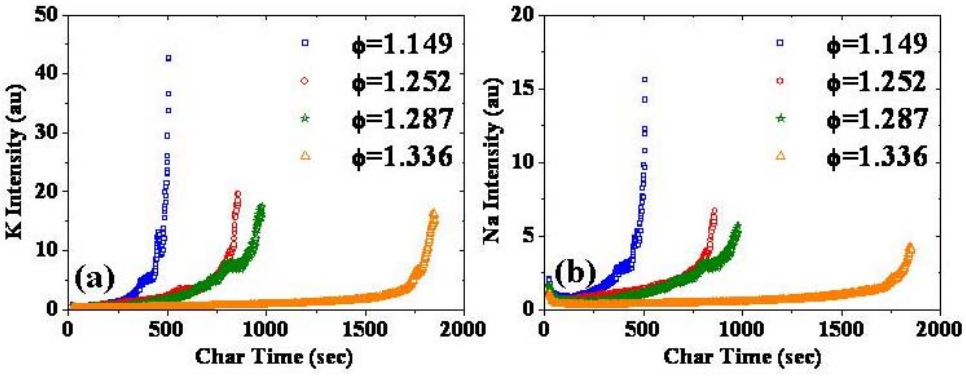

Figure 5-15 Atomic K (a) and Na (b) released during the char phase of burning pine wood particles were assessed under different equivalence ratios of 1.149, 1.252, 1.287 and 1.336.

equivalence ratios [146] performed during the devolatilisation phase takes into account the combustion rates, which coheres with the experimental results of atomic Na and K released from the burning wood particles.

The measured intensities demonstrate a decreasing tendency associated with richer conditions. The atomic Na and K under equivalence ratio of 1.149 were observed to experience the most intense release, lasting around 400 seconds. The slowest release, around 1800 seconds, occurred at condition of 1.336. Release profiles under equivalence ratios of 1.252 and 1.287 behaved differently, which agreed with the trend of the combustion conditions. At 1.252 and 1.287, regardless of the minor variation between the two conditions, the release profiles still behaved in good agreement with the equivalence ratio trend although the uncertainty between solid-fuel particles (8.4 and 3.5 % for coal and wood, respectively) can alter the tendency. This indicates the relationship between equivalence ratios (from 1.149 to 1.336) and combustion rates on char particles of the solid-fuel particles. For the future work, the relationship can be verified with wider range of equivalence ratios.

The time-resolved intensities of atomic Na and K released during the ash cooking stage of pine wood were investigated (**Figure 5-16**). The profiles are consistent with those in coal (**Figure 5-12**). Atomic K decayed dramatically and atomic Na exhibited persistent release rates under all four conditions. For the condition of 1.149, atomic Na and K decayed rapidly,

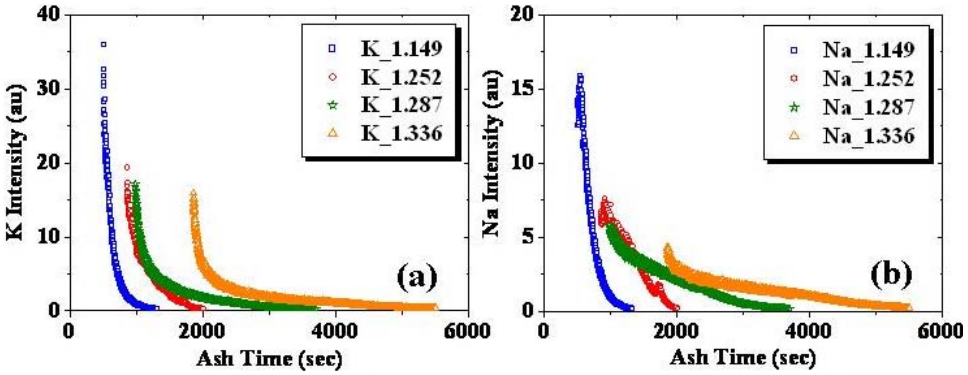

Figure 5-16 Atomic K (a) and Na (b) released during the ash cooking stage of pine wood were assessed under different equivalence ratios of 1.149, 1.252, 1.287 and 1.336 possessing agreement with exponential decay.

indicating that the release rates were affected by higher temperatures and that fewer alkali species were contained in the ash. The release tendency in the condition of 1.252 remained consistent with weaker intensities and took longer to dissipate. The intensities of atomic K under the conditions of 1.287 and 1.336 were observed to be weaker than those in other conditions and consistently lasted longer. Although combustion conditions dominated the behaviour of atomic K release during the ash stage, there was a consistent sharp decay rate in the first 200 seconds and then a linear decay. Therefore, the experimental results suggest that the temperatures of the flames and the content of the alkali species in the ash dominate the release records

5.3.3 Proposed Model of a Burning Particle

The temperature gradient within the entire mass of coal char particles during devolatilisation phase is illustrated in **Figure 5-17**. A temperature inversely proportional to the radius of the char particles was derived using the heat conduction equation on a sphere, as shown in following equations:

$$Q = -\mathrm{k} \cdot A_r \cdot \frac{\mathrm{dT}}{\mathrm{dr}}$$

$$Q \cdot \int_{r_1}^{r_2} \frac{1}{r^2} \cdot \mathrm{dr} = -4\pi \cdot k \cdot \int_{\mathrm{T}_1}^{\mathrm{T}_2} \mathrm{dT}$$

$$Q \cdot (\frac{1}{r_2} - \frac{1}{r_1}) = 4\pi \cdot k \cdot (\mathrm{T}_2 - \mathrm{T}_1)$$

$$\Delta\mathrm{T} = \frac{Q}{4\pi \cdot k} \cdot (\frac{1}{r_2} - \frac{1}{r_1})$$

Eq. 5-2 (a ~ d)

where, A_r is the surface area of a sphere; k is the thermal conductivity coefficient; Q is the heat transfer and T is the temperature at the corresponding radius of char particle, r (r_1 and r_2 corresponding to T_1 and T_2, respectively). Given that high temperature in the sintering process favours high density particles, temperature variation (ΔT) within the entire mass of solid-fuel

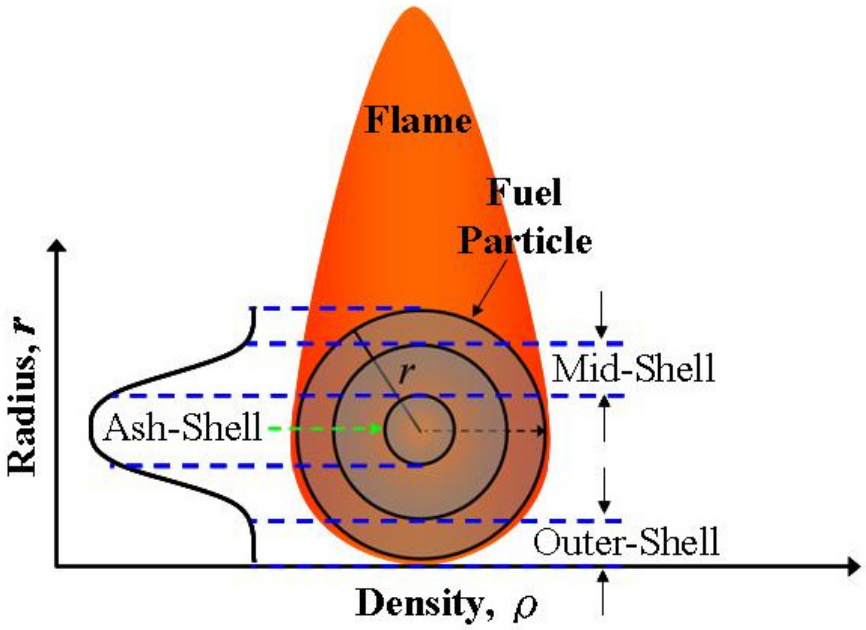

Figure 5-17 Solid-fuel char particles possess different densities in three areas, which are the outer-shell, mid-shell and ash-shell layers. Density decreases along with decreasing radius to the centre of the char particle. The outer-shell is the densest layer owing to being exposed the longest to the sintering process and the highest cooking temperature during the devolatilisation phase.

char particles during the devolatilisation phase causes the density gradient within the char particles to form a multi-layered structure (**Figure 5-17**). The multi-layered structure may have more sub-layers if a detailed model is developed. The ash-shell is the result of burning solid-fuel particles at the end of the char phase and the outer- and mid-shell layers are dominated by the conditions existing during the devolatilisation phase [146]. It should be noted that the three-layer structure is simply a proposed assumption. It demonstrates the general behaviour of a rapid sintering process on a small particle. The densities of the three shells decrease with decreasing radius. The outer-shell is the densest layer owing to the longest sintering process with the highest cooking temperature during the devolatilisation phase. A low sintering temperature results in a loose structure in the mid-shell layer and the loosest layer in the ash-shell layer.

Each shell may be precisely modelled using well-defined mechanisms. Each shell may contain multiple stages, owing to the minor effects of temperature variation, as shown in **Eq.**

5-2d, especially for the mid-shell. For rich conditions, it takes longer to burn char particles. The slower combustion rate leads to longer cooking that shifts the boundary between the outer- and mid-shell of the char particles because the outer flame continues heating the particles. This indicates that the mid-shell layer becomes thinner during slow combustion. The heating is considered to be sintering. The combustion time determines the thickness of the outer- and mid-shell layers, which means that part of the mid-shell, forms a thin layer with a higher density. The density of the layer is expected to be between the original densities of the outer- and mid-shell layers when the outer-shell layer is sintered and formed at 1800 K, the temperature of volatile flame (in the devolatilisation stage using fitting of Planck's law), as indicated in **Figure 5-18**, instead of 1500 K for the methane flame. Therefore, the structure of mid-shell layer may be slightly or significantly different form the original layer. This difference can be observed in the particle shrinking rate, which will be introduced in a later section. Due to the minor temperature effect during the cooking process, the outer- and ash-shell layers are generally constant.

Given that the structure of the coal char particle was determined during the devolatilisation

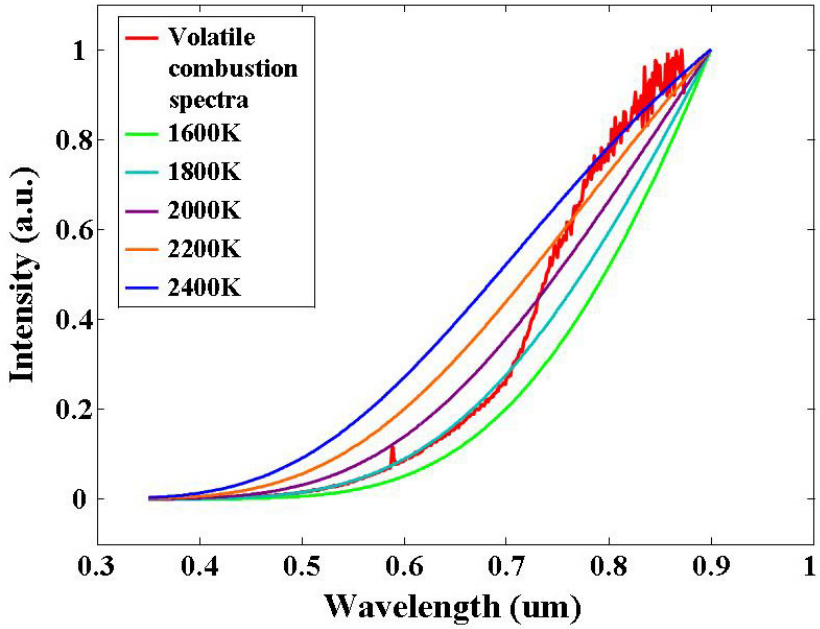

Figure 5-18 Temperature (1800 K) during the devolatilisation phase is investigated by fitting the radiation of continuum during the volatile combustion using Planck's Law.

phase, the general combustion behaviour will not be altered during the following combustion of char stage. The applied methane flame (~ 1500 K) provides continuous heat to the coal char particles while the particle size is shrinking and hence the boundary between the outer- and mid-shell layers shift. The combustion of the mid-shell layer occurs whilst the overall combustion rate overtops the effect of density transformation. Therefore the combustion rate is highly equivalence ratio dependent. The particle size of the solid-fuel is a crucial factor in terms of varying the combustion rate. The critical diameter of the coal particle has been reported as 80 μm [152], which should be similar for the solid-fuel particles. Although the critical size of the selected solid-fuel particles in this study was not verified, the size (3 or 4 mm) was much greater than 80 μm. The temperature gradient impacting particles below the critical diameter is considered to be uniform. It is not necessary, therefore, to consider the three-layered structure with the particles. For particles above critical diameter, the pore structures and equivalence ratio dominate the combustion rates of the char particles.

5.3.4 Shrinking Core Model

The solid-fuel particles of Loy Yang Brown coal and pine wood used for this study were pre-treated to produce spherical particles with diameters of 3 mm for coal and 4 mm for wood. Heat transfer through the solid-fuel particle has been described based on a standard heat conduction equation, as was shown in **Eq. 5-2**, which demonstrates temperature differences within a spherical fuel particle. However, it is insufficient to describe mass loss for burning solid-fuel particles.

For burning spherical particles [152], it is appropriate to employ a shrinking core model to describe reactions at the moving core surface [160, 235, 236], as presented below:

$$\rho \cdot c \cdot \frac{\mathrm{d}T}{\mathrm{d}t} = \frac{1}{r^2}\frac{\mathrm{d}}{\mathrm{d}r}(r^2 \cdot k_p \cdot \frac{\mathrm{d}T}{\mathrm{d}r}) + \Delta \mathrm{H} \cdot \frac{\mathrm{d}\rho}{\mathrm{d}t}$$

$$-k_p \cdot \left.\frac{\mathrm{d}T}{\mathrm{d}r}\right|_{\mathrm{r=R}} = h \cdot (T|_{r=R} - T_g) + \varepsilon \cdot \sigma \cdot (T^4 - T_g^4)$$

$$\left.\frac{\mathrm{d}T}{\mathrm{d}r}\right|_{r=0} = 0, \quad T_c = T|_{r=r_c}, \; T_s = T|_{r=R}, \quad T = T|_{r=r}$$

$$T(r,t) = T_0$$

Eq. 5-3 (a ~ d)

where;

T : the local particle temperature (K) T_g : the gas temperature (K)

T_0 : the initial particle temperature (K)

T_c : the temperature at core surface (K)

T_s : the temperature at particle surefce (K)

r_c : the core radius (m) r : the radial distance (m)

R : the particle radius (m) ρ : the particle solid density ($\mathrm{kg \cdot m^{-3}}$)

c : specific heat ($\mathrm{J \cdot kg^{-1} \cdot K^{-1}}$) k_p : thermal conductivity ($\mathrm{W \cdot m^{-1} \cdot K^{-1}}$)

ε : the emisivity σ : the Stefan - Boltzman constant ($\mathrm{W \cdot m^{-2} \cdot K^{-2}}$)

h : surface convection coefficient ($\mathrm{W \cdot m^{-2} \cdot K^{-1}}$)

This model characterises the diffusion of chemical species from their outer spherical boundaries through the spherical annulus (the shrinking layer). The reaction occurs at the unconsumed core surface, as indicated in **Figure 5-19**. It is assumed that the total volume conserves and hence the shrinking layer remains constant. In a burning fuel particle, the product layer grows, forming ash, as the particle shrinks. The model divides the solid-fuel particles into N shells to describe particle shrinkage during the devolatilisation and char phases. The density and composition of each shell change as the burning particle progresses so that the local shrinkage rate (dρ/dt), local thermal conductivity and specific heat change. Therefore, the overall histories of weight loss rate can be described.

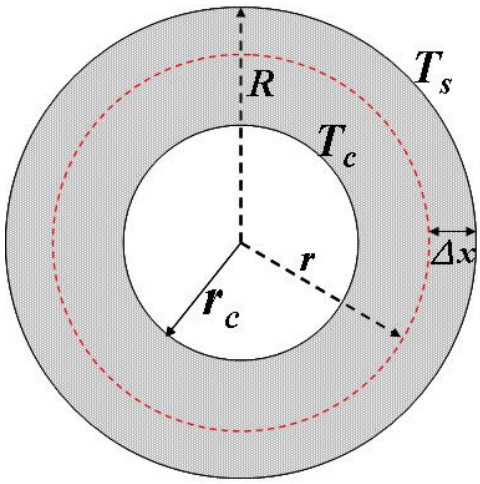

Figure 5-19 Illustration demonstrates the shrinking core model for burning solid-fuel particles. T_c and T_s represent the temperature of core and surface. $\boldsymbol{r}$ and $\boldsymbol{r_c}$ are the radii of reaction surface and unconsumed core, respectively. R is the radius of a virgin particle and Δx is the shrinking layer.

5.3.5 Pore Structures

Pore structure is formed in activated carbon during devolatilisation [146] , and the pores act as channels where gaseous and liquid substances (volatile matters) are transported from the inside to the outside of the particles. Combustion conditions determine the formation of three general types of pore structures: micro-, meso- and macro-pores, which are categorized by their radius. Generally, a radius less than 1 nm is defined as a micro-pore and between 1 ~ 25 nm and greater than 25 nm are defined as meso- and macro-pores, respectively. Granular char basically has macro-pores which are not found in ground activated carbon. Where macro-pores are formed, they cut through meso- and micro-pores (**Figure 5-20**) and are the major conduit for liquid transport. An oxygen-rich environment results in violent devolatilisation formation of large numbers of meso- and macro-pores within char particles, and, therefore, fast char combustion.

Figure 5-20 Illustration of three types of pore structure in char particles, namely micro-, meso- and macro-pores; a radius less than 1 nm is defined as micro-pores and between 1 ~ 25 nm and greater than 25 nm are defined as meso- and macro-pores, respectively.

Equivalence ratios influence the effects of pores on the emission of alkali species during combustion [146]. Although the pore densities of the char particles were not measured in this study, the effects of the pore structures were assessed by conducting a simple experiment. This can provide the indirect investigation of pore formation in char particles. The concept of the simple experiment is to investigate how equivalence ratios affect the formation of pore structures during devolatilisation. During the devolatilisation phase of the Loy Yang brown coal and pine wood pellets, pore structures were generated under the initial equivalence ratio (1.149 or 1.336) and the combustion condition was switched to the other three conditions. If the pore structures were not affected by the equivalence ratios, the intensities of atomic Na and K before and after the switching under the same equivalence ratio (1.149 and 1.336 in particular) should be similar.

The variation in intensities of atomic Na and K under the equivalence ratios of 1.149 and 1.336 before and after the 60^{th} second could be used to verify the effect of the pore structures on atomic Na and K release. The stronger atomic Na and K were released from char particles treated under the initial equivalence ratio of 1.149, as shown in **Figure 5-21** (a) for coal particles and (c) for wood particles before the 60^{th} s, compared with those intensities for the equivalence ratio of 1.149 presented in **Figure 5-21** (b) and (d), after the 60^{th} s. On the other hand, the intensities for the initial equivalence ratio of 1.336, as presented in **Figure 5-21** (b)

and (d) before the 60th s, are much weaker than those in **Figure 5-21** (a) and (c) after the 60th s. These observations indicate that the equivalence ratio affects the formation of the pore structures during devolatilisation.

The intensities of atomic Na and K became stronger when the flame condition was switched to the richer input at the 60th s, as shown in **Figure 5-21** (a) and (c), and weaker when switched to the leaner input at the 60th s, as shown in **Figure 5-21** (b) and (d). It should be noted that the high intensities of atomic Na and K [**Figure 5-21** (a) and (c)] are also a response to hydrogen reduction [38, 237]. The intensity of atomic Na demonstrates behaviour consistent with the results in Ref. [11]. Given the similar properties of alkali metals, it was anticipated that atomic K would display the same tendency. The variation between the release of atomic Na and K for char particles of coal and wood indicates that the equivalence ratio

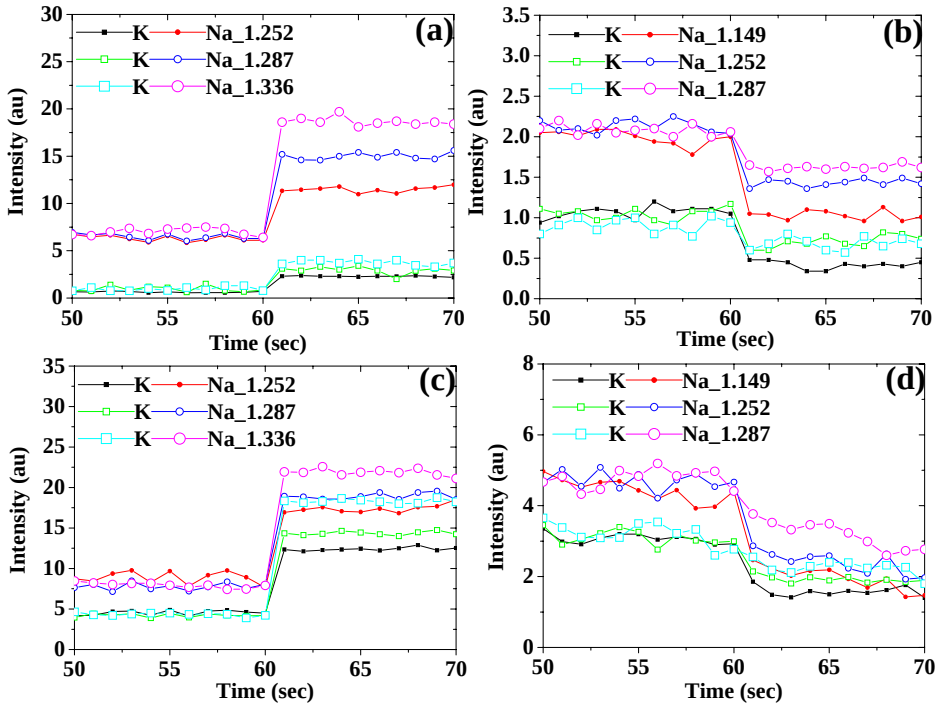

Figure 5-21 Char particles of (a) coal and (c) wood were treated under Φ = 1.149 and under Φ = 1.336 in (b) and (d). The initial condition (1.149 or 1.336) was switched to the other conditions at the 60th second. The intensities of atomic Na and K significantly increased when the condition was switched from 1.149 to three richer ones, as shown in (a) and (c). One the other hand, the intensities decreased when the condition was switched from 1.336 to three leaner ones, as shown in (b) and (d).

employed during the devolatilisation dominates the release rates of alkali species. Therefore, the intensities of atomic Na and K represent a good method by which to verify the effect of the pore structures without conducting a complicated porosity measurement. The method can only be used to investigate the effect on the formation of pore structures within the limited combustion conditions. However, the porosity of a char particle cannot be measured using the method. The equivalence ratio may also dominate the combustion rate, which is discussed in the following section.

5.3.6 Combustion Rate

Combustion rates of burning solid-particles are related to combustion conditions [146] and particle sizes [152]. Therefore, the combustion rates of the Loy Yang Brown coal and pine wood particles associated with their shrinking were investigated using a Canon D80 single-lens reflex camera. The investigation of particle shrinkage is based on the *x*-*y* ratio of the particle, as shown in **Figure 5-22**. The volume of raw particle, termed as $V_{x\text{-}y}$, can be determined by the following equation:

$$V_{x-y} = \frac{4\pi}{3} \cdot \left\{ \left[\left[\left(x/2 \right)^2 + \left(y/2 \right)^2 \right] / 2 \right]^{1/2} \right\}^3$$

Eq. 5-4

where, *x* and *y* are the geometric diameters of the particle in the x and y directions, as shown in **Figure 5-22**. The values of *x* and *y* as the two-dimensional length of raw particles used in this study are presented in **Table 5-2**. The images of solid-fuel particles in the stages of devolatilisation and char were taken every second and five seconds, respectively. The time-resolved shrinking solid-fuel particles have been recorded, as shown in **Figure 5-23**, which shows the shrinking coal and wood particles during three combustion phases. The shrinkage results of burning solid-fuel particles provide useful insight into the shrinking rates associated with equivalence ratios.

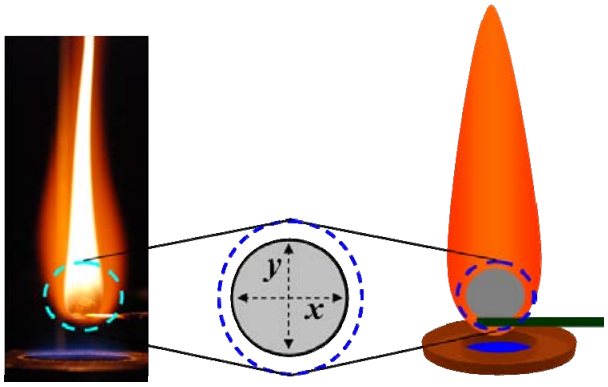

Figure 5-22 Time-resolved particle shrinkage is based on the measurement *x*-*y* ratio. The raw particle volume can be determined using **Eq. 5-4**.

The size variation between the coal and the wood particles is 8.4% and 3.5%, respectively, which leads to a certain variation in the amount of shrinking particle. The devolatilisation time of the burning coal and wood particles using four equivalence ratios has, however, been identified to be consistently 12 and 22 seconds, respectively, except for 25 seconds for burning a wood particle under the equivalence ratio of 1.336. The variation in the amount of shrinkage was therefore, expected. **Table 5-3** outlines the amount of shrinkage experienced by the burning coal and wood particles during the devolatilisation phase. It was observed that the amount of shrinkage (mm^3) during the devolatilisation phase was not consistent owing to the variation in the raw solid-fuel particles. It proved difficult to correlate the combustion

Table 5-2 Sizes of raw solid-fuel particles presented in geometric directions in *x*- and *y*-axis can be further employed to estimate the volume of solid-fuel particle.

Raw Particle	Φ	x(mm)	y(mm)
Coal	1.149	3.2	3
	1.252	3.1	2.9
	1.287	3.3	3.3
	1.336	3.1	3.1
Wood	1.149	4.1	3.9
	1.252	4.2	3.9
	1.287	4.1	4.1
	1.336	4.2	4

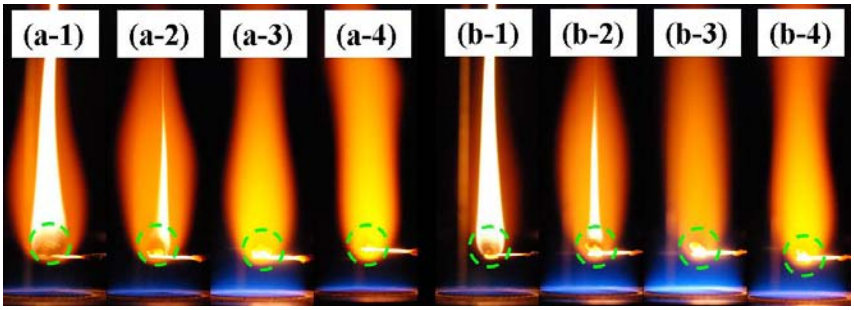

Figure 5-23 Images shows the shrinking burning particles of (a) pine wood (b) brown coal in stages of (1) beginning (2) end of the devolatilisation phase and (3) and (4) periods of char phase. The green circle indicates the location where the solid-fuel particle was burnt.

conditions with the amount of shrinkage. In order to eliminate variations in particle size, the shrinking results can be normalized by the volume of a raw solid-fuel particle to represent the time-resolved shrinking percentage (%/s).

The time-resolved particle shrinkage during the devolatilisation of coal and wood under four equivalence ratios was investigated, as illustrated in **Figure 5-24**. It was found that the volume of the virgin solid-fuel particles decreased during devolatilisation 10% in the case of brown coal and 15% in the case of pine wood. This remained consistent across four equivalence ratios. The variation is the result of the nature of the constituents of the solid-fuel particles, particularly the amounts of fixed carbon and moisture. While the contents of fixed carbon and moisture in wood-based biomass are generally 50% in dry basis and 50% by

Table 5-3 Amount of shrinkage of burning coal and wood particles during the devolatilisation phase shows the variation between solid-fuel particles.

Φ		1.149	1.252	1.287	1.336
Coal	Raw Volume	44.2	40.1	48.6	42.0
	Volume After τ_d	40.1	36.1	43.8	38.0
Shrinking volume (mm^3)		4.1	4	4.8	4
Wood	Raw Volume	94.9	98.6	102.1	102.2
	Volume After τ_d	79.8	83.7	85.9	87.5
Shrinking volume (mm^3)		15.1	14.9	16.2	14.7

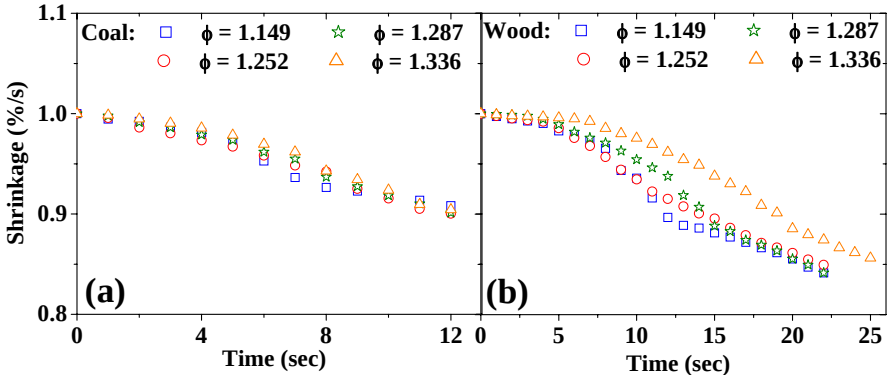

Figure 5-24 Burning particle shrinkage of (a) brown coal and (b) pine wood during the devolatilisation with four equivalence ratios of 1.149, 1.252, 1.287 and 1.336 reveal that the devolatilisation of wood particles are significantly affected by equivalence ratios.

weight, respectively, moisture content in coal is around 10% by weight and fixed carbon is generally 80% in dry basis. The content of volatile substance in wood-based biomass is, therefore, a highly volatile substance with a lower heating value. In addition, as presented in **Figure 5-24**, the shrinking rate of wood is more sensitive to equivalence ratios. The devolatilisation of pine wood lasts for 25 seconds under the equivalence ratio of 1.336. The particle shrinkage of coal during the devolatilisation is nearly independent of the equivalence ratios (**Figure 5-24**a). Unlike coal devolatilisation, multiple sub-stages of wood devolatilisation were observed (**Figure 5-24**b). However, it is difficult to interpret the difference between the devolatilisation of coal and wood in the current study. Judging from the nature of coal and wood particles, the difference may be related to their ingredients, in particular the three main compositions of wood, hemi-cellulose, cellulose and lignin.

Figure 5-25 represents the shrinkage of burning char particles for brown coal and pine wood under four equivalence ratios of 1.149, 1.252, 1.287 and 1.336. Due to the effect of the equivalence ratios used during the devolatilisation, combustion rates were determined by the pore structures [146]. The shrinkage profiles demonstrate the multiple stages consistent with the temperature gradient introduced in **Eq. 5-2**, larger particles leading to higher temperature variation, and greater density variation within the char particles, as was illustrated in **Figure 5-17**. Generally three distinct regions can be observed in the shrinkage of solid-fuel particles.

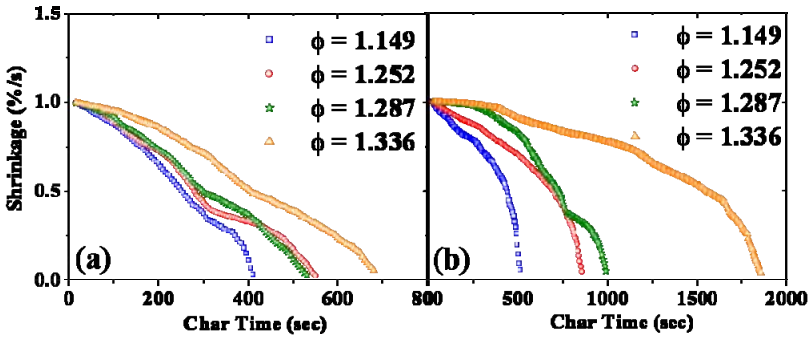

Figure 5-25 Particle shrinkage rates of (a) brown coal and (b) pine wood during the char stage with four equivalence ratios were investigated. The variation between shrinkage rates caused by equivalence ratio of 1.336 is significant due to the pore structures.

The first two regions became longer as conditions became richer. The last stage remained similar. Due to the burning process, the entire char particle is continuously heated by the outer methane flame leading to a variation in the densities within the particle allowing the longer burning process can facilitate the density variation.

The variation in density is significant in the mid-shell layer because the flame temperatures of the four equivalence ratios are between 1450 ~ 1500 K and the temperature of volatile flame for coal and wood is about 1800 K, estimated using Planck's Law, as shown in **Figure 5-18**. This results in the highest density being found in the outer-shell layer. The density induced by the methane flame, therefore, is not as high as the density in the outer-shell layer. Except for the major change in the shrinking rates in the three regions, it is evident that the shrinking rates change in the mid-shell layer for both coal and wood char particles. Moreover, the shrinkage of burning solid-fuel particles also provides a correlation between combustion rates and the release of atomic Na and K, as discussed in the following section.

5.3.7 Combustion Stages

5.3.7.1 Loy Yang Brown Coal

Time-resolved release of atomic Na and K during the burning of the solid-fuel particles was also observed. Therefore, the release of atomic Na and K ought to be associated with the shrinkage of solid-fuel particles. **Figure 5-26** demonstrates the linearity of shrinking coal particles, indicating that a global stage occurs in the devolatilisation of burning brown coal. The shrinkage rate was estimated to be approximately 1% per second for virgin coal particles with four equivalence ratios (10% during the devolatilisation phase, which lasts for 12s). The intensities of atomic alkali species were not distinguished, indicating that the release amounts of atomic alkali species during the devolatilisation phase might be independent of equivalence ratios.

Figure 5-27 demonstrates the shrinkage of coal char particles associated with the release of atomic Na and K with four equivalence ratios of 1.149, 1.252, 1.287 and 1.336. Three sections of time-resolved shrinkage for coal char particles were determined by conducting the derivative of the shrinking profiles presented in **Figure 5-25**. Each stage was determined based on the sharp volume loss. This provides preliminary determination of each combustion stage of char particles. However, the precise boundary between each stage needs to be verified in the future work. As introduced in **Figure 5-11**, longer periods of char stages occurred with

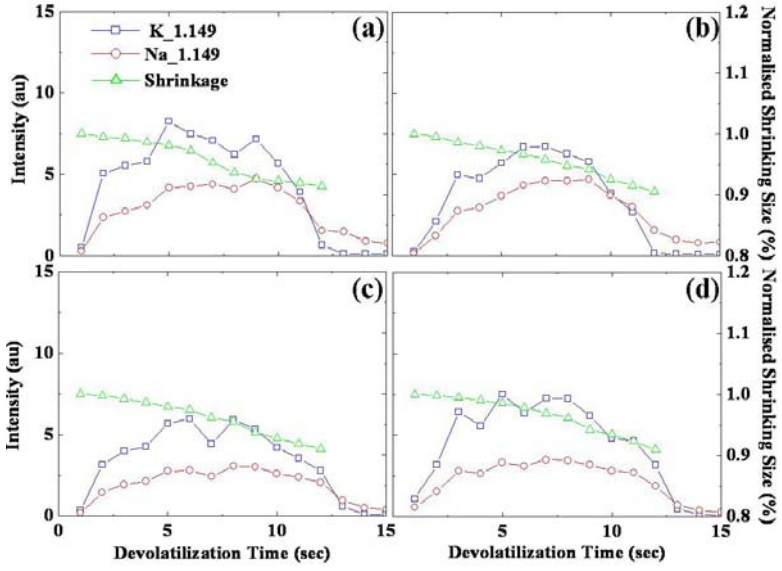

Figure 5-26 Releases of atomic Na and K during devolatilisation associated with shrinkage of coal particles under four equivalence ratios of (a) 1.149, (b) 1.252, (c) 1.287 and (d) 1.336. The shrinkage revealed the consistent linearity among the four combustion conditions.

Table 5-4 Periods of three sub-stages for coal char combustion under four equivalence ratios; it was found that the sub-stages became longer associated with richer combustion conditions and the sub-stage III remained similar.

	Φ	1.149	1.252	1.287	1.336
Section (sec)	I (Sec)	50	110	110	140
	II (Sec)	310	310	370	480
	III (Sec)	50	60	60	60

richer conditions and the burning char particles followed the three-layer combustion model, as presented in **Figure 5-17**. Section I, II and III of the graphs in **Figure 5-27** are three sub-stages of coal char combustion, as mentioned in **Figure 5-17**, outer-, mid- and ash-shell layers, respectively. The shrinking rates of coal particles were used to determine the three sub-stages of burning coal particles. The summary for the three sub-stages is presented in **Table 5-4**. The shrinkage of the coal char particles was consistent with the release profiles of atomic Na and K (as shown in **Figure 5-11**). Section I was similar for richer equivalence ratios, except for Φ = 1.149. Moreover, Section I under Φ = 1.336 last longer. This is because the low flame temperature and the low porosity during this sub-stage lead to a slow combustion rate, as recorded in Section I, while the outer-shell layer is formed. Combustion recorded in Section II was found to last longer and was associated with richer conditions. Section III on the graphs represents a combustion sub-stage that was found to be independent of equivalence ratios, and consistently around 50s combustion time.

One particularly interesting result for Section II was observed. During the combustion recorded in Section I, the char particle is continuously heated and that is considered to be the sintering process that enhances the density gradient within the mid-shell layer. The enhanced density varied the local shrinkage rate, $d\rho/dt$, so that changes to the slopes of the shrinking rates were observed. During the combustion of Section II, the density change would alter the local combustion rate. Therefore, the combustion rate in Section I varied frequently. Not only the porosity but also the enhanced density dominates Section II. Hence enhanced density corresponds with the longer period of Section II.

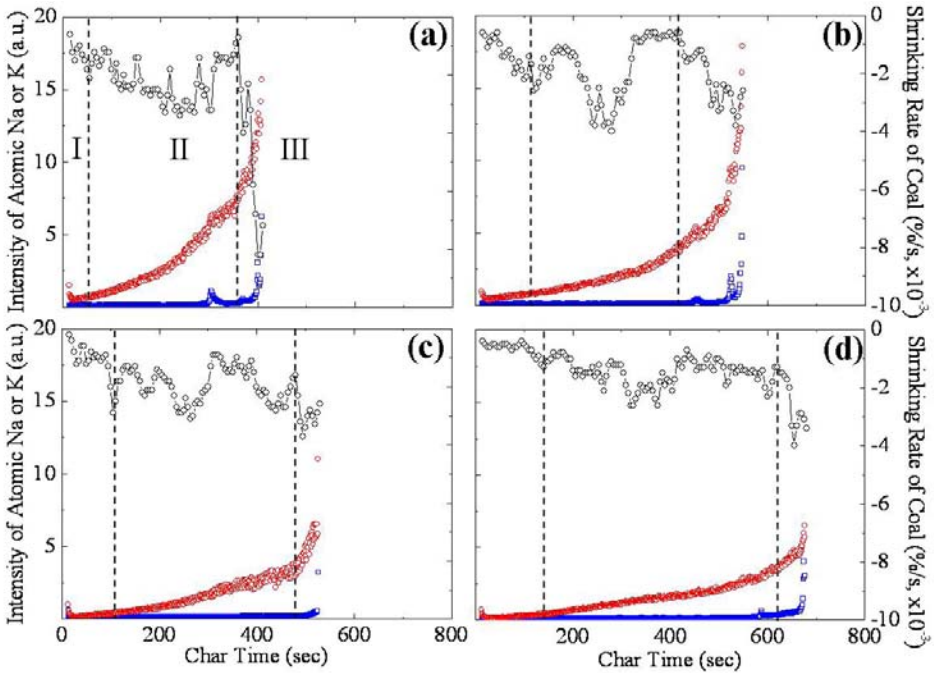

Figure 5-27 Three sections of combustion process for coal char particles associated with shrinking particle sizes (black dots) and the release of atomic Na (red dots) and K (blue dots) were observed under four equivalence ratios of (a) 1.149, (b) 1.252, (c) 1.287 and (d) 1.336. The purple circles in (a), (b) and (d) represent the intense atomic Na and K release when cracking occurs.

5.3.7.2 Pine Wood Pellet

The preceding section described how atomic Na and K release associated with burning coal particles was a global and a three sub-stage process during the devolatilisation and char stages, respectively. The three-layer model was employed to describe the historic emission of atomic Na and K and the shrinkage rates of burning coal particles. To identify atomic Na and K release associated with the combustion stages of the wood particles, the same model (as seen in **Figure 5-17**) was again applied.

Figure 5-28 demonstrates atomic Na and K release with simultaneous time-resolved particle shrinkage during devolatilisation under four equivalence ratios. Unlike the devolatilisation of brown coal, the three sub-stages of the shrinkage of the wood pellets during devolatilisation could be observed and the atomic Na and K release could be correlated with the particle

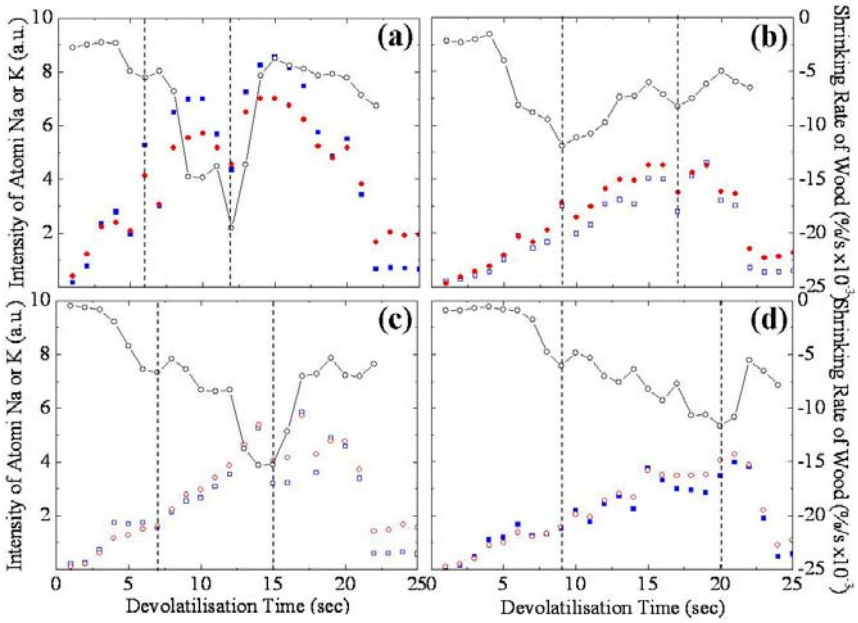

Figure 5-28 Simultaneous measurement of atomic alkali species release (blue for atomic K and red dot-lines for atomic Na) and shrinkage of wood particle (green dot line) during the devolatilisation phase with four equivalence ratios of (a) 1.149, (b) 1.252, (c) 1.287 and (d) 1.336

shrinkage. When studying the characteristic behaviour of burning wood particles, the kinetic properties of wood pyrolysis should be taken into account. The three sub-stage devolatilisation of the burning wood particles revealed properties of wood combustion which have been investigated using TGA [156]. Due to the kinetic properties of wood degradation, wood pyrolysis during the devolatilisation is associated with hemicellulose, cellulose and lignin degradation [153]. This indicates that the pyrolysis energies required for the combustion of hemicellulose, cellulose and lignin follow the kinetic properties of the wood. A sequential reaction model has been proposed to describe wood devolatilisation, as presented below:

$$\begin{aligned} A &\rightarrow \alpha \cdot B + (1-\alpha) \cdot \mathrm{V}_1 \\ \alpha \cdot B &\rightarrow \beta \cdot C + (\alpha-\beta) \cdot \mathrm{V}_2 \\ \beta \cdot C &\rightarrow \gamma \cdot D + (\beta-\gamma) \cdot \mathrm{V}_3 \end{aligned}$$

Eq. 5-5

where A is virgin wood; B, C and D are charred residues; V_1, V_2 and V_3 are lumped species representative of volatile species; α, β and γ are stoichiometric coefficients expressed as

Table 5-5 Periods of three sub-stages of the wood devolatilisation associated with four equivalence ratios. Section I and II became longer in richer conditions (compared to Φ = 1.149) consistent with that reported by Yu et al. [146]. However, Section III became shorter associated with richer conditions.

Φ		1.149	1.252	1.287	1.336
I	(Sec)	6	9	7	9
II	(Sec)	6	8	8	11
III	(Sec)	10	5	7	4

fractions of original wood. A loss of mass is associated with heat and permanent gases [238] released during pyrolysis. This indicates that the energies required for three compositions of wood during combustion are different. Therefore, the kinetic model is applicable when explaining the loss of mass during the experimental burning of wood particles. The shrinking core model provides a feasible reason for the loss of mass during the devolatilisation of burning wood particles.

The intensities of atomic Na and K were found to be stronger at the end of each sub-stage and the strongest release occurred at the lignin combustion. Given that the pore structures formed at the beginning of the devolatilisation dominate the combustion rates, the slow devolatilisation occurred with the richer equivalence ratio. Three sub-stages of wood devolatilisation were observed and related to the variation of equivalence ratios, as summarized in **Table 5-5**. Section I, **Table 5-5**, records the fact that the slowest process occurs under the equivalence ratio of 1.336. The intensities of atomic Na and K were found to be similar across four equivalence ratios. The combustion rate in Section II is fast, with an equivalence ratio of 1.149 owing to the porosity determined at the beginning of the devolatilisation [146]. The periods of Section I with Φ = 1.149 and 1.336, which are six and nine seconds, respectively, match the property of porosity. This also demonstrates that the pore structures formed during the devolatilisation phase under leaner conditions leads to the faster combustion rate [146]. The intensities of atomic Na and K become stronger than those in Section I. The highest intensities of atomic Na and K were observed in Section III. Due to

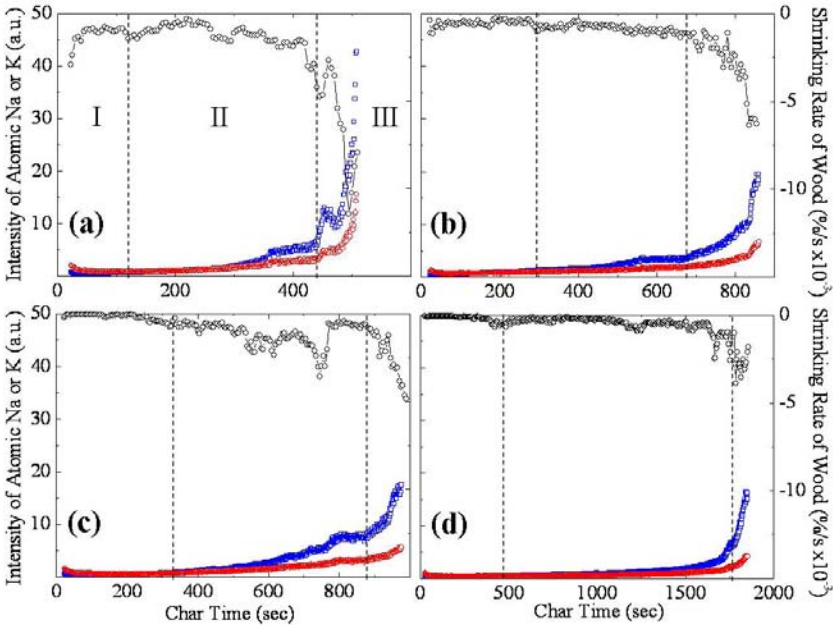

Figure 5-29 Time-resolved atomic Na (red dots) and K (blue dots) released during wood char combustion particle shrinkage rate (black dot line) under four equivalence ratios of (a) 1.149, (b) 1.252, (c) 1.287 and (d) 1.336; Section I, II and III are the three sub-stages of the wood char phase.

the longer periods of Section II under equivalence ratios of 1.252, 1.287 and 1.336, more volatile matter was released so that the shorter periods of Section III occurred.

The three sub-stage model (introduced in **Figure 5-17**) successfully describes the loss of mass from burning brown coal particles. **Figure 5-29** illustrates the tendency for mass to be lost from burning wood particles releasing atomic Na and K under four equivalence ratios. The summary of three-shell layers for wood char combustion under four equivalence ratios is presented in **Table 5-6**. Except for shrinking core model applied to describe mass loss from burning wood char particles, the kinetic properties are also able to predict the behaviour of mass loss during wood char combustion [153, 155, 156]. Kinetic models have been developed to predict wood char pyrolysis with a global step [153] or multiple steps mechanisms [155]. The global mechanism predicts general behaviour but cannot provide a detailed scenario. The multiple steps mechanism performs the better prediction of wood char pyrolysis. Hence a model with three consecutive steps has been employed here [155], as presented in the following equation:

$$A \rightarrow V_1; B \rightarrow V_2; C \rightarrow V_3$$

Eq. 5-6

where, *A*, *B*, and *C* are char fractions; V_1, V_2 and V_3 are lumped volatile products. The first two reactions represent char devolatilisation and the last one is char combustion indicating the layer reaction is considered in wood char pyrolysis leading to the time-resolved particle shrinkage.

For the intrinsic properties of the layer reaction, the time-resolved emission of atomic Na and K during the char phase may be considered to be the distribution of alkali species within the wood char particles. Because the sintering process with the temperature of volatile flame at 1800 K leads to the highest density in Section I (outer-shell layer), the shrinkage rate is slow to reveal a linear profile, as shown in **Figure 5-30**. Due to the fact that the longest sintering process occurs in Section I, the alkali species contained in volatile substances are released. The intensities of atomic Na and K are not significant, therefore. Moreover, the pore structures formed at the beginning of Section I dominate the combustion rates of the outer-shell layer under four equivalence ratios. While Section I is burning, the continuous sintering varies the density within Section II (mid-shell layer), owing to the temperature gradient from the outer methane flame.

Generally the periods of three-shell layers are dominated by the pore structures. For the mid-shell layer, the longer period of outer-shell layer combustion enhances the density within the mid-shell layer. Hence the shrinkage caused by burning demonstrates a consistent

Table 5-6 Summary of the periods for burning wood char particles in the three major layers of wood char particles with four equivalence ratios of 1.149, 1.252, 1.287 and 1.336

Φ		1.149	1.252	1.287	1.336
I	(Sec)	120	300	330	420
II	(Sec)	310	380	650	1400
III	(Sec)	80	170	110	60

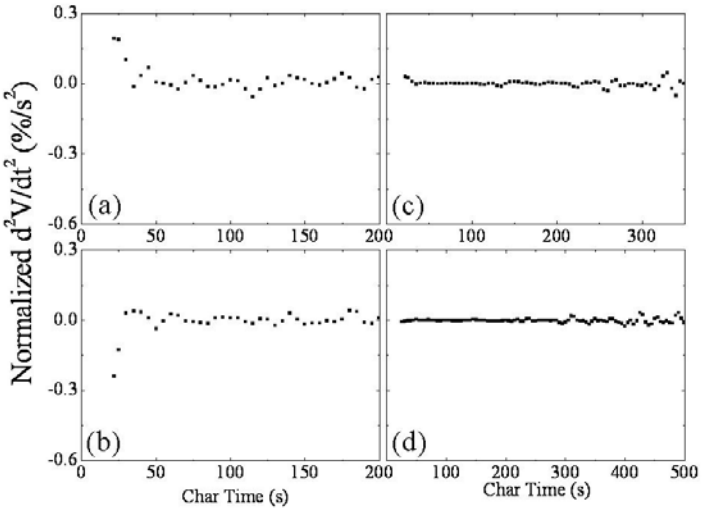

Figure 5-30 The second-derivative of the normalized shrinking wood particles with Φ = (a) 1.149 (b) 1.252 (c) 1.287 and (d) 1.336 in Section I were used to demonstrate the linearity of burning wood particles.

tendency. When the longer period of combustion of the mid-shell layer occurs, the layer can be divided into more sub-sections owing to the enhanced density.

Unlike the burning of coal char particles, the intensities of atomic Na and K for burning wood char at the end of mid-shell layer revealed a plateau. The platform shows the consistent period of 100 ± 20s under the three equivalence ratios, except for Φ = 1.336 (about 50s). **Figure 5-31** shows the detailed platform at the end of the mid-shell layer under the equivalence ratio of 1.336. The cause of the plateau is not clear. A feasible explanation is the stable combustion rate. During the char combustion, the mid-shell layer is continuously heated, leading to density transformation. The boundary between the mid-shell and the ash-shell layers shifts and the periods of the ash-shell layer are reduced. This effect is not observed in burning coal char particles because the lower amount of fixed carbon in the pine wood causes a looser density in the mid-shell layer. Pine wood contains low fixed carbon content so that the effect of the enhanced density at the end of mid-shell layer is not significant. Therefore, the platform could be viewed as the boundary between the mid-shell and the ash-shell layers. However, the pore structures do not seem to complete the scenario.

Temperature of char particles increases during char combustion [12]. Therefore, the

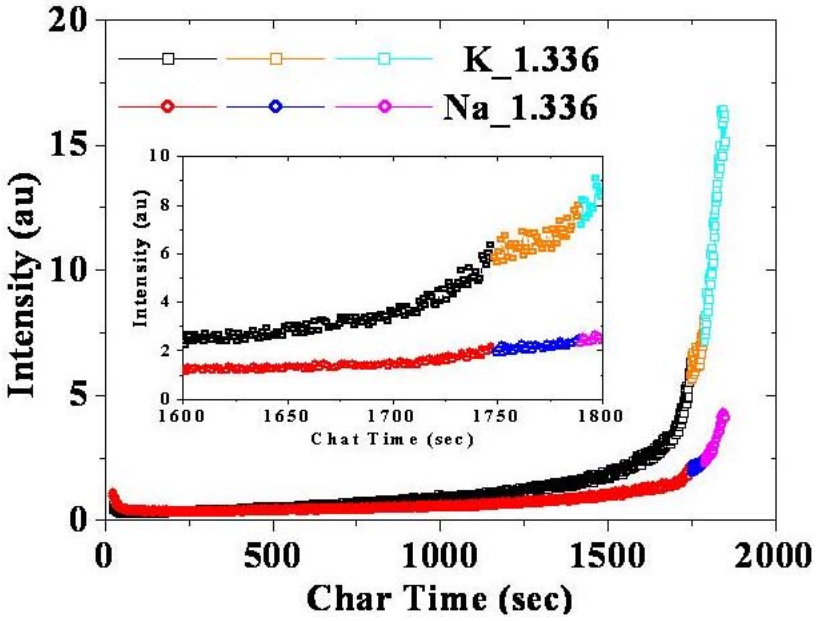

Figure 5-31 Detail for the end of mid-shell layer of pine wood char particles with the equivalence ratio of 1.336 shows the consistent tendency observed in other flame conditions.

combustion of fixed carbon is an exothermic reaction favouring particle temperature increasing, which provides enough energy to vaporize more inorganic substances leading to stronger intensities of atomic Na and K. The effect of the temperature gradient is continuously significant while the particle size is larger than the critical size so that the diffusion reaction still dominates the particle shrinkage. As long as the reaction is dominated by diffusion, the effect of the temperature gradient is still important. As the particles shrink, the effect of the temperature gradient weakens until the temperature gradient dissipates. Due to the loose density of the end of mid-shell layer, the pore structures dissipate so that the reaction rate dominates the combustion rate. The shrinkage rate within this region is constant, leading to the platform profiles of atomic Na and K release at the end of mid-shell layer.

As for the ash-shell layer, the pore structures have been consumed and hence the reaction rate dominates the combustion rates, leading to a dramatic increase in the rate of shrinkage. The temperature within this layer heats the char particles uniformly, and shows constant and sharp rates of particle shrinkage. For the continuous combustion of fixed carbon, the particle temperature reaches the highest level at the end of the ash-shell layer (the end of the char

phase) [12], leading to the greatest release of atomic Na and K.

It is also important to discuss the uncertainty of determination of three layers in a char particle. In addition to the particle variation (8.4 and 3.5 % for coal and wood, respectively), however, the uncertainty of determining the boundaries between three layers was not achievable in this study. Although the uncertainty was not demonstrated, the three-layer model described the fundamental tendency of burning solid-fuel particles.

In this thesis, the three-layer model is proposed to correlate the release of atomic Na and K with burning solid-fuel particles. However, the proposed model needs to be verified theoretically and experimentally in the future work, which is not conducted in this thesis. The results presented in this thesis provide a preliminary investigation in the relationship between the release of atomic Na and K and burning solid-fuel particles.

5.4 Conclusions

The simultaneous detection of atomic Na and K released from burning solid-fuel particles was investigated using atomic emission spectroscopy (AES). Three combustion phases, namely devolatilisation, char and ash phases, associated with the shrinking of wood particles were recorded. The AES technique provides a time-resolved measurement for qualitative analysis with rapid response. Compared to LIF technique, the AES technique can reveal the atomic Na and K released during the devolatilisation phase of burning solid-fuel particles. Due to the fundamental of AES technique, the detection of multiple species can be achieved. However, spatial and quantitative measurements using AES may not be achievable.

It was found that sizes of solid-fuel particles shrank consistently during the devolatilisation respectively 10% and 15% for virgin particles of brown coal (23 ± 3 mg, approximately spherical 3 mm diameter) and pine wood (63±3 mg, approximately spherical 4 mm diameter), under four equivalence ratios. The shrinkage of the virgin coal and the wood particles was observed to be a global and a three-stage process associated with atomic Na and K release.

Due to the intrinsic properties of wood pyrolysis, the burning of the wood particles may be related to the combustion of hemi-cellulose, cellulose and lignin consistent with the shrinkage profiles. The intensities of atomic Na and K release during the devolatilisation are dependent on the equivalence ratios which dominate the porosity formation of char particles. Due to the slow volatile release, the devolatilisation of wood with the equivalence ratio of 1.336 lasts longer. The temperature of the volatile flame was calculated to be about 1800 K using Planck's Law.

A simple experiment to demonstrate the effect of the porosity of char particles using AES was conducted. It demonstrated the intensities of atomic Na and K release during the char phase were affected by the initial equivalence ratio employed during the devolatilisation.

A three-layered model, namely outer-, mid- and ash-shell layers, is proposed to describe the shrinkage of burning char particles for brown coal and pine wood. The model successfully describes the particle shrinkage during the char phase. As the temperature gradient (described by a simple thermal conductivity equation) produces variations of solid densities within the burning char particles.

The profiles of atomic Na and K release were observed to be associated with the shrinking char particles. Due to the particle size, the reaction rate dominated the char combustion at the end of the mid-shell layer when the profiles of shrinkage rates and atomic Na and K release were analysed. For the particle size and density of the ash-shell layer, the reaction rate dominated the combustion of the ash-shell layer, leading to the dramatic increase in shrinking rates. With the increasing particle temperature caused by the exothermic reaction of burning fixed carbon, the highest particle temperature occurred at the end of char phase and resulted in the largest release of atomic Na and K.

The flame temperature dominates atomic Na and K release during the ash phase. The temperatures of premixed laminar methane flames with four equivalence ratios are 1450 ~ 1500 K. Therefore, the historic emission of atomic Na and K decays dramatically under the equivalence ratio of 1.149 and last much longer with the condition of 1.336.

CHAPTER 6

Sodium and Potassium Detection using Laser-Induced Breakdown Spectroscopy

6.1 Introduction

In the preceding chapter, the release of atomic Na or K during the burning of the particles of Loy Yang Brown coal and the pine wood was discussed. In this chapter, the ways in which Laser-Induced Breakdown Spectroscopy (LIBS) were applied to provide insight into the total release amount of target species measured at a single point are described. Compared to the difficulty of measuring quantitatively the release of atomic Na using PLIF [11-15], the LIBS measurement is able to detect and measure Na and K released during the devolatilisation phase of burning solid-fuel particles.

For the characteristics of LIBS measurement, plasma provides a high temperature environment (about 10,000 ~ 20,000 K) to dissociate alkali species into elemental forms. The total release of sodium ($[Na]_{total}$) and potassium ($[K]_{total}$) is defined as the time-resolved concentrations of total Na and K measured at a single point, as indicated in **Figure 6-1**, because Na and K species in the flame may exist in various forms, such as atomic alkali, alkali oxide, alkali chloride, alkali oxides and alkali hydroxide etc. This is an important limitation of the techniques, such as LIF, when used in reacting media to detect multiple species.

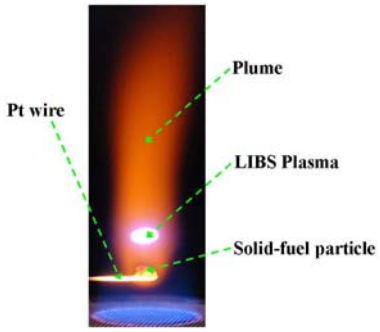

Figure 6-1 Arrangement of LIBS measurement for the time-resolved release of trace species in the plume

6.2 Experimental Arrangement

6.2.1 Burner and Laminar Premixed Flame

The same burner and equivalence ratios introduced in **Section 5.2.1** have been employed in the LIBS measurement, providing the same experimental environment. For the calibration process, another MFC was employed to control the flowrate of the seeding air constantly at 0.30 ± 0.015 ml_n, as shown in **Table 6-1**. To provide the same equivalence ratios, the flowrate of the seeding air is included in the total air flowrates. A nebulizer was employed to produce droplets of salt solution with a nominal diameter of 1 μm [11], as indicated in **Eq. 3-2**. To maintain the stability of flowrates for the gaseous mixture during the calibration process, a bottom outlet is designed to drain away any excess salt solution in the mixing chamber (as shown previously in **Figure 5-1**).

Table 6-1 Flowrates of main air, seeding air and methane for calibration process; the seeding air maintains a constant flowrate of 0.30 ml_n providing the consistent consumption rate of salt solution. The total air flowrate includes the seeding air flowrate providing the consistent equivalence ratios.

Φ		1.149		1.252		1.287		1.336	
Air (mln)	Main	6.150	6.450	6.330	6.630	6.150	6.450	5.250	5.550
	Seeding	0.3		0.3		0.3		0.3	
Methane (mln)		0.779		0.872		0.872		0.779	

6.2.2 Laser-Induced Breakdown Spectroscopy

The LIBS system, as presented in **Figure 6-2**, was applied to measure the quantitative and time-resolved histories of $[Na]_{total}$ and $[K]_{total}$ released into the plume by a single burning particle of coal (23 ± 3 mg, approximately spherical 3 mm diameter) or pine wood (63 ± 3 mg, approximately spherical 4 mm diameter) suspended on a platinum (Pt) wire at a height of 10 mm above the laminar burner. A summary of equipments for the LIBS measurement is listed in **Table 6-2**.

A Q-switched Nd:YAG laser (Spectra Physics) operating at the fundamental wavelength of 1064 nm (10 Hz repetition rate and pulse width of 8 ns) and equipped with an attenuator (Iskra electronics, NRC, model: 935-10) to vary the pulse energy to provide a laser beam of 240 mJ per pulse. The laser beam was focused by a quartz lens of 150 mm focal length to a spot soze 1 mm to generate plasma with an elliptical measurement volume at a position 10 mm above the burner surface during the calibration or 10 mm above the fuel particles. The emitted radiation was collected through a quartz lens of 150 mm focal length by a spectrometer (Triax series 320, Inc. Edison, NJ), which comprised a grating (300 grooves per mm) and an ICCD detector (Princeton instruments, model: 7483-0001). Due to the limitation of the grating (wavelength

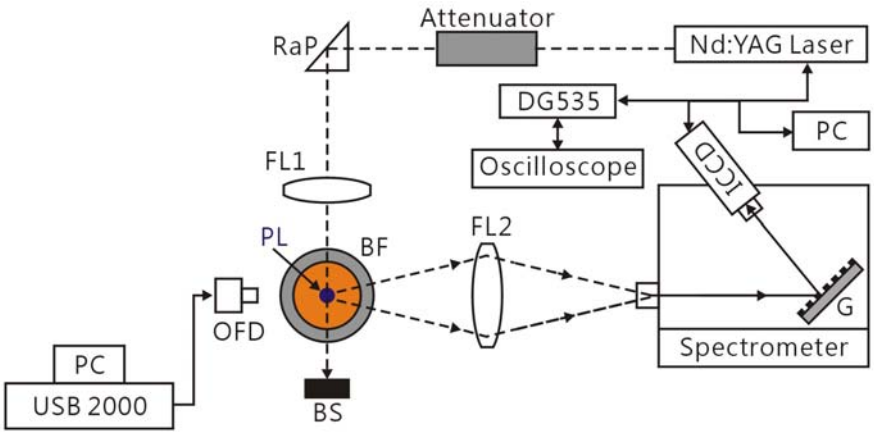

Figure 6-2 Arrangement of the LIBS measurement and the simultaneous atomic emission spectroscopy (SAES) comprises the conventional LIBS measurement and a simple AES spectrometer. Focal Lens: FL1 and FL2; PL: Plasma; RaP: Right Angled Prism; G: Grating; OF: Optical Fibre; BS: Beam Stopper; BF: Burner and Flame

Table 6-2 Summary of the equipments for present LIBS measurement

Equipments	Specification
Nd:YAG Laser system	Spectra Physics(10 Hz repetition rate and pulse width of 8 ns)
Spectrometer	Triax series 320, Inc. Edison, NJ
Intensified charge-coupled device (ICCD)	Princeton instruments, model: 7483-0001
Oscilloscope	Tektronix TDS 3054, 500 MHz
Pulse generator	Stanford Research Systems, DG535
Attenuator	Iskra electronics, NRC, model: 935-10

range), $[Na]_{total}$ and $[K]_{total}$ cannot be measured simultaneously. Although both of the elements can be measured simultaneously using commercial equipment for LIBS measurement, measurements of Na and K can be performed with better resolution in the present apparatus. A pulse generator (Stanford Research Systems, DG535) and an oscilloscope (Tektronix TDS 3054, 500 MHz) were used to trigger the laser and to optimize the gate delay and gate width, respectively, to reduce background noise.

The signals of Na and K using LIBS in the calibration process and the combustion of solid-fuel particles are presented in **Figure 6-3**. For calibration, the radiation was collected with various concentrations of salt solution containing Na or K. The LIBS plasma applied inside the plume of burning solid-fuel particles provided the time-resolved histories of $[Na]_{total}$ and $[K]_{total}$.

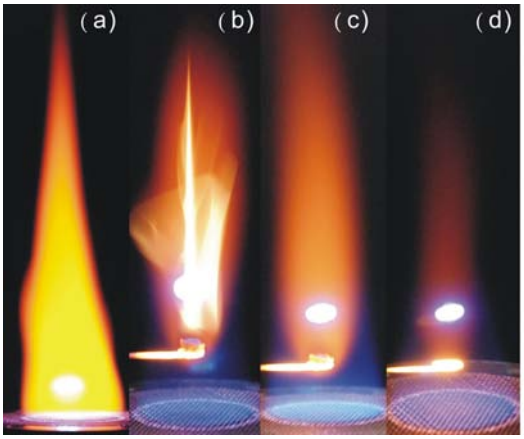

Figure 6-3 LIBS applied in (a) Seeded flame and combustion of solid-fuel particles during (b) Devolatilisation (c) Char (d) Ash phases.

6.2.3 Simultaneous Atomic Emission Spectroscopy

A spectrometer (Ocean Optics, USB 2000) was employed to measure the time-resolved release of atomic Na and K during combustion, simultaneously with LIBS measurement, termed as simultaneous atomic emission spectroscopy (SAES), as shown in **Figure 6-2** previously. This complements the measurement by LIBS, which cannot measure Na and K simultaneously, and adds to our understanding of the release of alkali species. The SAES measurement can therefore be used to investigate the difference between atomic Na and K released from burning solid-fuel particles and the variability between solid-fuel particles. Details of measurements using AES were included in **Chapter 5**.

6.2.4 Signal Acquisition

For the quantitative LIBS measurement of Na and K, a calibration process was conducted. The image was recorded every second, providing a time-resolved history of Na and K released from the burning solid-fuel particles and calibration process. Various spectral interferences are unavoidable in the region where the transition states of the target species are located, as indicated in **Figure 6-4**, including the background noise from the flames,

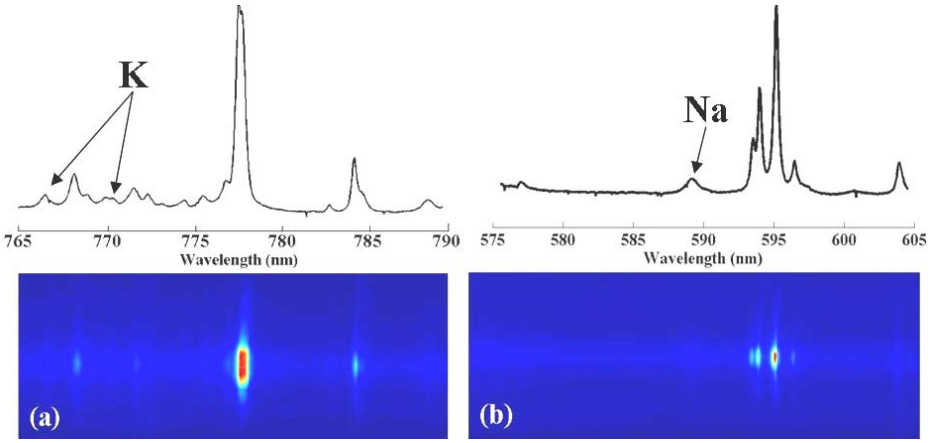

Figure 6-4 Spectral interferences across (a) atomic K (b) atomic Na using LIBS with a delay time of 200 ns and a gate width of 500 ns

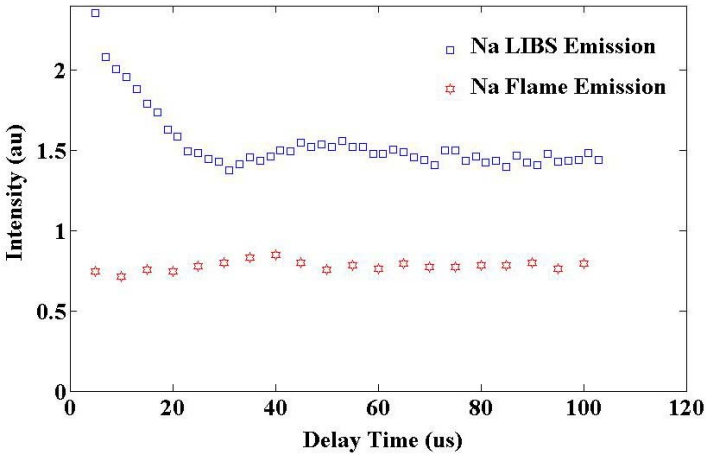

Figure 6-5 Spectral intensities of atomic Na were obtained at 589.592 nm for the flame emission and LIBS. The intensities of flame emission are stable while the intensities of LIBS emission become stable with a gate delay time of 30 μs.

especially during the emission of atomic Na and K from the seeded flames. Although these spectral interferences are distinguishable, the lines of the trace species could overlap, leading to interference errors. Moreover, the background noise caused by the emission of atomic Na and K from the seeded flame or the plume is more significant and persistent than those in LIBS plasma, as illustrated in **Figure 6-5**. For these reasons, two procedures were applied to eliminate the unwanted effects. Firstly, the spectral interferences have different lifetimes from the target species. This provided an opportunity to isolate the signals from the interferences by optimizing the gate delay (the time before signals) and the gate width (the time to collect signals). Secondly, the intensities of atomic Na and K were treated as background signals.

To improve the measurement of Na and K, it is important to identify the spectral interferences by optimizing gate delay and gate width. The spectral interferences across lines of atomic Na have been recognized [20, 42, 230] with 5 μs gate delay and the gate width, as shown in **Figure 6-6**. These do not seem to encourage errors in atomic Na measurement. As **Figure 6-5** showed, the contribution of flame emission to atomic Na measurement can easily be reduced by subtracting it from the LIBS intensity. Moreover, the intensity of atomic Na for the LIBS measurement becomes stable with a delay time of 30 μs due to the initial LIBS plasma reaching LTE, and the dramatic decay of the continuum of the initial LIBS plasma. The delay

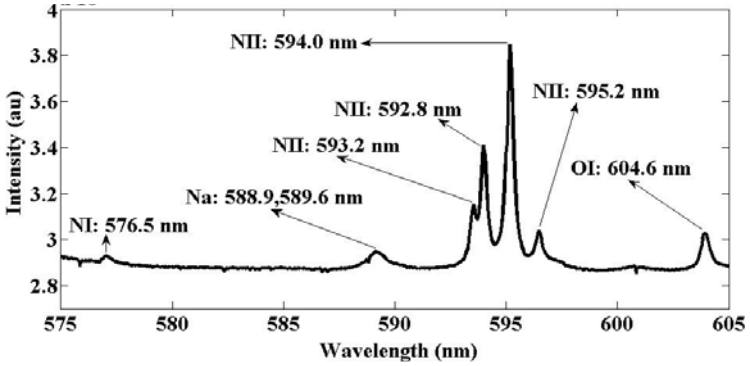

Figure 6-6 The recognized spectral interferences across lines of atomic Na at 588.992 and 589.592 nm are mainly N I and N II with 5 μs gate delay and gate width [20].

time for the atomic Na measurement using LIBS was therefore determined to be at least 30 μs.

Unlike the simple interferences of atomic Na, interference is more complicated for atomic K, as indicated in **Figure 6-4**a. For the low signal-to-noise ratio of atomic K in the seeded flame, the spectral interferences have been recognized [20], as shown in **Figure 6-7**. The critical spectral interference is hot water lines which may be caused by water molecules excited by the relatively high temperature plasma. The intensities of the H_2O lines dissipate with time. The LIBS plasma generated in a surface of an aluminium (Al) sample reaching LTE with a lower energy pulse has been shown to be between 0.5-5 μs or less than 1.5 μs for the higher pulsed energy (> 75 mJ) [239] so that the strong continuum signals occur after the laser fires. Although significant amount of the laser beam energy is used to ablate Al atoms from the

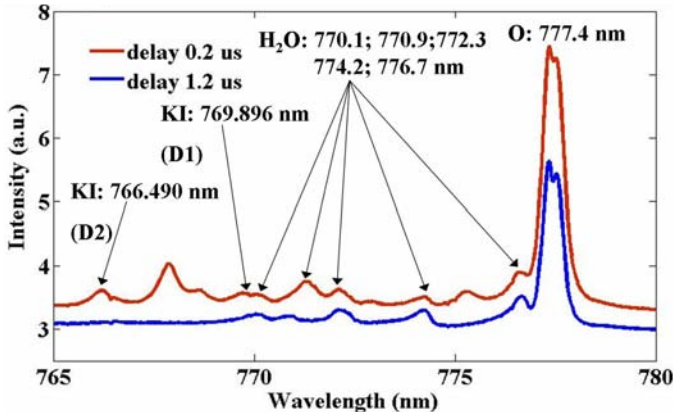

Figure 6-7 Spectral interferences across the D_1 and D_2 lines of atomic K (769.896 and 766.490 nm, respectively) are mainly hot water (H_2O) lines [20].

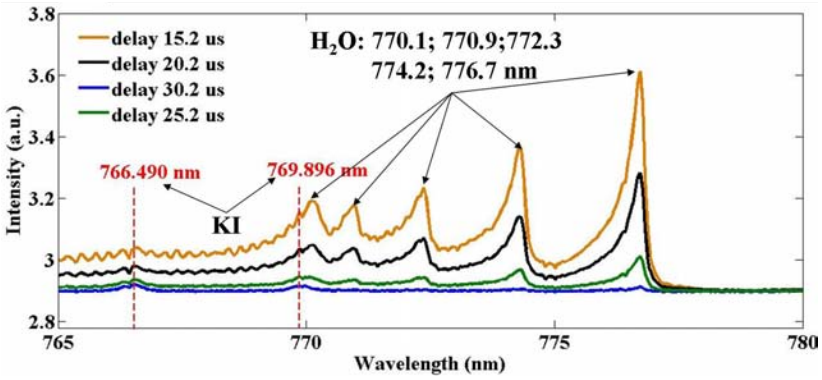

Figure 6-8 Water lines decay with the longer delay times of 15.2, 20.2, 25.2 and 30.2 μs. It is evident that the water lines diminish across the D_1 line of atomic K.

sample, a different case of gaseous samples in this study, the timing to reach LTE can provide reference to optimize the gate delay and the gate width. To eliminate the major spectral interferences, the proper delay time should be determined beforehand and then consideration given to other spectral interferences. However, water lines still overlap the D_1 of atomic K, indicating that some water lines are persistent and demonstrate various characteristics over the whole of their lifetime. It is evident that the water lines diminish with longer delay times of 10.2, 20.2, 25.2 and 30.2 μs, as shown in **Figure 6-8**. The spectral interferences of the D_1 line of atomic K for the delay time of 30.2 μs seem to be weak, which also suggests the delay time for the atomic K measurement ought to be at least 30.2 μs, consistent with that of the atomic Na measurement.

To eliminate the interference of water lines with atomic K, a longer delay time was considered. As to the gate width, it was fore-determined in order to achieve better signals for atomic Na and K. The optimized delay time and gate width were experimentally determined to be 45 and 5 μs, respectively. The $[Na]_{total}$ and $[K]_{total}$ were not measured simultaneously owing to the large wavelength difference between the D_1 bands of atomic Na and K, which were out of the range covered by the chosen grating. Nevertheless, commercial spectrometer products, such as the Echelle spectrometer [51, 77], are capable of measuring multiple elements simultaneously. Although Na and K were not measured simultaneously, if they had been, resolution would have been improved, along with LOD.

6.2.5 Data Processing

The raw intensities of Na and K in the D_1 line contain the background noise and spectral interference. To improve the LIBS measurement for the quantities of Na and K released from burning solid-fuel particles, the background noise, the intensities of flame emission, and the possible spectral interferences are corrected. To improve the accuracy, an average of 50 images for each measurement in the calibration process and background correction was recorded. The experimental intensities of atomic Na and K for the calibration and burning of solid-fuel particles were then obtained by subtracting the background noise and interferences.

6.2.6 Calibration Process

The experimental measurements of concentrations of Na ([Na]) and K ([K]) using LIBS were converted quantitatively by applying an appropriate calibration process. Unlike conventional calibration methods reported in the literature [77, 78] based on the relative intensities of the spectral lines of the reference and trace elements, the present calibration curves were based on the known quantity of seeded Na and K. Various concentrations of potassium sulfate (K_2SO_4) and sodium sulfite (Na_2SO_3) were entrained into the flame. Various alkali species distributed throughout the flame were dominated by the temperature. Atomic Na distribution, for example, decreases with the axial of the plume of burning coal particles [11, 12] and of burning black liquor droplets [13-15] using PLIF. On the other hand, Na formed other compounds when the temperature decreased rapidly. It indicated that the total released Na for the point measurement would be similar. Therefore, to estimate the [Na] and [K] in the seeded flames, the distribution of alkali salt in the seeded flame was assumed to be uniform.

The calculation of the time-resolved concentrations of Na and K distributed within the seeded flame was based on the seeding rate of the slat and flame conditions, which was briefly

introduced in **Section 2.4**. The details of the seeded concentration calculation are provided here:

Calculation begins with the measurement of the seeding rate of the salt solutions. Mass flowrate (υ_m, g·s^{-1}) was calculated as the product of the concentration of alkali salt (C_s, g·L^{-1}) and the consumption rate of salt solution (υ_s, L·s^{-1}), as shown below:

$$\upsilon_m = C_s \times \upsilon_s$$

Eq. 6-1

To calculate υ_s, the volumes of salt solutions before and after four hours consumption, with a constant seeding air flowrate of 0.300 ± 0.015 ml$_n$, were measured. Condensed salt solution on the bottom chamber of the burner was taken into account by feeding it back to the nebulizer system directly. Hence, the molar flow of alkali salts in the flame (υ_{ms}, mol·s^{-1}) was obtained, as shown below:

$$\upsilon_{ms} = a_m \cdot \upsilon_m / \mathrm{M}$$

Eq. 6-2

where, M is the molar mass of the salt and a_m is the molar ratio of alkali ions in the salt. It can be seen that the total gas flowrate (υ_f, L·s^{-1}) at the flame temperature T_f (K), is a function of the flowrate of methane (υ_g, L·s^{-1}), the flowrate of air (υ_a, L·s^{-1}) and T_r (room temperature, 298 K):

$$\upsilon_f = (\upsilon_g + \upsilon_a) \times T_f / T_r$$

Eq. 6-3

Then, using the ideal gas law, the molar flowrate of total gas (υ_{mf}, mol·s^{-1}) through the flame is obtained, as presented below:

$$\upsilon_{mf} = \mathrm{P} \cdot \upsilon_f / \mathrm{R} \cdot T_f$$

Eq. 6-4

where, R is gas constant (0.0821, $L \cdot atm \cdot mol^{-1} \cdot K^{-1}$) and P is atmospheric pressure (atm). In the final equation, the dimensionless concentrations ($C_{seeding,}$ ppm), namely [Na] and [K], in the flame are expressed in parts per million (ppm), as shown below:

$$C_{seeding} = \upsilon_{ms} / \upsilon_{mf}$$

Eq. 6-5

According to **Eq. 6-1** ~ **Eq. 6-5** and **Eq. 5-1**, two linear calibration equations of [Na] and [K] were obtained. In addition, the total seeded amounts of Na or K, indicating the number density of the target species (n_s, $atoms \cdot m^{-3}$), can also be obtained by dividing **Eq. 6-2** by **Eq. 6-3**. The details of the concentrations of seeded salts in the seeded flames are listed in **Table 6-3**.

6.3 Results and Discussion

The LIBS technique was employed to quantitatively detect $[Na]_{total}$ and $[K]_{total}$ at a single point in the plume of burning solid-fuel particles with calibration curves. The raw calibration curves were achieved by finding the relation of LIBS intensities corresponding to [Na] or [K] calculated mathematically. The seeded concentrations of Na and K are listed in **Table 6-3**.

Table 6-3 Seeded concentrations of [Na] and [K] based on the constant 0.30 ml_n seeding air flowrate and ten amounts of salts in weight are calculated by applying **Eq. 6-1** ~ **Eq. 6-5**

Concentration([Na],ppm) in the seeded flames calculated by using Eq. 6-1~Eq.6-5										
Seeded Na_2SO_3Salt (g)		0.25	0.50	0.75	1.00	1.25	1.50	1.75	2.00	2.25
Φ	1.149	1.12	2.24	3.35	4.47	5.59	6.71	7.83	8.95	10.06
	1.252	1.08	2.16	3.23	4.31	5.39	6.47	7.54	8.62	9.70
	1.287	1.10	2.21	3.31	4.42	5.52	6.62	7.73	8.83	9.94
	1.336	1.28	2.55	3.83	5.11	6.39	7.66	8.94	10.22	11.50

Concentration([K],ppm) in the seeded flames calculated by using Eq. 6-1~Eq.6-5										
Seeded K_2SO_4Salt (g)		0.25	0.50	0.75	1.00	1.25	1.50	1.75	2.00	2.25
Φ	1.149	0.81	1.62	2.43	3.24	4.04	4.85	5.66	6.47	7.28
	1.252	0.78	1.56	2.34	3.12	3.90	4.68	5.46	6.23	7.01
	1.287	0.80	1.60	2.40	3.19	3.99	4.79	5.59	6.39	7.19
	1.336	0.92	1.85	2.77	3.70	4.62	5.54	6.47	7.39	8.31

The calibration curves were corrected by considering the absorption, termed as signal trapping, caused by the atomic Na or K in the outer flame. By applying two calibration curves, the quantitative and instantaneous release records of total Na and K measured at a single point within the plume of burning solid-fuel particles could be achieved.

6.3.1 Self-Absorption in Calibration

By applying **Eq. 5-1** and **Eq. 6-5**, as shown below:

$$\ln(I_{exp}) = \ln(A) + b \cdot \ln(C_{species}) \quad \text{Eq. 5-1}$$

$$C_{seeding} = \upsilon_{ms} / \upsilon_{mf} \quad \text{Eq. 6-5}$$

Two calibration curves for $[Na]_{total}$ and $[K]_{total}$ were expected to be linear while self-absorption was negligible, i.e. b = 1. The calibration curves showed that the non-linear profiles indicating self-absorption was not negligible ($b < 1$) for the high concentrations of trace species. The same problem occurred to inductively coupled plasma-atomic emission spectrometry (ICP-AES) measurement. To obtain linear calibration curves by applying **Eq. 5-1**, the ICP-AES measurement requires dilute sample solutions of concentrations of less than 500 ppb. However, this is not always achievable for flame samples.

Radiation is emitted from the centre of the plasma in the initial generation and then the plasma starts to expand until it reaches LTE. The target species are excited to higher energy states in the initial plasma and then decay to lower or ground states, which are able to re-absorb radiation emitted from the following generated plasma. Due to the fact that plasma quenching leads to re-absorption, self-absorption is not avoidable in plasma-based techniques. For the conventional LIBS measurement of gaseous samples, self-absorption is the only issue causing significant variation in the quantitative measurement.

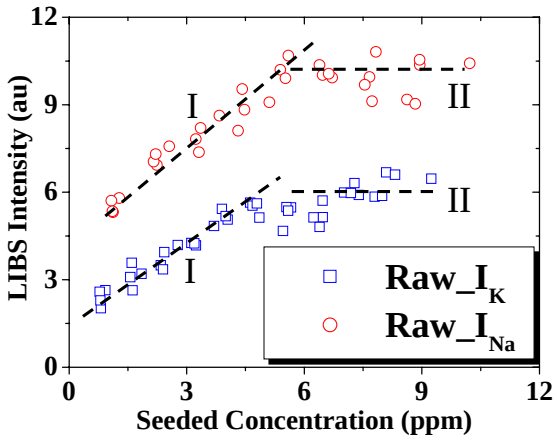

Figure 6-9 Raw calibration curves for $[Na]_{total}$ and $[K]_{total}$ indicate the presence of significant absorption.

6.3.1.1 Nonlinear Calibration

The intensities of Na and K using LIBS were recorded using 40 concentrations of salt solutions under four equivalence ratios (ten concentrations for each equivalence ratio). Unlike the characteristics of equivalence ratios particular to burning solid-fuel particles, the 40 data points can be used to develop reliable and accurate calibration curves. However, the raw calibration curves, as presented in **Figure 6-9**, demonstrate non-linear characteristics. Two sections of slopes and the significant *y*-offsets were observed in the calibration curves of both $[Na]_{total}$ and $[K]_{total}$. These imply the significant absorption dominating Section II and the *y*-offsets, although the y-offsets could be caused by systematic errors, including background noise and spectral interference. However, systematic errors should not be significant since correction was conducted.

In terms of conventional LIBS measurement, Section II indicates significant self-absorption with high [Na] and [K] resulting in saturation signals. For the particular LIBS measurement, however, absorption is caused by not only self-absorption but more significantly by flame absorption. Self-absorption is caused by the trace species which re-absorb radiation of a specific wavelength outside the expanding plasma. Therefore, self-absorption becomes

significant with high concentrations of trace species. To reduce self-absorption, the chosen transition (wavelength) of target species is other persistent spectral lines rather then the major resonant lines. However, other persistent lines of Na and K, such as 404.414, 404.721, 1169.021, 1176.962 and 1177.283 nm for K [20] and 819.482 nm for Na [20], were not observed with the gate delay and gate width (45 and 5 μs, respectively).

Conditions can be adjusted to measure other persistent lines. Nevertheless, the intensities are very weak and overlapped by other spectral interferences from which they are difficult to distinguish. Thus, the chosen wavelengths for Na and K in the present arrangement are the D_1 lines (589.592 and 769.896 nm, respectively). Due to the chosen spectral lines, the self-absorption could be significant in the presence of target species with high concentrations. As shown in **Eq. 5-1**, $b<1$ accounts for the self-absorption, which becomes more significant when the reversal of spectral lines occurs (b is very small, such as 0.1). Due to the particularity, another source of absorption for LIBS applied inside the seeded flame needs to be considered, as presented in **Figure 6-10**, indicating the absorption (defined as signal trapping) can be expressed by the Beer-Lambert law.

To simulate the best-fit of the nonlinear calibration curves in **Figure 6-9**, two types of absorption sources need to be considered. One is self-absorption caused by the re-absorption

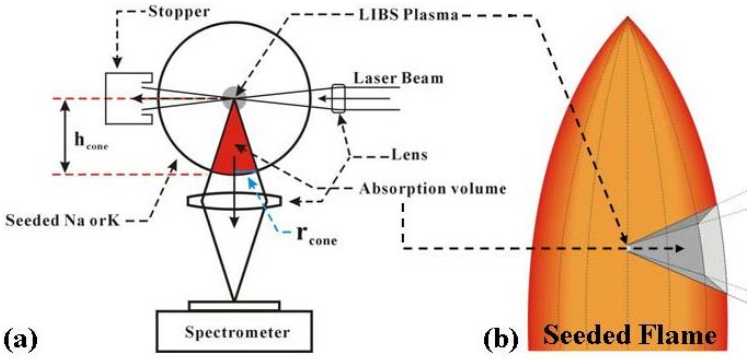

Figure 6-10 (a) A schematic is used to describe the flame absorption occurring when the radiation of trace species emits from the LIBS plasma through the seeded flame and is focused and collected by a convex lens and the spectrometer, respectively. (b) Diagram indicates the absorption volume is considered to be shaped like a cone

in the LTE status of LIBS plasma and the other is the signal trapping resulting from the atomic alkalis in the surrounding seeded flames. Hence, the best-fit can be presented as follows:

$$I_{exp} = I_{act} \cdot e^{-a_1 \cdot [X]_{species}} = a_2 \cdot [X]_{species} \cdot e^{-a_1 \cdot [X]_{species}}$$

Eq. 6-6

where, I_{exp} is the experimental intensity of the target species; I_{act} is the intensity emitted from the plasma; a_1 is a dimensional coefficient and $[X]_{species}$ is the concentration of target species and a_2 is a pre-factor constant. In terms of the self-absorption, the I_{act}, which is based on **Eq. 5-1**, associated with **Eq. 6-6**, can be expressed in the following equation:

$$I_{exp} = a_2 \cdot [\mathrm{X}]_{species}^{b} \cdot \mathrm{e}^{-a_1 \cdot [\mathrm{X}]_{species}}$$

Eq. 6-7

where, $I_{act} = a_2 \cdot [\mathrm{X}]_{species}^{b}$ and a_2 is a dimensional pre-factor constant. Two best-fit models are indicated in **Figure 6-11**, one based on **Eq. 6-7** [**Figure 6-11**(a)] and the other on **Eq. 6-6** [**Figure 6-11**(b)], with and without self-absorption, respectively. The simulation results based on **Eq. 6-6** and **Eq. 6-7** are presented below:

$$I_{LIBS,Na} = 5.374 \times 10^5 \cdot [\mathrm{Na}]_{total}^{0.52} \cdot \mathrm{e}^{-0.06 \cdot [\mathrm{Na}]_{total}}$$

Eq. 6-8

$$I_{LIBS,K} = 2.613 \times 10^5 \cdot [\mathrm{K}]_{total}^{0.52} \cdot \mathrm{e}^{-0.03 \cdot [\mathrm{K}]_{total}}$$

Eq. 6-9

and

$$I_{LIBS,Na} = 4.271 \times 10^5 \cdot [\mathrm{Na}]_{total} \cdot \mathrm{e}^{-0.155 \cdot [\mathrm{Na}]_{total}}$$

Eq. 6-10

$$I_{LIBS,K} = 2.153\times10^{5}\cdot[\mathrm{K}]_{total}\cdot e^{-0.134\cdot[\mathrm{K}]_{total}}$$

Eq. 6-11

where, $I_{LIBS,Na}$ and $I_{LIBS,K}$ are the intensities of atomic Na and K, respectively, using LIBS.

The **Eq. 6-8** and **Eq. 6-9** show the better simulation tendency in terms of self-absorption, as shown in **Figure 6-11**(a). Compared to **Eq. 6-10** and **Eq. 6-11**, however, the simulation tendency shown in **Figure 6-11**(b) reveals the variation without considering self-absorption. This indicates the self-absorption is significant with a self-absorption coefficient of 0.52, which is the average number of data points. Nevertheless, the self-absorption coefficient is specifically related to the concentration of target species. The overall $b = 0.52$ may not represent the self-absorption coefficient. It is difficult to identify the individual self-absorption coefficient that corresponds to the concentration of the target species. If the absorption

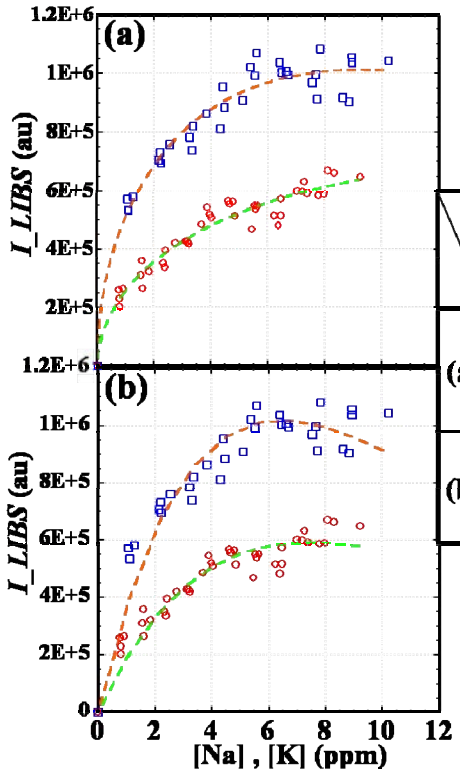

$I_{LIBS,x} = a_2\cdot[x]^{b}_{species}\cdot e^{-a_1\cdot[x]_{species}}$ (c)

	x	a_2 (x10^5)	b	a_1
(a)	Na	5.374	0.52	0.060
	K	2.613		0.030
(b)	Na	4.271	1	0.155
	K	2.153		0.134

Figure 6-11 Simulation of raw calibration curves using LIBS with the consideration based on (a) **Eq. 6-7**: b = 0.52 indicates significant self-absorption; (b) **Eq. 6-6**: b = 1 indicates the negligible self-absorption. (c) The table lists the simulation results with two regimes, as indicated in **Eq. 6-10** and **Eq. 6-11** for case (a) and **Eq. 6-8** and **Eq. 6-9** for case (b). □: Na; ○: K; ---: fitting of Na; ---: fitting of K

coefficient, b, can be determined, the pre-factor, a_2, can also be obtained. When the absent self-absorption (b = 1) based on **Eq. 5-1** in the conventional LIBS measurement is taken into consideration, it may be possible to determine a_2. However, the LIBS intensity is involved in not only the self-absorption but the signal trapping. It was not possible to determine both values using the arrangement.

It is possible to demonstrate the real LIBS intensities corresponding to concentrations using the simulation results. However, in terms of practical application, it is only necessary to apply **Eq. 6-6** to obtain calibration curves (**Eq. 6-10** and **Eq. 6-11**) without considering self-absorption. Indeed this is an acceptable approximation within a certain concentration range. Details in the next section describe the signal trapping (the exponential part in **Eq. 6-6**). The correction of LIBS intensities, as indicated in **Eq. 6-10** and **Eq. 6-11**, can be completed. For the ultimate application, calibration curves shall be linear rather than to be exponential.

6.3.1.2 Flame Absorption

The LIBS plasma is surrounded by the seeded flame, as shown in **Figure 6-3**(a). The seeded flame contains atomic Na or K which absorbs a particular wavelength of plasma radiation. The absorption (signal trapping) becomes intense with high concentrations of seeded salts, which are exposed to the flame. The energy provided by the flame temperature is used to excite Na or K in the seeded flame where the number densities of atomic Na and K in the outside seeded flame are determined. The signal trapping increases proportionally to the amount of atomic Na or K in the outside seeded flame until the flame is saturated. Therefore, the signal trapping (flame absorption) interprets the saturation-like calibration curves in Section II observed in **Figure 6-9**. Moreover, the signal trapping also induces the y-offsets in the calibration curves because the self-absorption coefficient, b, becomes critical to LIBS intensities.

To improve the calibration curve by reducing self-absorption, the concentrations of the seeding salt solutions should be as low as possible [52]. Low concentrations of seeding salt solutions also reduce the flame absorption. Therefore, it may not be necessary for the quantitative measurement to take into consideration the self-absorption and flame absorption with low concentrations of trace species. This chapter describes the way in which a technique for measuring Na and K in the plume of burning solid-fuel particles was developed, and illustrates why further development is planned.

Unlike unavoidable self-absorption, flame absorption can be corrected using the Beer-Lambert law which is well-established [207, 240], which is given by:

$$\ln(\frac{I_{act}}{I_{exp}}) = \alpha(\omega) \cdot x$$

Eq. 6-12

$$\alpha(\omega) = n_s \cdot \sigma_a(\omega)$$

Eq. 6-13

where, I_{exp} is the experimental radiation intensity of atomic Na or K; I_{act} is the actual radiation intensity of atomic Na or K without signal trapping; x is the absorption length in the flame (m); $\alpha(\omega)$ is the absorption coefficient of atomic Na or K at angular frequency (s^{-1}); $\sigma_a(\omega)$ is the absorption cross-section of atomic Na or K at angular frequency (s^{-1}) and n_s is the number density of atomic Na or K (n_s: atoms·m^{-3}). Given the measured values of I_{act}, I_{exp} and x in **Eq. 6-12**, the absorption coefficient of atomic Na or K, $\alpha(\omega)$, can be determined. It is possible to calculate the n_s of target species using **Eq. 6-13**, which has been conducted to measure the atomic Na released from burning coal particles [11, 12] and black liquor [13-15] quantitatively using PLIF. It is possible to apply **Eq. 6-12** and **Eq. 6-13** not only to calculate the n_s of the target species in the flame but to demonstrate the absorption level of the media. However, the absorption cross-section should be determined in advance.

To determine $\sigma_a(\omega)$, the Einstein coefficients for spontaneous emission, A_{21}, stimulated

emission, B_{21}, and absorption, B_{12}, at a specific angular frequency of the transition, $\omega_{12} = \omega_{21}$, can be given by [207, 240]:

$$B_{21} = \frac{A_{21}}{F(\nu)} = \left(\frac{\pi^2 \cdot c^3}{\hbar \cdot \omega_{21}^3}\right) \cdot A_{21}$$

$$B_{21} = \frac{g_1}{g_2} \cdot B_{12}$$

Eq. 6-14

where;

$$F(\nu) = \frac{8\pi \cdot \hbar \cdot \nu^3}{c^3} \qquad \omega_{21} = \frac{2\pi \cdot c}{\lambda}$$

c: light speed ($m \cdot s^{-1}$) — λ: the wavelength of the transition (nm)

$\hbar$: Planck's constant divided by 2π ($J \cdot s$) — ν: the frequency of the transition (s^{-1})

For the D_1 lines of atomic Na and K, the A_{21} are respectively 6.14×10^7 and 3.74×10^7 s^{-1} [20]. In addition, the degeneracy state (g_i) of atomic Na and K in the D_1 lines are both $g_1 = g_2 = 2$ [20]. Thus, the values of B_{12} of atomic Na and K were determined to be 4.75×10^{21} and 6.44×10^{21} $m^3 \cdot J^{-1} \cdot s^{-2}$, respectively.

The relationship between $\sigma_a(\omega)$ and B_{12} is expressed in the following equation:

$$\sigma_a(\omega) = \frac{\hbar \cdot \omega_{12} \cdot B_{12} \cdot I(\omega_{12})}{c}$$

Eq. 6-15

where, $I(\omega_{12})$ is the normalised function that is used to describe the variation between different systems and is governed by **Eq. 3-15** so that the variation can be normalized:

$$\int_{-\infty}^{+\infty} I(\omega) \cdot d\omega = 1$$

Eq. 3-15

For LIBS measurement, $I(\omega)$ was determined by measuring the variation of the system with ω for a narrow band around the D_1 of atomic Na (589.59 nm) or K (769.896 nm) to obtain a function of the angular frequency, $f(\omega)$. Unlike the intensities of target species varying wavelengths in the PLIF measurement to determine $I(\omega)$ [11], it is easy for the present LIBS

measurement to obtain the normalized function. **Figure 6-4** represents the radiation intensities of atomic Na or K in the narrow band width, which were directly used to obtain the partition function. This function was numerically integrated to obtain the constant, κ, which is give by **Eq. 3-16**:

$$\int_{-\infty}^{+\infty} f(\omega) \cdot \mathrm{d}\omega = \kappa \qquad \text{Eq. 3-16}$$

By dividing $f(\omega)$ by the constant, κ, which compares to **Eq. 3-15**, $I(\omega)$ is determined. Therefore, the absorption cross-section of atomic Na and K in the seeded flames can be determined.

As shown in **Figure 6-3**a, the radiation emitted from the LIBS plasma is transmitted through the seeded flame by which the radiation is absorbed. Although flame absorption accompanies self-absorption, the flame absorption may be corrected whilst self-absorption is unavoidable. The calibration curves may be significantly improved by correcting the flame absorption. Flame absorption may be corrected by, firstly, using a schematic to describe the absorption scheme, as shown in **Figure 6-10**a. A top view of the schematic reveals that the isotropic radiation emitting from the LIBS plasma transmits through the seeded flame where the flame absorption occurs. Unlike normal absorption, flame absorption ought to be considered a volumetric absorption. The volumetric absorption has been taken into account to modify **Eq. 6-12** and **Eq. 6-13**, as presented in the following equations:

$$\ln\left(\frac{I_{act}}{I_{exp}}\right) = \sum \alpha(\omega) \cdot \sum x_i$$
$$\sum \alpha(\omega) = \varepsilon \cdot \sum (n_s \cdot \sigma_a(\omega))$$

Eq. 6-16

where;

$\sum$: volumetriccalculation of $\alpha(\omega)$, $\sigma_a(\omega)$ and x

$\sum \alpha(\omega) : m^{-3}$ (total α in the cone) $\qquad$ $\sum x_i : m^3$ (total absorption length in a cone)

ε: ratio of atomic Na or K of $[\mathrm{Na}]_{total}$ or $[K]_{total}$ in the seeded flames

For normal absorption, the Beer-Lambert law is used to measure the number density of atoms per unit volume (n_s) to which the absorption is proportional, as indicated in **Eq. 6-13**. n_s can be obtained using **Eq. 6-2** divided by **Eq. 6-3** based on the assumption of a constant seeding process. Due to the particularity of the flame absorption, once the concentrations of the seeded alkali salts were calculated, and the concentrations of atomic Na and K in the seeded flame, for the approximate flame temperature of 1500 K, could be estimated. The factor, ε, was estimated to be 0.020 and 0.018 for atomic Na and K, respectively. The value of ε for atomic Na in the flame was experimentally verified in **Section 3.3.8**. The $\sum(n_s \cdot \sigma_a(\omega))$ was considered to be the summation of the product of the absorption cross-section and number density and $\sum x_i$ are considered to be a cone whose volume is given by:

$$\sum x_i = \Delta v = \frac{1}{3} \cdot \pi \cdot r_{cone}{}^2 \cdot h_{cone}$$

Eq. 6-17

where, r_{cone} is the radius of the base circle (m) and h_{cone} is the height of the cone (m), as indicated in **Figure 6-10**. Thence, a modified Beer-Lambert law was obtained to correct the raw experimental intensities of $[Na]_{total}$ and $[K]_{total}$, as described below:

$$\ln(I_{act}) = [\varepsilon \cdot \sum (n_s \cdot \sigma_a(\omega)) \cdot \Delta v] \cdot \ln(I_{exp})$$

Eq. 6-18

By use of **Eq. 6-16** and **Eq. 5-1** and assigning b the value of 1 in **Eq. 5-1**, two modified calibration curves for both of $[Na]_{total}$ and $[K]_{total}$, (**Figure 6-12**), can be obtained, as in the following equations:

$$I_{Na} = 426.674 \cdot C_{Na}$$

Eq. 6-19

$$I_K = 219.500 \cdot C_K$$

Eq. 6-20

where, I_{Na} and I_K are LIBS intensities corresponding to the concentrations of Na and K seeded

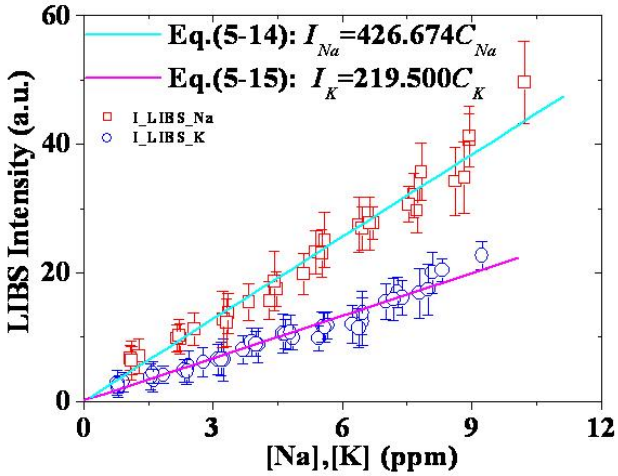

Figure 6-12 Final calibration curves for the measurement of $[Na]_{total}$ and $[K]_{total}$ using LIBS, corrected for signal trapping, as shown in **Eq. 6-19** and **Eq. 6-20**; the error was multiplied by a factor of 10 to clearly present the error bars. The errors of the fitting equations of [Na] and [K] are respectively 2.68 and 2.89%.

into flames. As shown in **Figure 6-12**, two calibration curves reveal good linearity without evidence of self-absorption, indicating that LIBS is capable of instantaneously measuring the concentrations of target species during combustion. However, a larger variation of experimental intensities with higher concentrations of seeded salts was observed, indicating that self-absorption had become more significant due to higher concentrations of seeded salts led to greater self-absorption. Therefore, the application of the LIBS measurement for high concentration measurement is constrained by significant self-absorption.

6.3.2 Quantitative Measurement

Temporal release intensities of Na and K with four equivalence ratios using LIBS, as presented in **Figure 6-13**, demonstrate three combustion stages which are consistent with those introduced in **Chapter 5** using AES. The time-resolved release of $[Na]_{total}$ and $[K]_{total}$ measured at a single point during the burning of solid-fuel particles was quantitatively investigated by applying two appropriate calibration curves, as shown in **Figure 6-14**. The $[Na]_{total}^{max}$ and $[K]_{total}^{max}$ measured at a single point in the plume of burning solid-fuel particles during the devolatilisation and char phases with four equivalence ratios using LIBS have been

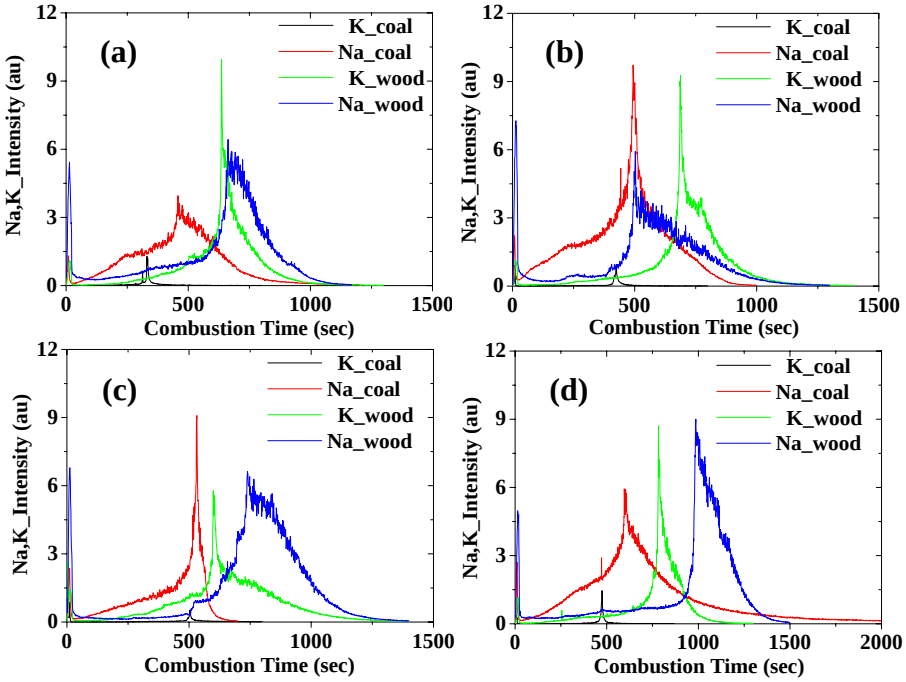

Figure 6-13 Raw time-resolved measurements of $[Na]_{total}$ and $[K]_{total}$ at a single point of the plume of burning solid-fuel particles using LIBS with equivalence ratios of (a) 1.149 (b) 1.252 (c) 1.287 and (d) 1.336

summarized in **Table 6-4**. The $[Na]_{total}^{max}$ and $[K]_{total}^{max}$ during the char phase were observed to occur at the end of this phase, which was observed in **Chapter 5** using the AES technique.

Due to the variation of wavelength between the D_1 lines of atomic Na and K, both species were individually measured which improves the LOD. For the present LIBS measurement, it is difficult to conduct a Na-to-K ratio ($R_{K/Na}$) owing to the variation of composition of each solid-fuel particle. When using LIBS and SAES, $R_{K/Na}$ may only be only available for wood combustion with an equivalence ratio of 1.149. The SAES measurement supports the present LIBS measurement, providing qualitative investigation during combustion.

6.3.2.1 Devolatilisation Phase

For PLIF measurement, the SNR is too low to measure atomic Na during the devolatilisation phase of a burning Loy Yang Brown coal particle owing to the sooty interference [11]. To investigate Na and K release quantitatively, the time-resolved release of $[Na]_{total}$ and $[K]_{total}$

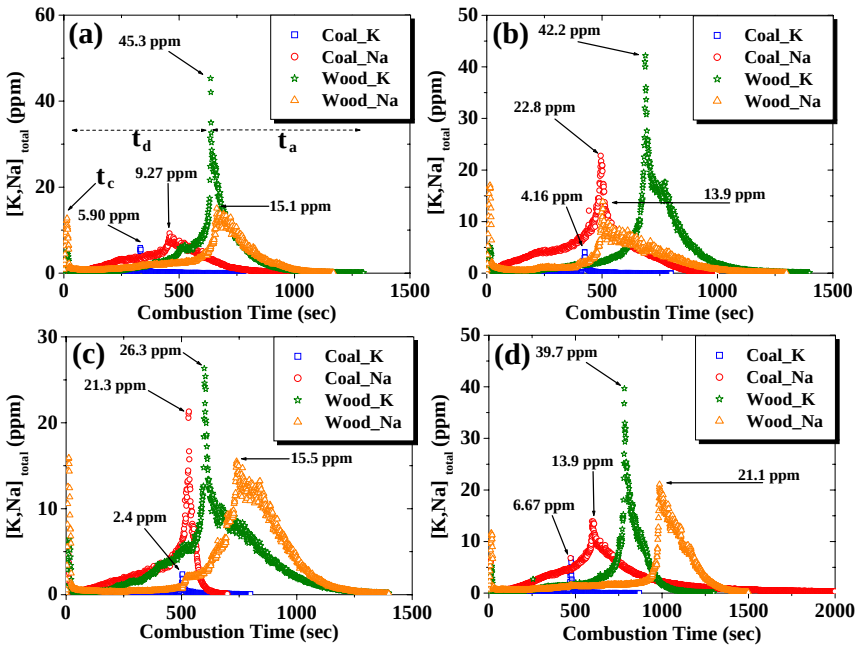

Figure 6-14 By applying calibration, the time-resolved $[Na]_{total}$ and $[K]_{total}$ can be achieved using LIBS with equivalence ratios of (a) 1.149 (b) 1.252 (c) 1.287 and (d) 1.336. τ_d, τ_c and τ_a have been defined in **Chapter 5**.

during the burning of solid-fuel particles using LIBS was performed. The release during the devolatilisation was investigated quantitatively with four equivalence ratios of 1.149, 1.252, 1.287 and 1.336, as shown in **Figure 6-15**. The $[Na]_{total}^{max}$ during the devolatilisation of wood combustion was readily observed to be high, indicating that the emission of abundant Na species may lead to significant issues, such as slagging and fouling [6]. This particular investigation showed that Na species release during the devolatilisation of wood is significant.

Comparing the ratios of the peak intensities of atomic Na or K released during the char and devolatilisation phases in **Figure 5-9** and **Figure 5-12** ($R_{K\_char/de}$ and $R_{Na\_char/de}$) with those of the $[Na]_{total}^{max}$ and $[K]_{total}^{max}$ during the char and devolatilisation phases illustrated in **Figure 6-13** ($R_{K\_total\_char/de}$ and $R_{Na\_total\_char/de}$), the $R_{K\_char/de}$ and $R_{Na\_char/de}$ can be observed to decrease with richer equivalence ratios, while a random pattern was found for the $R_{K\_total\_char/de}$ and $R_{Na\_total\_char/de}$. This indicates that the $R_{K\_char/de}$ and $R_{Na\_char/de}$ using AES are affected by flame temperatures, which are dominated by equivalence ratios, because the formation of atomic Na and K in the flame relies on the atomization conditions [38, 237]. In addition, as well as

Table 6-4 Summary of the $[Na]_{total}^{max}$ and $[K]_{total}^{max}$ released from burning solid-fuel particles with four equivalence ratios using LIBS; the errors of [Na] and [K] are respectively 2.89 and 2.69%.

Stages		Devolatilization	Char
Peak Release		$[K]_{Total}^{max}/[Na]_{total}^{max}$(ppm)	
Coal	1.149	3.53/3.06	5.90/9.27
	1.252	4.16/5.18	4.16/22.8
	1.287	3.88/5.51	2.40/21.3
	1.336	3.03/6.35	6.67/13.9
Wood	1.149	5.12/12.8	45.3/15.1
	1.252	5.19/17.0	42.2/13.9
	1.287	6.50/15.9	26.3/15.5
	1.336	5.22/11.6	39.7/21.1

certain flame conditions, the $R_{K\_total\_char/de}$ and $R_{Na\_total\_char/de}$ (using the LIBS technique) were affected by the stability of laser energy and composition variation of the solid-fuel particles. In order to reduce the impact of laser energy and any induced uncertainty, therefore, an average of 50 images was produced during calibration. Although the composition variation proved unpredictable for both methods, the flame condition was the only factor dominating the measurement of atomic Na and K using AES (rapid response). Time-resolved intensities using AES demonstrated a consistent tendency, while those using LIBS revealed the unexpected patent.

The ratio between the intensities of atomic Na and K using LIBS in the present arrangement was meaningless, but the AES measurement provided a qualitative analysis of atomic Na and K release that was able to indicate the relative amount of atomic Na and K released during combustion. Moreover, the quantitative analysis using LIBS provided evidence that significant amounts of Na species, except atomic Na, were released during volatile combustion. This may be an issue if a sticky deposit forms on heat transfer surfaces [1, 6] when wood is used for combustion. In addition, alkali chlorides were formed leading to corrosion with high Cl content during the devolatilisation [1, 178].

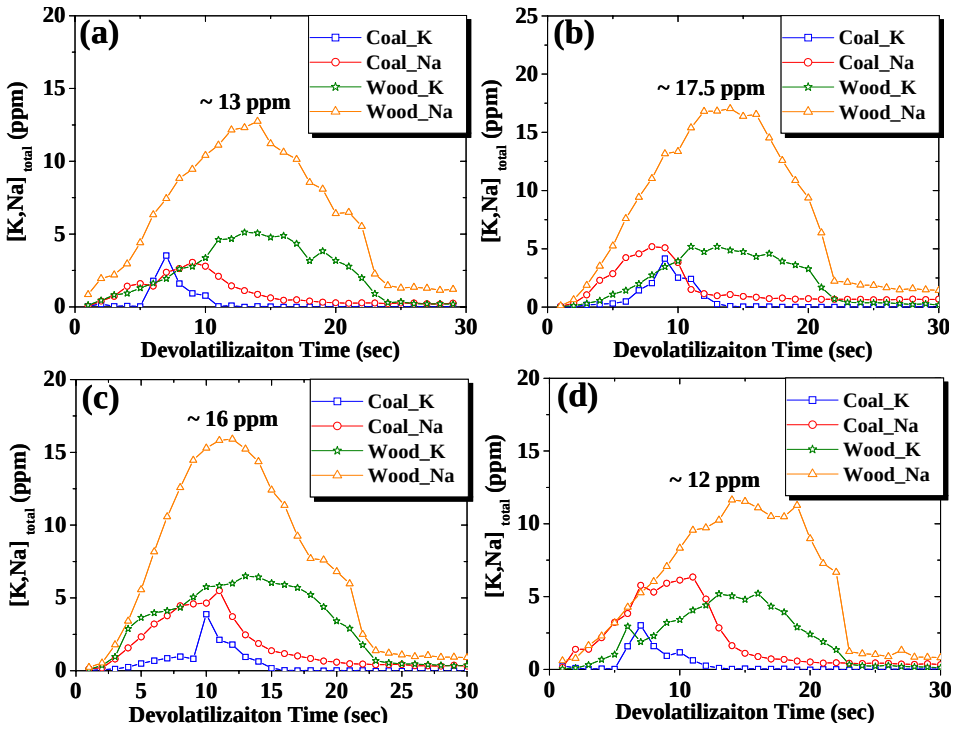

Figure 6-15 $[Na]_{total}$ and $[K]_{total}$ during the devolatilisation of burning solid-fuel particles with equivalence ratios of (a) 1.149 (b) 1.252 (c) 1.287 and (d) 1.336

Three sub-stages of atomic Na and K release associated with particle shrinkage were observed in **chapter 5**. However, this is not evident in **Figure 6-15**. This is because the intensities of atomic Na and K reported in the previous chapter were dominated by the release rates associated with the combustion for the three compositions of wood. The instantaneous records of $[Na]_{total}$ and $[K]_{total}$, on the other hand, show that the $[Na]_{total}^{max}$ and $[K]_{total}^{max}$ occur in the middle of the wood devolatilisation. This timing is consistent with the shrinking rates introduced in **Figure 5-28** that the peak intensities of atomic Na and K that occur at the end of cellulose combustion (the second sub-stage). Alkali species release increases during devolatilisation, and the intensities of atomic Na and K are sensitive to the temperature of the volatile flame. The variation between the intensity of atomic Na or K was therefore observed to be associated with the three sub-stages of wood devolatilisation. However, $[Na]_{total}$ and $[K]_{total}$ also account for other alkali species in the volatile flame, which were not measured in **Chapter 5**, leading to the indistinct boundaries between the three sub-stages.

6.3.2.2 Char Phase

As indicated in **Figure 6-14**, the time-resolved $[Na]_{total}$ and $[K]_{total}$ were measured using quantitative LIBS with four equivalence ratios. The LIBS results were slightly inconsistent with the results reported in **Chapter 5**. Atomic Na and K release and the shrinkage of solid-fuel particles were profiled, as were the periods of char phase increased. Observations were that both the release rates and intensities of atomic Na and K decreased with richer equivalence ratios. Anomalies in $[Na]_{total}$ and $[K]_{total}$ during the char phase of burning solid-fuel particles are presented in **Figure 6-16**. The anomaly, especially $[Na]_{total}^{max}$ in coal, may be caused by the variation in the compositions of solid-fuel particles.

For the AES measurement conducted in **Chapter 4**, the intensities of atomic Na and K release were affected by flame temperatures. For example, significant composition variation occurred to induce greater intensity of atomic Na for coal, as shown in **Figure 5-9**b. The profiles

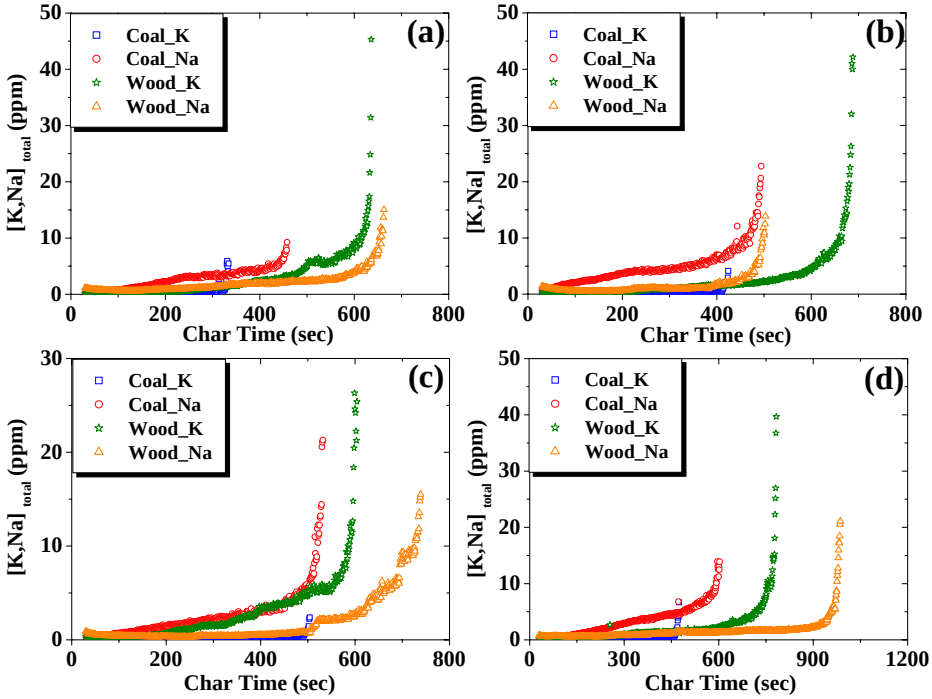

Figure 6-16 Time-resolved concentrations of $[Na]_{total}$ and $[K]_{total}$ for Loy Yang brown coal and pine wood with four equivalence ratios of (a) 1.149 (b) 1.252 (c) 1.287 and (d) 1.336 during the char phase demonstrate the multiple sub-stages consistent with those proposed in **Chapter 5**.

(**Figure 6-16**) generally exhibit a tendency consistent with the results in **Figure 5-9** and **Figure 5-12** showing richer equivalence ratios inhibit the release of atomic Na and K. Therefore, the ash phase was observed to last longer in richer conditions than that in leaner ones and the intensities of atomic Na and K were weaker. In addition, the instantaneous records of $[Na]_{total}$ and $[K]_{total}$ were not measured simultaneously so that the contribution of composition variation was enhanced. However, the time-resolved concentrations demonstrated a similar tendency to longer duration during the char phase, which shows in the sharp slopes of the temporal histories at the end of char phase and both intensities of atomic Na and K were proposed in **Chapter 5**.

The temporal histories of $[Na]_{total}$ and $[K]_{total}$ for the combustion of coal and wood char particles reveal multiple sub-stages (in **Figure 6-16**) consistent with those reported in **Chapter 4** and the quantity of atomic Na released from burning coal particles measured using PLIF and associated with the shrinking particles [12]. This indicates that alkali species are released in conjunction with shrinking particle size. Although the historical results are not identical to those introduced in **Chapter 5**, due to the variation between the two techniques, similarity between the results obtained using the two methods has been observed and is able to verify the assumption of the three-shell layer for the combustion of char particles.

6.3.2.3 Ash Phase

As introduced in **Chapter 5**, alkali species release during the ash phase is mainly dominated by the flame temperature (the provided thermal energy). The historic results, as shown in **Figure 6-17**, demonstrate a tendency similar to that reported when using AES. Potassium species decayed rapidly in the early ash phase revealing similar behaviour that indicates Na and K species are dominant in ash and flue gas, respectively. Except for the possible presence of Cl favouring K release to form KCl [232, 233, 241-243] (Cl has been released with the temperature above 1000 K), the lower thermal pyrolysis energy for K compounds is the likely

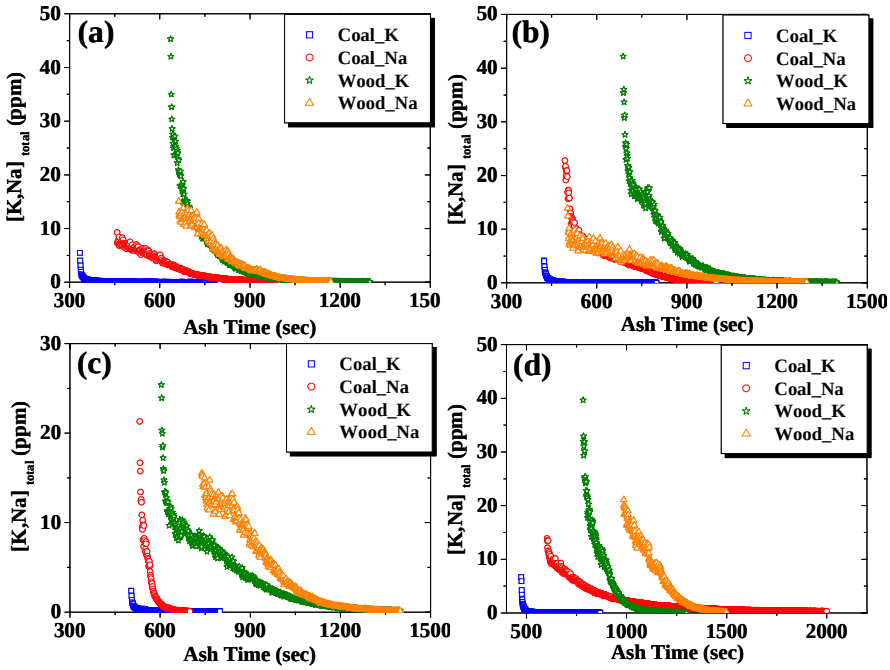

Figure 6-17 Time-resolved profiles of $[Na]_{total}$ and $[K]_{total}$ for Loy Yang brown coal and pine wood with four equivalence ratios of (a) 1.149 (b) 1.25 (c) 1.87 and (d) 1.336 during the ash phase demonstrate different release behaviours of [Na] and [K].

reason for sharp decay rate of K species.

For brown coal ash, due to the enormous amount of Al_2O_3 and significant SiO_2 (see **Table 2-1**), the possible alkali compounds are sanidine ($K_2O \cdot Al_2O_3 \cdot 6SiO_2$), albite ($Na_2O \cdot Al_2O_3 \cdot 6SiO_2$) and alkali aluminates ($K_2O \cdot Al_2O_3$ and $Na_2O \cdot Al_2O_3$). The initial Na and K release contribute to the thermal pyrolysis of alkali aluminates and then the later release through thermal pyrolysis of sanidine and albite. The slow and persistent release profiles are the results of the higher pyrolysis energy required. For pine wood, ash mainly contains alkali silicates and minor sanidine and albite.

Given that richer conditions inhibit the release of alkali species during the char phase, similar results using quantitative LIBS have been observed, as presented in **Table 6-5**. Generally the release of alkali species during the devolatilisation is not significant compared to the total amount released. However, this does not mean the release of alkali species during devolatilisation is not critical. In fact, a sticky deposit forms on the heat transfer surfaces [1, 170] and the deposit reacts with Cl and sulphur (S) favouring corrosion [244]. Furthermore,

Table 6-5 Release ratios of $[Na]_{total}$ and $[K]_{total}$ for the Loy Yang brown coal and pine wood particles during the three combustion stages with four equivalence ratios. Generally, alkali species release is inhibited with richer equivalence ratios during the char phase. The errors of total Na and K released from burning coal and wood particles are respectively 8.4 and 3.5%.

	Loy Yang coal		Pine wood		Loy Yang coal		Pine wood	
	Φ=1.149				Φ=1.252			
	K	Na	K	Na	K	Na	K	Na
τ_d	6%	1%	1%	5%	11%	1%	1%	7%
τ_c	50%	46%	39%	38%	43%	54%	33%	23%
τ_a	44%	53%	60%	57%	45%	45%	65%	69%
	Φ=1.287				Φ=1.336			
τ_d	11%	2%	2%	4%	7%	1%	2%	3%
τ_c	44%	76%	33%	30%	44%	37%	39%	32%
τ_a	45%	22%	66%	66%	49%	62%	60%	65%

co-firing with a high Cl biomass favours the release of atomic K during the devolatilisation of coal particles to form $KCl_{(g)}$, which is a most stable compound at temperatures above 1000 K [245]. Although S additives have been used to reduce alkali chloride [246], this also raises another environmental issue, sulphide release. In addition, the release of Na species during the devolatilisation of wood is also significant in terms of deposing sticky residue on the heat transfer surfaces.

Table 6-5 shows that generally the richer equivalence ratios inhibit the release of alkali species. Due to the variation in the individual solid-fuel particles, anomaly occurs. However, the overall tendency in the particle behaviour can still be observed. The particular anomaly occurring in the Na release of the burning coal particle with the equivalence ratio of 1.287 might result from the sudden falling ash particles due to the loose ash structure of burning solid-fuel particles.

6.3.3 Limit of Calibration Curve

The quantitative LIBS measurement introduced in this chapter is based on the calibration curves performed at different [Na] and [K] levels. The curves were corrected by the particular sort of signal trapping used in the present experimental arrangement. Although the calibration

curves successfully calibrated the emission of $[Na]_{total}$ and $[K]_{total}$ at a single point inside the plume of burning solid-fuel particles, two particular issues need to be addressed. The first issue is the self-absorption of plasma, which has been ignored thus far. It requires further investigation to determine the self-absorption coefficient, *b*, as shown in **Eq. 6-7**:

$$I_{exp} = a_2 \cdot [\mathrm{X}]_{species}^{b} \cdot \mathrm{e}^{-a_1 \cdot [\mathrm{X}]_{species}} \qquad \text{Eq. 6-7}$$

To correct the self-absorption may be achieved by conducting the calibration process with very low concentrations of seeded salt solutions as the self-absorption coefficient, *b*, can be considered to be 1. In a typical ICP-AES measurement, the liquid sample is diluted about 1000 times to reduce self-absorption. Then a slope of the calibration curve is obtained using these low concentrations. (the self-absorption coefficient is considered to be 1 within certain range of low concentrations of seeders). It is important that the slope represents the value, a_2. If the calibration curve exhibits a consistent slope, and there is a high concentration regime where the self-absorption is not negligible, the individual value of the self-absorption coefficient that corresponds to the concentration of the target species can be determined. This can be used to correct the individual LIBS intensity shown in **Figure 6-11** to eliminate self-absorption in the calibration curves.

The second issue is related to the reliability of the calibration curves. As shown in **Figure 6-12**, the concentration range of the calibration process is about 10 ppm. However, the $[Na]_{total}^{max}$ or $[K]_{total}^{max}$ reaches the level of 45 ppm. In the future, research should be conducted into the calibration process using a wider concentration range, such as lower and higher concentrations than those used in the current work. When considering the linear calibration curves with the same slopes and the $[Na]_{total}^{max}$ or $[K]_{total}^{max}$, which are out of calibration range, it is reasonable to extrapolate the calibration curves to the higher concentration regimes.

6.3.4 Simultaneous Atomic Emission Spectroscopy

Given the wavelength difference between the D_1 lines of atomic Na and K, the [K] and [Na] were not measured simultaneously. Simultaneous atomic emission spectroscopy (SAES) was, however, simultaneously performed with using quantitative LIBS technique which compensates for the missing information to correlate the release tendency proposed in **Chapter 5**. The temporal histories using SAES with the equivalence ratios of 1.149 and 1.336, as presented in **Figure 6-18**, were observed consistently with the results with AES. The SAES measurement shows that the peak emission of atomic Na and K both occurred at the end of the char phase which corresponds to the timing of $[K]_{total}^{max}$ and $[Na]_{total}^{max}$ using the quantitative LIBS (see **Figure 6-14**). Moreover, the SAES measurement verified the time-resolved [K] and [Na] found using the quantitative LIBS, which was consistent with results from AES. This indicates that the emission of atomic Na and K is proportional to the total release temporally because of the flame temperatures, which are used to atomize Na and K species. Furthermore, the flame conditions dominate not only the flame temperatures but also the hydrogen reduction process.

In the current study, the SAES measurement was only applied to provide complementary information. In any future experiments, experimental intensities should be correlated using SAES with those from quantitative LIBS in order to provide insight into combustion

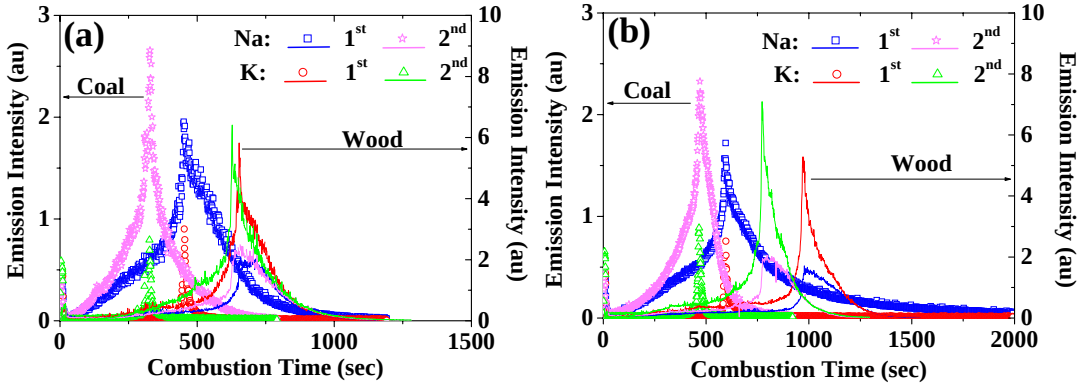

Figure 6-18 The SAES measurement was conducted with the quantitative LIBS with the equivalence ratios of (a) 1.149 and (b) 1.336. It provides information about Na and K released at the end of char phase.

modelling of burning solid-fuel particles.

6.3.5 Limit of Detection (LOD)

The property of the LIBS technique, the Limit of Detection (LOD), is important and can be calculated by [86, 87, 247]:

$$\text{L.O.D.} = \frac{3 \cdot \sigma}{S}$$

Eq. 6-21

where, σ is the mean relative standard deviation (R.S.D.) and S is the slope of the calibration equation. The values of S for Na and K, which can be obtained from the calibration curves (as represented in **Eq. 6-19** and **Eq. 6-20**) are 426.674 and 219.500, respectively, as shown in **Figure 6-12**. The values of σ for Na and K in the current study were calculated to be respectively 4.125% and 5.268% for [Na] and [K]. Therefore, the LOD for Na and K were 29 and 72 ppb, respectively. The LOD was found to be more competitive than other species proposed in the literature [51, 55, 58, 247], generally ranging from 0.22 to 136 ppm. Along with variations in the methods of measurement, the LOD is related to the type of sample, which is flame in this study. For solid samples, more energy is required to break the lattice bonding and then to disassociate molecules into atomic form. Significant heat loss is caused by the thermal conduction which results in the higher LOD. The energy required for a gaseous sample and the heat loss are lower than those for solid and liquid samples, which results in a better LOD (smaller values).

For the sample in flames, the flame provides a high temperature environment which partially atomizes the alkali species and the heat loss of LIBS plasma is low. Therefore, the thermal perturbation inside the LIBS plasma is weak because the laser energy used to disassociate alkali compounds into atomic forms, leading to the better LOD. This is the advantage of LIBS when it is employed as a real-time technique to monitor the emission of target species in

solid-fuel combustion.

6.3.6 Release Ratio ([K]/[Na])

The release ratio of [K]/[Na] for the burning solid-fuel particles reveals the relationship between equivalence ratios and release behaviour. The ratio demonstrates the release of alkali species during the burning of solid-fuel particles. The ratio of $[\mathrm{K}]_{total}^{max}/[\mathrm{Na}]_{total}^{max}$, as indicated in **Figure 6-19**, along with the peak release during the phases of devolatilisation and char combustion, reveal how equivalence ratios affect the release of alkali species associated with burning solid-fuel particles. There appears to be a tendency for richer equivalence ratios to inhibit the release of alkali species except for the ratio of $[\mathrm{K}]_{total}^{max}/[\mathrm{Na}]_{total}^{max}$ in the wood devolatilisation. Although the ratio was obtained based only on the peak concentrations released during the devolatilisation and char phases, it still demonstrates the release scenario. It is not clear whether the real regime of Na species release during the wood devolatilisation fits the conclusion proposed in **Chapter 5**. There is the implication that the characteristics of the characteristics of the Na species released from the volatile combustion of pine wood are more complicated than can be account for by the simple pore structures. The ratio of [K]/[Na] for different purposes can provide insight into the modelling of alkali species release during solid-fuel combustion. Unlike the release ratio obtained in **Chapter 5** demonstrating the qualitatively relative intensities between atomic Na and K, the quantitative ratio of [K]/[Na] reveals the fundamental properties of alkali species release. However, [K] and [Na] were measured using two individual solid-fuel particles. Due to the possible variation between solid-fuel particles, the ratio of [K]/[Na] cannot be used to represent the fundamental release during combustion. Therefore, it is necessary to choose two results with a similar time frame and intensities for a meaningful ratio of [K]/[Na].

Figure 6-14(a) and **Figure 6-18**(a) reveal that the release profiles of burning wood at the equivalence ratio of 1.149 appropriately represent the ratio of $[K]_{total}/[Na]_{total}$, as indicated in **Figure 6-20** for the devolatilisation phase and **Figure 6-21** for the char and ash phases, because of the similarity of the combustion time-frame and the profiles. The three stages of release occurred during the devolatilisation at 0~3, 4~17 and 18~22 seconds, consistent with expectations outlined in **Chapter 5**, indicating that Na and K releases were associated with the devolatilisation of pine wood combustion.

The ratio of $[K]_{total}/[Na]_{total}$ presented in **Figure 6-21** indicates that the similar behaviour of the three-stage release during the char phase of pine wood particles is also consistent with other observations. This reveals the intrinsic properties of the alkali species release during the combustion of pine wood particles. Moreover, the profile of alkali species release during the ash phase similar to that reported in **Chapter 5**. Although the curve ($[K]_{total}/[Na]_{total}$) is not entirely consistent with the results from the use of AES in **Chapter 5** owing to the variation between pine wood particles, it still demonstrates the fundamental tendencies to be observed in alkali species release. For future investigations (sodium and potassium releases are simultaneously measured) about the ratios of [K]/[Na] for solid-fuel particle combustion, accurate and reliable results can be experimentally determined.

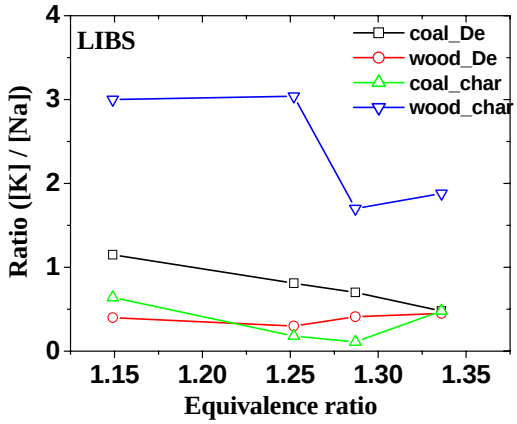

Figure 6-19 Equivalence ratios, namely 1.149, 1.252, 1.287 and 1.336, dominate the release ratio of $[K]_{total}^{max}/[Na]_{total}^{max}$ for burning solid-fuel particles. The error estimated based on the uncertainty of the calibration curves was 5%.

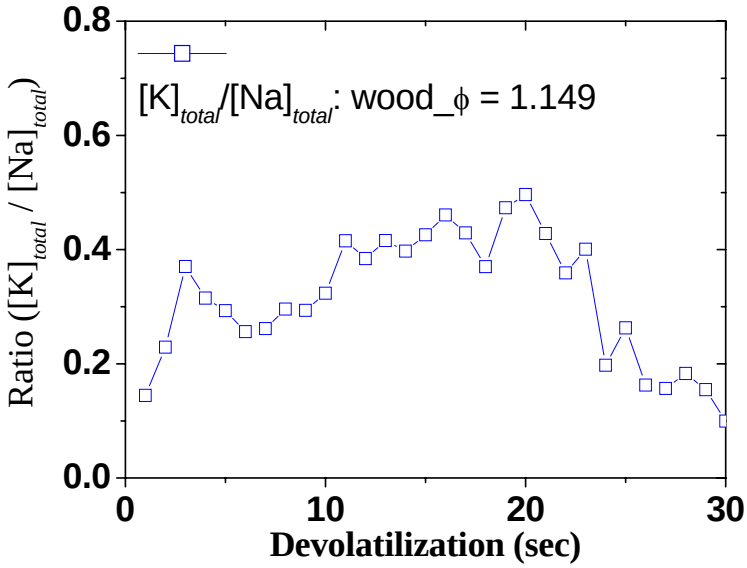

Figure 6-20 Time-resolved release ratio of $[K]_{total}/[Na]_{total}$ for the devolatilisation of a burning pine wood particle with the equivalence ratio of 1.149

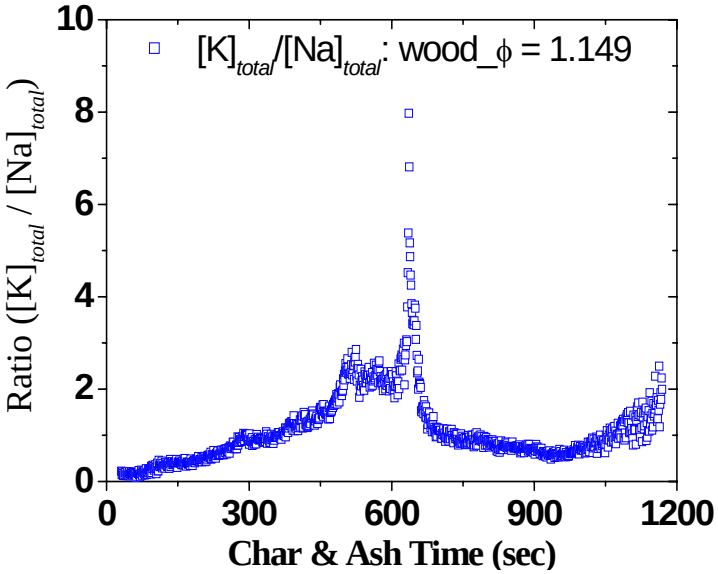

Figure 6-21 Time-resolved release ratio of $[K]_{total}/[Na]_{total}$ for the char and ash phases of a burning pine wood char particle with the equivalence ratio of 1.149

6.4 Conclusions

Laser-induced breakdown spectroscopy (LIBS) as used in the present study was shown to be a feasible technique to measure [Na] and [K] released during the instantaneous burning of solid-fuel particles. The LIBS measurement possesses the advantages of a laser technique, such as time-resolved, non-intrusive and quantitative measurements. Compared to AES and PS techniques, the LIBS technique is capable of quantitative measurement. A particular characteristic of the LIBS technique is unique. The total concentration of target species can be quantitatively investigated in a single location, which cannot be done with LIF. However, the spatial detection of [Na] and [K] using LIBS is not applicable in burning solid-fuel particles.

For the element detection using conventional LIBS, the chosen transition (wavelength) of the target species is usually persistent spectral lines other than the major resonant D_1 lines in order to reduce self-absorption. However, the chosen wavelengths for Na and K in the present arrangement are the D_1 lines (589.592 and 769.896 nm, respectively) because other persistent lines have not been observed. The gate delay and gate width were optimized to be 45 and 5 μs, respectively, reducing spectral interferences, such as the hot water lines that overlapped the D_1 line of atomic K and the natural emission of atomic Na and K emitted from the seeded flames. The critical absorption, nominated as signal trapping, was identified and expressed using the Beer-Lambert law. Using LIBS measurement has provided the practical calibration curves able to measure alkali species release quantitatively. Although the measured $[Na]_{total}^{max}$ and $[K]_{total}^{max}$ exceeded the calibration range, it was reasonable to extrapolate the calibration from the concentration range.

The time-resolved histories of $[Na]_{total}$ and $[K]_{total}$ released from the burning solid-fuel particles of Loy Yang brown coal (23 ± 3 mg, approximately spherical 3 mm diameter) and pine wood pellets (63 ± 3 mg, approximately spherical 4 mm diameter), under four

equivalence ratios of 1.149, 1.252, 1.287 and 1.336 in a premixed laminar methane flame were investigated. Three stages of devolatilisation, char and ash were observed, which was consistent with results reported in **Chapter 5**.

The $[Na]_{total}^{max}$ and $[K]_{total}^{max}$ released during the devolatilisation of the burning coal particles were found to reach the levels of 6.5 and 4 ppm, respectively. Moreover, the $[Na]_{total}^{max}$ and $[K]_{total}^{max}$ released during the devolatilisation of the burning pine wood particles were found to be 17.5 and 5 ppm, respectively. This is first time that alkali species release during the devolatilisation phase has been quantitatively measured. The $[Na]_{total}^{max}$ and $[K]_{total}^{max}$ released during the char phase of the burning coal particles were found to reach the levels of 22.8 and 6.67 ppm, respectively. In addition, the $[Na]_{total}^{max}$ and $[K]_{total}^{max}$ released during the char phase of the burning pine wood particles were found to be 21.1 and 45.3 ppm, respectively. The $[Na]_{total}^{max}$ released during the devolatilisation of a burning pine wood particle was found to be critical and a possible factor in significant corrosion and slagging in commercial power plants.

The richer equivalence ratios were observed to generally prohibit alkali species from being released during the char phase of burning solid-fuel particles. The time-resolved concentrations of alkali species released from burning wood particles were associated with particle shrinkage. The three sub-stages of $[Na]_{total}$ and $[K]_{total}$ released from burning wood char particles were consistent with results reported in **Chapter 5**. In the current study, the temporal concentrations of $[Na]_{total}$ and $[K]_{total}$ were not measured simultaneously so that the ratio, $[K]_{total}/[Na]_{total}$ obtained with four equivalence ratios, can not entirely represent the actual ratio measured in the same solid-fuel particle. However, the ratio obtained with the equivalence ratio of 1.149, due to the similar time frames of Na and K, still demonstrates the fundamental properties of alkali species released from burning solid-fuel particles.

The values of LOD for $[Na]_{total}$ and $[K]_{total}$ in the present experiment were 29 and 72 ppb,

respectively, which were significantly lower than those reported in the literature [51, 55, 58, 247]. This result was due to the target alkali Na and K being tested as in the gaseous samples, which were flames in this study.

CHAPTER 7

Conclusions

The aim of the study was to assess three optical techniques used to detect metals in high temperature environments. The five specific aims addressed in this thesis were:

(1) to demonstrate the feasibility of polarisation spectroscopy to be used for the metal detection, in particular atomic sodium (Na I) or iron (Fe I), in strong background environment

(2) to assess the feasibility of polarisation spectroscopy to be used for the quantitative measurement of atomic Na

(3) to assess the capability of existing atomic emission spectroscopy technique in the detection of atomic Na and potassium (K) released from the burning solid-fuel particles

(4) to develop the quantitative LIBS technique to be employed to detect the time-resolved [Na] and [K] released from the burning solid-fuel particles

(5) to assess the advantages and disadvantages among three techniques for metal detection in high temperature environment. The characteristics comparison among three spectroscopic techniques is shown in **Table 7-1**.

In this work, the PS measurement was divided into three parts:

- develop the mathematical equation
- detect atomic Na released from burning solid-fuel particles
- detect atomic Fe in the atmospheric welding fume.

Table 7-1 The characteristics comparison of three spectroscopic techniques employed in this work are listed. The term "Achievable" represents the theoretical feasibility with further effort but is not applicable in this work. The cost is only compared among three techniques.

	Spectroscopy Techniques		
Characteristics of Techniques	Polarization Sepctroscopy (PS)	Atomic Emission Spectroscopy (AES)	Laser-Induced Breakdown Spectroscopy (LIBS)
Quantitative	Achievable	Achievable	YES
Time-Resolved	YES	YES	YES
In-situ	YES	YES	YES
Species Subjective	Atomic forms of Na and Fe	Atomic forms of Na and K	Total Amount of Na and K
Spatial Resolution	Achievable	Achievable	NO
Calibration Process	Achievable	Achievable	YES
Cost	Highest	Lowest	Middle

THE EQUATION

The wavelengthscan results of atomic Na in the premixed laminar methane flame with rich conditions have been successfully simulated by **Eq. 3-5**:

$$I_{PS\_FIT}(\omega) = I_{baseline} + I_{PS} \times \left\{ \frac{1}{1+\left[\frac{2\times(\Delta\omega-\Delta\omega_{shift})}{\Delta\omega_{PS}}\right]^2} \right\}^n \times exp\left[\frac{-\alpha_0 \cdot L_{abs}}{1+\left(\frac{2\times\Delta\omega}{\Delta\omega_{abs}}\right)^2} \right] \qquad \text{Eq. 3-5}$$

Compared to conventional PS (only the first two parts, including the baseline and pure PS signal), the PS measurement employed in this work experiences the absorption, which is represented in the third part of **Eq. 3-5**. To use the second part of the equation, the pure PS signals can be extracted. It was found that power broadening is significant in the low concentration of atomic Na. The FWHM of atomic Na in a pure PS lineshape with a strong fluence of pump beam varies with concentrations of seeded Na. Eventually the collision dominates the power broadening in the low pump beam fluence. Moreover, the power broadening has also been verified by examining the FWHM under each concentration varied

with the pump beam fluences. The FWHM under 0.127×10^{18} atoms/m^3 with lower fluences is smaller and becomes broader with the strong pump beam fluence indicating the occurrence of power broadening.

DETECTION OF ATOMIC SODIUM

A specific wavelength chosen from the wavelengthscan results recorded the time-resolved history of atomic Na released from burning solid-fuel particles. Due to the nonlinearity of PS measurement, a quantitative measurement using PS is not applicable. However, the historical record of atomic Na released from burning solid-fuel particles was observed, especially the result of atomic Na released from volatile flames.

Simultaneous laser absorption measurement provided the absolute concentration of atomic Na in the seeded flame. The measured absolute concentration (n_s), in comparison with the total amount of seeded Na, supports the value of ratio, ε, which was assumed to be 0.02 (2%) for atomic Na present in the rich premixed laminar methane flames used in this work. Detailed information has been presented in **Table 3-4**.

DETECTION OF ATOMIC IRON

The PS measurement, as an application, was employed to detect atomic Fe in atmospheric welding fumes. It was observed that the Stark shift of atomic Fe was present in the wavelengthscan result. The wavelengthscan results have also been simulated using **Eq. 3-5**. Due to presence of the Stark shift, the wavelengthscan of atomic Fe in the atmospheric plasma comprises two regimes, which can both be simulated by **Eq. 3-5**. The transition, 385.990 nm, was selected to investigate the behaviour of atomic Fe dependent on the welding currents, content of buffer gases, radial position within the welding fume and energies of the pump beam. It was found that the welding current required to generate the same population of atomic Fe is lower in the shielding gas He. The low welding current applied in the buffer gas

He implies that it may reduce the hazard of welding in the workplace, and reduce energy consumption.

BURNING SOLID-FUEL PARTICLES

The historic records of atomic Na and K released from the burning of solid-fuel particles was measured simultaneously and revealed instantaneous shrinkage. The combustion stages were found to be consistent with those observed using PS. The shrinking records of burning solid-fuel particles imply a three-layered burning model, and the shrinkage is consistent with the pore structures formed during devolatilisation [152].

The devolatilisation phase of burning coal and wood particles last for 12 and 22 seconds, respectively, in four equivalence ratios of 1.149, 1.252, 1.287 and 1.336, except for 25 seconds for wood particles burnt in the condition of 1.336. The timeframe of the char phase becomes longer as conditions become richer. Moreover, the intensities of atomic Na and K are weaker when solid-fuel particles are burnt in the richer conditions. It was observed that the peak releases of atomic Na and K both occur at the end of the char phase. Although the AES measurement proved sensitive to atomic Na and K, it was not applicable for quantitative measurement in the present experimental arrangement.

The quantitative measurement of the total Na ($[Na]_{total}$) and K ($[K]_{total}$) released at a single point in the plume of burning solid-fuel particles using LIBS was achieved. To achieve the quantitative measurement using LIBS, a particular type of absorption, termed as signal trapping, was identified. The signal trapping occurring in the calibration process is caused by the outer seeded flame where atomic Na or K is present. The correction of the signal trapping is based on the Beer-Lambert law. The two calibration curves of $[Na]_{total}$ and $[K]_{total}$, as are presented in **Eq. 6-19** and **Eq. 6-20**:

$$I_{Na} = 426.674 \cdot C_{Na} \qquad \text{Eq. 6-19}$$

$$I_K = 219.500 \cdot C_K \quad \text{Eq. 6-20}$$

reveal good linearity indicating that the signal trapping dominates the self-absorption. If the self-absorption is considered, the accuracy of quantitative measurement of $[Na]_{total}$ and $[K]_{total}$ released from burning solid-fuel particles is more precise.

The $[Na]_{total}^{max}$ and $[K]_{total}^{max}$ released during the devolatilisation of burning coal particles were found to reach the levels of 6.5 and 4 ppm, respectively. Moreover, the $[Na]_{total}^{max}$ and $[K]_{total}^{max}$ released during the devolatilisation of burning pine wood particles were found to be 17.5 and 5 ppm, respectively. This is the first time the monitoring of the release of alkali species during the devolatilisation phase has been quantitatively measured. The $[Na]_{total}^{max}$ and $[K]_{total}^{max}$ released during the char phase of the burning coal particles were found to reach the levels of 22.8 and 6.67 ppm, respectively. In addition, the $[Na]_{total}^{max}$ and $[K]_{total}^{max}$ released during the char phase of the burning pine wood particles were found to be 21.1 and 45.3 ppm, respectively. It was observed that the amount of $[Na]_{total}^{max}$ released during the devolatilisation of a burning pine wood particle was critical in that $[Na]_{total}^{max}$ in sufficient quantities may cause significant corrosion and slagging in commercial power plants. The $[Na]_{total}^{max}$ and $[K]_{total}^{max}$ released during the devolatilisation and char phases were summarized in **Table 6-4**.

The richer equivalence ratio inhibits the release of alkali species during combustion in four conditions discussed in this work. The pore structure formed during the devolatilisation phase dominates the combustion rate [152], which relates to the release rates of alkali species. The variation between solid-fuel particles was observed using the LIBS and SAES techniques. Although the variation of alkali content between each solid-fuel particle results in the quantitative analysis being variable, the tendency can be still observed. The richer equivalence ratio was found to inhibit the release of alkali species during the char phase of the

burning of solid-fuel particles, as shown in **Table 6-5**.

The LOD is a crucial characteristic of quantitative LIBS measurement representing the accuracy of the calibration curves. The LOD is sensitive to the types of samples being used: solid, liquid, aerosol or gas. Generally, LOD is better in gaseous samples because less energy is lost as there is no need to vaporize and dissociate the samples. For example, Yamamoto et al. [55] reported that the LODs of Ba, Be, Pb and Sr in soil samples are respectively 265, 93, 298 and 42 ppm. Unlike the poor LOD for soil samples, the LOD of $[Na]_{total}$ and $[K]_{total}$ in the flames, which are gaseous media, for the present LIBS arrangement were respectively 29 and 72 ppb due to the low dissociation energy required in the flame. Moreover, the flame medium forms a temperature barrier that reduces heat loss for LIBS plasma. Therefore, the thermal variation of LOD in gases is weaker when compared to LIBS applied to solid and liquid samples.

In summary, the optical techniques employed in this work, either qualitative or quantitative analysis, demonstrate the characteristics and limits to each technique. These results provide a comprehensive investigation of the metal detection in high temperature environments. The PS technique is able to suppress background noise for metal detection, such as Na and Fe, in high temperature environments. It can also provide a time-resolved measurement of atomic Na released from burning solid-fuel particles. The quantitative PS measurement in the present optical arrangement is not applicable, however.

Compared to laser diagnostic techniques, the AES technique provides a sensitive, rapid and simple measurement for the detection of alkali metals in flames. The intensities of atomic Na and K were the summation of radiation emitted from the entire flame, which led difficult in determining the emission volume. Therefore, quantitative measurement using the AES optical arrangement described in this study is not applicable. However, the LIBS technique employed in flames with appropriate calibration curves provides the quantitative measurement of total Na and K at a single location within flames.

Outlook

For the further investigation using quantitative LIBS, the accuracy may be improved by conducting a broad range of calibration, particularly when using rather low concentrations of calibration references due to the occurrence of weak self-absorption. When considering a target species at a highly populated level, the correction of self-absorption may improve the reliability of the calibration curves. The improvement of calibration curve reliability could complete the capability of quantitative LIBS in combustion applications. Moreover, other species released during fuel combustion may also be quantitatively determined. Mercury, for example, is a serious issue when burning coal and its control would benefit from more accurate measurement.

Quantitative PS us another area ripe for further research, which may be achievable by applying a mathematical equation. The instantaneous concentration of target species, extracted from a mathematical equation, may be achievable. This would demonstrate the advantages of PS measurement for every species released from fuel combustion. However, quantitative PS requires a fast-scan laser system in order to achieve one wavelengthscan (about 3 nm) within a few micro-seconds.

Bibliography

[1] R. W. Bryers, "Fireside slagging, fouling, and high-temperature corrosion of heat-transfer surface due to impurities in steam-raising fuels," *Progress in Energy and Combustion Science,* vol. 22, pp. 29-120, 1996.

[2] R. L. Bain, "Electricity from biomass in the Untied States: Status and future direction," *Bioresource Technology,* vol. 46, pp. 86 - 93, 1993.

[3] H. Rodriguez, R. Alvarez, and A. Enriquez, "Evaluation of different alkali treatments of bagasse pith for cultivation of Cellulomonas sp.," *World Journal of Microbiology and Biotechnology,* vol. 9, pp. 213 - 215, 1993.

[4] J. H. Turnbull, "Use of biomass in electric power generation: The california experience," *Biomass and Bioenergy,* vol. 4, pp. 75 - 84, 1993.

[5] B. Olanders and B.-M. Steenari, "Characterization of ashes from wood and straw," *Biomass and Bioenergy,* vol. 8, pp. 105-115, 1995.

[6] T. R. Miles, T. R. Miles, L. L. Baxter, R. W. Bryers, B. M. Jenkins, and L. L. Oden, "Boiler deposits from firing biomass fuels," *Biomass and Bioenergy,* vol. 10, pp. 125-138, 1996.

[7] B. M. Jenkins, L. L. Baxter, T. R. M. Jr., and T. R. Miles, "Combustion properties of biomass," *Fuel Processing Technology,* vol. 54, pp. 17 - 46, 1998.

[8] M. Steinberg and K. Schofield, "The controlling chemistry in flame generated surface deposition of Na2SO4 and the effects of chlorine," *Symposium (International) on Combustion,* vol. 26, pp. 1835-1843, 1996.

[9] M. Neville and A. F. Sarofim, "The fate of sodium during pulverized coal combustion," *Fuel,* vol. 64, pp. 384-390, 1985.

[10] B. G. Kutchko and A. G. Kim, "Fly ash characterization by SEM-EDS," *Fuel,* vol. 85, pp. 2537-2544, 2006.

[11] P. J. van Eyk, P. J. Ashman, Z. T. Alwahabi, and G. J. Nathan, "Quantitative measurement of atomic sodium in the plume of a single burning coal particle," *Combustion and Flame,* vol. 155, pp. 529-537, 2008.

[12] P. J. van Eyk, P. J. Ashman, Z. T. Alwahabi, and G. J. Nathan, "Simultaneous measurements of the release of atomic sodium, particle diameter and particle temperature for a single burning coal particle," *Proceedings of the Combustion Institute,* vol. 32, pp. 2099-2106, 2009.

[13] W. L. Saw, G. J. Nathan, P. J. Ashman, and Z. T. Alwahabi, "Assessment of the release of atomic Na from a burning black liquor droplet using quantitative PLIF," *Combustion and Flame,* vol. 156, pp. 1471-1479, 2009.

[14] W. L. Saw, G. J. Nathan, P. J. Ashman, Z. T. Alwahabi, and M. Hupa, "Simultaneous measurement of the surface temperature and the release of atomic sodium from a burning black liquor droplet," *Combustion and Flame*, vol. 157, pp. 769-777, 2010.

[15] W. L. Saw, G. J. Nathan, P. J. Ashman, and M. Hupa, "Influence of droplet size on the release of atomic sodium from a burning black liquor droplet in a flat flame," *Fuel*, vol. 89, pp. 1840-1848, 2010.

[16] A. C. Eckbreth, *Laser diagnostics for combustion temperature and species*, 2nd ed.: Amsterdam : Gordon and Breach, 1996.

[17] O. Lucas, Z. T. Alwahabi, V. Linton, and K. Meeuwissen, "Laser Diagnostics of Welding Plasma by Polarization Spectroscopy," *Applied Spectroscopy*, vol. 61, pp. 565-569, 2007.

[18] Z. T. Alwahabi, J. Zetterberg, Z. S. Li, and M. Aldén, "High resolution polarization spectroscopy and laser induced fluorescence of CO2 around 2 μm," *The European Physical Journal D*, vol. 42, pp. 41-47, 2007.

[19] D. Alter, "On Certain Physical Properties of Light Produced by the Combustion of Different Metals in an Electric Spark Refracted by a Prism," *American Journal of Science Arts*, vol. 18, pp. 55-57, 1854.

[20] J. E. Sansonetti and W. C. Martin, "Handbook of Basic Atomic Spectroscopic Data," *Journal of Physical and Chemical Reference Data*, vol. 34, pp. 1559-2259, 2005.

[21] J. E. Sansonetti, "Wavelengths, Transition Probabilities, and Energy Levels for the Spectra of Sodium (Na I--Na XI)," *Journal of Physical and Chemical Reference Data*, vol. 37, pp. 1659-1763, 2008.

[22] J. E. Sansonetti, "Wavelengths, Transition Probabilities, and Energy Levels for the Spectra of Potassium (K I through K XIX)," *Journal of Physical and Chemical Reference Data*, vol. 37, pp. 7-96, 2008.

[23] J. R. Fuhr and W. L. Wiese, "A Critical Compilation of Atomic Transition Probabilities for Neutral and Singly Ionized Iron," *Journal of Physical and Chemical Reference Data*, vol. 35, pp. 1669-1809, 2006.

[24] W. Demtröder, *Laser Spectroscopy: Vol. 1 Basic Principles*, 4th ed. ed.: Springer Berlin Heidelberg, 2008.

[25] P. Monkhouse, "On-line diagnostic methods for metal species in industrial process gas," *Progress in Energy and Combustion Science*, vol. 28, pp. 331-381, 2002.

[26] D. Alter, "On Certain Physical Properties of the Light of the Electric Spark, Within Certain Gases, as Seen Through a Prism," *American Journal of Science Arts*, vol. 19, pp. 213-214, 1855.

[27] R. J. Reynolds and K. C. Thompson, *Atomic absorption, fluorescence, and flame emission spectroscopy: a practical approach*: New York: Wiley, 1978.

[28] A. Stefánsson, I. Gunnarsson, and N. Giroud, "New methods for the direct determination of dissolved inorganic, organic and total carbon in natural waters by Reagent-Free Ion Chromatography and inductively coupled plasma atomic emission

spectrometry," *Analytica Chimica Acta,* vol. 582, pp. 69-74, 2007.

[29] J. M. Mermet, "Is it still possible, necessary and beneficial to perform research in ICP-atomic emission spectrometry," *Journal of Analytical Atomic Spectrometry,* vol. 20, pp. 11-16, 2005.

[30] E. G. Wang, Z. G. Guo, J. Ma, M. M. Zhou, Y. K. Pu, S. Liu, G. Y. Zhang, and D. Y. Zhong, "Optical emission spectroscopy study of the influence of nitrogen on carbon nanotube growth," *Carbon,* vol. 41, pp. 1827-1831, 2003.

[31] T. Ikegami, F. Nakanishi, M. Uchiyama, and K. Ebihara, "Optical measurement in carbon nanotubes formation by pulsed laser ablation," *Thin Solid Films,* vol. 457, pp. 7-11, 2004.

[32] M. Nishio, S. Akita, and Y. Nakayama, "Cooling effect on the growth of carbon nanotubes and optical emission spectroscopy in short-period arc-discharge," *Thin Solid Films,* vol. 464-465, pp. 304-307, 2004.

[33] J. Ma, M. N. R. Ashfold, and Y. A. Mankelevich, "Validating optical emission spectroscopy as a diagnostic of microwave activated $CH_4/Ar/H_2$ plasmas used for diamond chemical vapor deposition," *Journal of Applied Physics,* vol. 105, pp. 043302-12, 2009.

[34] M. Gulás, F. Le Normand, and P. Veis, "Gas phase kinetic and optical emission spectroscopy studies in plasma-enhanced hot filament catalytic CVD production of carbon nanotubes," *Applied Surface Science,* vol. 255, pp. 5177-5180, 2009.

[35] Y. S. Woo, D. Y. Jeon, I. T. Han, N. S. Lee, J. E. Jung, and J. M. Kim, "In situ diagnosis of chemical species for the growth of carbon nanotubes in microwave plasma-enhanced chemical vapor deposition," *Diamond and Related Materials,* vol. 11, pp. 59-66, 2002.

[36] D. R. Crosley, Ed., *Laser Probes for Combustion Chemistry, Copyright, ACS Symposium Series, FOREWORD* (Laser Probes for Combustion Chemistry. American Chemical Society), 1980.

[37] J. Kiefer, A. Meyerhoefer, T. Seeger, A. Leipertz, Z. S. Li, and M. Ald´en, "OH-thermometry using laser polarization spectroscopy and laser-induced fluorescence spectroscopy in the OH A-X (1,0) band," *journal of Raman Spectrsocopy,* vol. 40, pp. 828-835, 2009.

[38] A. J. Hynes, M. Steinberg, and K. Schofield, "The chemical kinetics and thermodynamics of sodium species in oxygen-rich hydrogen flames," *The Journal of Chemical Physics,* vol. 80, pp. 2585-2597, 1984.

[39] C. Brackmann, J. Nygren, X. Bai, Z. Li, H. Bladh, B. Axelsson, I. Denbratt, L. Koopmans, P.-E. Bengtsson, and M. Aldén, "Laser-induced fluorescence of formaldehyde in combustion using third harmonic Nd:YAG laser excitation," *Spectrochimica Acta Part A: Molecular and Biomolecular Spectroscopy,* vol. 59, pp. 3347-3356, 2003.

[40] W. Demtröder, *Laser Spectroscopy: Vol. 2 Experimental Techniques,* 4th ed. ed.:

Springer Berlin Heidelberg, 2008.

[41] C. Chan and J. W. Daily, "Measurement of temperature in flames using laser induced fluorescence spectroscopy of OH," *Applied Optics,* vol. 19, pp. 1963-1968, 1980.

[42] D. R. Grieser and R. H. Barnes, "Nitric Oxide Detection in Flames by Laser Fluorescence," in *Laser Probes for Combustion Chemistry*, ed: American Chemical Society, 1980, pp. 153-158 SE-9.

[43] T. Rossmann, M. G. Mungal, and R. K. Hanson, "Nitric-Oxide Planar Laser-Induced Fluorescence Applied to Low-Pressure Hypersonic Flow Fields for the Imaging of Mixture Fraction," *Applied Optics,* vol. 42, pp. 6682-6695, 2003.

[44] C. Schulz, V. Sick, J. Heinze, and W. Stricker, "Laser-induced-fluorescence detection of nitric oxide in high-pressure flames with A-X(0, 2) excitation," *Applied Optics,* vol. 36, pp. 3227-3232, 1997.

[45] C. M. Christoph Mitscherling, Alexei A. Veselov and Karl-Heinz Gericke, "Laser-induced fluorescence spectroscopy of $^{14}N^{18}O$ and its application to breath analysis," *Isotopes in Environmental and Health Studies,* vol. 45, pp. 59-67, 2009.

[46] B. J. Kirby and B. K. Hanson, "Imaging of CO and CO2 using infrared planar laser-induced fluorescence," *Proceedings of the Combustion Institute,* vol. 28, pp. 253-259, 2000.

[47] F. Brech and L. Cross, "Optical microemission stimulated by a ruby maser," *Applied Spectroscopy,* vol. 16, p. 59, 1962.

[48] E. R. Runge, R. W. Minck, and F. R. Bryan, "Spectrochemical analysis using a pulsed laser source," *Spectrochimica Acta Part B: Atomic Spectroscopy,* vol. 20 pp. 733-736, 1964.

[49] J. Vrenegor, R. Noll, and V. Sturm, "Investigation of matrix effects in laser-induced breakdown spectroscopy plasmas of high-alloy steel for matrix and minor elements," *Spectrochimica Acta Part B: Atomic Spectroscopy,* vol. 60, pp. 1083-1091, 2005.

[50] P. K. Diwakar, P. B. Jackson, and D. W. Hahn, "The effect of multi-component aerosol particles on quantitative laser-induced breakdown spectroscopy: Consideration of localized matrix effects," *Spectrochimica Acta Part B: Atomic Spectroscopy,* vol. 62, pp. 1466-1474, 2007.

[51] W. T. Y. Mohamed, "Improved LIBS limit of detection of Be, Mg, Si, Mn, Fe and Cu in aluminum alloy samples using a portable Echelle spectrometer with ICCD camera," *Optics & Laser Technology,* vol. 40, pp. 30-38, 2008.

[52] S. Thakur, *Laser-Induced Breakdown Spectroscopy*: Elsevier Science, 2007.

[53] V. Hohreiter and D. W. Hahn, "Calibration Effects for Laser-Induced Breakdown Spectroscopy of Gaseous Sample Streams: Analyte Response of Gas-Phase Species versus Solid-Phase Species," *Analytical Chemistry,* vol. 77, pp. 1118-1124, 2005.

[54] T. Amodeo, C. Dutouquet, O. Le Bihan, M. Attoui, and E. Frejafon, "On-line determination of nanometric and sub-micrometric particle physicochemical characteristics using spectral imaging-aided Laser-Induced Breakdown Spectroscopy

coupled with a Scanning Mobility Particle Sizer," *Spectrochimica Acta Part B: Atomic Spectroscopy,* vol. 64, pp. 1141-1152, 2009.

[55] K. Y. Yamamoto, D. A. Cremers, M. J. Ferris, and L. E. Foster, "Detection of Metals in the Environment Using a Portable Laser-Induced Breakdown Spectroscopy Instrument," *Applied Spectroscopy,* vol. 50, pp. 222-233, 1996.

[56] F. W. Fifield and P. J. Haines, *Environmental Analytical Chemistry*: Blackwell Publishing, 2000.

[57] K. Y. Yamamoto, D. A. Cremers, L. E. Foster, M. P. Davies, and R. D. Harris, "Laser-Induced Breakdown Spectroscopy Analysis of Solids Using a Long-Pulse (150 ns) Q-switched Nd:YAG Laser," *Applied Spectrosopy,* vol. 59, pp. 1082-1097, 2005.

[58] G. Arca, A. Ciucci, V. Palleschi, S. Rastelli, and E. Tognoni, "Trace Element Analysis in Water by the Laser-Induced Breakdown Spectroscopy Technique," *Applied Spectroscopy,* vol. 51, pp. 1102-1105, 1997.

[59] L. Dudragne, P. Adam, and J. Amouroux, "Time-Resolved Laser-Induced Breakdown Spectroscopy: Application for Qualitative and Quantitative Detection of Fluorine, Chlorine, Sulfur, and Carbon in Air," *Applied Spectroscopy,* vol. 52, pp. 1321-1327, 1998.

[60] P. Stavropoulos, A. Michalakou, G. Skevis, and S. Couris, "Laser-induced breakdown spectroscopy as an analytical tool for equivalence ratio measurement in methane-air premixed flames," *Spectrochimica Acta Part B: Atomic Spectroscopy,* vol. 60, pp. 1092-1097, 2005.

[61] P. Stavropoulos, A. Michalakou, G. Skevis, and S. Couris, "Quantitative local equivalence ratio determination in laminar premixed methane-air flames by laser induced breakdown spectroscopy (LIBS)," *Chemical Physics Letters,* vol. 404, pp. 309-314, 2005.

[62] M. S. Mansour, H. Imam, K. A. Elsayed, and W. Abbass, "Local equivalence ratio measurements in turbulent partially premixed flames using laser-induced breakdown spectroscopy," *Spectrochimica Acta Part B: Atomic Spectroscopy,* vol. 64, pp. 1079-1084, 2009.

[63] J. Kiefer, J. W. Tröger, T. Seeger, A. Leipertz, B. Li, Z. S. Li, and M. Aldén, "Laser-induced breakdown spectroscopy in gases using ungated detection in combination with polarization filtering and online background correction," *Measurement Science & Technology,* vol. 21, p. 065303, 2010.

[64] M. Broström, H. Kassman, A. Helgesson, M. Berg, C. Andersson, R. Backman, and A. Nordin, "Sulfation of corrosive alkali chlorides by ammonium sulfate in a biomass fired CFB boiler," *Fuel Processing Technology,* vol. 88, pp. 1171-1177, 2007.

[65] T. Ctvrtnickova, M. P. Mateo, A. Yañez, and G. Nicolas, "Laser Induced Breakdown Spectroscopy application for ash characterisation for a coal fired power plant," *Spectrochimica Acta Part B: Atomic Spectroscopy,* vol. 65, pp. 734-737, 2010.

[66] A. Stankova, N. Gilon, L. Dutruch, and V. Kanicky, "A simple LIBS method for fast

quantitative analysis of fly ashes," *Fuel*, vol. 89, pp. 3468-3474, 2010.

[67] L. G. Blevins, C. R. Shaddix, S. M. Sickafoose, and P. M. Walsh, "Laser-Induced Breakdown Spectroscopy at High Temperatures in Industrial Boilers and Furnaces," *Applied Optics*, vol. 42, pp. 6107-6118, 2003.

[68] A. Molina, P. M. Walsh, C. R. Shaddix, S. M. Sickafoose, and L. G. Blevins, "Laser-induced breakdown spectroscopy of alkali metals in high-temperature gas," *Applied Optics*, vol. 45, pp. 4411-4423, 2006.

[69] L. L. Baxter, T. R. Miles, T. R. Miles, B. M. Jenkins, T. Milne, D. Dayton, R. W. Bryers, and L. L. Oden, "The behavior of inorganic material in biomass-fired power boilers: field and laboratory experiences," *Fuel Processing Technology*, vol. 54, pp. 47-78, 1998.

[70] A. Uhl, K. Loebe, and L. Kreuchwig, "Fast analysis of wood preservers using laser induced breakdown spectroscopy," *Spectrochimica Acta Part B: Atomic Spectroscopy*, vol. 56, pp. 795-806, 2001.

[71] M. P. Mateo, G. Nicolas, and A. Yañez, "Characterization of inorganic species in coal by laser-induced breakdown spectroscopy using UV and IR radiations," *Applied Surface Science*, vol. 254, pp. 868-872, 2007.

[72] A. Mansoori, B. Roshanzadeh, M. Khalaji, and S. H. Tavassoli, "Quantitative analysis of cement powder by laser induced breakdown spectroscopy," *Optics and Lasers in Engineering*, vol. 49, pp. 318-323, 2011.

[73] E. Tognoni, V. Palleschi, M. Corsi, and G. Cristoforetti, "Quantitative micro-analysis by laser-induced breakdown spectroscopy: a review of the experimental approaches," *Spectrochimica Acta Part B: Atomic Spectroscopy*, vol. 57, pp. 1115-1130, 2002.

[74] D. Mukherjee, A. Rai, and M. R. Zachariah, "Quantitative laser-induced breakdown spectroscopy for aerosols via internal calibration: Application to the oxidative coating of aluminum nanoparticles," *Journal of Aerosol Science*, vol. 37, pp. 677-695, 2006.

[75] C. López-Moreno, S. Palanco, and J. J. Laserna, "Quantitative analysis of samples at high temperature with remote laser-induced breakdown spectrometry using a room-temperature calibration plot," *Spectrochimica Acta Part B: Atomic Spectroscopy*, vol. 60, pp. 1034-1039, 2005.

[76] S. Laville, M. Sabsabi, and F. R. Doucet, "Multi-elemental analysis of solidified mineral melt samples by Laser-Induced Breakdown Spectroscopy coupled with a linear multivariate calibration," *Spectrochimica Acta Part B: Atomic Spectroscopy*, vol. 62, pp. 1557-1566, 2007.

[77] M. Sabsabi, V. Detalle, M. A. Harith, W. Tawfik, and H. Imam, "Comparative study of two new commercial echelle spectrometers equipped with intensified CCD for analysis of laser-induced breakdown spectroscopy," *Applied Optics*, vol. 42, pp. 6094-6098, 2003.

[78] B. Le Drogoff, J. Margot, M. Chaker, M. Sabsabi, O. Barthélemy, T. W. Johnston, S. Laville, F. Vidal, and Y. von Kaenel, "Temporal characterization of femtosecond laser

pulses induced plasma for spectrochemical analysis of aluminum alloys," *Spectrochimica Acta Part B: Atomic Spectroscopy,* vol. 56, pp. 987-1002, 2001.

[79] E. Tognoni, G. Cristoforetti, S. Legnaioli, and V. Palleschi, "Calibration-Free Laser-Induced Breakdown Spectroscopy: State of the art," *Spectrochimica Acta Part B: Atomic Spectroscopy,* vol. 65, pp. 1-14, 2010.

[80] L. Sun and H. Yu, "Correction of self-absorption effect in calibration-free laser-induced breakdown spectroscopy by an internal reference method," *Talanta,* vol. 79, pp. 388-395, 2009.

[81] S. Palanco and J. J. Laserna, "Full automation of a laser-induced breakdown spectrometer for quality assessment in the steel industry with sample handling, surface preparation and quantitative analysis capabilities," *Journal of Analytical Atomic Spectrometry,* vol. 15, pp. 1321-1327, 2000.

[82] M. Kraushaar, R. Noll, and H. U. Schmitz, "Slag Analysis with Laser-Induced Breakdown Spectrometry," *Applied Spectroscopy,* vol. 57, pp. 1282-1287, 2003.

[83] F. R. Doucet, T. F. Belliveau, J.-L. Fortier, and J. Hubert, "Use of Chemometrics and Laser-Induced Breakdown Spectroscopy for Quantitative Analysis of Major and Minor Elements in Aluminum Alloys," *Applied Spectroscopy,* vol. 61, pp. 327-332, 2007.

[84] M. Z. Martin, N. Labbé, T. G. Rials, and S. D. Wullschleger, "Analysis of preservative-treated wood by multivariate analysis of laser-induced breakdown spectroscopy spectra," *Spectrochimica Acta Part B: Atomic Spectroscopy,* vol. 60, pp. 1179-1185, 2005.

[85] J. D. Ingle and S. R. Crouch, *Spectrochemical Analysis,* 1st ed.: Prentice Hall, 1988.

[86] M. Sabsabi and P. Cielo, "Quantitative Analysis of Aluminum Alloys by Laser-Induced Breakdown Spectroscopy and Plasma Characterization," *Applied Spectroscopy,* vol. 49, pp. 499-507, 1995.

[87] P. W. J. M. Boumans, "Chapter 4: Basica Concepts and Characteristics of ICP-AES," in *Inductively-Coupled Plasma Emission Spectroscopy, Part I: Methodology, Instrumentation and Performance*, ed New York: John Wiley and Sons, Inc., 1987, p. 100.

[88] R. Feinberg, T. W. Hänsch, A. L. Schawlow, R. E. Teets, and C. Wieman, "Laser polarization spectroscopy of atoms and molecules," *Optics Communications,* vol. 18, pp. 227-228, 1976/7// 1976.

[89] R. E. Teets, F. V. Kowalski, W. T. Hill, N. Carlson, and R. W. Haensch, "LASER POLARIZATION SPECTROSCOPY," *SPIE Semin Proc,* vol. 113, pp. 80-87, 1977.

[90] W. G. Tong and E. S. Yeung, "Polarization Spectroscopy for Elemental Analysis at Trace Concentrations," *Analytical Chemistry,* vol. 57, p. 70, 1985.

[91] G. Zizak, J. Lanauze, and J. D. Winefordner, "Cross-beam polarization in flames with a pulsed dye laser," *Applied Optics,* vol. 25, pp. 3242-3246, 1986.

[92] Z. T. Alwahabi, Z. S. Li, J. Zetterberg, and M. Aldén, "Infrared polarization

spectroscopy of CO2 at atmospheric pressure," *Optics Communications,* vol. 233, pp. 373-381, 2004.

[93] Z. S. Li, M. Rupinski, J. Zetterberg, Z. T. Alwahabi, and M. Aldén, "Mid-infrared polarization spectroscopy of polyatomic molecules: Detection of nascent CO2 and H2O in atmospheric pressure flames," *Chemical Physics Letters,* vol. 407, pp. 243-248, 2005.

[94] K. Nyholm, R. Maier, C. G. Aminoff, and M. Kaivola, "Detection of OH in flames by using polarization spectroscopy," *Applied Optics,* vol. 32, pp. 919-924, 1993.

[95] K. Nyholm, "Measurements of OH rotational temperatures in flames by using polarization spectroscopy," *Optics Communications,* vol. 111, pp. 66-70, 1994.

[96] A. A. Suvernev, A. Dreizler, T. Dreier, and J. Wolfrum, "Polarization-spectroscopic measurement and spectral of OH ($A^2\Sigma$-$X^2\Pi$) and NH ($A^3\Pi$-$X^3\Sigma$) transitions in atmospheric pressure flames simulation," *Applied Physics B: Lasers and Optics,* vol. 61, pp. 421-427, 1995.

[97] T. B. Settersten, R. L. Farrow, and J. A. Gray, "Infrared-ultraviolet double-resonance spectroscopy of OH in a flame," *Chemical Physics Letters,* vol. 369, pp. 584-590, 2003.

[98] Z. S. Li, C. Hu, J. Zetterberg, M. Linvin, and M. Aldén, "Midinfrared polarization spectroscopy of OH and hot water in low pressure lean premixed flames," *Journal of Chemical Physics,* vol. 127, p. 084310, 2007.

[99] X. Chen, B. D. Patterson, and T. B. Settersten, "Time-domain investigation of OH ground-state energy transfer using picosecond two-color polarization spectroscopy," *Chemical Physics Letters,* vol. 388, pp. 358-362, 2004.

[100] K. Nyholm, R. Fritzon, and M. Aldén, "Two-dimensional imaging of OH in flames by use of polarization spectroscopy," *Optics Letters,* vol. 18, pp. 1672-1674, 1993.

[101] J. Reppel and Z. T. Alwahabi, "A uniaxial gas model of the geometrical dependence of polarization spectroscopy," *Journal of Physics D: Applied Physics,* vol. 34, pp. 2670-2678, 2001.

[102] K. Nyholm, M. Kaivola, and C. G. Aminoff, "Polarization spectroscopy applied to C_2 detection in a flame," in *Applied Physics B: Lasers and Optics* vol. 60, ed: Springer Berlin / Heidelberg, 1995, pp. 5-10.

[103] A. Dreizler, T. Dreier, and J. Wolfrum, "Polarization spectroscopic measurement of the NH ($A^3\Pi$ - $X^3\Sigma$) transition in an ammonia / oxygen flame," *Journal of Molecular Structure*, vol. 349, pp. 285-288, 1995.

[104] B. Löfstedt, R. Fritzon, and M. Alédn, "Investigation of NO detection in flames by the use of polarization spectroscopy," *Applied Optics,* vol. 35, pp. 2140-2146, 1996.

[105] Z. S. Li, M. Rupinski, J. Zetterberg, and M. Aldén, "Mid-infrared PS and LIF detection of CH4 and C2H6 in cold flows and flames at atmospheric pressure," *Proceedings of the Combustion Institute,* vol. 30, pp. 1629-1636, 2005.

[106] A. De Giacomo, M. Dell'Aglio, O. De Pascale, and M. Capitelli, "From single pulse to

double pulse ns-Laser Induced Breakdown Spectroscopy under water: Elemental analysis of aqueous solutions and submerged solid samples," *Spectrochimica Acta Part B: Atomic Spectroscopy,* vol. 62, pp. 721-738, 2007.

[107] J. Kiefer, Z. Li, J. Zetterberg, M. Linvin, and M. Aldén, "Simultaneous laser-induced fluorescence and sub-Doppler polarization spectroscopy of the CH radical," *Optics Communications,* vol. 270, pp. 347-352, 2007.

[108] T. B. Settersten, R. L. Farrow, and J. A. Gray, "Coherent infrared-ultraviolet double-resonance spectroscopy of CH3," *Chemical Physics Letters,* vol. 370, pp. 204-210, 2003.

[109] K. Nyholm, R. Fritzon, N. Georgiev, and M. Aldén, "Two-photon induced polarization spectroscopy applied to the detection of NH3 and CO molecules in cold flows and flames," *Optics Communications,* vol. 114, pp. 76-82, 1995/1/15/ 1995.

[110] C. F. Kaminski, B. Liifstedt, R. Fritzon, and M. Aldén, "Two-photon polarization spectroscopy and (2 + 3) -photon laser induced fluorescence of N_2," *Optics Communications,* vol. 129, pp. 38-43, 1996.

[111] C. F. Kaminski and T. Dreier, "Investigation of Two-Photon-Induced Polarization Spectroscopy of the a-X (1, 0) Transition in Molecular Nitrogen at Elevated Pressures," *Applied Optics,* vol. 39, pp. 1042-1048, 2000.

[112] W. D. Kulatilaka, R. P. Lucht, S. F. Hanna, and V. R. Katta, "Two-color, two-photon laser-induced polarization spectroscopy (LIPS) measurements of atomic hydrogen in near-adiabatic, atmospheric pressure hydrogen/air flames," *Combustion and Flame,* vol. 137, pp. 523-537, 2004.

[113] T. A. Reichardt and R. P. Lucht, "Theoretical calculation of line shapes and saturation effects in polarization spectroscopy," *Journal of Chemical Physics,* vol. 109, pp. 5831-5843, 1998.

[114] T. A. Reichardt, W. C. Giancola, and R. P. Lucht, "Experimental investigation of saturated polarization spectroscopy for quantitative concentration measurements," *Applied Optics,* vol. 39, pp. 2002-2008, 2000.

[115] J. Seidel, "Theory of Two-Photon Polarization Spectroscopy of Plasma-Broadened Hydrogen λ Line," *Physical Review Letters,* vol. 57, p. 2154, 1986.

[116] S. A. Edelman, L. Y. Margolin, N. Y. Polynovskaya, and L. N. Pyatnitsky, "Measurements of the local temperature of atoms in a discharge plasma by polarization spectroscopy," *Physica B+C,* vol. 123, pp. 263-266, 1984.

[117] L. J. H. Z.T. Alwahabi, "In Preparation."

[118] V. Häyrinen, R. Oikari, and R. Hernberg, "Continuous Monitoring of Alkali Metals in Gas Flows Using Direct-Current Plasma Excited Atomic Spectroscopy," *Applied Spectroscopy,* vol. 58, pp. 111-121, 2004.

[119] B. N. Barman, V. L. Cebolla, A. K. Mehrotra, and C. T. Mansfield, "Petroleum and Coal," *Analytical Chemistry,* vol. 73, pp. 2791-2804, 2001.

[120] J. Bai, W. Li, and B. Li, "Characterization of low-temperature coal ash behaviors at

high temperatures under reducing atmosphere," *Fuel*, vol. 87, pp. 583-591, 2008.

[121] V. S. Somerset, L. F. Petrik, R. A. White, M. J. Klink, D. Key, and E. Iwuoha, "The use of X-ray fluorescence (XRF) analysis in predicting the alkaline hydrothermal conversion of fly ash precipitates into zeolites," *Talanta*, vol. 64, pp. 109-114, 2004.

[122] S. K. Gupta, R. P. Gupta, G. W. Bryant, and T. F. Wall, "The effect of potassium on the fusibility of coal ashes with high silica and alumina levels," *Fuel*, vol. 77, pp. 1195-1201, 1998.

[123] S. Gomes, M. François, M. Abdelmoula, P. Refait, C. Pellissier, and O. Evrard, "Characterization of magnetite in silico-aluminous fly ash by SEM, TEM, XRD, magnetic susceptibility, and Mössbauer spectroscopy," *Cement and Concrete Research*, vol. 29, pp. 1705-1711, 1999.

[124] M. Tiainen, J. Daavitsainen, and R. S. Laitinen, "The Role of Amorphous Material in Ash on the Agglomeration Problems in FB Boilers. A Powder XRD and SEM-EDS Study," *Energy & Fuels*, vol. 16, pp. 871 - 877, 2002.

[125] S. Wang, L. Baxter, and F. Fonseca, "Biomass fly ash in concrete: SEM, EDX and ESEM analysis," *Fuel*, vol. 87, pp. 372-379, 2008.

[126] M. Tsukada, H. Yamada, and H. Kamiya, "Analysis of biomass combustion ash behavior at elevated temperatures," *Advanced Powder Technology*, vol. 14, pp. 707-717, 2003.

[127] F. Scala and R. Chirone, "An SEM/EDX study of bed agglomerates formed during fluidized bed combustion of three biomass fuels," *Biomass and Bioenergy*, vol. 32, pp. 252 - 266, 2008.

[128] L. Fryda, C. Sobrino, M. Cieplik, and W. L. van de Kamp, "Study on ash deposition under oxyfuel combustion of coal/biomass blends," *Fuel*, vol. 89, pp. 1889-1902, 2010.

[129] Y. Liu, L. Zheng, X. Li, and S. Xie, "SEM/EDS and XRD characterization of raw and washed MSWI fly ash sintered at different temperatures," *Journal of Hazardous Materials*, vol. 162, pp. 161-173, 2009.

[130] M. Svane, M. Hagstrom, and J. B. C. Pettersson, "Chemical Analysis of Individual Alkali-Containing Aerosol Particles: Design and Performance of a Surface Ionization Particle Beam Mass Spectrometer," *Aerosol Science and Technology*, vol. 38, pp. 655 - 663, 2004.

[131] L. Douglas Smoot, "Modeling of coal-combustion processes," *Progress in Energy and Combustion Science*, vol. 10, pp. 229-267, 1984.

[132] S. Choi and C. H. Kruger, "Modeling coal particle behavior under simultaneous devolatilization and combustion," *Combustion and Flame*, vol. 61, pp. 131-144, 1985.

[133] P. K. Agarwal, "A single particle model for the evolution and combustion of coal volatiles," *Fuel*, vol. 65, pp. 803-810, 1986.

[134] M. Saito, M. Sadakata, M. Sato, and T. Sakai, "Devolatilization characteristics of single coal particles for combustion in air and pyrolysis in nitrogen," *Fuel*, vol. 66, pp.

717-721, 1987.

[135] V. S. Gururajan, T. F. Wall, and J. S. Truelove, "The combustion of evolved volatile matter in the vicinity of a coal particle--An evaluation of the diffusion limited model," *Combustion and Flame,* vol. 72, pp. 1-12, 1988.

[136] G. R. Johnson, P. Murdoch, and A. Williams, "A study of the mechanism of the rapid pyrolysis of single particles of coal," *Fuel,* vol. 67, pp. 834-842, 1988.

[137] S. C. Saxena, "Devolatilization and combustion characteristics of coal particles," *Progress in Energy and Combustion Science,* vol. 16, pp. 55-94, 1990.

[138] J. F. Stubington, G. Huang, and A. W. Scaroni, "Devolatilization times of mm-size coal particles," *Fuel,* vol. 70, pp. 1105-1108, 1991.

[139] Y. Zhao, M. A. Serio, and P. R. Solomon, "A general model for devolatilization of large coal particles," *Symposium (International) on Combustion,* vol. 26, pp. 3145-3151, 1996.

[140] Y. Ninomiya, L. Zhang, A. Sato, and Z. Dong, "Influence of coal particle size on particulate matter emission and its chemical species produced during coal combustion," *Fuel Processing Technology,* vol. 85, pp. 1065-1088, 2004.

[141] P. A. Bejarano and Y. A. Levendis, "Single-coal-particle combustion in O2/N2 and O2/CO2 environments," *Combustion and Flame,* vol. 153, pp. 270-287, 2008.

[142] R. ZajdlIk, L. Jelemenský, B. Remiarová, and J. Markos, "Experimental and modelling investigations of single coal particle combustion," *Chemical Engineering Science,* vol. 56, pp. 1355-1361, 2001.

[143] R. H. Essenhigh, "Combustion and flame propagation in coal systems: A review," *Symposium (International) on Combustion,* vol. 16, pp. 353-374, 1977.

[144] A. Williams, R. Backreedy, R. Habib, J. M. Jones, and M. Pourkashanian, "Modelling coal combustion: the current position," *Fuel,* vol. 81, pp. 605-618, 2002.

[145] M. Xu, R. Yan, C. Zheng, Y. Qiao, J. Han, and C. Sheng, "Status of trace element emission in a coal combustion process: a review," *Fuel Processing Technology,* vol. 85, pp. 215-237, 2004.

[146] J. Yu, J. A. Lucas, and T. F. Wall, "Formation of the structure of chars during devolatilization of pulverized coal and its thermoproperties: A review," *Progress in Energy and Combustion Science,* vol. 33, pp. 135-170, 2007.

[147] G. A. Simons, "The role of pore structure in coal pyrolysis and gasification," *Progress in Energy and Combustion Science,* vol. 9, pp. 269-290, 1983.

[148] A. K. Sadhukhan, P. Gupta, and R. K. Saha, "Characterization of porous structure of coal char from a single devolatilized coal particle: Coal combustion in a fluidized bed," *Fuel Processing Technology,* vol. 90, pp. 692-700, 2009.

[149] I. Külaots, A. Hsu, and E. M. Suuberg, "The role of porosity in char combustion," *Proceedings of the Combustion Institute,* vol. 31, pp. 1897-1903, 2007.

[150] I. Külaots, I. Aarna, M. Callejo, R. H. Hurt, and E. M. Suuberg, "Development of porosity during coal char combustion," *Proceedings of the Combustion Institute,* vol.

29, pp. 495-501, 2002.

[151] A. K. Sadhukhan, P. Gupta, and R. K. Saha, "Modelling of combustion characteristics of high ash coal char particles at high pressure: Shrinking reactive core model," *Fuel,* vol. 89, pp. 162-169, 2010.

[152] C. A. Gurgel Veras, J. Saastamoinen, J. A. Carvalho Jr, and M. Aho, "Overlapping of the devolatilization and char combustion stages in the burning of coal particles," *Combustion and Flame,* vol. 116, pp. 567-579, 1999.

[153] C. Branca and C. Di Blasi, "Global interinsic kinetics of wood oxidation," *Fuel,* vol. 83, pp. 81-87, 2004.

[154] C. Branca, A. Albano, and C. Di Blasi, "Critical evaluation of global mechanisms of wood devolatilization," *Thermochimica Acta,* vol. 429, pp. 133-141, 2005.

[155] C. Branca and C. Di Blasi, "Global Kinetics of Wood Char Devolatilization and Combustion," *Energy & Fuels,* vol. 17, pp. 1609-1615, 2003.

[156] C. Branca and C. D. Blasi, "Parallel-and Series-Reaction Mechanisms of Wood and Char Combustion," *Thermal Science,* vol. 8, pp. 51-63, 2004.

[157] C. Di Blasi, F. Buonanno, and C. Branca, "Reactivities of some biomass chars in air," *Carbon,* vol. 37, pp. 1227-1238, 1999.

[158] E. Bar-Ziv and I. I. Kantorovich, "Mutual effects of porosity and reactivity in char oxidation," *Progress in Energy and Combustion Science,* vol. 27, pp. 667-697, 2001.

[159] S. K. Bhatia and B. J. Vartak, "Reaction of microporous solids: The discrete random pore model," *Carbon,* vol. 34, pp. 1383-1391, 1996.

[160] K. B. Bischoff, "Accuracy of the pseudo steady state approximation for moving boundary diffusion problems," *Chemical Engineering Science,* vol. 18, pp. 711-713, 1963.

[161] G. B. DAVIS and J. M. HILL, "A Moving Boundary Problem for the Sphere," *IMA Journal of Applied Mathematics,* vol. 29, pp. 99-111, July 1, 1982 1982.

[162] G. F. Carey and P. Murray, "Perturbation analysis of the "Shrinking core"," *Chemical Engineering Science,* vol. 44, pp. 979-983, 1989.

[163] A. Kharab, "Numerical approximation to a moving boundary problem for the sphere," *Computers & Chemical Engineering,* vol. 21, pp. 559-562, 1997.

[164] A. Galgano and C. D. Blasi, "Modeling Wood Degradation by the Unreacted-Core-Shrinking Approximation," *Industrial & Engineering Chemistry Research,* vol. 42, pp. 2101-2111, 2003.

[165] K. C. Liddell, "Shrinking core models in hydrometallurgy: What students are not being told about the pseudo-steady approximation," *Hydrometallurgy,* vol. 79, pp. 62-68, 2005.

[166] A. K. Sadhukhan, P. Gupta, and R. K. Saha, "Modelling of pyrolysis of large wood particles," *Bioresource Technology,* vol. 100, pp. 3134-3139, 2009.

[167] H. Lu, E. Ip, J. Scott, P. Foster, M. Vickers, and L. L. Baxter, "Effects of particle shape and size on devolatilization of biomass particle," *Fuel,* vol. 89, pp. 1156-1168,

2010.

[168] C. Di Blasi, "Combustion and gasification rates of lignocellulosic chars," *Progress in Energy and Combustion Science,* vol. 35, pp. 121-140, 2009.

[169] I. Glassman and R. A. Yetter, "Environmental Combustion Considerations," in *Combustion*, 4th, Ed., ed Burlington: Academic Press, 2008, pp. 409-494.

[170] Y. Zheng, P. A. Jensen, A. D. Jensen, B. Sander, and H. Junker, "Ash transformation during co-firing coal and straw," *Fuel,* vol. 86, pp. 1008-1020, 2007.

[171] K. O. Davidsson, L.-E. Amand, and B. Leckner, "Potassium, Chlorine, and Sulfur in Ash, Particles, Deposits, and Corrosion during Wood Combustion in a Circulating Fluidized-Bed Boiler," *Energy & Fuels,* vol. 21, pp. 71 - 81, 2007.

[172] L. L. Baxter, T. R. Miles, T. R. M. Jr., B. M. Jenkins, T. Milne, D. Dayton, R. W. Bryers, and L. L. Oden, "The behavior of inorganic material in biomass-fired power boilers: field and laboratory experiences," *Fuel Processing Technology,* vol. 54, pp. 47 - 78, 1998.

[173] S. Srinivasachar, J. J. Helble, D. O. Ham, and G. Domazetis, "A kinetic description of vapor phase alkali transformations in combustion systems," *Progress in Energy and Combustion Science,* vol. 16, pp. 303-309, 1990.

[174] J. Hulston, G. Favas, and A. L. Chaffee, "Physico-chemical properties of Loy Yang lignite dewatered by mechanical thermal expression," *Fuel,* vol. 84, pp. 1940-1948, 2005.

[175] D. K. Shen, S. Gu, K. H. Luo, A. V. Bridgwater, and M. X. Fang, "Kinetic study on thermal decomposition of woods in oxidative environment," *Fuel,* vol. 88, pp. 1024-1030, 2009.

[176] L. J. Wibberley and T. F. Wall, "Alkali-ash reactions and deposit formation in pulverized-coal-fired boilers: experimental aspects of sodium silicate formation and the formation of deposits," *Fuel,* vol. 61, pp. 93-99, 1982.

[177] X. Wei, C. Lopez, T. v. Puttkamer, U. Schnell, S. Unterberger, and K. R. G. Hein, "Assessment of Chlorine-Alkali-Mineral Interactions during Co-Combustion of Coal and Straw," *Energy & Fuels,* vol. 16, pp. 1095 - 1108, 2002.

[178] L. A. Hansen, H. P. Nielsen, F. J. Frandsen, K. Dam-Johansen, S. Horlyck, and A. Karlsson, "Influence of deposit formation on corrosion at a straw-fired boiler," *Fuel Processing Technology,* vol. 64, pp. 189 - 209, 2000.

[179] H. P. Nielsen, F. J. Frandsen, K. Dam-Johansen, and L. L. Baxter, "The implications of chlorine-associated corrosion on the operation of biomass-fired boilers," *Progress in Energy and Combustion Science,* vol. 26, pp. 283 - 298, 2000.

[180] B. M. Jenkins, R. R. Bakker, and J. B. Wei, "On the properties of washed straw," *Bionmss and Biomergy,* vol. 10, pp. 177 - 200, 1996.

[181] A. Demirbas, "Sustainable cofiring of biomass with coal," *Energy Conversion and Management,* vol. 44, pp. 1465 - 1479, 2003.

[182] M. D. Mastrandrea and S. H. Schneider. (2005, *Global warming (World Book Online*

Reference Center. World Book, Inc ed.). Available: http://www.worldbookonline.com/wb/Article?id=ar226310

[183] P. A. Leighton, "Chapter 10," in *Photochemistry of air pollution*, 1st ed New York: Academic Press, 1961.

[184] B. A. Lomakin, *Zeitschrift für Anorganische und Allgemeine Chemie*, vol. 187, p. 75, 1930.

[185] G. Scheibe and O. Schnettler, *Naturwiss*, vol. 19, p. 134, 1931.

[186] A. Dinklage, *Plasma physics confinement, transport and collective effects* vol. 670. Berlin ; New York: Springer,, 2005.

[187] L.-J. HSU, "可提高成長奈米碳管之裝置 (A device improves the yield of carbon nanotube)," Taiwan Patent M241422, 2004.

[188] H. W. Kroto, J. R. Heath, S. C. O'Brien, R. F. Curl, and R. E. Smalley, "C60: Buckminsterfullerene," *Nature*, vol. 318, pp. 162-163, 1985.

[189] S. Iijima, "Helical microtubules of graphitic carbon," *Nature*, vol. 354, pp. 56-58, 1991.

[190] Y. M. Lai and et al., "A new 45° homo-biepitaxial YBCO grain boundary junction process fabricated using off-axis RF sputtering," *Journal of Physics D: Applied Physics*, vol. 40, p. 3670, 2007.

[191] T. S. Lai, W. F. Liao, H. F. Cheng, and I. N. Lin, "Epitaxial Growth and Characteristics of the YBCO/STO/YBCO Tunneling Junctions," *Chinese Journal Of Physics*, vol. 36, pp. 382-387, 1998.

[192] A. Służalec, *Theory Of Thermomechanical Processes In Welding*. Netherlands: Springer, 2005.

[193] G. P. Huffman, F. E. Huggins, N. Shah, and A. Shah, "Behavior of basic elements during coal combustion," *Progress in Energy and Combustion Science*, vol. 16, pp. 243-251, 1990.

[194] C. Di Blasi, E. G. Hernandez, and A. Santoro, "Radiative Pyrolysis of Single Moist Wood Particles," *Industrial & Engineering Chemistry Research*, vol. 39, pp. 873-882, 2000.

[195] C. Di Blasi and C. Branca, "Kinetics of Primary Product Formation from Wood Pyrolysis," *Industrial & Engineering Chemistry Research*, vol. 40, pp. 5547-5556, 2001.

[196] H. Thunman and B. Leckner, "Thermal conductivity of wood--models for different stages of combustion," *Biomass and Bioenergy*, vol. 23, pp. 47-54, 2002.

[197] H. Thunman, B. Leckner, F. Niklasson, and F. Johnsson, "Combustion of wood particles--a particle model for eulerian calculations," *Combustion and Flame*, vol. 129, pp. 30-46, 2002.

[198] R. J. Lang, "Ultrasonic Atomization of Liquids," *The Journal of the Acoustical Society of America*, vol. 34, pp. 6-8, 1962.

[199] D. W. Marquardt, "An Algorithm for Least-Squares Estimation of Nonlinear

Parameters," *Journal of the Society for industrial and Applied Mathematics,* vol. 11, pp. 431-441, 1963.

[200] A. E. N. Cable, NJ, US), Larsson, Johan Michael (Gothenburg, SE), Sandstrom, Lars Goran (Askim, SE), Kleman, Bengt (Gothenburg, SE), "Compact multimode laser with rapid wavelength scanning," United States Patent, 2010.

[201] T. N. Anderson, R. P. Lucht, T. R. Meyer, S. Roy, and J. R. Gord, "Diode-laser-based ultraviolet-absorption sensor for high-speed detection of the hydroxyl radical," *Optics Letters,* vol. 30, pp. 1321-1323, 2005.

[202] T. R. Meyer, S. Roy, T. N. Anderson, R. P. Lucht, R. Barron-Jimenez, and J. R. Gord, "10 kHz detection of CO2 at 4.5 μm by using tunable diode-laser-based difference-frequency generation," *Optics Letters,* vol. 30, pp. 3087-3089, 2005.

[203] Terrence R. Meyer, S. Roy, Thomas N. Anderson, Joseph D. Miller, Viswanath R. Katta, Robert P. Lucht, and James R. Gord, "Measurements of OH mole fraction and temperature up to 20 kHz by using a diode-laser-based UV absorption sensor," *Applied Optics,* vol. 44, pp. 6729-6740, 2005.

[204] J. Walewski, C. F. Kaminski, S. F. Hanna, and R. P. Lucht, "Dependence of partially saturated polarization spectroscopy signals on pump intensity and collision rate," *Physical Review A,* vol. 64, p. 063816, 2001.

[205] M. J. Jongerius, A. R. D. Van Bergen, T. Hollander, and C. T. J. Alkemade, "An experimental study of the collisional broadening of the Na-D lines by Ar, N2 and H2 perturbers in flames and vapor cells--I. The line core," *Journal of Quantitative Spectroscopy and Radiative Transfer,* vol. 25, pp. 1-18, 1981.

[206] J. W. Daily and C. Chan, "Laser-induced fluorescence measurement of sodium in flames," *Combustion and Flame,* vol. 33, pp. 47-53, 1978.

[207] R. C. Hilborn, "Einstein coefficients, cross sections, f values, dipole moments, and all that," *American Journal of Physics,* vol. 50, pp. 982-986, 1982.

[208] W. R. Hindmarsh and J. M. Farr, "Collision broadening of spectral lines by neutral atoms," *Progress in Quantum Electronics,* vol. 2, pp. 141, 143-214, 1973.

[209] M. J. Jongerius, T. Hollander, and C. T. J. Alkemade, "An experimental study of the collisional broadening of the Na-D lines by Ar and N2 perturbers in flames and vapor cells--II. The line wings," *Journal of Quantitative Spectroscopy and Radiative Transfer,* vol. 26, pp. 285-302, 1981.

[210] N. F. Allard, J. F. Kielkopf, and F. Allard, "Impact broadening of alkali lines in brown dwarfs," *The European Physical Journal D - Atomic, Molecular, Optical and Plasma Physics,* vol. 44, pp. 507-514, 2007.

[211] D. F. T. Mullamphy, G. Peach, V. Venturi, I. B. Whittingham, and S. J. Gibson, "Collisional broadening of alkali doublets by helium perturbers," *Journal of Physics B: Atomic, Molecular and Optical Physics,* vol. 40, p. 1141, 2007.

[212] A. Asfaw, T. B. Bacha, and D. D. Venable, "Shift and broadening of Na D lines at low pressure," *Journal of Quantitative Spectroscopy and Radiative Transfer,* vol. 84, pp.

325-337, 2004.

[213] J. F. Kielkopf, "Predicted alkali collision broadening by noble gases based on semiempirical potentials," *Journal of Physics B: Atomic and Molecular Physics*, vol. 9, p. L547, 1976.

[214] N. Lwin and et al., "Semiclassical collision calculations for the broadening and shift of the sodium D lines by noble gases," *Journal of Physics B: Atomic and Molecular Physics*, vol. 9, p. L161, 1976.

[215] J. F. Kielkopf, "Measurement of the width, shift and asymmetry of the sodium D lines broadened by noble gases," *Journal of Physics B: Atomic and Molecular Physics*, vol. 13, p. 3813, 1980.

[216] N. Allard and J. Kielkopf, "The effect of neutral nonresonant collisions on atomic spectral lines," *Reviews of Modern Physics*, vol. 54, p. 1103, 1982.

[217] M. J. O'Callaghan and A. Gallagher, "Sodium Doppler-free collisional line shapes," *Physical Review A*, vol. 39, p. 6190, 1989.

[218] F. Schuller and W. Behmenburg, "Perturbation of spectral lines by atomic interactions," *Physics Reports*, vol. 12, pp. 273-334, 1974.

[219] D. M. Bruce, M. Y. Mirza, and W. W. Duley, "Collision broadening and shift of the sodium 3S-4D and 3S-5S lines by He, Ar and N2," *Optics Communications*, vol. 27, pp. 76-78, 1978.

[220] F. Biraben and et al., "Broadening and shift of the sodium 3S-4D and 3S-5S two-photon lines perturbed by noble gases," *Journal of Physics B: Atomic and Molecular Physics*, vol. 10, p. 2369, 1977.

[221] M. Elbel, B. Kamke, and W. B. Schneider, "Collisional depolarization of excited sodium atoms," *Physica*, vol. 77, pp. 137-147, 1974.

[222] J. P. Woerdman, "Self-broadening of the Na 3S-5S and 3S-4D two-photon transitions," *Optics Communications*, vol. 28, pp. 69-72, 1979.

[223] J. F. Lancaster, *The Physics of Welding*, second ed.: Pergamon Press, 1986.

[224] Z. Bingul and G. E. Cook, "A real-time prediction model of electrode extension for GMAW," *Mechatronics, IEEE/ASME Transactions on*, vol. 11, pp. 47-54, 2006.

[225] J. Emsley, *The Elements*, 3rd ed. Oxford: Clarendon Press, 1998.

[226] A. B. Murphy, M. Tanaka, K. Yamamoto, S. Tashiro, J. J. Lowke, and K. Ostrikov, "Modelling of arc welding: The importance of including the arc plasma in the computational domain," *Vacuum*, vol. 85, pp. 579-584, 2010.

[227] S. F. Panter and J. S. Foster, "Stark effect in iron and the contrast with pole effect," *Proceedings of the Royal Society of London Series a-Mathematical and Physical Sciences*, vol. 162, pp. 0336-0348, Oct 1937.

[228] W. H. Press, B. P. Flannery, S. A. Teukolsky, and W. T. Vetterling, *Numerical Recipes in C*. New York: Cambridge University Press, 1988.

[229] S. Prucker, W. Meier, and W. Stricker, "A flat flame burner as calibration source for combustion research temperatures and species concentrations of premixed H2/air

flames," *Review of Scientific Instruments,* vol. 85, pp. 2908-2911, 1994.

[230] R. L. Gleason and D. W. Hahn, "The effects of oxygen on the detection of mercury using laser-induced breakdown spectroscopy," *Spectrochimica Acta Part B: Atomic Spectroscopy,* vol. 56, pp. 419-430, 2001.

[231] H. Oleschko and M. Muller, "Influence of Coal Composition and Operating Conditions on the Release of Alkali Species During Combustion of Hard Coal," *Energy & Fuels,* vol. 21, pp. 3240 - 3248, 2007.

[232] H. Oleschko, A. Schimrosczyk, H. Lippert, and M. Muller, "Influence of coal composition on the release of Na-, K-, Cl-, and S-species during the combustion of brown coal," *Fuel,* vol. 86, pp. 2275 - 2282, 2007.

[233] D. Nutalapati, R. Gupta, B. Moghtaderi, and T. F. Wall, "Assessing slagging and fouling during biomass combustion: A thermodynamic approach allowing for alkali/ash reactions," *Fuel Processing Technology,* vol. 88, pp. 1044 - 1052, 2007.

[234] P. Thy, S. Grundvig, B. M. Jenkins, R. Shiraki, and C. E. Lesher, "Analytical Controlled Losses of Potassium from Straw Ashes," *Energy & Fuels,* vol. 19, pp. 2571 - 2575, 2005.

[235] K. B. Bischoff, "Further comments on the pseudo steady state approximation for moving boundary diffusion problems," *Chemical Engineering Science,* vol. 20, pp. 783-784, 1965.

[236] J. Ray Bowen, "Comments on the pseudo-steady state approximation for moving boundary problems," *Chemical Engineering Science,* vol. 20, pp. 712-713, 1965.

[237] C. T. J. Alkemade, T. Hollander, W. Snelleman, and P. J. T. Zeegers, *Metal vapours in flames*. Oxford [Oxfordshire] ; New York :: Pergamon Press, 1982.

[238] P. A. Horne and P. T. Williams, "Influence of temperature on the products from the flash pyrolysis of biomass," *Fuel,* vol. 75, pp. 1051-1059, 1996.

[239] A. H. Galmed and M. A. Harith, "Temporal follow up of the LTE conditions in aluminum laser induced plasma at different laser energies," *Applied Physics B: Lasers and Optics,* vol. 91, pp. 651-660, 2008.

[240] R. Hilborn, "Einstein coefficients, cross sections, f values, dipole moments, and all that," 2002.

[241] K. Schofield, "A New Method to Minimize High-Temperature Corrosion Resulting from Alkali Sulfate and Chloride Deposition in Combustion Systems. I. Tungsten Salts," *Energy & Fuels,* vol. 17, pp. 191 - 203, 2003.

[242] J. N. Knudsen, P. A. Jensen, and K. Dam-Johansen, "Transformation and Release to the Gas Phase of Cl, K, and S during Combustion of Annual Biomass," *Energy & Fuels,* vol. 18, pp. 1385 - 1399, 2004.

[243] S. C. Cha and M. Spiegel, "Local reactions between NaCl and KCl particles and metal surfaces," *Corrosion Engineering, Science and Technology,* vol. 40, pp. 249 - 254, 2005.

[244] M. Muller, K.-J. Wolf, A. Smeda, and K. Hilpert, "Release of K, Cl, and S Species

during Co-combustion of Coal and Straw," *Energy & Fuels,* vol. 20, pp. 1444 -1449, 2006.

[245] D. C. Dayton, D. Belle-Oudry, and A. Nordin, "Effect of Coal Minerals on Chlorine and Alkali Metals Released during Biomass/Coal Cofiring," *Energy & Fuels,* vol. 13, pp. 1203 - 1211, 1999.

[246] P. Henderson, P. Szakalos, R. Pettersson, C. Andersson, and J. Hogberg, "Reducing superheater corrosion in wood-fired boilers," *Materials and Corrosion,* vol. 57, pp. 128 - 134, 2006.

[247] F. Y. Yueh, R. C. Sharma, J. P. Singh, and H. Zhang, "Evaluation of the potential of laser-induced breakdown spectroscopy for detection of trace element in liquid," *Journal of the Air & Waste Management Association,* vol. 52, pp. 1307-1315, 2002.

Appendix

A. Seeding Concepts

A-1. Cylindrical Premixed Laminar Burner

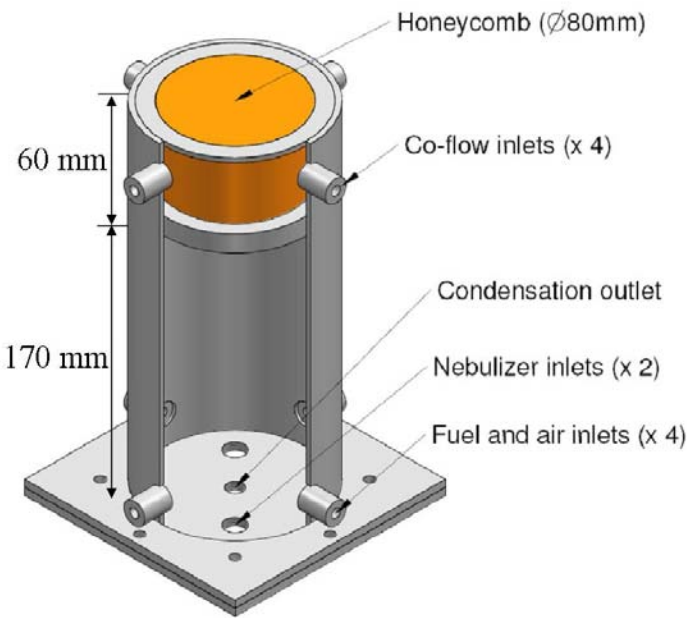

Figure A-1 Schematic cylindrical premix laminar burner employed in **Chapter 6** (Prepared by Shaun Chan)

A-2 Seeding Rate of Salt

The seeding rate is critical to calculate the temporal number density of seeded target species (n_s, ppm or atoms/m^3) in the flame that is the fundamental reference of calibration process. The calculation concept of temporal number density is eligible for the estimation of temporal concentration of the target species in the entire flame. It is assumed that the calculation is uniform within the flame. It should be aware that the n_s specifically indicates the total concentration of [Na] ($[Na]_{total}$) and [K] ($[K]_{total}$) instead of the seeded salt molecule. This can avoid the variation between different alkali salts regarding the difference molar mass of various applicable alkali salts.

The chosen alkali salts of [Na] and [K] are sodium sulphite (Na_2SO_3) and potassium sulphate (K_2SO_4). In order to determine the seeding rate based on the constant seeding air flowrate, the consumption amount of salt solution in a four-hour seeding process was measured in the volume variation before and after the experiment with a high accuracy measuring jug. The experimental consumption rate of the seeded salt solution, $12\ \mathrm{ml/hr} \pm 4.17\%$, was repeated five times and the standard deviation could be determined. Furthermore, condensation was considered. The condensed solution on the bottom of the burner flowed back to the nebulising system during the calibration process. This can improve not only the accuracy of calculated n_s but also the stability of premixed laminar seeded flame.

B. Analysis of solid-fuel Particles

NOTE:
This appendix is included on pages iii-v of the print copy
of the thesis held in the University of Adelaide Library.

C. Quarter-wave Plate

In the case of linearly polarised pump beam, a quarter-wave plate (QwP) introduced in **Figure 3-1** was applied. To achieve this, the specific arrangement has been revealed, as shown in **Figure C-1**. Given that the angle, α, must be satisfied with, the distance **R** between the Point A and C is related to the chosen distance **d** between the Point A and B. Therefore, once the **d** is determined, it is simple to align the optics checking if the reflection of pump beam locates in the Point C leading to the sufficient distance, which can be calculated using d·tan(2α), to the Point A

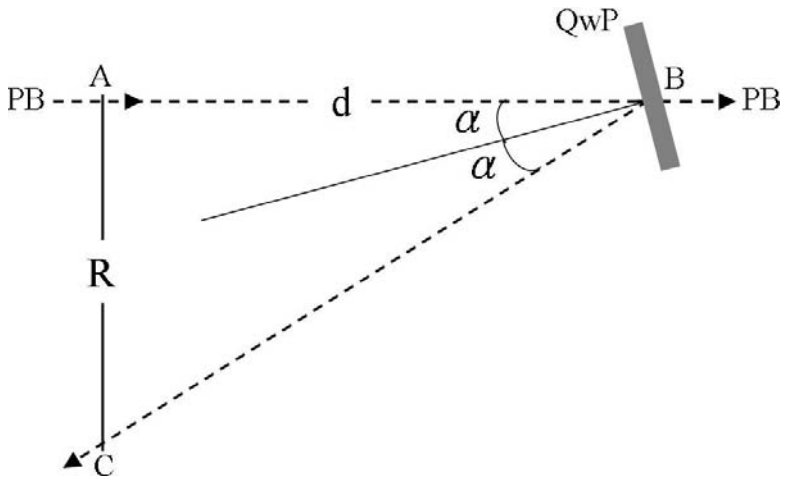

Figure C-1 Arrangement of the quarter-wave plate and the polariser in the path of pump beam (PB) provides the linear polarisation of pump beam. α = 6.3° in the present arrangement for **d** = 200 mm

D. ND Filter

The transmittance (T_{ND}) of various models of Natural Density filter (ND filter) can be obtained, as follows:

$$T_{ND} = 10^{-x/100}$$

Eq. D-1

where, *x* is the model number, namely 0, 10, 20, 30, 40, 50, 80, 100, 200 and 300.

E. Kramers-Kronig relation

The Kramers–Kronig relation is mathematical properties representing the real and imaginary parts of any complex function, which is analytic in the upper half-plane. This relation represents the real and imaginary parts of response functions in physical systems. The causality implies the analyticity condition is satisfied. Conversely, analyticity implies causality of the corresponding physical system.

F. Polarisation Dependent Numerical Factor

Table F-1 The factor $\zeta_{J_f \leftarrow J_i}$ gives the J dependence of the polarisation signal for circular polarised light

	$J_2=J+1$	$J_2=J$	$J_2=J+1$
$J_1=J+1$	$\frac{3(2J^2+J(4+r)+1+r)}{2(J+1)(2J+3)}$	$-\frac{3}{2(J+1)}$	$-\frac{3}{2}$
$J_1=J$	$-\frac{3}{2(J+1)}$	$\frac{3}{2J(J+1)}$	$\frac{3}{2J}$
$J_1=J-1$	$-\frac{3}{2}$	$\frac{3}{2J}$	$\frac{3(2J^2-rJ-1)}{2J(2J-1)}$

Table F-2 The factor $\zeta_{J_f \leftarrow J_i}$ gives the J dependence of the polarisation signal for linear polarised light

	$J_2=J+1$	$J_2=J$	$J_2=J+1$
$J_1=J+1$	$\frac{3(2J^2+J(4+5r)+5+5r)}{10(J+1)(2J+3)}$	$-\frac{3(2J-1)}{10(J+1)}$	$\frac{3}{10}$
$J_1=J$	$-\frac{3(2J-1)}{10(J+1)}$	$\frac{3(2J+3)(2J-1)}{10J(J+1)}$	$-\frac{3(2J+3)}{10J}$
$J_1=J-1$	$\frac{3}{10}$	$-\frac{3(2J+3)}{10J}$	$\frac{3(2J^2-5rJ+3)}{10J(2J-1)}$

G. Dichroism

Dichroism is the selective absorption for two orthogonal polarisation components of incident electromagnetic radiation. If the characteristic modes of polarisation of propagation in the medium are linearly polarised, selective absorption of one linearly polarised state is termed as linear dichroism. Similarly, for characteristic propagation of orthogonal circularly polarised states, the required term is defined as circular dichroism.

H. Birefringence

A substance is birefringent indicating it exhibits different refractive indices for two orthogonal polarisation components of incident radiation. Regarding dichroism, the birefringence may be linear or circular for the cases of linearly or circularly polarised characteristic modes of propagation in the medium respectively.

I. Matlab Codes

I-1 Image Process of a 9x9 Matrix

```
leftCirclePosition = [0 0];
midCirclePosition = [190 0];
rightCirclePosition = [460 0];
leftCircleSize = [170 200];
midCircleSize = [210 200];
rightCircleSize = [115 200];

leftCircleCrop = [leftCirclePosition leftCircleSize];
midCircleCrop = [midCirclePosition midCircleSize];
rightCircleCrop = [rightCirclePosition rightCircleSize];

file = ['C:\sample.tif'];

K = 2334;

wcircleSum = zeros(K, 3);

for i = 1:K
    image    = double(imread(file,i));
    leftCircleImage   = imcrop(image,leftCircleCrop);
    maxLC = max(max(leftCircleImage));
    for m = 1:size(leftCircleImage, 1)
        for n = 1:size(leftCircleImage, 2)
            if (leftCircleImage(m,n) == maxLC)
                maxLC = [m,n];
             end
        end
    end
    tempLC = imcrop(leftCircleImage,[maxLC(2)+-4, maxLC(1)+-4,8,8]);

    midCircleImage   = imcrop(image,midCircleCrop);
```

```
    maxMC = max(max(midCircleImage));
    for m = 1:size(midCircleImage, 1)
        for n = 1:size(midCircleImage, 2)
            if (midCircleImage(m,n) == maxMC)
                maxMC = [m,n];
            end
        end
    end
    tempMC = imcrop(midCircleImage,[maxMC(2)+-4, maxMC(1)+-4,8,8]);

    rightCircleImage   = imcrop(image,rightCircleCrop);
    maxRC = max(max(rightCircleImage));
    for m = 1:size(rightCircleImage, 1)
        for n = 1:size(rightCircleImage, 2)
            if (rightCircleImage(m,n) == maxRC)
                maxRC = [m,n];
            end
        end
    end
    tempRC = imcrop(rightCircleImage,[maxRC(2)+-4, maxRC(1)+-4,8,8]);

    leftCircleSum=sum(sum(tempLC));
    midCircleSum=sum(sum(tempMC));
    rightCircleSum=sum(sum(tempRC));
    wcircleSum(i,:) = [leftCircleSum midCircleSum rightCircleSum];
end
```

J. Appendix of Autobiography

J-1 Education

- Ph. D., since July 2006, School of Chemical Engineering, University of Adelaide, South Australia, Australia
  Major: Laser diagnostic techniques
  Topic: Measure alkali species released from burning solid-fuel particles.
- Postgraduate: Master of Science in Physics , 1999 ~ 2001, University of Chung Yuan, Taiwan
  Major: The synthesis of carbon nanotubes using chemical vapor deposition (CVD)
  Topic: The synthesis carbon nanotubes and properties measurement
- Bachelor of Science in Physics , 1995 ~ 1999, University of Chung Yuan, Taiwan
  Major: The synthesis of carbon nanotubes using Arc discharge
  Topic: Optimization of the synthesis of carbon nanotubes using Arc discharge

J-2 Experience

R&D Engineer, AFOP, Taiwan 2004- 2006

Responsibilities included characterization of new materials and processes leading to viable fibre optic products. This included evaluating new materials, benchmarking competitive products, modification to match new product specifications and optimizing manufacturing processes.

R&D Engineer, TECONANO, Taiwan 2002-2004

Responsibilities included the investigation and qualification of advanced nano-material, optimizing manufacturing processes.

R&D Engineer, Uni Lite, Taiwan 2001-2002

Responsibilities included the development and improvement for LED production.

J-3 Publications

Journal Papers:

Hsu, L.J., Alwahabi, Z.T., Nathan, G.J., Li, Y., Li, Z.S. and Aldén, M. (2011), Na and K released from burning particles of brown coal and pine wood in a laminar premixed methane flame using quantitative Laser-Induced Breakdown Spectroscopy, *Applied Spectroscopy* vol. 65, No. 6, pp. 684-691.

Alwahabi, Z.T., **Hsu, L.J.**, Linton, V., Meeuwissen, K. (2011), Detection of Nascent Iron Atoms in Metal Welding by Polarisation Spectroscopy, *Applied Spectroscopy*, ***To be submitted.***

Hsu, L.J., Alwahabi, Z.T., Nathan, G.J., King, K.D., Ashman, P.J., Li, Z.S. and Aldén, M. (2011), Assessment of atomic Na and K released from burning pine wood particles using atomic emission spectroscopy, *Optics and Lasers in Engineering*, ***To be submitted.***

Hsu, L.J., Alwahabi, Z.T., Nathan, G.J., van Eyk, Philip, King, K.D., Ashman, P.J., Li, Z.S. and Aldén, M. (2011), Combustion Model of solid-fuel particles associated with atomic Na and K release using atomic emission spectroscopy, *Combustion and Flame*, ***To be submitted.***

Hsu, L.J., Alwahabi, Z.T., Nathan, G.J., Wang, J., King, K.D., Ashman, P.J. (2011), Mathematical simulation in the experimental detection atomic sodium in the seeded flame using polarisation spectroscopy, *Applied Optics*, ***To be submitted.***

Conference Papers:

Hsu, L.J., Alwahabi, Z.T. , Nathan, G.J. , Li, Z.S. and Aldén, M. (2010), Study of the quantitative release of sodium and potassium from brown coal and pine wood in a laminar pre-mixed methane flame using LIBS, *2009 Annual Bulletin of the Australian Institute of High Energetic Materials* **1**, 17-22.

Hsu, L.J., Alwahabi, Z.T., Nathan, G.J., Li, Y., Li, Z.S. and Aldén, M. (2010), Quantitative concentrations of sodium and potassium released from brown coal and pine wood in a laminar premixed flame using LIBS, *Chemeca: The 40th Australasian Chemical Engineering Conference*, paper #246 (11 pages). ISBN: 978-085-825-9713.

Hsu, L.J., Li, Y., Alwahabi, Z.T. , Nathan, G.J. , Li, Z.S. and Aldén, M. (2009), Quantitative measurement of sodium and potassium released from Australian Loy Yang coal and pine wood by using laser induced breakdown spectroscopy, 'Australasian Conference on Optics, Lasers and Spectroscopy and Australian Conference on Optical Fibre Technology' The University of Adelaide, Adelaide, Australia, pp. 453-464.

Hsu, L.J., Alwahabi, Z.T. , Nathan, G.J. , Li, Z.S. and Aldén, M. (2009), Study of Released

Atomic Potassium and Sodium of Loy Yang Coal and Pine Wood in a Laminar Pre-mixed Methane Flame, 'Proceedings of the Australian Combustion Symposium' The University of Queensland, Australia, pp. 211-214.

Hsu, L.J., Alwahabi, Z.T. , Nathan, G.J. , Li, Z.S. and Aldén, M. (2009), Study of the quantitative release of sodium and potassium from brown coal and pine wood in a laminar pre-mixed methane flame using LIBS, 'Interdisciplinary Conference on Chemical, Mechanical and Materials Engineering (2009 ICCMME)' Australian Institute of High Energetic Materials, Melbourne, Australia, pp. 77-75.

ISSN/0004-0966X/04/3502-0825, (2004) Spray-coating process for preparing CNT-FED cathode, SID.

Pattern:

『Equipment of improving the growth of carbon nanotubes』Patent in Republic of China (2003), the patent announcement number M241422 of the Republic of China.

Master Thesis:

『Carbon nanotubes synthesized by chemical vapor deposition of pyrolytic methane』, (2001) Thesis for the Master of Science in Physics, Chung Yuan Christian University, Taiwan.